Modelling surfactant adsorption and transport in porous media : influence of adsorption thermodynamics and kinetics

Zaineb Zaafouri

THÈSE

Pour obtenir le grade de

DOCTEUR DE L'UNIVERSITE GRENOBLE ALPES

Spécialité : **PHYSIQUE APPLIQUÉE**

Arrêté ministériel : 25 mai 2016

Présentée par

Zaineb ZAAFOURI

Thèse dirigée par **Benoit COASNE,** CNRS

préparée au sein du **Laboratoire Interdisciplinaire de Physique** dans **l'École Doctorale Physique**

Modélisation de l'adsorption et du transport des surfactants en milieu poreux: Influence de la thermodynamique et de la cinétique de l'adsorption

Modeling Surfactant Adsorption and Transport in Porous Media: Influence of Adsorption Thermodynamics and Kinetics

Thèse soutenue publiquement le **06 Novembre 2020**
devant le jury composé de :

Madame Joelle Aubin
DIRECTRICE DE RECHERCHE, Laboratoire De Genie Chimique Toulouse, CNRS/UNIVERSITE DE TOULOUSE, Rapportrice

Madame Flor Siperstein
PROFESSEUR, CEAS - Academic & Research, Department of Chemical Engineering & Analytical Science/ University Of Manchester, Rapportrice

Madame Elise Lorenceau
DIRECTRICE DE RECHERCHE, Laboratoire Interdisciplinaire de Physique, CNRS/UNIVERSITE GRENOBLE ALPES, Présidente

Monsieur Benjamin Rotenberg
DIRECTEUR DE RECHERCHE, Laboratoire PHysicochimie des Electrolytes et Nanosystèmes InterfaciauX, CNRS/SORBONNE UNIVERSITE, Examinateur

Université Grenoble Alpes
Ecole doctorale de physique - Laboratoire Interdisciplinaire de Physique
IFP Energies Nouvelles – Département Géofluides et Roches

Modeling Surfactant Adsorption and Transport in Porous Media: Influence of Adsorption Thermodynamics and Kinetics

By: **Zaineb Zaafouri**

Doctoral Thesis in Applied Physics

Doctoral Advisor: **Dr. Benoit Coasne**
Doctoral Tutor: **Dr. Daniela Bauer**

Presented and defended publicly on the 6th of November 2020

To a jury composed of:

Dr.	Joelle	**Aubin**	Reviewer
Prof.	Flor	**Siperstein**	Reviewer
Dr.	Elise	**Lorenceau**	President of the jury
Dr.	Benjamin	**Rotenberg**	Examinator
Dr.	Benoit	**Coasne**	Member of the jury
Dr.	Daniela	**Bauer**	Member of the jury
Dr.	Guillaume	**Batôt**	Member of the jury
Dr.	Carlos	**Nieto-Draghi**	Member of the jury

Acknowledgment

This thesis work is the fruit of the contributions of a good number of people whose exchanges, ideas and constructive criticism have greatly helped me to progress throughout these three years. I would like to express my deepest gratitude to all of them.

This thesis work was carried out within the Geosciences division of IFP Energies nouvelles. I would like therefore to thank IFPEN and more particularly Olga Vizika, Benjamin Hezhaft and Jean-Marc Lombard for giving me the opportunity to integrate this division and particularly the Geofluids and Rocks Department.

I thank my thesis director Benoit Coasne for his precious advice, his scientific rigor and his availability in spite of all his responsibilities. I would like to thank him as well for his patience and all the time devoted to this thesis.

I warmly thank my promoters at IFPEN: Daniela Bauer, Guillaume Batôt and Carlos Nieto-Dragui for their involvement and exceptional support in my thesis. I thank them for first approving my internship at IFPEN and giving me confidence needed to pursue the PhD. Without you, this work would not have been as successful as it is.

Thank you, Daniela, for your timely and astute guidance on both technical and general levels. Thank you for your investment in this thesis and for helping me shape the way forward in the key periods of this work. Thank you, Guillaume, for your continuous support, you have always pushed me to give the best of myself and for the significant time spent explaining the LBM code and reviewing this PhD report. Thank you, Carlos, for the time you gave me, especially during the writing process, for your rigor and constructive advice.

I am deeply grateful to all of you, thank you for your numerous advice, the rigor you transmitted to me, your constructive criticisms which helped me a lot, for always being there when I needed it and for everything you taught me. I learned a lot with you: during our meetings and I enjoyed it very much. You have helped me to overcome all the difficult steps throughout these three years.

I would like to thank the members of the jury for taking the time to review this work and for the very interesting and enriching scientific discussions we were able to have. Many thanks to Professor Flor Siperstein and Doctor Joelle Aubin for evaluating this work as reviewers and special thanks to Doctor Elise Lorenceau and Doctor Benjamin Rotenberg for participating in this jury as examinators.

I also thank all the people I have been able to interact with over the past three years at the IFPEN who have contributed in one way or another to this work: Jalila, Souhail and Patience. I would like to thank Sylvie, Meriem, Djamela and Amel for their administrative support from the first to the last day at IFPEN.

The doctoral experience was infinitely better thanks to the friendships I made. I would like to thank my fellow doctoral students and friends for the shared moments during these three years: Imane G., Imane Y., Ines R., Dandan Y., Sophie L., Adriana T., Nargess D., Gael,C., Massinissa H., Hamza T., Mohamed C., Hanen B., Eli A. and Arij B. I also thank my office colleagues: Seny K., Pierre C. and Konchana K., even though each of them was there for a few months, but it was a pleasure to be able to share the office with them.

Imane Y. these last three years could not have passed without your presence, our laughter and our shared meals, and our discussions about everything and nothing on the way home. You are a genuine and caring person and I cherish your friendship.

I also thank my best friend and sister by heart Roua, for being present during my doubtful phases. I thank my friends: Sana, Fida, Adnen for their presence and encouragement.

I thank my family: my parents and brothers. Zied and Amir, I thank you from the bottom of my heart for your unwavering trust and unconditional love, despite the distance, you have always supported me. Mom, Dad, I feel very honored and blessed to have you as my parents. I would not have gotten to where I am today without you in my life. You have been pillars of support, guidance and love in my life since the day I was born. I feel so good today, and words cannot express how important your guidance is to me. This accomplishment would not have been possible without your support, thank you so much for believing in me. You are the best parents in the world.

Contents

List of Figures

List of Tables

Nomenclature

List of abbreviations

BET Brunauer–Emmett–Teller

BGK Bhatnagar, Gross and Krook

CFD Computational Fluid Dynamics

DR Dubinin–Radushkevich

FHP Frisch, Hasslacher and Pomeau

HPC High-performance computing

HPP Hardy, Pazzis and Pomeau

LBM Lattice Boltzmann method

LGA Lattice gas automata

LGCA Lattice gas cellular automata

MRT Multi-relaxation-time

SPT Scaled particle theory

TRT Two relaxation-time

TVFM Volume-filled micropore theory

List of lattice Boltzmann Method symbols

c_a^{∞} Maximum concentration for adsorbed tracer molecules

Δt Lattice Boltzmann time unit

Δt_0 Injection time

Δx Lattice Boltzmann length unit

$\Gamma(\mathbf{r},t) = c_a(\mathbf{r},t)\Delta x$ Adsorbed amount corresponding to surface concentration

Γ^{∞} Maximum adsorbed concentration per position r

Λ, $\Lambda^{\pm}$ LBM-TRT numerical parameters

$\lambda^{\pm}$ Relaxation rates

$\rho(\mathbf{r},t) = \sum_{q=0}^{Q_m} f_q(\mathbf{r},t)$ Fluid density

$\sigma_x^2(t)$ Displacement variance

$\mathbf{r} = (x,y)$ Discrete accessible position

$\mathbf{v}_q$ Discrete velocity in LBM-TRT scheme

$\tilde{\tilde{c}}(\mathbf{r},t) = \sum_q \tilde{\tilde{g}}_q(\mathbf{r},t)$ Post-adsorption concentration of the free tracer molecules

$\tilde{\tilde{c}}_a(\mathbf{r},t)$ Post-adsorption concentration of the adsorbed tracer molecules

$\tilde{\tilde{c}}_{a_{m'}}(\mathbf{r},t)$ Post-adsorption concentration of adsorbed aggregated monomers

$\tilde{\tilde{c}}_{a_m}(\mathbf{r},t)$ Post-adsorption concentration of adsorbed isolated monomers

$\tilde{\tilde{g}}_q(\mathbf{r},t)$ Post-adsorption molecule distribution

$\tilde{c}(\mathbf{r},t) = \sum_q \tilde{g}_q(\mathbf{r},t)$ Post-collision concentration of the free tracer post collision

$\tilde{f}_q(\mathbf{r},t)$ Post-collision distribution of particles for Stokes simulation

$\tilde{g}_q(\mathbf{r},t)$ Post-collision distribution of particles for ADE and adsorption simulation

$\tilde{x}_q(\mathbf{r},t) = \tilde{g}_q(\mathbf{r},t)/\tilde{c}(\mathbf{r},t)$ Fraction of molecules having a velocity along q at time t and position $\mathbf{r}$

$\tilde{c}_{a,m'}(\mathbf{r},t)$ Post-collision concentration of adsorbed aggregated monomers

$\tilde{c}_{a,m}(\mathbf{r},t)$ Post-collision concentration of adsorbed isolated monomers

$c(\mathbf{r},t) = \sum_{q=0}^{Q_m} g_q(\mathbf{r},t)$ Concentration of the free tracer particles

$c_a(\mathbf{r},t)$ Concentration of the adsorbed tracer molecules

$c_l(x,t) = \frac{1}{L_y}\sum_y c(\mathbf{r},t)$ Normalized concentration at lateral position x

$c_a(\mathbf{r},t)$ Post-collision concentration of the adsorbed tracer molecules

$D(t) = \frac{1}{2}\frac{\partial \sigma_x^2(t)}{\partial t}$ Time derivative of the displacement variance

$D_{xx} = D_{yy} = D_m/\Lambda^-$ Numerical diffusion coefficient

$e_q^{\pm}$ Symmetric/anti-symmetric equilibrium components

$f_q^{\pm}$ Symmetric/Anti-symmetric components

L_x, L_y 2D Channel dimension

$n_q^{\pm}$ Symmetric/anti-symmetric non-equilibrium components

$p'_A = k'_A \Delta t / \Delta x$ LB cooperative model adsorption rate

$p'_D = k'_D \Delta t$ LB cooperative model desorption rate

$P(\delta x, t)$ Propagator corresponding to displacement distribution

$p_A = k_A \times \Delta t / \Delta x$ LB adsorption rate

$p_D = k_D \times \Delta t$ LB desorption rate

$Q_m = Q - 1$ Number of non-zero velocity

t_q^m, t_q^*, t_q^a Isotropic weight families (coordinate,diagonal)

t_{disp} t at the stationary dispersive regime where $\frac{\partial^2 \sigma_x^2(t)}{\partial t^2} < 10^{-9}$

U Average velocity

$U_x(y)$ Poiseuille velocity profile of the flow

U_{max} Maximum velocity of the flow

v_e Diffusion-scale equilibrium parameter

v_s Lattice Boltzmann sound velocity

x Lateral position within the geometry

x_0 Lateral injection position within the geometry

$\boldsymbol{U}(\mathbf{r}, t) = \frac{\mathbf{j}(\mathbf{r}, t)}{\rho}$ Macroscopic velocity vector

$\mathbf{j}(\mathbf{r}, t) = \sum_{q=1}^{Q_m} f_q(\mathbf{r}, t).\mathbf{v}_q$ Macroscopic momentum vector

$f_q(\mathbf{r}, t)$ Distribution of particles in position $\mathbf{r}$ at time t for Stokes simulation

$g_q(\mathbf{r}, t)$ Distribution of particles in position $\mathbf{r}$ at time t for ADE and adsorption simulation

c_0 Initial concentration at position $\mathbf{r}$

List of physical symbols

β Packing fraction of the aggregated monomers

$\boldsymbol{f}$ Applied force to induce transport

$\boldsymbol{U}$ Velocity vector of the fluid

Γ Adsorbed amount of molecules

Γ^{∞} Maximum adsorption capacity

Γ_e Adsorbed amount of molecules at equilibrium

Γ_m Adsorbed amount of individual monomers

$\Gamma_m(c,t)$ Surface concentration of individual adsorbed monomers m

Γ_m^{∞} Maximum adsorption capacity for monolayer saturation

Γ_z Amount of vacant sites

Γ_{hm} Adsorption amount of hemimicelles

$\Gamma_{m'}(c,t)$ the surface concentration in aggregated monomers m'

μ Fluid dynamic viscosity

ν Fluid kinematic viscosity

Ω Collision term in Boltzmann equation

ϕ Porous media porosity

ρ Fluid density

σ^2 Variance of the concentration distribution

σ^2_{disp} Variance from the displacement distribution of the concentration at the dispersive regime ($t \to \infty$)

$\mathrm{Pe} = \frac{UL}{D_m}$ Peclet number

$\mathrm{Re} = \frac{UL}{\nu}$ Reynolds number

CMC Critical Micelle Concentration

A, B, α_{RP} Redlich-Peterson isotherm parameters

c Solute concentration

c_e Concentration at equilibrium

c_s Critical surface concentration

D_m Molecular self-diffusion coefficient

D_{eff}^{ads} Effective diffusion coefficient for Henry adsorption

f Particle distribution in Boltzmann equation

J_A Advective flux

J_D Diffusive flux

K Porous medium permeability

$k' = \frac{k'_A}{k'_D}$ Cooperative model adsorption ratio

k'_A Cooperative model adsorption rate

k'_D Cooperative model desorption rate

$k = k_A/k_D$ Adsorption ratio

k_A Adsorption coefficient

k_D Desorption coefficient

k_f Freundlich adsorption constant

k_H Henry constant

k_L Langmuir constant

k_m Monomers adsorption ratio

k_s, α_s Sips adsorption parameters

k_{hm} Adsorption ratio for hemimicellization

k_{Lf}, α_{Lf} Langmuir-Freundlich isotherm parameters

L Characteristic dimension

n Aggregation number

P Pressure

U Flow velocity

D_{eff} Effective dispersion coefficient

Introduction

General introduction

In recent years, there has been a new momentum in the field of adsorption science and technology [5]; in addition to traditional applications such as air and water purification, adsorption processes are now widely used in the oil and petrochemical sectors as well as in the preparation of industrial gases. Among important adsorption applications, we can mention gas mask manufacture by using activated carbon to trap toxic gases, ion exchange methods used to soften water, adsorption chromatography to purify and separate pigments, etc. The widespread use of adsorption is linked to the important number of different materials available to design processes "on demand". Indeed, the huge number of adsorbate/adsorbent combinations makes adsorption a mature technology for a broad range of applications. The presence of an adsorbate at the adsorbent surface alters the porous solid properties. Among well-known adsorbates, surfactants is an important family which allows covering a broad spectrum of properties, applications, etc. Surfactants, which are amphiphilic molecules combining a hydrophilic head with a hydrophobic tail, constitute an important class in Soft Matter. Besides their ability to decrease surface tension by getting adsorbed at interfaces, surfactants in water exhibit a complex phase diagram, i.e. at low concentrations they are present as individual monomers in solution and above a certain concentration, the critical micelle concentration (CMC), surfactants form ordered mesoscopic assemblies – typically spherical micelles. Owing to their tendency to form micelles and reduce surface tension, surfactants are at the heart of many applications where they are used as detergents, dispersants, emulsifiers, etc. [6, 7, 8].

Several models are available to describe adsorption processes – the most popular frameworks being the Henry and Langmuir models. The Henry model accurately describes the ad-

sorption of individual molecules at low concentrations, while the Langmuir model covers a broader concentration range by considering the formation of an adsorbate monolayer at the solid surface. Despite the broad applicability of these two seminal models, they are not suitable to capture the complex phenomena involved in surfactant adsorption. Depending on the nature of the surfactant and solid surface considered, different interaction types are involved in the adsorption process; attractive or repulsive interaction between the hydrophilic group and the surface, attractive interaction between the hydrophobic group and the surface, and lateral interactions between the adsorbed surfactants. These interactions lead to cooperative effects which significantly impact the thermodynamics and dynamics of the adsorbed layer. Such cooperative effects, which are intrinsically linked to the chemical structure/composition of the adsorbate, are responsible for the rich adsorption behavior including the formation of ordered or disordered self-assemblies at the host surface.

As already stated, increasing attention is paid to adsorption technologies with significant efforts made to improve existing processes. For purification, in particular, it is necessary to better assess and understand the migration of pollutants into natural or synthetic porous media. These pollutants can adsorb to the surface of the porous medium following specific underlying adsorption kinetics [9, 10]. If these adsorbates are in contact long enough with the adsorbent, a local equilibrium is reached between the amount of adsorbed molecules and the molecules transported in solution. Understanding molecule transport and adsorption kinetics is therefore crucially needed to develop and improve processes. To do so, from a technical viewpoint, it is important to integrate adsorption kinetics into transport models but also to consider different phenomena involved (mass transfer, diffusion, and adsorption). In this context, the study of the interplay between transport and adsorption is considered as one of the most important scientific issues in the field of adsorption. The porous medium structure is of course another ingredient that significantly influences the transport behavior of adsorbing molecules as well as adsorption (since the latter is also sensitive to the geometry/structure of the solid/fluid interface). Depending on the porous structure, features such as constrictions or low porosity zones induce strong coupling between fluid transport and molecular adsorption. Therefore, understanding the interplay between the structural heterogeneity of the porous medium and the adsorption thermodynamics and kinetics is also considered as an important issue.

Thesis objectives

The objective of this thesis is two-fold. First, an adsorption model capable to capture the cooperative effects involved in surfactant adsorption will be derived. Second, the interplay between adsorption and transport will be considered using a robust numerical scheme.

As far as the first objective is concerned, we will examine surfactant adsorption by considering specifically microscopic cooperation effects involved for such complex molecules. Such effects lead to a non-ideal adsorption behavior (lateral interaction and the formation of mesoscopic aggregates), which results in complex underlying kinetics. As will be shown, this rich adsorption kinetics behavior is a key element required to understand and design specific adsorption processes. In particular, such kinetic aspects coupled with transport flow are important to design efficiently industrial adsorption devices. It is therefore very important to include such cooperative effects in the definition of adsorption kinetics when dealing with surfactants. Therefore, in this thesis, a detailed definition of the cooperative effects involved in adsorption is considered. First, we derive a new adsorption model that considers these cooperative adsorption effects as well as surface aggregation. This model is based on simple adsorption kinetics with adsorption and desorption coefficients that are dependent on the surfactant surface concentration. This ingredient provides an improved description of adsorption for individual monomers as well as for micelles by accounting for hindered or facilitated adsorption.

As for the second objective, the study of the coupling between transport and adsorption is considered. Such interplay between adsorption kinetics and transport flow is taken into account using a numerical method. The latter is considered efficient and robust as it allows in particular to obtain information on both the adsorption and dynamical properties. Indeed, experimentally, detailed information on adsorbed quantities is not easily accessible since only adsorbate free concentrations in solution are assessed. Moreover, while conducting an experimental parametric study (by considering parameters such as adsorption and desorption coefficients) is not simple, numerical methods allow the determination of even nanometric quantities. These methods provide a better understanding of the influence of adsorption on transport. In this thesis,

we will study the transport of non-adsorbing and adsorbing molecules using the Lattice Boltzmann method within the Two Relaxation Time scheme. This technique will be used to solve the Advection–Diffusion equation. The Lattice Boltzmann method is a powerful technique for the computational modeling of a wide variety of fluid flow problems including single and multi-phase flow in complex geometries. As will be discussed in this manuscript, it allows incorporating different adsorption kinetics in an effective but robust fashion.

This manuscript is divided into five chapters. The first chapter provides a short literature review on the fundamental concepts at the heart of this work. We introduce the main elements to characterize transport – both flow and diffusion – and adsorption in porous media. Then, we present the main principles of the Lattice Boltzmann scheme. In Chapter 2, we introduce the formalism used to conduct the numerical simulations: the Two Relaxation Time Lattice Boltzmann scheme applied to a two-dimensional geometry. We present the equations that were specifically implemented to address Stokes flow problems as well as those required to solve the advection diffusion equation. This framework is then validated by presenting the results obtained for the transport of passive i.e. non adsorbing tracers. In Chapter 3, we discuss the cooperative effects involved in surfactant adsorption. After a brief presentation of the existing models in the literature and their limitations, we present our new model. The assumptions at the root of the model and its validation against experimental data are discussed. In Chapter 4, we integrate in the Lattice Boltzmann approach a local description of the adsorption kinetics based on Henry and Langmuir modeles but also using the cooperative adsorption model developed in the previous chapter. We also present the validation of the adsorption kinetics implemented under static conditions (in the absence of fluid flow). Chapter 5 examines the influence of adsorption on molecular transport by discussing the differences observed when various models/conditions are considered. We also perform simulations in increasingly complex pore geometries to evaluate the impact of the pore structure heterogeneity on the transport of adsorbing molecules.
We note that a significant part of chapter 3 in this manuscript is taken from our submitted article " Cooperative Effects Dominating the Thermodynamics and Kinetics of Surfactant Adsorption in Porous Media: From Lateral Interactions to Surface Aggregation ".

Chapter I

State of the art

Contents

This chapter is devoted to providing the fundamental background for this work: adsorption and transport of adsorbate particles within porous media. This chapter is divided into three sections which correspond to its main keywords. The first section is dedicated to a general overview of transport in porous media. We provide some generalities on porous media and on fluid flows in the porosity of such heterogeneous environments. Then, the different transport mechanisms – advection and diffusion – are succinctly presented. Finally, dispersion of particles within a liquid flowing through a porous medium is described in more details as it is at the heart of the present thesis. The second section of this chapter focuses on surfactant adsorption. After a brief introduction to surfactants – characteristics, types and functionalities – we discuss adsorption of such complex molecules under both static and dynamic conditions. Throughout this thesis, static and dynamic conditions refer to adsorption in a non-flowing and flowing liquid, respectively. The third section of this chapter introduces the Lattice Boltzmann method (LBM). This general presentation is short as a more detailed discussion will be provided in Chapter 2. Here, we only describe the main principles and the different Lattice Boltzmann schemes.

A. Transport in porous media

Transport in a porous medium is relevant to a large body of domains and applications. This includes the following non-exhaustive list: reservoir engineering with hydrocarbon transport in rocks formations, geoscience with pollutant transport in soil or radioactive waste storage in the underground, construction engineering with moisture transport control, hydrogeology with water circulation in aquifers or contaminants dispersion at the subsurface, etc. Other applications are relevant to chemistry and physical chemistry such as in catalysis, chromatography, bio/nanomedicine (drug delivery using encapsulating media to brain), etc. Understanding transport in porous media requires to better describe the link between the descriptors that characterize porous media and the fluid flow mechanisms within their porosity.

1. Porous medium and fluid flow

Fluid flow in porous media is of significant importance in many areas of science and engineering. Therefore, to develop and operate projects in these fields, we need an accurate representation of the porous media as well as of the fluid flow behavior.

1.1. Porous medium

Many porous media can be found in Nature. There exist natural porous media with both inorganic solids such as rocks, soils, etc. and organic or organic/inorganic compounds such as bones and kidney. There exist also a large number of man-made porous media which are used as fabrics, filters, etc. [11]. In the frame of this thesis, we are interested in studying the transport of adsorbing particles in rocks that are subjected to a flowing liquid. In short, porous media can be defined as solid materials containing voids/cavities – the so-called pores [12]. These pores can be connected or unconnected and of various geometry/sizes (only connected pores allow fluid flow through the porosity). The International Union of Pure and Applied Chemistry (IUPAC) has proposed a nomenclature of porous media based on their pore size: microporous solids < 2 nm (e.g. zeolites, active carbons), mesoporous solids 2-50 nm (e.g. oxides such as porous silica/alumina), and macroporous solids > 50 nm (e.g. sponges) [13].

At minimum, fluid flow through porous media can be defined at the engineering level using the following descriptors/parameters. (1) porosity ϕ which corresponds to the fraction of pore volume to the total – pore and solid – volume. (2) Permeability K which corresponds to the capacity of the porous medium to transport fluids through its porosity [14] (a more robust definition will be given below). In practice, transport in porous media often relies on more or less complex parameters such as pore structure and fluid properties and concepts such as tortuosity [15].

1.2. Flow in porous media

In porous media, upon adding surfactants or pollutants in a flowing fluid (e.g. water), they tend to disperse in the solid porosity. Before presenting the different transport/adsorption mechanisms, we introduce in this section the main ingredients to understand fluid flow in porous media.

The Reynolds number Re compares the inertia forces with the viscous forces. On the one hand, the viscous forces characterize the fluid resistance to the fluid flow while inducing parallel streamlines in lamination (i.e. laminar flow for small Re). On the other hand, the inertia forces cause irregular fluid movements which induce motions that do not correspond to lamination (i.e. turbulent flow for high Re). The Reynolds number Re is the ratio between these two forces:

$$\mathrm{Re} = \frac{\rho\, UL}{\mu} = \frac{UL}{\nu} \tag{I .1}$$

where ρ is the fluid density, U the flow velocity, L the characteristic dimension (typically, taken as the typical pore size when considering fluid flow in porous media). μ and ν are the dynamic and kinematic viscosities of the fluid, respectively.

In porous media, the flow of an incompressible fluid can be described using Darcy's law. This equation states that the fluid flow rate U is proportional and oriented along the pressure gradient $\boldsymbol{\nabla} P$, $U \sim \nabla P$. The proportionality coefficient between these two quantities is defined as the hydraulic conductivity of the porous medium. More in detail, the hydraulic conductivity corresponds to the ratio of the porous medium permeability K and the fluid dynamic viscosity μ. Darcy's law was proposed by Henry Darcy in 1856 following experimental studies of one-dimensional water flow through compacted sands at low velocity [16]. This equation is valid for small Reynolds number Re (therefore, typically, in low velocity regimes as is often the case in porous media due to the restricted lengthscale L imposed by the pore geometry). Darcy's equation for a homogeneous fluid writes:

$$\boldsymbol{U} = -\frac{K}{\mu}\boldsymbol{\nabla} P \tag{I .2}$$

where we recall that K is the porous medium permeability and $\boldsymbol{U}$ is the fluid flow velocity.

From a very general standpoint, in fluid mechanics, the flow of a fluid is described by means of Navier-Stokes equations. Various approximations and conditions can be used to simplify these equations. Let us consider incompressible Newtonian fluids in a laminar regime. In the stationary state, the fluid velocity does not change over time as long as external factors such as pressure, temperature, etc. remain constant. In this case, the Stokes equation provides an

accurate description of fluid flow:

$$\nabla P - \mu \Delta \boldsymbol{U} = \boldsymbol{f} \tag{I .3}$$

where P is the pressure and $\boldsymbol{f}$ is the applied force inducing transport.

2. Transport mechanisms

Fluid transport in porous media (e.g. carrier fluids) and mass transport (e.g. pollutants, surfactants) through flowing fluids (e.g. water, oil, air) is impacted by different phenomena such as nonlinear chemical reactions, adsorption, etc. In porous media, Re is usually small so that the flow remains essentially laminar so that the dispersion/mass transport of particles within the flowing liquid is governed by the two following mechanisms: advection and diffusion. In what follows, the two phenomena – advection and diffusion – are presented.

2.1. Advection in porous media

Advection refers to the fluid mass moving through the pores as described in the previous paragraph. It is affected both by the fluid and porous medium properties. Advection or the flowing fluid participate to the transport of adsorbing/non-adsorbing particles; adding particles within the fluid flow induces an advective motion along the flow streamlines which causes a translation of the concentration field. The advective flux J_A simply depends on the fluid mass per unit volume (i.e. density) ρ and the flow velocity U: $J_A = \rho U$.

2.2. Diffusion in porous media

The added particles to the flowing fluid are also transported i.e. scattered within the porous media through diffusion. Diffusion, which is described using Fick's first law, corresponds to the mass transfer that tends to more uniform molecule distributions in space as time passes (e.g. impurity dispersion in water or air at rest). Depending on the time/length scale considered, two diffusion types can be observed: (1) Turbulent diffusion at the macroscopic scale which is caused by random bulk movements and (2) When no external driving forces are involved, molecular diffusion caused by local fluctuating density gradients occurs. Even when particles

are uniformly distributed in space, self-diffusion – i.e. Brownian motion – occurs at the microscopic/molecular scale as particles move randomly and independently of the host solution due to microscopic effects [17]. In what follows, we focus on molecular diffusion. Molecular diffusion, which occurs in gases, liquids and solids, corresponds to the process by which the thermal motion of individual molecules causes a flux of dissolved particles from areas of higher concentration to areas of lower concentration. This microscopic phenomenon can be described by Fick's first law, which relates the diffusive flux J_D to the local concentration gradient through the molecular self-diffusion coefficient D_m, $J_D = -D_m \nabla \rho$.

The diffusion coefficient of molecules confined in a given porous medium depends on many parameters such as thermodynamic quantities (concentration, temperature, etc.) but also material properties (porosity, pore size, etc.). Particle diffusion in a liquid flowing through a porous medium involve different complex mechanisms such as surface diffusion, Knudsen diffusion, stop-and-go diffusion, etc. In the next section, we address the specific problem of transport involving coupled diffusion/advection in porous media. While advection often prevails in porous media, there is a number of situations – typically when the pore size is very small – where the advective flux is low so that diffusion is the dominant transport mechanism at long time.

3. Dispersion

Dispersion is the phenomenon that results from the combination of advection and diffusion in porous media. Understanding such dispersion phenomena in porous media is important since this behavior is encountered in various domains: contaminant dispersion in groundwater, injected polymer distribution in water in reservoirs, etc. After injection, in the long time limit, solute particles in a flowing fluid will be dispersed homogeneously. Therefore, understanding the time dependence of particle distribution provides a mean to better design engineering processes (enhanced oil recovery, groundwater remediation, etc.). Before explaining the principles of particle dispersion in porous media, we first introduce a parameter that provides a quantitative mean to predict the dominant transport regime: the Peclet number Pe. This dimensionless number is defined as the ratio of diffusive and advective fluxes:

$$\mathrm{Pe} = \frac{J_A}{J_D} = \frac{UL}{D_m}. \tag{I .4}$$

Diffusion prevails for Pe $<<$ 1 while advection prevails for Pe $>>$ 1 (Pe $\sim$ 1 corresponds to a balance between the advection/diffusion components).

3.1. Dispersion in porous media

Fluid flow through a porous medium can exhibit a rich behavior as a result of the complexity of the porous structure. Collision with pore edges and changes in fluid pathways lead to the mixing and re-arrangement of the moving particles. Such dispersion, which manifests itself at the macroscopic level, results from the simultaneous action of mechanical phenomenon and a macroscopic phenomenon [18, 19]:

- Mechanical dispersion results from the fact that the fluid is moving at both higher and lower velocities than the mean velocity [20]. More in detail, like in a Poiseuille flow, the fluid in the pore center is displaced at a faster rate than the fluid at the pore surface. Moreover, the flowing fluid follows preferential fluid pathways as its transport through small pores is slower than through large pores. As a result, since particles do not move at the same velocity everywhere, the important dispersion is observed along the flow paths. In turn, such dispersion leads to a broad distribution of solute particles at the flow edge. This dispersion in the direction of flow is called longitudinal dispersion while the dispersion normal to the flow direction is referred to as transverse dispersion [20].

- Macroscopic dispersion corresponds to the spreading of solute particles caused by the heterogeneity at the porous medium scale (i.e. well beyond the pore scale). Such medium heterogeneity causes variations in the permeability that lead to heterogeneous flows with significant spatial variations in the advective transport velocity field.

The dispersion theory focuses on the asymptotic and time-dependent spatial distribution of a passive tracer in a fluid flowing through a porous medium (typically, the fluid flow is induced by an external pressure gradient). The main objective of this theory is to predict the average velocity with which the tracers move. Dispersion corresponds to the particle density variations observed around the average density distribution. Dispersion is related to the physical parameters characterizing the transport properties of the system but also the main descriptors related to the host porous medium. These parameters include the molecular diffusion coefficient of the tracers, the Stokes velocity field of the flowing fluid, the kinematic and rheological properties

of the fluid (*in situ* viscosity, shear effect of the flow), and the geometry of the porous medium (in particular, its porosity and its characteristic interstitial length).

Considering transport processes involving both advection/diffusion, the mass conservation of non-reactive species transported by the flow in porous media can be described by the so-called advection diffusion equation (ADE):

$$\frac{\partial c}{\partial t} + \boldsymbol{U} \cdot \boldsymbol{\nabla} c - \boldsymbol{\nabla} \cdot (D_m \boldsymbol{\nabla} c) = 0 \tag{I .5}$$

where c is the solute concentration in the bulk fluid, $\boldsymbol{U}$ the velocity vector and D_m the molecular self-diffusion coefficient. Dispersion always takes time to reach its asymptotic state – the dispersion coefficient is taken in the asymptotic regime (i.e. for long time t).

Gaussian or normal dispersion. The general solution of the advection-diffusion equation is a Gaussian function for the solute concentration $c(\mathbf{r},t)$. When transport can be modeled using the ADE, the dispersion is coined as "normal". The variance σ^2 of the concentration profile $c(\mathbf{r},t)$ is proportional to time i.e. $\sigma^2 \propto t$. Typical examples of such normal dispersion includes CO_2 atmospheric dispersion after leakage from transportation facilities or non-reactive pollutant dispersion in air.

Non-gaussian dispersion. Non-Gaussian dispersion arises with porous media exhibiting significant structural heterogeneity that impacts the fluid velocity field. Structural heterogeneity generates either stagnant zones where the fluid is delayed or preferential flow zones where the fluid is accelerated. In this case, the variance σ^2 of the concentration profile $c(\mathbf{r},t)$ scales as a power law of time, i.e. $\sigma^2 \propto t^a$, in the long time limit ($t \to \infty$). The following regimes are often listed in the literature: (1) sub-diffusion for $0 < a < 1$, (2) normal or Gaussian dispersion for $a = 1$, (3) super-diffusion for $1 < a < 2$, and (4) ballistic regime for $a > 2$.

3.2. Taylor dispersion in a tube

As mentioned earlier, dispersion can take different forms. Under most circumstances, it corresponds to the normal dispersion mode with a concentration profile having a Gaussian shape.

Such a regime, known as Taylor dispersion, corresponds to the expected dispersion for non-reactive particles (soluble solutes) in a fluid laminar flow (taken in the asymptotic limit). As already discussed, such dispersion results from the combination of molecular diffusion and advection phenomena. More in detail, the particles are carried down the porous medium by the shear flow. Taylor dispersion corresponds to the resulting diffusion of the particle distribution in the channel in the same direction-shear augmented diffusion, as presented in Fig. 1.

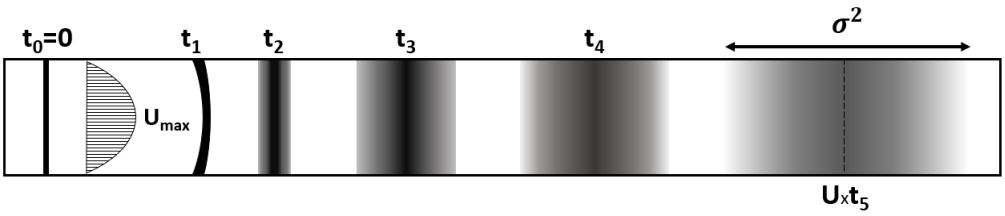

Figure 1: Tracer distribution profile over time in a two parallel plates geometry (Taylor dispersion). The geometry is exposed to a fluid flow, with the maximum velocity U_{max}. Particles are injected at $t = 0$. At t_1, the tracer distribution follows the shape of the velocity profile, i.e. the advection regime is reached and for large times (t_3, t_4 and t_5), the tracer distribution is homogeneously redistributed reflecting the Taylor dispersion regime limit.

The Taylor–Aris solution of ADE is based on the assumption that the time evolution of the solute concentration correponds to a diffusive-like regime called the dispersive regime. In this regime, the variance of the solute concentration profile becomes stationary and the problem becomes unidirectional (i.e. along the advective flow direction). Taylor showed that longitudinal dispersion is governed by a diffusion-like equation in the mobile frame along the flow direction:

$$\frac{\partial c}{\partial t}(\bar{x},y) = D_{eff}\frac{\partial^2 c}{\partial x^2} \tag{I .6}$$

where $\bar{x} = x - Ut$ and D_{eff} is the effective dispersion coefficient. D_{eff} is related to the variance σ^2_{disp} of the mean square displacement:

$$\lim_{t\to\infty}\frac{d}{dt}\sigma^2_{disp}(t)(t) = 2D_{eff} \tag{I .7}$$

The expression of D_{eff} can be determined by equating the transfer rate of a solute through a defined cross-section given by ADE – given in Eq. (I .5) – and the diffusive flux described by Fick's law – given in Eq. (I .6). As shown in Ref. [21], for Newtonian fluids, the effective Taylor dispersion coefficient in a channel formed by two parallel plates is:

$$D_{eff} = D_m + \frac{1}{210}\frac{U^2L^2}{D_m} = D_m\left(1+\frac{\mathrm{Pe}^2}{210}\right) \tag{I .8}$$

When considering complex porous media, the major obstacle to the application of Taylor-Aris lies in the fact that it is limited to fluid movements that are locally unidirectional. In other words, the local fluid velocity vector is everywhere parallel to the mean fluid velocity vector as it is the case for Poiseuille flow through a tube. This condition is not necessarily met for fluid flow through real porous media (where the flow streamlines around individual particles are curvilinear rather than straight).

B. Surfactant adsorption in porous media

1. Surfactant

1.1. Definition and types

Surfactant is a contracted expression that stands for "surface active agent". These molecules possess a hydrophilic head and a hydrophobic tail. The hydrophobic part is usually an 8 to 18 carbon chain which can be aliphatic, aromatic or a mixture of both. These hydrophobic tails typically stem from natural fat and oil, petroleum fractions, relatively short synthetic polymers, or relatively high molecular weight synthetic alcohols. The hydrophilic groups, which lead to the primary classification of surfactants, are anionic, cationic, nonionic or Zwitterionic.

Surfactant types	Use examples	Characteristics
Anionic hydrophilic groups	Carboxylates (soaps), sulfates, sulfonates or phosphates	A negatively charged polar head
Cationic hydrophilic groups	Some amine products	A positively charged polar head in aqueous solution
Nonionic surfactants	Food ingredient, alcohol	Do not have a charged head but contain hydrophilic groups
Zwitterionic surfactants	Betaine	Neutral but are composed of two ionic parts

Table 1: Classification and properties of surfactants.

Owing to their tendency to orient at surfaces and form micelles, surfactants possess important functions including the ability to modify interfacial energy and reduce surface tension. The term interface indicates a boundary between two immiscible phases; the term surface refers to

an interface where one of the phases involved is a gas. For a system at low concentration, surfactants alter the interfacial free energy i.e. the minimum amount of work required to increase the interface area. Surfactants usually work to reduce the interfacial free energy although there are rare situations where they can lead to increased interfacial free energies. On the other hand, these amphiphilic molecules lower the surface tension[1] between two liquids, between a gas and a liquid, or between a liquid and a solid. Surfactants can be considered as adsorbing substances as they stick together and bond to surfaces/interfaces. Even at low concentrations, they adsorb at interfaces which significantly changes the amount of work required to expand these interfaces. Surfactants may act as detergents, wetting agents, emulsifiers, foaming agents, and dispersants.

1.2. Surfactants in solution

Fig. 2 presents the phase diagram of surfactants in solution as their concentration c is varied. Individual surfactant molecules are called "monomers" while aggregated surfactants molecules

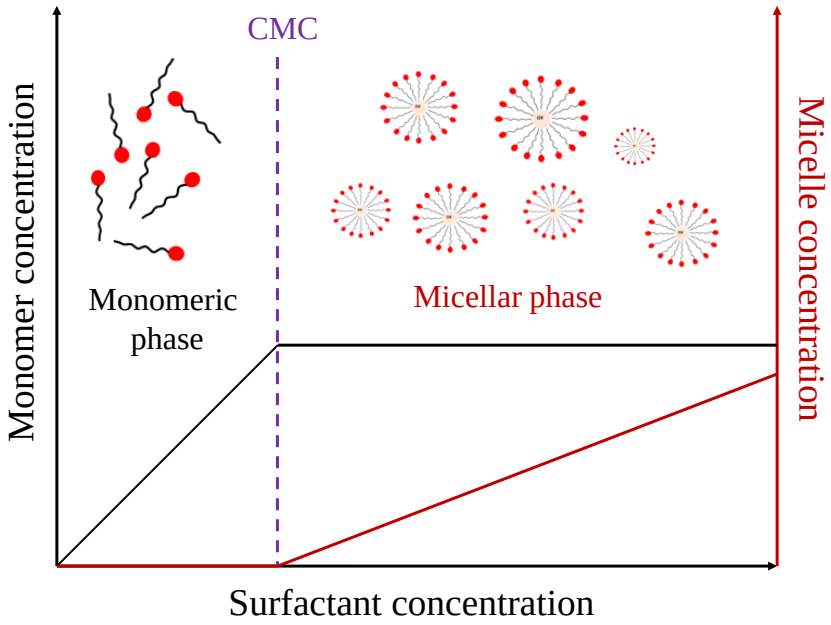

Figure 2: Concentration c phase diagram of surfactants. The surfactants adopt particular spatial configurations. At low concentrations, the monomers are solubilized within the solvent, the red and black parts denote the hydrophilic head and the hydrophobic tail of the surfactant. Above a certain concentration, the so-called CMC (Critical Micelle Concentration), the monomers aggregate to form micelles [1].

[1]Upon measuring the surface tension of a liquid, one probes the interfacial free energy per unit area of the boundary between the liquid and its vapor pressure.

are referred to as "micelles". At low concentrations c, the monomers are dispersed/solubilized in the solvent (typically water). At a certain concentration, the so-called Critical Micelle Concentration (CMC), the monomer concentration remains constant as the addition of surfactants leads to an increase in micelle concentration or micelle size. Micelles are monomer clusters/aggregates whose size and conformation depend on the nature of the surfactant. In general, the hydrophilic heads are oriented towards the solvent while the hydrophobic tails stick to each other inside the micelle. When the concentration is further increased, a second critical concentration is obtained above which the surfactants are no longer organized in spherical micelles but in other complex aggregated structures. Typically, in some surfactant systems, vesicles can form. Other critical concentrations are successively achieved where the arrangement of cylindrical micelles become hexagonal, etc.

1.3. Surfactant aggregates at interfaces

As mentioned in the previous paragraph, a key feature of surfactants lies in their ability to adsorb at surfaces and interfaces. Surfactant adsorption at various interfaces is often used to control wetting and solution penetration, stabilize foam and emulsions, and recover minerals upon flotation operation. To optimize such application conditions, it is important to relate the amount of adsorbed surfactant to the surfactant concentration in solution but also to obtain information on the structure of the surfactant adsorbed layer. In this context, surfactant adsorption can involve various adsorbed layer structures. Typically, the adsorbed monomers at solid/liquid interfaces organize themselves to form different structures depending on the nature of the surface: hydrophilic (cylinders, spheres, bilayers, etc.) or hydrophobic (hemicylinders, hemispheres, monolayers, etc.).

The structure of the adsorbed layer at a surface can be characterized by assuming a multilayer spreading over the entire surface of the adsorbent (mostly monolayer or bilayer) or by considering the formation of "local" aggregates. The aggregates can form 2-dimensional objects at the interface between the solid and the liquid. These aggregates, which are usually called "solloids" for surface colloids, lead to an increase in the adsorbed density/concentration [22]. These sur-

face aggregates can be of different types as shown in Fig. 3: “hemimicelles” (local monolayer in which the surfactant is adsorbed with their headgroup in contact with the surface or with their tail in contact with the surface), “admicelles” (set of local bilayers with headgroups in contact with the surface and other headgroups directed towards the solution) and “surface micelles” (structures similar to micelles in solution but adsorbed at the surface) [2].

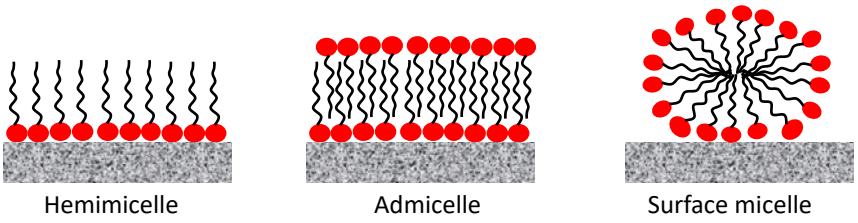

Figure 3: Types of surface aggregates on a hydrophilic surface, we consider the monolayer form: the hemi-micelles, the bilayer forms: the admicelles as well as the surface micelles [2]. The grey part represent the adsorbent hydrophilic surface and to illustrate the surfactant: the red and black parts present respectively, the hydrophilic head and the hydrophobic tail.

2. Adsorption

Adsorption is the phenomenon of accumulation of molecular species at the surface of liquid or solid phases due to unbalanced or residual forces (i.e. forces acting to hold and attract particles to be in contact with the surface). Adsorption leads to a change in concentration of the molecules at the interface compared to the surrounding bulk phase [23]. Depending on the phases in contact, gas or liquid molecules bind to a solid or liquid interface (the so-called adsorbent). The adsorbed molecules, which are physically or chemically attached to the interface, form an atomic or molecular adsorbate film. The adsorption of surfactants at a solid-liquid interface is strongly influenced by several factors [24]:

- The nature of the structural groups at the surface of the solid. Typically, the presence of highly charged or uncharged sites at the solid surface will lead to strong differences in adsorption. Moreover, the structure of the atoms forming the solid surface also affects the adsorption of molecules from a gas or liquid phase.

- The molecular structure of the adsorbed surfactant (ionic, non-ionic, Zwitterionic, etc.) and the specificity of the hydrophobic group (long/short, straight/branched, aliphatic/aromatic chain).

- The aqueous phase properties: temperature, pH, ionicity, additives, etc.

Altogether, these key factors determine the mechanisms by which adsorption occurs as well as the resulting surface aggregation (if any).

2.1. Adsorption types

Depending on the forces which hold adsorbate molecules to the surface, adsorption is classified into two types: physical adsorption and chemical adsorption.

Physical adsorption/Physisorption. Physical adsorption resembles the condensation mechanisms that makes molecules from a gas phase condensate into a liquid phase. It is driven by physical interactions such as van der Waals forces between the solid adsorbent and the adsorbate molecules. There is no specificity in physisorption; any gas tends to be adsorbed at any solid provided the temperature is sufficiently low. Physical adsorption obeys the following rules:

- Reversible. If the pressure is increased, more molecules get adsorbed. Reciprocally, by decreasing the pressure, molecules can be removed from the solid surface. Low temperature promotes physical adsorption while high temperature decreases the adsorption rate;

- Exothermic process. Upon adsorption, heat is released by the adsorbate/adsorbent system as adsorbed molecules are in a lower (more negative) energy level than the bulk molecules.

- No activation energy. Physical adsorption/desorption does not require to overcome an energy barrier.

- Multilayer films can form upon physisorption.

Chemical adsorption/Chemisorption. In chemical adsorption, gases are held to a solid surface by chemical bonds that are specific to each surface/gas couple. Chemical adsorption usually involves higher interaction energies than those involved in physical adsorption. Furthermore,

chemical adsorption is typically a slower process than physical adsorption and, like most chemical reactions, usually involves overcoming an activation energy. Chemical adsorption obeys the following rules:

- Chemical adsorption is irreversible.
- Chemisorption energies are of the same order of magnitude as the energy change in a chemical reaction.
- Chemisorption can be exothermic or endothermic.
- Due to chemical bond formation, the enthalpy of chemisorption is high (typically 1 eV *versus* 0.1 eV for physisorption) [25].
- Chemisorption only results in the formation of mono-molecular layers/films.

2.2. Adsorption isotherms and models

2.2.1. Literature review

A detailed presentation on the adsorption at the liquid-solid boundary can be found in textbooks and reviews [26, 27, 23]. The development of adsorption is now considered a distinct discipline from the physical sciences – representing an area of mainly multidisciplinary work between chemistry, physics, biology and engineering [23]. The most important principle in adsorption science is the "adsorption isotherm". It refers to the equilibrium function between the amount of adsorbed substance and the pressure or concentration in the fluid bulk phase at constant temperature [23]. Adsorption isotherms provide information on the adsorption mechanism as well as on the interactions between the adsorbate and the adsorbent molecules. Experimental adsorption isotherms can be accurately understood using mathematical modeling of adsorption processes. The hypotheses of these mathematical models are based on experimental observations. Until 1914, there was no theory for the interpretation of adsorption isotherms [23]. The Freundlich equation [28] was used as a convenient empirical form but it has no theoretical justification. According to McBain [29], it was first introduced by van Bemmelen in 1888 and then employed by Baedeker in 1895 as an empirical equation. New descriptions of adsorption phenomena were later published. First, the Eucken-Polanyi theory was introduced [30, 31, 32]

and in 1918 the Langmuir isotherm was derived for the first time [33].

Langmuir's equation [33], which was first derived from kinetic considerations, treats the adsorbent surface with a predefined number of adsorption sites. Each site is capable of adsorbing a single molecule from a perfect gas. Localized adsorption was considered to be different from non-localized adsorption; in the latter approach, the adsorbed molecules can move along the surface. In contrast, in localized adsorption, chemical or physical bonds form at the adsorption sites which are strong enough to prevent the adsorbed molecules from moving on the surface [23]. The Langmuir model considers the bulk as an ideal gas and neglects the lateral interaction between adsorbed molecules. The adsorbed molecules form a monolayer phase at the surface of the adsorbent. In his pioneering work, Langmuir presented the first clear concept of "monomolecular adsorption on energetically homogeneous surfaces" with a significant physical parameter: the adsorption constant [33, 23]. The Langmuir model does not account for the heterogeneity of the solid adsorbent and the multilayer nature of adsorption. Langmuir's work on gas adsorption has led to various results: the formulation of a general treatment for the kinetics of surface reactions, the kinetics of surface reactions according to his monolayer equation and also the use of the adsorption isotherm to interpret the kinetics of various surface reactions [23]. Langmuir's equation is a useful equation that describes the "ideal localized monolayer". Despite the assumptions of this model, it is important in the surface science and adsorption science [34, 23].

In 1938, a new isothermal equation was proposed: the multilayer isothermal equation proposed by Brunauer et al. [35]. To derive this model, Brunauer and Emmett first published two important papers in 1935 [36] and 1937 [37]. They proposed for the first time to determine the amount of monolayer adsorption from point B[2] of the experimental isotherm [36, 37]. The Brunauer–Emmett–Teller (BET) equation was conceived as a follow-up to Langmuir's model since its derivation is also based on kinetics studies. The main assumption of the BET equation is that the first layer is adsorbed according to the Langmuir model. The surface sites are there-

[2]Point B is the inflection point that occurs near the completion of the first monolayer adsorbed. Once the monolayer coverage is complete, the change in curvature of the adsorption isotherm is abrupt as opposed to a more gradual curvature which indicates the beginning of multilayer adsorption [38].

fore energetically identical with no lateral interactions between the adsorbed molecules. The adsorbed molecules, which form a given layer, constitute adsorption sites for the molecules of the next layer. The second hypothesis in this model is that the adsorption energy of the layers beyond the first layer is assumed to be equal to the energy of gas liquefaction. Initially, this model was defined for a given number of adsorption layers but it was then extended to tend towards infinity when the equilibrium pressure tends towards the saturating vapor pressure [39]. Different approaches were later proposed to model multilayer adsorption such as the model developed by Frenkel, Halsey and Hill (FHH theory) [40]. These models have been developed to correct the BET theory by taking into account lateral interactions and the decreasing energy of the successive layers according to the distance to the surface [41, 42]. The criticism of the BET theory focuses on two main points: the starting hypotheses and the field of application. With regard to the upper layers, if lateral interactions are neglected, it is difficult to consider the energy condensation of the adsorbate in its liquid form since this would necessarily imply lateral interactions. The second criticism concerns the use of this theory for the characterization of real porous solids (the heterogeneity of the structure, having pores of different widths, does not allow assuming equal energies for adsorption or condensation) [41]. Despite its limitations, the BET theory is a universal and unavoidable method to understand physical adsorption. It describes the entire isothermal cycle, including the areas of monomolecular adsorption, polymolecular adsorption, and condensation [23].

Other robust theories appeared in the second decade of the twentieth century – namely the theory of adsorption potential introduced by Eucken and Polanyi [30, 31, 32]. This theory, known today as Polanyi's theory, served as the basis for the development of the theoretical foundations of the Dubinin-Radushkevich model known as the volume-filled micropore theory (TVFM) [43]. The main features of Polanyi's theory are the introduction of the adsorption potential and the characteristic adsorption curve. Using a thermodynamic framework, Polanyi derived this physical adsorption theory by assuming that molecules close to the surface feel an attractive potential generated by the adsorbent. The magnitude of this potential depends on the proximity of the adsorbate molecule to the solid surface. In general, this potential is seen as corresponding to the van der Waals' attraction [43, 44]. The characteristic adsorption curve

relates the adsorption potential to the distance from the solid surface. It is fixed by the structure of the porous solid and has no specific mathematical form [45, 23]. Since the van Der Walls' forces are temperature independent, Polanyi supposed that the model parameters are also temperature independent [31, 32, 23]. The model derived by Polanyi led to the identification of the differential molar work of adsorption A (where the 'A' stands for adsorption potential). This was the basis of the work by Dubinin–Radushkevich (DR) who introduced the adsorption potential as the negative work performed by the adsorption system $A = -\Delta G$. In this case, A is the Gibbs free energy involved in the transfer of a molecule from the gas to the adsorbed phase at temperature T and pressure P [46, 47, 23]. In recent years, much attention has been paid to the DR adsorption isotherm. It provides a good description of experimental data for adsorption on heterogeneous surfaces – both for porous and non-porous solids. This adsorption isotherm is very important for the characterization of industrial adsorbents which often exhibit a complex porous structure. [48, 49, 23].

2.2.2. Adsorption isotherm models

Several adsorption isotherm models have been developed to describe adsorption – either using a robust theoretical framework or simply as empirical equations. These models include but are not limited to the Henry, Freundlich, Langmuir, Brunauer-Emmett-Teller, and Kisliuk models. The hypotheses at the root of some theoretical models such as the Langmuir and Freundlich equations often limit their applications. As a result, several empirical models – combining elements of the Langmuir and Freundlich models – have been proposed. This includes the empirical models by Redlich-Peterson, Sips or Langmuir-Freundlich. In what follows, we review in a non-exhaustive fashion the most important models used to describe surfactant adsorption onto surfaces. In the different adsorption isotherms below, adsorption is considered instantaneous and the concentration c is defined as the surfactant concentration at equilibrium $c = c_e$.

Henry model. This is the simplest adsorption isotherm. The adsorbed amount is assumed to be proportional to the bulk concentration of adsorbate molecules:

$$\frac{\Gamma_e}{\Gamma^\infty} = k_H c_e \tag{I .9}$$

where Γ_e is the adsorbed amount (typically in ng/cm^2 or $mmol/m^2$). Γ^∞ is the maximum adsorption capacity and k_H is the Henry constant for adsorption. With this simple model, the adsorbed amount increases linearly with the molecules concentration c at equilibrium c_e.

Langmuir model. The Langmuir adsorption isotherm writes [33]:

$$\frac{\Gamma_e}{\Gamma^\infty} = \frac{k_L c_e}{1 + k_L c_e} \tag{I .10}$$

where k_L is the Langmuir equilibrium constant. In this model, it is assumed that the molecules are adsorbed on well-defined sites at the adsorbent surface. All sites are identical and each site can adsorb only one molecule so that adsorption only leads to monomolecular layers. The energy of each adsorbed molecule is independent of the neighboring sites (no lateral interactions between neighboring adsorbed molecules). Langmuir was able to express the existence of a dynamic equilibrium between the molecules which are attached to the surface and those that leave the surface. If the concentration is very small, the Langmuir model is equivalent to Henry's model $(k_L c_e << 1)$. The Langmuir model often makes it possible to fit the experimental results because of its mathematical simplicity.

Freundlich model. Mathematically, the Freundlich adsorption isotherm is expressed as [28]:

$$\Gamma_e = k_f c_e^{1/n_f} \tag{I .11}$$

where k_f is the adsorption constant and $1/n_f$ a constant related to the strength of the adsorption process. This model assumes that there is an exponential decay in the energy distribution of adsorption sites (therefore, corresponding to a heterogeneous surface). With this adsorption model, multilayer adsorption can be described. In the Freundlich model, the constant n_f is a correction factor which is used to characterize the adsorption process. While adsorption is favorable for $0.1 < 1/n_f < 1$ adsorption is unfavorable for $1/n_f > 1$ (as shown in Fig. 4). In contrast to the Langmuir adsorption isotherm, which exhibits a plateau (Γ^∞), a continuous increase in the adsorbed quantity is observed in the Freundlich model as the concentration c_e increases. There is therefore no surface saturation for $1/n_f > 1$ and $n_f = 1$. This is often critical because there is usually a maximum saturation of the surface for most systems.

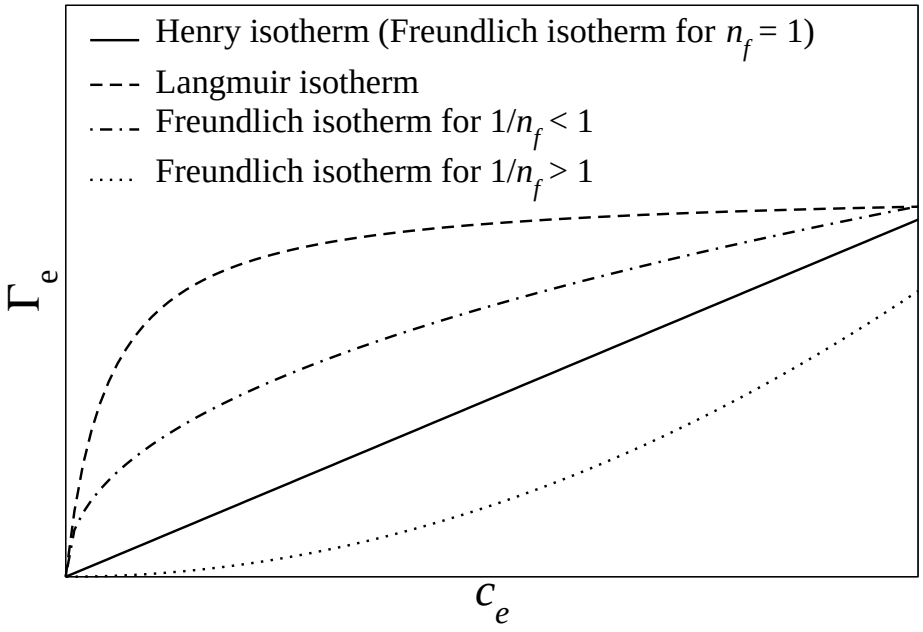

Figure 4: Henry, Langmuir and Freundlich adsorption isotherms. For the latter, two values $1/n_f$ are considered.

Redlich-Peterson. This adsorption model is a hybrid version of the Langmuir and Freundlich adsorption isotherms [50]. The numerator corresponds to that in the Langmuir isotherm (which approaches the Henry region at infinite dilution):

$$\Gamma_e = \frac{Ac_e}{1 + Bc_e^{\alpha_{RP}}} \tag{I .12}$$

where A and B are the so-called Redlich-Peterson constants while α_{RP} is an exponent between 0 and 1. By combining elements from the Langmuir and Freundlich equations, the adsorption mechanism described in this model does not follow the ideal monolayer adsorption.

Sips model. Sips et al. identified the problem of a continuous increase in the adsorption rate with the assumed concentration in the Freundlich equation [51]. They proposed a modified Freundlich equation with a finite limit at high concentration (adsorption plateau) as described by the following general expression

$$\Gamma_e = \frac{k_s c_e^{\alpha_s}}{1 + k_s c_e^{\alpha_s}} \tag{I .13}$$

where Γ^{∞} is the Sips maximum adsorption capacity, k_s the Sips equilibrium constant, and α_s is the Sips exponent.

Langmuir-Freundlich Model. The Langmuir-Freundlich isotherm is similar to the Sips model but involves a heterogeneity parameter to describe adsorption on a heterogeneous solid [52]:

$$\Gamma_e = \frac{\Gamma^{\infty}(k_{Lf}c_e)^{\alpha_{Lf}}}{1+(k_{Lf}c_e)^{\alpha_{Lf}}} \tag{I .14}$$

where Γ^{∞} is the Langmuir-Freundlich adsorption capacity, k_{Lf} the equilibrium constant for a heterogeneous solid, and α_{Lf} a heterogeneity parameter between 0 and 1.

2.3. Adsorption and surface aggregation

2.3.1. Surfactant adsorption

Significant efforts have been devoted to better understand the nature of surfactant adsorption on various solid surfaces [24, 2]. Different theoretical models have been proposed to describe such adsorption at solid-liquid interfaces. The most advanced models are those taking into account the formation of surface aggregates. This includes the approaches by authors such as Zhu and Gu, Israelachvili, Levitz, Drach, Rudinzki who have investigated the formation of aggregates on surfaces [2]. In the spirit of the work by Kwok et al. [3], the adsorption of surfactant molecules from a solution can be represented using the following elementary/reversible reaction mechanism:

$$\{Monomer\} + \{Vacant\ site\} \leftrightarrows \{Adsorbed\ monomer\} \tag{I .15}$$

Such adsorption phenomenon involves a one-stage process which corresponds to a type I Langmuir isotherm (L1). The underlying adsorption rate writes:

$$\frac{\partial \Gamma_m}{\partial t} = k_A c(\Gamma_m^{\infty} - \Gamma_m) - k_D \Gamma_m \tag{I .16}$$

where k_A and k_D are the adsorption and desorption rate constants for a surfactant monomer. Γ_m is the adsorbed amount (or surface concentration) of surfactant monomers while c is the surfactant concentration in the bulk solution. Γ_m^{∞} is the maximum adsorption capacity for monolayer saturation while $(\Gamma_m^{\infty} - \Gamma_m)$ is the concentration of remaining vacant sites. In the low concentration range, adsorption follows the Henry regime where the adsorbed amount increases linearly with the concentration c. Then, upon further increasing the concentration c, the adsorption rate decreases and the adsorbed amount reaches a plateau for high concentrations. The shape of

the Langmuir isotherm is determined by the adsorption capacity and thermodynamic equilibrium of the system [3]. If adsorption is rapid and limited to an adsorbed monolayer, it can be correctly described using the Langmuir adsorption isotherm as described in Eq. (I .10) with $k_L = k_m = k_A/k_D$ and $\Gamma^{\infty} = \Gamma_m^{\infty}$.

According to the surfactant and surface types, adsorption can be considered as a two-step process involving a change in the orientation of the surfactant molecules at the surface. We present in Fig. 5 a schematic diagram that illustrates the different steps expected in stepped adsorption processes. This figure also presents the associated orientation of the surfactant at the surface. According to the classification proposed by Giles et al. [53], it corresponds to the Type IV Langmuir adsorption isotherm with the following steps:

- 1^{st} step: Surfactant monomer adsorption in a monolayer
- 2^{nd} step: Monolayer saturation
- 3^{rd} step: Increase in the adsorption with shift of the weakly adsorbed chains
- 4^{th} step: Tilting of the head-groups by a small angle with a limiting concentration: critical hemimicelle[3] concentration (above this value, surface aggregation occurs).
- 5^{th} step: Surfactant monomer condensation from the liquid phase onto an adsorbed monomer due to van der Waals and hydrophobic bonding forces.

The stepped adsorption isotherm can be modeled using the Langmuir-sigmoid model as proposed by Zhu and Gu [54, 55]. It is a general adsorption isotherm equation based on an equilibrium hemi-micellization model. The first stages of the model – from Step 1 to Step 3 – can be described as the adsorption of individual surfactant monomers due to the resulting balance between hydration of the surfactant molecules and surface attraction forces. Therefore, the process described in Eqs. (I .15) (I .16) corresponds to an underlying adsorption ratio k_m with the following definition:

$$k_m = \frac{\Gamma_m}{\Gamma_z c_e} \tag{I .17}$$

[3]Hemimicelles are aggregates produced at the solid/liquid interface when the surfactant concentration exceeds a critical value (c_{hmc} known as the critical hemimicelle concentration).

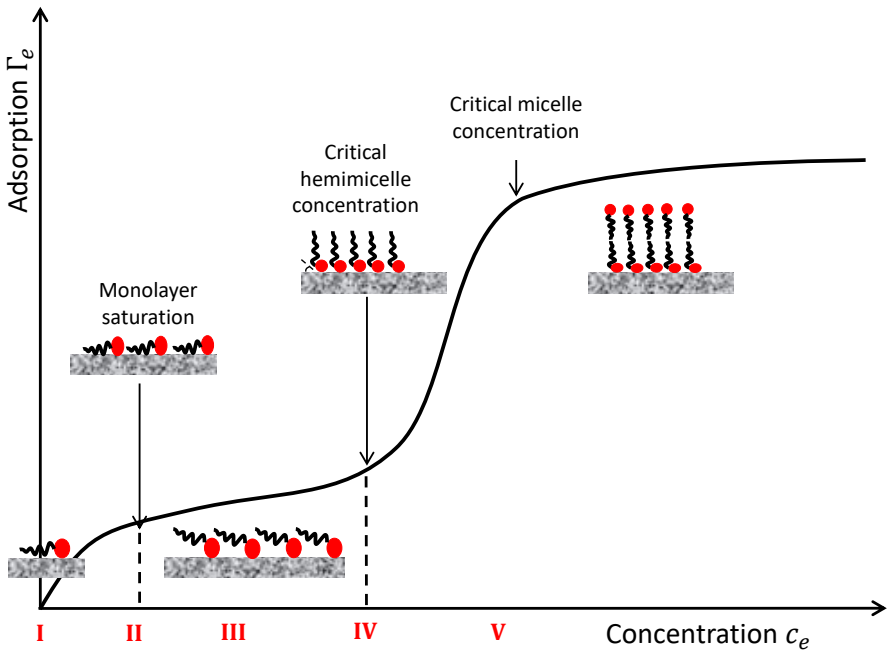

Figure 5: Type IV adsorption isotherm to model the adsorption of surfactant, the adsorbed amount Γ_e as a function of the concentration at equilibrium c_e. The orientation of surfactant molecules at the surface is also shown for each stage. The red and black parts denote respectively, the hydrophilic head and the hydrophobic tail and the gray bloc illustrate the adsorbent surface [3].

where c_e is the concentration of free monomers at equilibrium and Γ_z is the number of vacant sites. The adsorption isotherm reaches a first plateau as the adsorption surface is saturated with adsorbed monomers (monolayer saturation, Γ_m^{∞}). For the second stage, adsorption occurs as a result of surface aggregation forming hemimicelles. Each adsorbed monomer acts as a central element of a hemimicelle with $(n-1)$ additional monomers where n is the aggregation number of the hemimicelle (we recall that hemimicelles result from the accumulation of individual monomers at this stage). This second adsorption mechanism can be described by the following chemical reaction:

$$(n-1)\{Monomer\} + \{Adsorbed\ monomer\} \leftrightarrows \{Hemimicelle\} \tag{I.18}$$

with the following adsorption ratio for hemimicellization:

$$k_{hm} = \frac{\Gamma_{hm}}{\Gamma_m c_e^{n-1}} \tag{I.19}$$

where Γ_{hm} is the amount of adsorbed hemimicelles. The equilibrium adsorbed amount Γ_e at a

bulk concentration c_e can be determined by writing the following mass balance equations:

$$\begin{aligned} \Gamma_e &= \Gamma_m + n\Gamma_{hm} \\ \Gamma^{\infty} &= n(\Gamma_z + \Gamma_m + \Gamma_{hm}) \end{aligned} \tag{I .20}$$

where we recall that Γ^{∞} is the maximum adsorption capacity. From the considerations above, the general adsorption isotherm for this model can be obtained upon combining Eqs. (I .17) - (I .20):

$$\frac{\Gamma_e}{\Gamma^{\infty}} = \frac{k_m c_e/n + k_m k_{hm} c_e^n}{1 + k_m c_e + k_m k_{hm} c_e^n} \tag{I .21}$$

As can be noted from this equation, Eq. (I .21) for $k_m c_e << 1$ and $n > 1$ allows recovering the one-step formation of hemimicelle adsorption models [54]:

$$\frac{\Gamma_e}{\Gamma^{\infty}} = \frac{k_m k_{hm} c_e^n}{1 + k_m k_{hm} c_e^n} \tag{I .22}$$

The model proposed by Zhu and Gu is for nonionic surfactants. This model allows one to describe various adsorption isotherm shapes using appropriate values for Γ^{∞}, k_m, k_{hm} and n: Langmuir type (Ll), S type (L3) and two-plateau type (L4). The main advantage of this model is that it provides a simple description for the adsorbed layer which can be composed of aggregates stabilized by the presence of the surface (if $n > 1$). On the other hand, the Zhu and Gu model provides no information on the structure of the aggregates as it simply offers a mean to describe the adsorbed amount in an effective/empirical fashion [56].

2.3.2. Surface aggregation

Besides surfactant adsorption, different models have been proposed to investigate the shape of the surfactant aggregates/clusters at the solid surface. The "surface micelle isotherm" model, which was proposed by Israelachvili [57], is an extension of his previous formalism on the correlation between surfactant structure and aggregate shape in bulk solutions. This model, which is based on simple thermodynamic principles, leads to a 2D non-ideal equation of state [4]. This adsorption isotherm equation, which describes continuous phase transitions between monolayers, allows the determination of various micelle properties (i.e., aggregation number from the

[4]This equation of state relates state variables to describe the state of matter under a given set of physical conditions such as pressure, volume, temperature, internal energy, etc.

adsorption isotherm shape). Using this model, it was shown that the size and shape of 2D aggregates vary with the structure of the surfactant [57].

A more complex model describing surface micelles was proposed by Levitz et al. [2]. These authors analyzed the particular properties of a "fragmented" adsorption layer [58]. Their model identifes different trends in the adsorption of non-ionic surfactants on weakly interactive hydrophilic solids. A mass action law[5] is written by relating the structure of the surface aggregates to the structure of the surfactant molecules. In this model, the aggregates are formed at the surface before they form in solution due to the favorable interactions of the monomers with the surface. When the interaction with the surface is weak, the aggregate structure is determined by the primary structural parameters of the surfactant (surfactant amphipolarity, spatial separation between headgroup and apolar tail, and chemical differences between both parts of the molecule).

Rudzinski and co-workers [59, 60] have also developed models to account for surfactant aggregation onto surfaces. In 1993, these authors presented a first important model; the adsorbed phase is treated as a mixture of oblate aggregates of various dimensions interacting via excluded volume interactions. A three-parameter equation for the adsorption isotherm was developed and, then, successfully applied to fit experimental adsorption isotherms above c_{hmc}. In 1994, a second model was derived to generalize their theoretical approach to adsorption involving two surface aggregate types coexisting on a solid surface ("admicelles" and "hemimicelles"). This extended theoretical model can be applied also to monomer—admicelle surface equilibrium. In these models, the Scaled Particle Theory (SPT) is used for the intermicellar interactions but the interactions with the surface and within the micelles are kept as simple as possible.

In 2002, Drach et al. investigated the effect of short-range interactions between the adsorbed surfactant aggregates on the adsorption isotherm [61]. These authors extended the model of surfactant adsorption based on the SPT by taking into account possible short-range interactions between the adsorbed surfactant aggregates and accounting for the effects of the surface ener-

[5]The mass action law simply describes that n monomers are needed to form a micelle

getic heterogeneity of a polar substrate. In their latest contribution [62], these authors assumed that the surface layer is a mixture of single dispersed surfactant molecules and aggregates of various sizes/shapes which are in equilibrium with the surfactant monomers and micelles in the bulk phase. Surface aggregates having similar shapes to those formed in the bulk solution was also considered in this modeling approach.

2.4. Adsorption under dynamic – in flow – conditions

2.4.1. Adsorption equilibrium

The general advection-dispersion equation for mass transport in porous media (Eq. I .5) can be modified to include the effect of adsorption [63]:

$$\frac{\partial c}{\partial t} + \boldsymbol{U} \cdot \boldsymbol{\nabla} c - \boldsymbol{\nabla} \cdot (D \boldsymbol{\nabla} c) + \frac{1-\phi}{\phi} \frac{\partial \Gamma}{\partial t} = 0 \tag{I .23}$$

where c is the concentration of the adsorbing molecules in the liquid phase, Γ is the quantity of adsorbed molecules, ϕ is the average porosity, $\boldsymbol{U}$ is the velocity vector, and D is the dispersion tensor. As discussed in this Chapter, Γ can be related to the concentration c in the liquid phase under equilibrium and non-equilibrium conditions.

For a diluted surfactant solution, the adsorption process can be approximated by Henry's law, i.e. $\Gamma_e = kc_e$, where the adsorption ratio k is Henry's constant $k = k_H$ [63]. Under such conditions, the adsorption rate simply writes $\partial \Gamma_e / \partial t = k \partial c_e / \partial t$. Under instantaneous adsorption $\Gamma = \Gamma_e$, Eq. (I .23) becomes:

$$R \frac{\partial c}{\partial t} + \boldsymbol{U} \cdot \boldsymbol{\nabla} c - \boldsymbol{\nabla} \cdot (D \boldsymbol{\nabla} c) = 0 \tag{I .24}$$

where $R = 1 + k(1-\phi)/\phi$ is called the retardation factor since it delays the appearance of a breakthrough curve upon transport into a porous medium.

Assuming reversible and instantaneous adsorption $\Gamma \sim \Gamma_e$, k can be determined from the Langmuir adsorption isotherm i.e. $k = k_L$. Considering the Langmuir model given in Eq. (I .10), the rate of adsorption can be expressed as the time derivative of the equilibrium condition:

$$\frac{\partial \Gamma_e}{\partial t} = \frac{\partial \Gamma_e}{\partial c_e} \frac{\partial c_e}{\partial t} = \frac{\Gamma^{\infty} k_L}{(1 + k_L c_e)^2} \frac{\partial c_e}{\partial t} \tag{I .25}$$

This expression of $\partial \Gamma_e / \partial t$ can be substituted directly into Eq. (I .23) leading to the same math-

ematical formula as Eq. (I .24). However, the resulting differential equation will be non-linear since the retardation factor is a function of the bulk surfactant concentration, i.e.

$$R = 1 + \frac{1-\phi}{\phi}\frac{\Gamma^{\infty} k_L}{(1+k_L c_e)^2} \tag{I .26}$$

For other non-linear equilibrium adsorption or rate-controlled adsorption processes (i.e. when Eqs. (I .16) and (I .23) are coupled), a simple expression for R may not be possible. In this case, the transport equation must be solved numerically.

2.4.2. Adsorption kinetics

In the context of this thesis, we are interested in the modeling of surfactant adsorption under dynamic conditions i.e. under flow conditions. In particular, we aim at considering how flow/transport couple with adsorption kinetics. In what follows, we present the analytic form of different adsorption kinetics: Henry, Langmuir and Sips adsorption models.

The underlying kinetics for Henry adsorption isotherm is defined as follows:

$$\frac{\partial \Gamma}{\partial t} = k_A c \Gamma^{\infty} - k_D \Gamma \tag{I .27}$$

where k_A and k_D are the adsorption and the desorption rates. The solution resulting from Henry's kinetics in Eq. (I .27) is given by:

$$\Gamma(t) = \Gamma^{\infty}(1 - e^{-k_D t})kc \text{ with } k = \frac{k_A}{k_D} \tag{I .28}$$

The underlying kinetics for Langmuir adsorption is defined as follows:

$$\frac{\partial \Gamma}{\partial t} = k_A c(\Gamma^{\infty} - \Gamma) - k_D \Gamma \tag{I .29}$$

The solution resulting from the Langmuir kinetics in Eq. (I .29) is given by:

$$\Gamma(t) = (1 - e^{-k_D(1+kc)t})\frac{\Gamma^{\infty} kc}{1+kc} \text{ with } k = \frac{k_A}{k_D} \tag{I .30}$$

The kinetics for Sips adsorption isotherm is defined as follows:

$$\frac{\partial \Gamma}{\partial t} = k_A c^{\alpha}(\Gamma^{\infty} - \Gamma) - k_D \Gamma \tag{I .31}$$

which leads to the following solution:

$$\Gamma(t) = (1 - e^{-k_D(1+kc^{\alpha})t})\frac{\Gamma^{\infty}kc^{\alpha}}{1+kc^{\alpha}}$$

2.4.3. Dispersion coefficient of an adsorbing molecules

Dispersion in porous media has been extended since Taylor's pioneering work to include more challenging situations: complex porous geometries, oscillating flows, chemical reactions, etc. An important generalization of the problem is to take into account "wall effects" (adsorption/desorption, surface diffusion, etc.) [64]. In 2012, Levesque et al. studied the situation where Taylor dispersion under bulk flow is coupled to adsorption/desorption processes taking place at the walls confining the fluid [65]. As stated by these authors, the theoretical analysis of the resulting process under such complex conditions has been limited to the two situations.

- The transverse motion is not explicitly considered. This physically corresponds to the infinitely well-stirred limit of the high diffusion coefficient D_m. A representative example of this class of problems is the two-state chromatography model introduced by Giddings and Eyring in 1955. In this model, a fluid particle can be either in the mobile phase (in the flow) or in the immobile phase (adsorbed at the confining walls) and the change rate between the two phases is assumed to be constant [66].

- The transverse motion is explicitely considered but for specific adsorption/desorption kinetics only. In ref. [67], the dispersion coefficient is calculated when the transfer with the surface is infinitely fast (local chemical equilibrium). On the other hand, Biswas and Sen have considered the situation of irreversible adsorption on the surface [68].

Levesque et al. developed a thorough theoretical analysis of Taylor dispersion in the presence of Henry adsorption/desorption processes. These authors used a stochastic approach in which:

- They derive explicit expressions for the dispersion coefficient using the canonical example of Poiseuille flow in planar and cylindrical geometries. Both stationary and oscillating velocity fields are considered, therefore paving the way to the determination of heterogeneous rate constants from the mean velocity and dispersion coefficient.

- They recover the fact that, in the case of a stationary velocity field, dispersion effects associated with bulk transport and adsorption/desorption add up.

- They show that the dispersion coefficient can be optimized and discuss possible implications in the context of molecular sorting.

If surface diffusion is neglected, Levesque et al. obtained the following equation for the effective diffusion coefficient:

$$\frac{D_{eff}^{ads}}{D_m} = 1 + \frac{K_v^{Pois}}{D_m} = 1 + \frac{1}{D_m}\left(\alpha \frac{L^2U^2}{D_m}\frac{\beta L \frac{k_A}{k_D}^2 + \gamma L^2 \frac{k_A}{k_D} + L^3}{(L+\frac{2k_A}{k_D})^3} + \frac{U^2}{k_D}\frac{2L^2\frac{k_A}{k_D}}{(L+\frac{2k_A}{k_D})^3}\right) \quad \text{(I .32)}$$

where α, β and γ are to be substituted by constants $1/210$, 102 and 18 in the planar case. L is the characteristic width of the channel and D_m stands for the molecular diffusion coefficient in the bulk. All these calculations, which are complex and tedious, were rederived in the frame of the present thesis. For the sake of simplicity, these detailed calculations are omitted here but they can be found in the Appendix A.

C. Lattice Boltzmann Method

1. LBM approach and applications to fluid flows

The Lattice Boltzmann method (LBM) is a powerful tool in Computational Fluid Dynamics (CFD). This numerical scheme was first used to solve Navier-Stokes equation numerically. It is a discrete method which allows high-performance computing simulations (HPC). The technical aspects of the LBM method will be described in more details in Chapter 2. Here, we intend to provide a simple, brief introduction. The origin of LBM approaches lies in the statistical mechanics description of particle populations. The basic idea of LBM is to formulate a numerical model that uses physical terms based on the understanding of the interactions between different molecules [69]. We present in Fig. 6 the interest raised in the scientific community by LBM over the last years. This graph provides evidence for the enormous attention paid to research and development in this CFD method throughout the years. LBM is considered as a valuable approach for flow simulations in porous media. It provides a simple tool to model transport properties in complex geometries since the structure is simply defined in terms of fluid

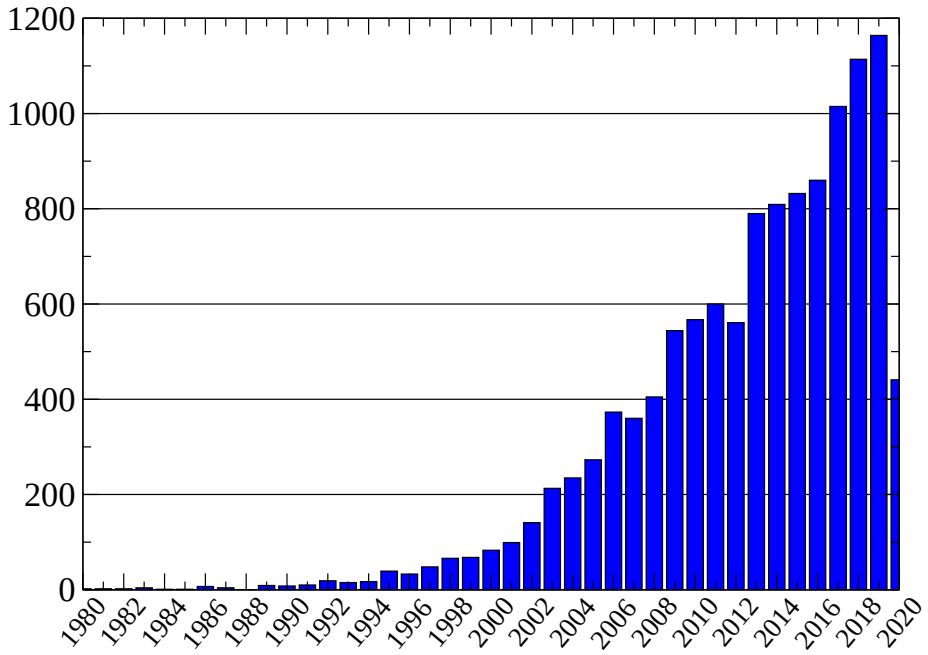

Figure 6: Number of publications involving LBM over the years. From Scopus scientific database until 2020 (adapted and extended from [4]).

or solid nodes [70]. Just a few years after its introduction, LBM has achieved recognition as a powerful technique to study single-phase/multiphase and multicomponent flows [71, 72, 73] as well as reactive transport [74, 75] in porous media. Among complex physical systems that can be considered, it also allows simulating hydrodynamic and magnetohydrodynamic interactions [76, 77, 78, 79, 80, 81].

The Lattice Boltzmann method stems from Ludwig Boltzmann's kinetic theory of gases in which gases and fluids are considered as made up of a large number of particles [82, 83]. The Boltzmann equation (BE), which describes the evolution in time and space of the particle density distribution f, is defined in the absence of external forces using the following expression:

$$\frac{\partial f}{\partial t} + \boldsymbol{U} \cdot \boldsymbol{\nabla} f = \Omega, \tag{I .33}$$

where f is the probability to find a molecule at a position $\mathbf{r}$ with a velocity $\mathbf{v}$ at a time t. $\boldsymbol{U}$ is the particle velocity vector and Ω is the collision term. The collision term represents the effect of collisions between particles. Different researches were carried out to define this collision operator. This started with the work by D. Enskog [84] followed by the extension by Chapman

in 1990 [85]. Following the work by P. L. Bhatnagar, E. P. Gross and M. Krook in 1954 [86], the "BGK" collision operator is taken as a relaxation operator of the particles at a given time towards equilibrium as described by the "Maxwell-Boltzmann distribution"[6].

The lattice Boltzmann equation can be studied as a special finite difference scheme for the kinetic equation of the discrete-velocity distribution function. Single and multi discrete-velocity distribution functions were introduced by researchers [87, 88]. Despite the discretization of the particle velocity, the space and time were treated as continuous. This topic was unveiled in 1976 by Hardy, Pazzis and Pomeau (HPP). They studied the transport properties of fluids using a fully discrete particle velocity model: the Lattice gas automata (LGA) method [89]. Its main feature is the use of Boolean variables to describe the particle occupancy. These particles are positioned on nodes of the lattice and they go through two steps: the collision and the propagation steps. The main issue with the HPP model was its departure to the Navier-Stokes equation in the macroscopic limit. This issue was solved in 1986 by Frisch, Hasslacher and Pomeau (FHP) who recognized the importance of the lattice symmetry (i.e. with a higher symmetry than the HPP model). These authors used a lattice gas automaton with a hexagonal lattice [90]. The LGA, which is also referred to as the Lattice gas cellular automata (LGCA), simulates the macroscopic behavior of a fluid based on its microscopic properties such as sound velocity and viscosity. A general theory of this method was given by Wolfram in 1986 and by Frisch et Al. in 1987. LGCA is affected by noise that increases exponentially with the number of molecules attached to each lattice site. To upgrade LGCA modeling, researchers have revived Boltzmann equation by introducing the so-called lattice Boltzmann method. In 1988, McNamara and Zanetti replaced the particle occupation variables (Boolean variables) by single-particle distribution functions (Real variables) while retaining the same collision operator as in the LGCA model [76]. This solved the noise problem but not the viscosity limit. To solve the problem with the viscosity, Higuera & Jiménez (1989) introduced a linear collision operator that changes with viscosity [78]. Over the past two decades, various approaches have been proposed using a linearized collision operator so that the LBM has become a numerical method independent of its LGCA foundations. In summary, the LBM theory is rooted in the

[6]The Maxwell–Boltzmann distribution describes the spatial velocity distribution of gaseous particles at their thermodynamic equilibrium.

Chapman-Enskog analysis of the LGA method. The LBM method introduces an important feature that distinguishes it from other numerical methods: the collision operator (or propagation process) of the LBM method in phase space (or velocity space) is linear. Its main objective is to provide a robust numerical tool to describe at the mesoscopic scale the the dynamics of fluids. It allows modeling important problems in which both macroscopic hydrodynamics and microscopic physics are important.

The difference between the LBM method and the traditional CFD numerical methods lies in its algorithm structure. It allows modeling in an easy and robust fashion complex boundaries in a geometry while offering very efficient method parallelization [91, 92, 93]. The LBM method avoids the need to solve complicated kinetic equations such as the complete Boltzmann equation. Since it uses a simplified kinetic model – that is essentially based on the introduction of the essential microscopic and mesoscopic physical process – it ensures a correct description of the macroscopic behavior of fluid flows. To solve flow problems, different lattice Boltzmann schemes can be used. The simplest scheme corresponds to the BGK model [94] with a single relaxation time, the multi-relaxation-time (MRT) [95, 96], and the two-relaxation-time (TRT) [97, 98, 99]. The BGK model is known to be prone to numerical instabilities within certain limits [100, 101] unlike the MRT and TRT models (which can be rendered more stable by adjusting the relaxation parameters) [102, 103, 104]. The TRT model, with only two relaxation parameters, is more convenient than the MRT schemes because it allows retaining the simplicity of the BGK model [105, 106]. Other alternatives for these schemes exist such as the General Propagation Lattice Boltzmann Model (GPLB) – which was introduced to improve the numerical stability of the BGK model by adding two free parameters in the propagation step [107, 108, 109]. The Lattice Boltzmann method is quite resource-consuming since the discrete probability distribution functions used in this model require more memory for their storage than the hydrodynamic variables of the Navier-Stokes equations. However, using modern computers, required resources turn out to be no longer a problem as it is largely compensated by exceptional computational efficiency. The LBM, which is particularly well suited for calculations on a parallel architecture, has become a powerful computational method for the study of various complex systems on modern computers. In this study, as will be discussed in Chapter 2,

we use the LBM-two relaxation time (TRT) model to have a numerical solution of the Stokes equation and the advection-diffusion equation at the porous network scale.

2. LB-based method for Adsorption

The use of LBM to model surface interaction is far less conventional than its use to model fluid dynamics phenomena. To model adsorption using the LBM approach, different approaches can be found. In the work of Guo et al. [110], a computational scheme to model adsorption under hydrodynamic flows of the adsorbate was proposed. The adsorption isotherm is accounted for by using the Shan-Chen model – pseudo-potential model – and the adsorption energy with Lattice Boltzmann surface interactions. These authors rely on the adequate gas equation of state and the corresponding adsorption energy to get various types of adsorption isotherms. In the recent work by Xu et al. [111, 112], these authors simulate gas adsorption in shale gas. They studied the two phase separation and account for the adsorption at nanopore walls. These authors were able to reproduce the Langmuir isotherm using a D_2Q_9 LBM model. To consider adsorption, they also applied the same approach as in Guo et al. [110]. They were also able to model other types of adsorption isotherms (and provided evidence of the effect of significant adsorption in smaller pores). Finally, they were able to study the phase behavior and the liquid/gas densities to measure/predict adsorption isotherms under realistic conditions.

The studies above only account for adsorption in no-flow conditions. To include adsorption under the transport situations, Ning et al. have introduced a LBM-MRT model coupled with adsorption to simulate natural gas flows in confined systems (organic nanopores) [113]. These authors studied the impact of gas slippage and adsorption on the gas flow behavior in shale formations. To consider adsorption, they applied the pseudo-potential LBM to model the interaction between free and adsorbed gas molecules. Moreover, they used the adsorptive force introduced by Sukop and Or [114] to model the interactions between the bulk molecules and the pore surface. Using this approach, it was shown that, in small pores, gas transport is significantly affected by the transport of adsorbed gas at the surface. Adsorption reduces the velocity in small pores; the velocity in the bulk-like region is no longer large compared to the boundary velocity. This effect decreases and becomes insignificant as the pores get large enough. To account for

transport, Agarwal et al. [115] introduced the LBM model to investigate a fixed bed packed with adsorbents under different dynamic conditions. These authors presented breakthrough curves in 1D flow on non-porous surfaces. The model was shown to be capable of modeling adsorption within tube walls. In their approach, the concentration in the system obeys two equilibrium conditions: in the bulk phase and at the surface. This model works in the low concentration regime when adsorption is linear (Henry adsorption isotherm). However, this model can be extended to model non-linear adsorption if the desorption rate is made surface concentration dependent. In the work of Manjhi et al. [116], the LBM scheme d_3Q_{19} was used to simulate 2D unsteady state breakthrough curves. These authors introduced a first order adsorption-desorption kinetics between the gas and the solid phase. In their model, the mass transport equation is of the same form as the ADE with a modified dispersion coefficient and velocity profile (these two quantities vary with the solute adsorption isotherm slope). They used the LBM to solve the ADE coupled with the adsorption for different velocity profiles. They were able to present the adsorption breakthrough curves at different times/positions. The algorithm in these studies is based on imposing an initial dispersion coefficient, which prevents the study of the influence of adsorption on the other transport regimes. In the recent work of Vanson et al [117], the LBM scheme was used to couple the adsorption kinetics with the tracer dynamics. In their seminal work, adsorption occurs on fluid nodes directly in contact with neighboring solid nodes. At each position/node, an adsorbed quantity and a free quantity are defined to describe the equilibrium after each adsorption step. The transport behavior is described using the moment propagation method [118, 119] by introducing propagators for both the bulk and adsorbed phases. This allows computing the dynamical properties of the dispersed solute in the fluid. This method is interesting but it considers a system in a stationary regime. In contrast, in our approach (described in detail in Chapter 2), we will attempt to study transport of adsorbing molecules in different stages: diffusive regime, advection dominated regime and dispersive regime. The influence of the adsorption isotherm type on these different regimes will be investigated.

Chapter Conclusion

The short bibliographical study in this chapter was intended to highlight the basic concepts used in this thesis: transport in porous media, surfactant adsorption and the LBM approach. In particular, we have presented the different adsorption models as well as the structure of the adsorbed layer and of the surfactant aggregates. It has been concluded that a new adsorption model should be introduced to account for the complex structure/adsorption of the monomer/aggregates at the pore surface. The influence of adsorption on the dispersive transport regime was also presented. As will be discussed in this thesis, this will serve as a robust theoretical validation tool in our work.

Chapter II

Lattice Boltzmann method with the Two Relaxation Time scheme

Contents

This chapter, which presents the Lattice Boltzmann method (LBM) that was used in the frame of this thesis, is divided into two sections. The first section introduces the principles of the specific numerical scheme used to simulate the adsorption of tracer particles being transported in a flowing liquid. This numerical formalism, known as the Two Relaxation Time scheme (TRT), is a powerful technique that combines numerical efficiency and stability. The second section focuses on its application to the calculation of Stokes flow and tracer dispersion. The implementation and validation of the method are discussed in detail.

A. Two Relaxation Time scheme

The LBM using the TRT scheme employs two relaxation parameters which characterize the relaxation of particle distributions towards an equilibrium state. The first relaxation time corresponds to a physical time scale while the second relaxation time corresponds to a numerical parameter that ensures the numerical stability of the method. This approach combines the implementation simplicity of the BGK method as introduced in Chapter 1 with numerical accuracy and stability of the Multi Relaxation Times (MRT) scheme. Since its first development, the LBM-TRT has been applied to fluid flow and dispersion phenomena so that it can be considered as the ideal framework to address the questions at the heart of this PhD work.

1. Fundamentals and methods

1.1. Lattice Boltzmann

The fluid particles in a Lattice Boltzmann simulation occupy well-defined positions – the so-called nodes – on a prescribed lattice. Their displacements over time only occur through a set of velocities that connect adjacent nodes. This implies that an underlying lattice domain and a velocity space must be first introduced. In this context, it is convenient to introduce the classification scheme d_xQ_y where "d_x" indicates the dimensionality of the system (x = 1, 2 or 3) while "Q_y" denotes the set of velocities to be considered. As an example, Fig. 7 illustrates the d_3Q_{15} lattice model. It is a 3-dimensional lattice model on a cubic grid. Particles located at a given node can be transferred to 15 nodes: each of the 6 neighboring nodes that share a surface,

the 8 neighboring nodes sharing a corner, and the central node itself (i.e., particles at rest).

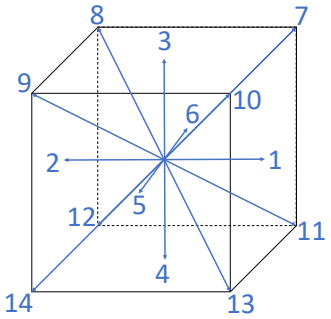

Figure 7: 3D Lattice model with 15 nodes: d_3Q_{15}.

The numerical space and time in the Lattice Boltzmann approach are discretized using the following incremental units: Δx and Δt. In what follows, unless stated otherwise, we set $\Delta t = \Delta x = 1$ (dimensionless Lattice Boltzmann units). The main variable in the LBM is the particle distribution function $f_q(\mathbf{r},t)$ which corresponds to the probability of finding a particle in a discrete accessible position (node located at the position vector $\mathbf{r}$) with a discrete velocity $\mathbf{v}_q$ at a time t. $\mathbf{v}_q$ represents the velocity set across the lattice that connects each node to its neighbors. It is defined for $q \in \{0,1,...,Q_m\}$ where $Q_m = Q-1$; $q=0$ corresponds to to the zero velocity $\mathbf{v}_0 = 0$ for molecules that do not leave the node while each non zero velocity $\mathbf{v}_q$ ($q>0$) has an opposite velocity $\mathbf{v}_{\bar{q}} = -\mathbf{v}_q$, $q \in \{1,...,Q_m/2\}$, $\bar{q} = q + Q_m/2$.

The particles interact in each node and propagate along the lattice so that two dynamical steps are performed at each timestep t: collision and propagation. The collision step involves particle collisions which are modeled using the collision operator Ω. The propagation step involves the redistribution between the particle distribution at a node $\mathbf{r}$ with its different neighboring nodes $\mathbf{r} + \mathbf{v}_q\Delta t$. Such processes, which are presented in more detail below, can be expressed as:

$$f_q(\mathbf{r}+\mathbf{v}_q\Delta t, t+\Delta t) = f_q(\mathbf{r},t) + \Omega[f(\mathbf{r},t)]_q \qquad \text{(II .1)}$$

The most important feature in the LBM is the construction of the collision operator Ω. Physically, it represents the effects of molecular collisions that induce relaxation towards the equilibrium distribution. When implementing the Lattice Boltzmann model, the propagation and collision steps are processed individually and boundary conditions are introduced through additional features.

Collision step. In the collision step, at each node position $\mathbf{r}$, the distribution function f_q evolves over a timestep Δt according to the collision operator Ω. This operator depends on the macroscopic properties of the system such as the fluid density as defined in Stokes equation and the fluid particle concentration as defined in the advection-diffusion equation (the operator Ω also depends on numerical Lattice Boltzmann parameters). The particle distribution function f_q is updated using the following equation:

$$\tilde{f}_q(\mathbf{r},t) = f_q(\mathbf{r},t) + \Omega[f(\mathbf{r},t)]_q \tag{II .2}$$

Propagation step. In the propagation step, the distribution function f_q is exchanged between neighboring nodes with respect to the velocity set:

$$f_q(\mathbf{r}+\mathbf{v}_q\Delta t, t+\Delta t) = \tilde{f}_q(\mathbf{r},t) \tag{II .3}$$

Fig. 8 illustrates for a given node $\mathbf{r}$ the main steps involved in Lattice Boltzmann simulations. The pre-collision stage – shown in Fig. 8(a) – shows an initial distribution $f_q(\mathbf{r},t)$. The particle

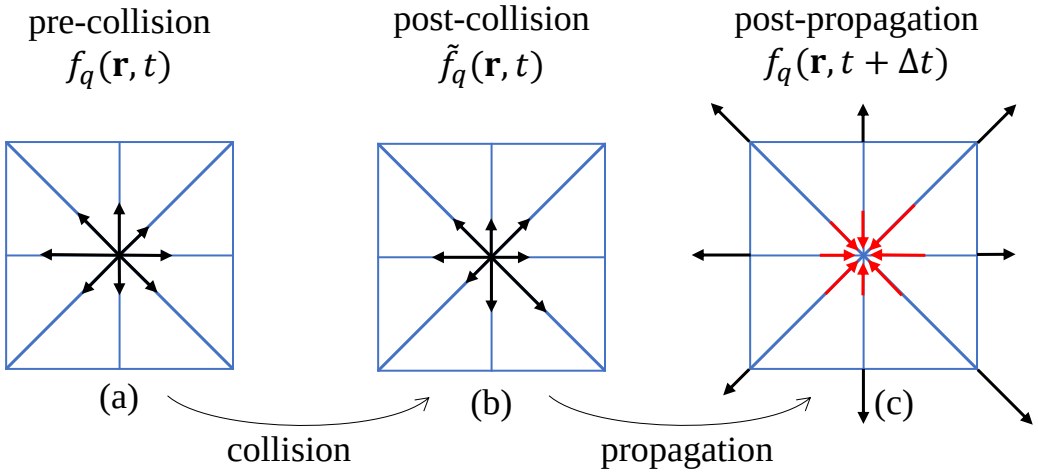

Figure 8: Illustration of the collision and propagation steps at a lattice node $\mathbf{r}$. The black arrows denote the distribution function at position $\mathbf{r}$ with a velocity q: before the collision step $f_q(\mathbf{r},t)$ (a) and after the collision step $\tilde{f}_q(\mathbf{r},t)$ (b). After the propagation step (c), the red arrows correspond to the incoming distribution function $\tilde{f}_q(\mathbf{r}-\mathbf{v}_q\Delta t,t)$ of the neighboring nodes with position $r-\mathbf{v}_q\Delta t$. On the other hand, the black arrows correspond to the distribution function $\tilde{f}_q(\mathbf{r},t)$ leaving node $\mathbf{r}$.

distribution then goes through the collision step before redistribution through the propagation step leading to $\tilde{f}(\mathbf{r},t)$. The post-collision distribution function – see Eq. (II .2) – is illustrated in Fig. 8(b). The final stage is obtained after the propagation step as depicted in Fig. 8(c): the particles initially at node $\mathbf{r}$ move to the node $\mathbf{r}+\mathbf{v}_q\Delta t$ (black arrows) while the particles initially located at the node $\mathbf{r}-\mathbf{v}_q\Delta t$ are displaced to node $\mathbf{r}$ (red arrows).

1.2. Relaxation times

The two relation time method (TRT) is an extended Lattice Boltzmann scheme where the collision operator involves different relaxation rates for the symmetric and anti-symmetric components. The symmetric components are defined as $f_q^+ = \frac{1}{2}(f_q + f_{\bar{q}})$ while the anti-symmetric components are defined as $f_q^- = \frac{1}{2}(f_q - f_{\bar{q}})$ for $q \in \{1,...,Q_m/2\}$ (for $q=0$, we have $f_0^+ = f_0$ and $f_0^- = 0$). In the two relaxation time approach, the update rule as defined in Eq. (I.1) is performed separately for the symmetric and the anti-symmetric equilibrium components $e_q^{\pm}$ and with two relaxation parameters: λ^+ for all symmetric non-equilibrium components $n_q^+ = f_q^+ - e_q^+$ and λ^- for all anti-symmetric non-equilibrium components $n_q^- = f_q^- - e_q^-$. For the zero velocity, $e_0^+ = e_0$ and $e_0^- = 0$.

The collision update rule for the LBM-TRT is given by the following equations for $q \in \{1,..,Q_m/2\}$ [99]:

$$\begin{aligned}
\tilde{f}_q(\mathbf{r},t) &= f_q(\mathbf{r},t) + \lambda^+ n_q^+ + \lambda^- n_q^- \\
\tilde{f}_{\bar{q}}(\mathbf{r},t) &= f_{\bar{q}}(\mathbf{r},t) + \lambda^+ n_q^+ - \lambda^- n_q^- \\
\tilde{f}_0(\mathbf{r},t) &= f_0(\mathbf{r},t)\ (1+\lambda^+) - \lambda^+ e_0
\end{aligned} \tag{II .4}$$

With the previous definitions and the use of the different components at $\bar{q}$ (i.e the opposite direction), the LBM algorithm is simplified since the symmetric components are defined as $f_q^+ = f_{\bar{q}}^+$ and $n_q^+ = n_{\bar{q}}^+$ and the anti-symmetric components as $f_q^- = -f_{\bar{q}}^-$, $n_q^- = -n_{\bar{q}}^-$. This implies that only half of the components have to be calculated/derived, therefore drastically minimizing the instructions in the LBM code. The LBM-TRT requires the definition of a set of numerical parameters $\Lambda^{\pm}$ and Λ to ensure that the solutions correspond to a stable algorithm.

These parameters are linked to the relaxation parameters $\lambda^{\pm}$ and defined as follows [99]:

$$\begin{cases} \Lambda = \Lambda^{+}\Lambda^{-} \\ \Lambda^{\pm} = -(1/2 + 1/\lambda^{\pm}) \text{ for } -2 < \lambda^{\pm} < 0 \end{cases} \tag{II .5}$$

To ensure the algorithm stability of the Lattice Boltzmann schemes, Ginzburg et al. [120, 103] have established that the numerical error is controlled by the particular set of the LBM numerical parameters $\Lambda^{\pm}$ - the so-called "magic number Λ". If we change physical parameters such as the viscosity (Stokes) or the molecular diffusion (ADE), the numerical errors stay invariant provided the adequate numerical "free" parameter is chosen. More precisely, for the Stokes flow problem, the kinematic viscosity is related to Λ^{+} and the "free" numerical parameter becomes Λ^{-}. For the advection-diffusion problem, the molecular diffusion coefficient is defined using Λ^{-} and the "free" numerical parameter is Λ^{+}. Therefore, once the physical parameters are defined, the free parameters Λ^{+} (advection-diffusion) and Λ^{-} (Stokes flow) are used to meet the prerequisite value of Λ that yields steady state solutions using Eq. (II .5). This is defined as the optimal TRT subclass [103].

2. Applications to fluid dynamics

In this section, we first introduce the lattice model that was adopted to conduct the Lattice Boltzmann simulations performed in this work. As the collision operator changes depending on the equation to be solved, we first present the formalism for Stokes flow before introducing the formalism for dispersion (advection diffusion equation). Fig. 9 presents the lattice classification used to perform all our simulations d_2Q_9. For this two dimensional model, the particles

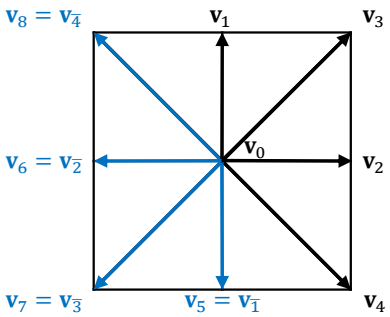

Figure 9: 2D Lattice Boltzmann model with 9 nodes: d_2Q_9

are allowed to stream in 9 directions following a velocity set $\mathbf{v}_q$ where $q \in \{0,..,Q_m\}$. The immobile (zero velocity) population corresponds to the index 0. The d_2Q_9 velocity set has four "coordinate" velocities $\mathbf{v}_q = (\pm 1,0),(0,\pm 1)$ and four "diagonal" velocities $\mathbf{v}_q = (\pm 1,\pm 1)$. To avoid any possible ambiguity, we use $f_q(\mathbf{r},t)$ to denote the solvent particle distribution (Stokes flow) and $g_q(\mathbf{r},t)$ to denote the tracer particle distributions (advection-diffusion).

2.1. Stokes flow

The objective of this section is to present the TRT scheme used to solve the Stokes flow which relates the momentum $\mathbf{j}$ to the pressure gradient $\boldsymbol{\nabla} P$ inducing the flow and the fluid kinematic viscosity ν. The Stokes equation in the absence of external forces – besides the pressure gradient inducing the flow – is given by:

$$\begin{aligned} \boldsymbol{\nabla}\mathbf{j} &= 0 \\ \boldsymbol{\nabla} P &= \nu \Delta \mathbf{j} \end{aligned} \tag{II .6}$$

Based on the work by Ginzburg et al. [121], the general form of the equilibrium distribution $e_q^{\pm}$ used to solve the Stokes flow problem in Lattice Boltzmann is defined as:

$$\begin{cases} e_q^+(\mathbf{r},t) = v_s^2 \rho(\mathbf{r},t) t_q^* \\ e_q^-(\mathbf{r},t) = t_q^*(\mathbf{j}(\mathbf{r},t).\mathbf{v}_q) \\ e_0^+(\mathbf{r},t) = \rho(\mathbf{r},t) - \sum_{q=1}^{Q_m} e_q^+(\mathbf{r},t) \\ e_0^- = 0 \end{cases} \tag{II .7}$$

where v_s is the fluid sound velocity and t_q^* correspond to isotropic physical weights obeying two constraints:

$$\sum_{q=1}^{Q_m} t_q^* \mathrm{v}_{q\alpha} \mathrm{v}_{q\beta} = \delta_{\alpha\beta} \text{ and } \sum_{q=1}^{Q_m} t_q^* \mathrm{v}_{q\alpha}^2 \mathrm{v}_{q\beta}^2 = \frac{1}{3}, \forall \alpha \neq \beta$$

with $\alpha,\beta \in \{1,2\}$ and $\delta_{\alpha\beta} = \{0 \text{ if } \alpha \neq \beta,\ 1 \text{ if } \alpha = \beta\}$. t_q^* take the value $t_q^* = \left\{\frac{1}{3}; \frac{1}{12}\right\}$ for the first (coordinate) and the second (diagonal) neighbor link in the d_2Q_9 scheme [121]. A proper derivation of Eq. (II .7), following step by step the approach by Ginzburg et al. [121], is given in Appendix B.1.

The calculation of the equilibrium functions requires to compute the fluid density ρ and the momentum $\mathbf{j}$. They are expressed as [121]:

$$\rho(\mathbf{r},t) = \sum_{q=0}^{Q_m} f_q(\mathbf{r},t) \tag{II .8}$$

$$\mathbf{j}(\mathbf{r},t) = \sum_{q=1}^{Q_m} f_q(\mathbf{r},t)\mathbf{v}_q \tag{II .9}$$

while the fluid velocity $\boldsymbol{U}$ is given by:

$$\boldsymbol{U}(\mathbf{r},t) = \frac{\mathbf{j}(\mathbf{r},t)}{\rho} \tag{II .10}$$

In the Stokes equation given in Eq. (II .6) the pressure is defined as $P = v_s^2\rho$ and the kinematic viscosity as $\nu = \frac{\Lambda^+}{3} = -\frac{1}{3} \times (\frac{1}{2} + \frac{1}{\lambda^+})$.

v_s is an adjustable positive parameter that must verify the following condition: $v_s^2 < v_s^{max2}$. Based on the stability analysis by Ginzburg et al. [122], v_s^{max2} must be set to $\frac{1}{3}$. Here, to satisfy this criterion, we choose $v_s^2 = \frac{1}{5}$. The steady-state condition for the Stokes flow simulation is fulfilled by using $\Lambda = 3/16$ [122]. In our case, we choose $\nu = 1/10$, so $\Lambda^+ = 3/10$ and $\Lambda^- = 10/16$.

In order to solve the Stokes equation using the Lattice Boltzmann approach, we consider two types of boundary conditions. The first condition set corresponds to the inlet/outlet geometry while the second condition set corresponds to the solid/liquid interface.

Inlet/Outlet condition. To induce fluid flow, we apply a pressure difference between the inlet and outlet of the lattice geometry. In practice, for the simulations, the pressure difference is applied by imposing a density difference $\Delta\rho = \Delta P/v_s^2$ with $\Delta\rho = \rho_{in} - \rho_{out}$ within the *simplified mixed anti-bounce back approach*. Inspired by the work by Talon et al. [123] and Ginzburg et al. [124], we have the following distribution function for $x = 0$ and $x = Lx - 1$:

$$\begin{cases} f_{\bar{q}}(\mathbf{r},t+\Delta t) = -\tilde{f}_q(\mathbf{r},t) + 2t_q^* v_s^2 \rho_{in} + (\lambda^+ + 2)n_q^+ - 6t_q^* \mathrm{v}_{qy}\mathrm{j}_y(\mathbf{r},t); & \forall \mathbf{r} = (0,y) \\ f_{\bar{q}}(\mathbf{r},t+\Delta t) = -\tilde{f}_q(\mathbf{r},t) + 2t_q^* v_s^2 \rho_{out} + (\lambda^+ + 2)n_q^- - 6t_q^* \mathrm{v}_{qy}\mathrm{j}_y(\mathbf{r},t); & \forall \mathbf{r} = (L_x - 1,y) \end{cases} \tag{II .11}$$

Solid/fluid interface. The discrete distribution function has to reflect the boundary conditions to which the fluid flow is subjected (null velocity at the solid/fluid interface). To do so, throughout this work, the *bounce-back boundary condition* is applied at each wall boundary node. The bounce-back rule consists in reordering the incoming density distribution functions from the fluid node to its former directions (i.e., along the incoming flow directions). In LBM, the bounce-back rule is fulfilled by adopting the following propagation condition:

$$f_{\bar{q}}(\mathbf{r},t+\Delta t) = \tilde{f}_q(\mathbf{r},t) \tag{II .12}$$

This rule places the solid-liquid interface midway between the two lattice sites in the fluid and in the solid for the Stokes simulation (this ensures that a straight velocity profile is obtained when using a parallel plates geometry).

In practice, the algorithm steps used to conduct Stokes flow simulations can be summarized as follows:

1. Initialization. The distributions $f_q(\mathbf{r},0)$ for a Stokes flow in a lattice geometry of a length L_x are given by:

$$\begin{aligned} f_0(\mathbf{r},0) &= \rho_{in} - \frac{x}{L_x - 1}\Delta\rho \\ f_q(\mathbf{r},0) &= 0 \; ; \; q \in \{1,..,Q_m\} \end{aligned} \tag{II .13}$$

2. Propagation. The distributions $f_q(\mathbf{r},t)$ are propagated (i.e. displaced) in the direction $\mathbf{v}_q$ using equation (II .3)

3. Fluid properties computation. $\rho(\mathbf{r},t)$ and $\mathbf{j}(\mathbf{r},t)$ are directly obtained from $f_q(\mathbf{r},t)$ using Eqs. (II .9) and (II .10)

4. Collision. The distribution functions are updated through Eq. (II .4) using the equilibrium components $e_q^{\pm}$ defined in Eq. (II .7) to obtain $\tilde{f}_q(\mathbf{r},t)$.

5. Iteration. Steps 2 to 4 are repeated until convergence to steady state is obtained.

2.2. Dispersion

Coupling between advective and diffusive transport – which results in the well-known dispersion effect – can be analytically described using the advection-diffusion equation (ADE). With isotropic diffusion (i.e. same diffusion coefficient in every direction of space), the ADE reads:

$$\frac{\partial c(\mathbf{r},t)}{\partial t} + \boldsymbol{U}.\nabla c(\mathbf{r},t) - D_m \Delta c(\mathbf{r},t) = 0 \tag{II .14}$$

where c is the solute concentration in the fluid, $\boldsymbol{U}$ is the flow velocity vector and D_m is the molecular self-diffusion coefficient. The equilibrium components for the d_2Q_9 scheme are [99]:

$$\begin{cases} e_q^+(\mathbf{r},t) = c(\mathbf{r},t)E_q^+ \\ e_q^-(\mathbf{r},t) = c(\mathbf{r},t)E_q^- \\ e_0^+(\mathbf{r},t) = e_0 = c(\mathbf{r},t)E_0 \\ e_0^-(\mathbf{r},t) = 0 \end{cases} \tag{II .15}$$

with

$$\begin{cases} E_q^+ = t_q^* v_e + \dfrac{t_q^*}{2}(3(\boldsymbol{U}.\mathbf{v}_q)^2 - \boldsymbol{U}^2) \\ E_q^- = t_q^*(\boldsymbol{U}.\mathbf{v}_q) \\ E_0 = \left(1 - \displaystyle\sum_{q=1}^{Q_m} E_q^+(\mathbf{r},t)\right) \end{cases} \tag{II .16}$$

where the diffusion-scale equilibrium parameter v_e is defined as $v_e = \frac{D_{xx}+D_{yy}}{2}$ and the diffusion coefficients as $D_{xx} = D_{yy} = D_m/\Lambda^-$. The isotropic weights are set to $t_q^* = \left\{\frac{1}{3}; \frac{1}{12}\right\}$ and $\boldsymbol{U} = \{U_x, U_y\}$ is the advective velocity with $\boldsymbol{U}^2 = U_x^2 + U_y^2$. As mentioned by Ginzburg et al. [99], an optimal TRT subclass requires to choose (Λ^+, Λ^-) such that $\Lambda = \frac{1}{4}$ (in this work, we use $\Lambda^+ = 4$ and $\Lambda^- = 1/16$). A proper derivation of Eq. (II .16) is given in Appendix B.2.

The result for the ADE simulation is the local concentration of the tracer $c(\mathbf{r},t)$ computed at each time step t from:

$$c(\mathbf{r},t) = \sum_{q=0}^{Q_m} g_q(\mathbf{r},t) \tag{II .17}$$

The velocity vector $\boldsymbol{U}$ is obtained from the Stokes simulation results at equilibrium.

Like for the Stokes flow, we need to consider specific boundary conditions to address the prob-

lem of advection/diffusion. For the ADE simulation, we apply the no-slip boundary condition at the solid/fluid interfaces by using the bounce-back condition:

$$g_{\bar{q}}(\mathbf{r}, t+\Delta t) = \tilde{g}_q(\mathbf{r}, t)$$

The algorithm steps in solving the ADE using Lattice Boltzmann calculations are as follows:

1. Initialization. $\boldsymbol{U}$, $g_q(\mathbf{r}_0, 0)$; $\forall \mathbf{r}_0 = (x_0, y)$

$$\begin{aligned} g_0(\mathbf{r}_0, 0) &= c_0 \\ g_q(\mathbf{r}_0, 0) &= 0 \; ; \; q \in \{1..Q_m\} \end{aligned} \tag{II .18}$$

   with c_0 the initial concentration at position $\mathbf{r}_0$.

2. Propagation. The particle distribution $g_q(\mathbf{r}, t)$ is displaced in the direction $\mathbf{v}_q$ using Eq. II .3

3. Local concentration computation. $c(\mathbf{r}, t)$ is updated at time step t from $g_q(\mathbf{r}, t)$ using Eq. (II .17).

4. Collision. The distribution function g_q is updated following the definition in Eq. (II .4) with respect to the equilibrium components $e_q^{\pm}$ given in Eqs. (II .15) and (II .16).

5. Iteration. Steps 2 to 4 are repeated until convergence towards steady state is reached.

B. Validation

The numerical system is composed of two infinite parallel plates of length L_x and width L_y.

First, we perform the Stokes simulation, to generate the flow in the geometry. Then we carry out the dispersion simulations.

In this section, we will present the results between the simple parallel plates, for complex regular geometry, the results are in Appendix B.5.

1. Stokes flow

1.1. Implementation

In this section, we apply the LBM-TRT approach to solve the Poiseuille flow in a 2D geometry as shown in Fig. 10. The Poiseuille flow, which is a simple flow problem that can be used to understand blood flow in arteries, is a seminal aspect in fluid mechanics. The fluid flow, which is parallel to the channel direction (x-axis in our case), is driven by a pressure difference between the entrance and the exit of the channel (see Fig. 10). The fluid flow, which is assumed to be incompressible and laminar, is described in the steady state limit.

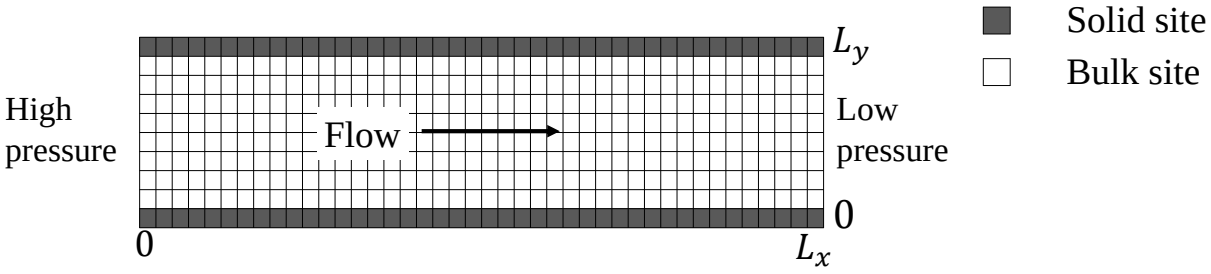

Figure 10: Illustration of the Poiseuille flow between two parallel plates of length L_x and distant by L_y.

Fig. 11 shows the result of Lattice Boltzmann simulations for the Stokes flow at equilibrium in the geometry given in Fig. 10. The velocity profile corresponding to Poiseuille flow is related to the maximum velocity U_{max} and the pressure difference ΔP through the following equation:

$$U_x(y) = U_{max}\left(\frac{4y}{L_y} - \frac{4y^2}{L_y^2}\right) \tag{II .19}$$

with $U_{max} = \Delta P L_y^2/8L_x\mu$ where μ is the fluid dynamic viscosity. Fig. 12 compares the result from a LBM-TRT simulation and the analytical solution given in Eq. (II .19)). The numerical and analytical solutions are in very good agreement. The difference between the analytical expression and the simulation result, which is maximum at the border of the geometry, is of the order of 0.1%. Otherwise, in the bulk-like region of the fluid flow, the error is less than 0.001%.

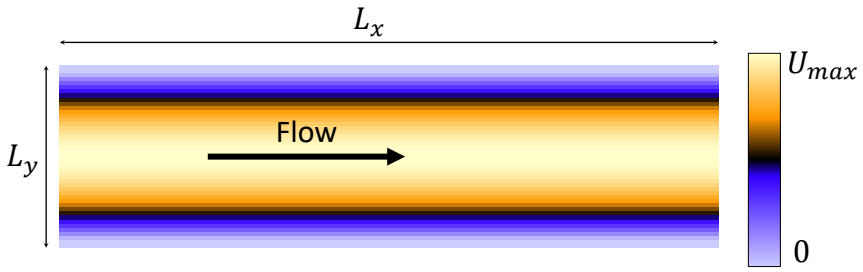

Figure 11: Flow between two parallel plates where $L_x = 2000\Delta x$ and $L_y = 41\Delta x$ (Stokes simulation using the Lattice Boltzmann approach).

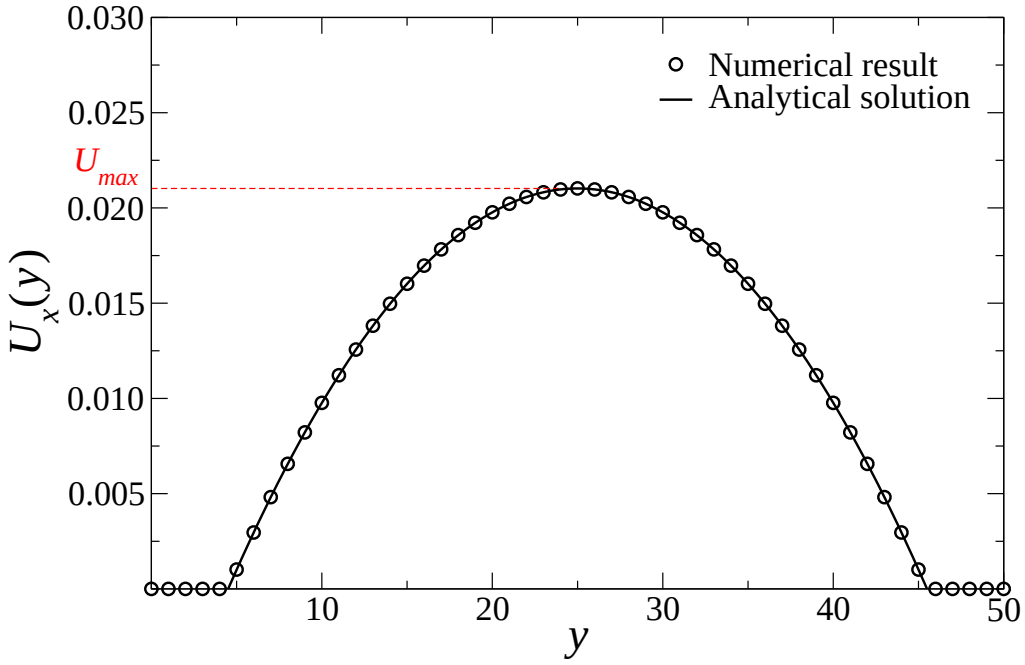

Figure 12: The velocity profile obtained in a geometry of two parallel plates for a Newtonian fluid. The symbols and the solid line respectively denote the data obtained from LB simulations and the analytical solution.

1.2. Numerical resolution/accuracy

With numerical simulations, the employed mesh including its resolution is expected to play an important role in the determination of accurate solutions. Therefore, we examine in what follows to what extent the geometric resolution can be reduced without significantly decreasing the accuracy of the simulations. To test the influence of the number of nodes on the simulation results, we have performed three simulations with identical parameters but different number of nodes for a fluid conducting channel of dimensions L_y = 9, 21 and 41. An odd number is used in order to have the maximum flow rate in the central node. Fig. 13 shows that, for both low and

high node numbers, the simulation data are in good agreement with the analytical expression of the Poiseuille flow profile. As already mentioned, the numerical error is larger at the geometry border than in the channel center. However, even when only 9 nodes are used, the error is lower than 0.2%. In conclusion, the LBM-TRT proves to be an efficient numerical method for the simulation of Stokes flow problems. The validity of the code has been verified by comparing the numerical solution to the exact known solution of a steady-state Poiseuille flow between parallel plates for different node numbers. This result follows the stability study by Ginzburg

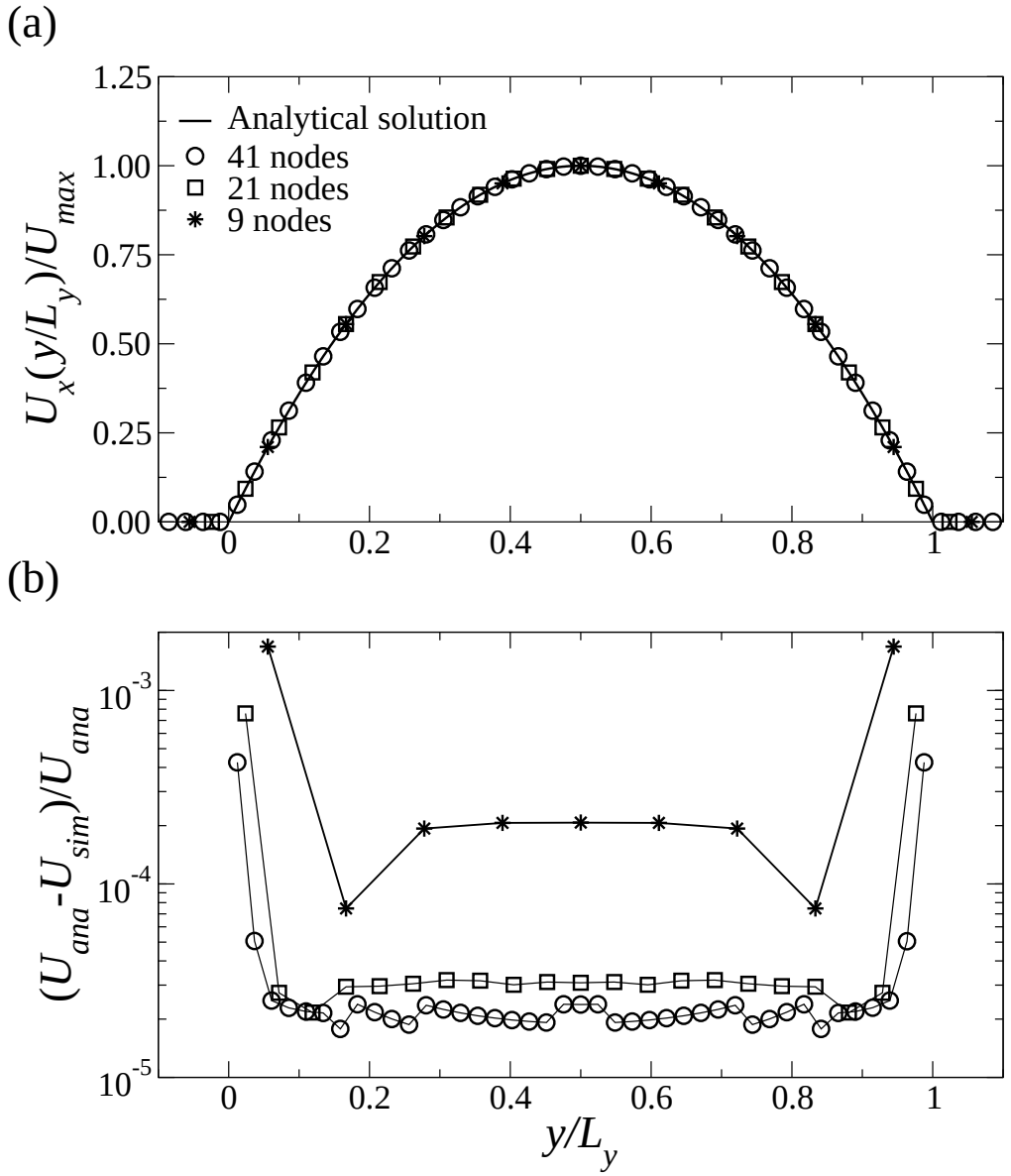

Figure 13: (a) Velocity profile obtained in a geometry consisting of two parallel plates for a Newtonian fluid. The symbols and the solid line denote the data obtained from LB simulations for different number of nodes and the analytical solution, resolutions. (b) Numerical error between the analytical expression and the simulation results.

et al. who determined the value required for Λ to guarantee accurate solutions for a minimum node number.

2. Passive tracer dispersion

In this section, the LBM-TRT is used to solve the advection/diffusion equation in a two dimension channel. The numerical accuracy is assessed by comparing our numerical results with known analytical solutions. As already discussed in Chapter 1, upon isotropic diffusion in a unidirectional flow (along the x-axis in our case), the transport of passive tracers is described on a local scale by means of the advection diffusion equation:

$$\frac{\partial c(\mathbf{r},t)}{\partial t} + U(\mathbf{r})\frac{\partial c(\mathbf{r},t)}{\partial x} = D_m \Delta c(\mathbf{r},t) \qquad \text{(II .20)}$$

with $c(\mathbf{r},t)$ the tracer concentration at time t at a node $\mathbf{r}(x,y)$. D_m is the molecular diffusion coefficient of the passive tracer while Δ is the Laplace operator. $U(\mathbf{r}) = U_x(\mathbf{r})$ is the velocity of the fluid flow in the x direction as obtained from the Stokes equation. Here, we emphasize that by "passive" we refer to non-adsorbing tracers.

2.1. Injection

A simple channel geometry consisting of two parallel plates is used to simulate the dispersion of the passive tracers. This geometry having dimensions $L_x \times L_y$ is shown in Fig. 14(a) where the white sites correspond to bulk-like regions of the system and the black sites denote the solid sites. In the simulations, our geometry is exposed to a fluid flow that obeys Stokes flow with an average flow rate U. The Peclet number Pe takes the value $\mathrm{Pe} = UL_y/D_m$. At a time $t = 0$, the tracer particles are injected with an initial concentration c. The concentration injection can be performed in several ways: (1) a concentration Dirac peak in time is injected at a lateral position in the geometry or (2) a concentration is injected continuously for a fixed time period. These two configurations consist in defining a lateral position $x = x_0$ in the geometry and injecting the concentration at this position for a determined period of time $\Delta t_0 = n\Delta t$. According to the value of n we can have a continuous "slug" injection ($n > 1$) or a Dirac injection ($n = 1$). Such situations are illustrated in Fig. 14(b).

More precisely for a position $\mathbf{r}_0 = (x_0, y)$, we inject tracer particles with the initial concentration c_0, to have $c(\mathbf{r}_0) = c_0$ over a period $\Delta t_0 = n\Delta t$. For $n = 1$, Fig. 14(c) shows the concentration distribution as a function of time which displays the dispersion of the tracer particles.

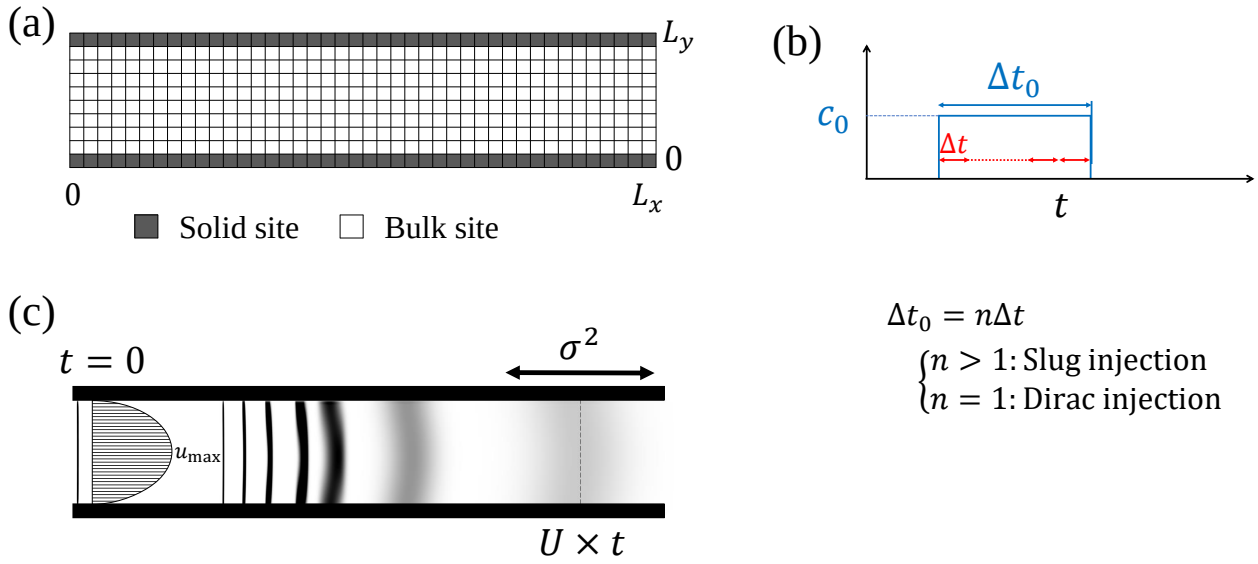

Figure 14: (a) The two parallel plates geometry with length L_x and a width L_y. (b) Concentration injection over time: the concentration is injected for a period $\Delta t_0 = n\Delta t$. (c) The concentration distribution in the geometry for a Dirac injection ($n = 1$).

2.2. Slug injection

We performed simulations for continuous "slug" injection of the passive tracers with a concentration $c_0 = 1$ at $x_0 = 0$. The injection time varies from $t = 0$ to $t = \Delta t_0 = 1.5\ 10^6 \Delta t$ and the channel geometry is defined as $L_x = 10000\Delta x$, $L_y = 41\Delta x$. Fig. 15 shows the evolution in time of the concentration at different lateral positions x as obtained in the course of the Lattice Boltzmann simulations. More in detail, we plot $c_l(x,t) = 1/L_y \times \sum_y c(\mathbf{r},t)$ for various positions in the channel. As expected, for large x, the tracers reach the maximum concentration c_0 at a longer time (a comparison of the concentration profile $c_l(x,t)$ with analytical solution is presented in Appendix B.4.). As shown in Fig. 16, mass conservation was checked along the simulation by monitoring in time the sum of all concentrations $\sum_t c_l(x,t)$ at different lateral positions. The total mass inside the system (i.e. amount of tracers) is well conserved as it is equal at all times to the injected mass (within very small numerical errors).

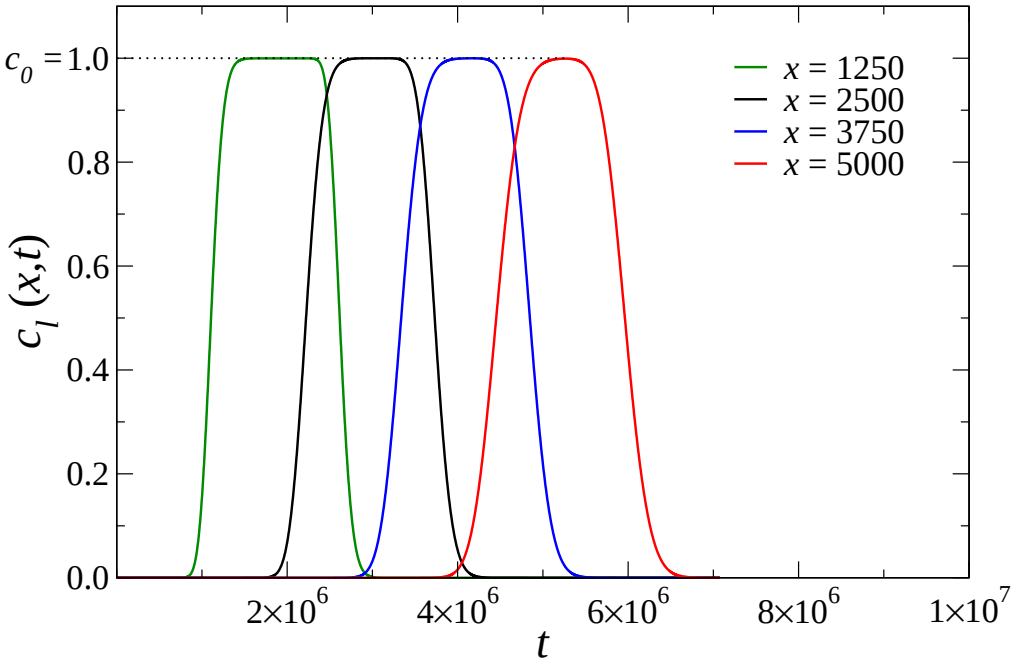

Figure 15: Evolution in time of the average concentration at different lateral positions x in a 2D channel geometry. For these simulations, the advective flow and diffusion constant are such that Pe $= 9.2$.

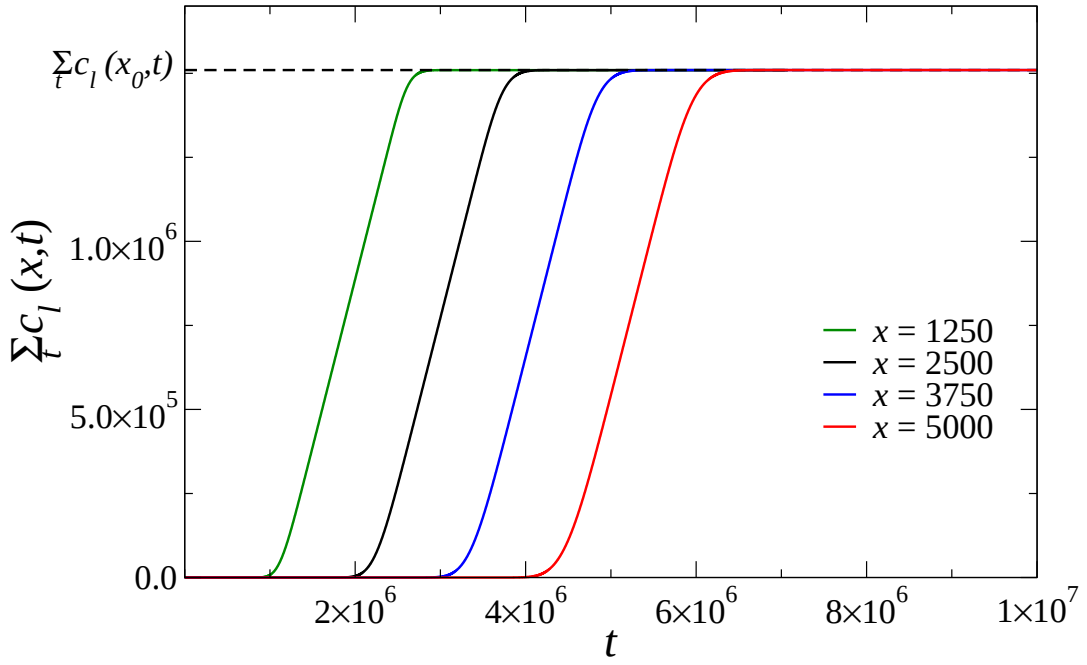

Figure 16: Mass conservation for passive tracer transport between two parallel plates with $L_x = 10000\Delta x$, $L_y = 41\Delta x$. The injection times vary from $t = 0$ to $t = \Delta t_0 = 1.5\ 10^6\Delta t$. the data are shown for different lateral positions within the channel geometry: $x = 1250$, $x = 2500$, $x = 3750$ and $x = 5000$.

2.3. Dirac injection

Dispersion coefficient To further validate the LBM-TRT simulation for dispersion, we compute the effective Taylor dispersion coefficient D_{eff}. For a geometry formed by two parallel plates, the latter can be expressed as [21]:

$$\frac{D_{eff}}{D_m} = \left(1 + \frac{\mathrm{Pe}^2}{210}\right) \tag{II .21}$$

The effective dispersion coefficient can be computed from the displacement variance as: $\lim_{t\to\infty} D(t)/D_m$ where $D(t)/D_m$ is given by:

$$\frac{D(t)}{D_m} = \frac{1}{2D_m}\frac{\partial \sigma_x^2(t)}{\partial t}. \tag{II .22}$$

The displacement variance $\sigma_x^2(t)$ as a function time is defined as $\sigma_x^2(t) = \left\langle x(t)^2 \right\rangle - \langle x(t) \rangle^2$ with

$$\langle x(t) \rangle = \sum_{x,y} \sum_{q=0}^{Q_m} g_q(x,y,t)(x - x_0)$$

$$\text{and } \left\langle x(t)^2 \right\rangle = \sum_{x,y} \sum_{q=0}^{Q_m} g_q(x,y,t)(x - x_0)^2$$

For a given problem, $\sigma_x^2(t)$ depends on the Peclet number Pe: $(\mathrm{Pe} \to 0)$ for pure diffusion and $(\mathrm{Pe} \to \infty)$ for pure advection. For finite Peclet numbers (Pe), three regimes can be observed as explained in what follows. To simulate dispersion using Lattice Boltzmann simulations, we inject at a time $t = 0$ the tracer particles with a concentration $c_0 = 1$ at a lateral position $x_0 = 200$. To probe the differences observed between the different transport regimes, we present in Fig 17(a) the tracer concentration in the channel at different times t ($\mathrm{Pe} = 50$ was used in these simulations). These data show the three different regimes that are observed in the course of these dispersion simulations. At t_1, transport evolves from the diffusion regime to the advection regime. The advection-dominated regime is observed in between t_2 and t_3. The dispersion regime is reached for t_4 and t_5.

Fig. 17(b) shows for different Peclet numbers the normalized displacement variance $D(t)/D_m$ as a function of time t. At first, the diffusive regime characterized by the first plateau with $D(t) = D_m$ is observed. Then, a transient regime is observed as the diffusive regime evolves

towards the advective regime. In the long time limit, the dispersive regime is observed as the numerical dispersion coefficient reaches a plateau corresponding to the effective dispersion coefficient $D(t \to \infty) = D_{eff}$ [125]. In this figure, the dashed lines show the analytical values as derived from Eq. (II .21). Our numerical results were compared with the analytical solution of the Taylor dispersion coefficient D_{eff}/D_m as given in Eq. (II .21). This comparison is shown in Table 2 for different Peclet numbers. These values are obtained in the stationary dispersive regime taken at t_{disp}) defined as the timescale where $\frac{\partial^2 \sigma_x^2(t)}{\partial t^2} < 10^{-9}$. Good agreement between the analytical and numerical values is observed, therefore validating our numerical approach.

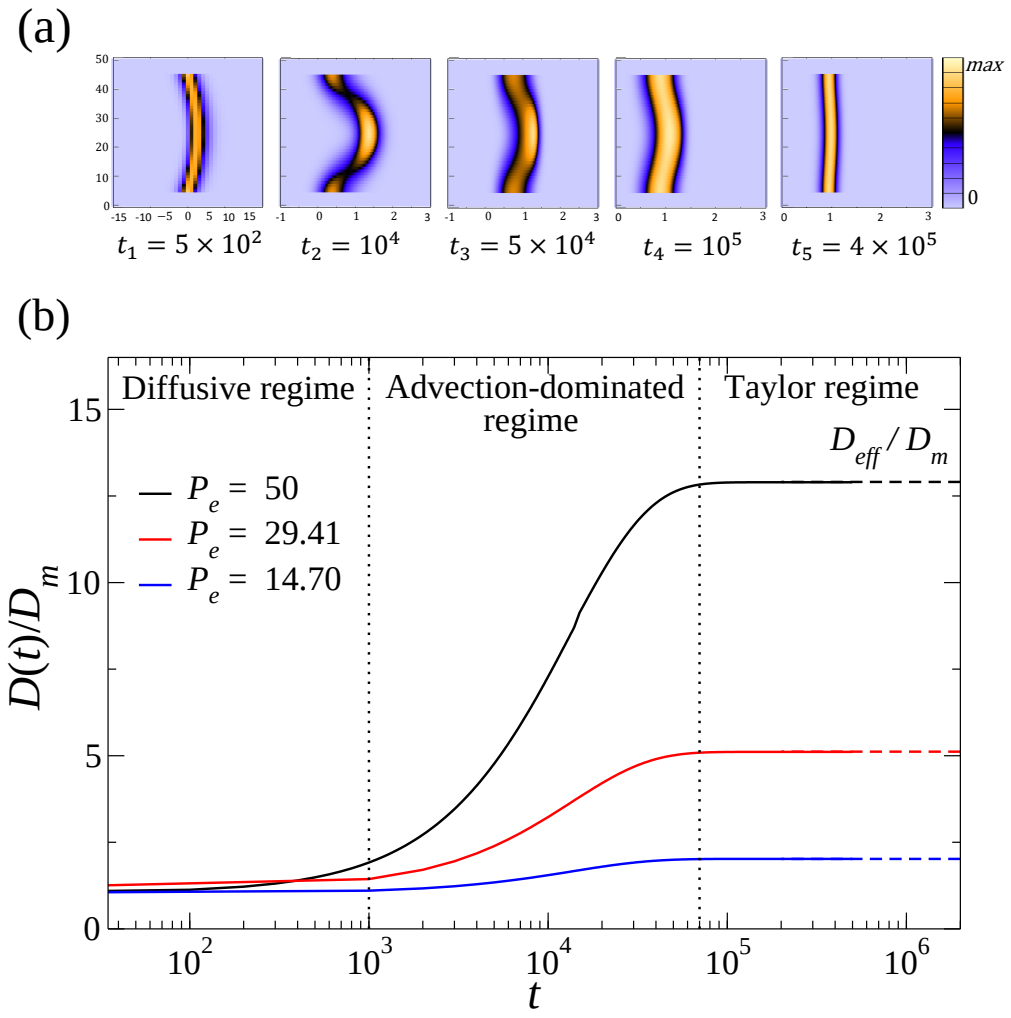

Figure 17: (a) Concentration profile of passive tracers confined between two parallel plates with $L_x = 10000\Delta x$ and $L_y = 41\Delta x$. The data, which are shown for different times t, were obtained for a Peclet number Pe $=$ 50. The abscissas are plotted in units of $(x - x_0)/Ut$ where x_0 is the lateral injection position and U the mean velocity. (b) Normalized displacement variance $D(t)/D_m$ as a function of time t for different Peclet numbers Pe. The solid lines denote the simulation results while the dashed lines correspond to the analytical solution for D_{eff}/D_m.

Peclet number Pe	**Numerical value** $\lim_{t\to\infty}\frac{D(t)}{D_m}$	**Analytical value** $\frac{D_{eff}}{D_m}=(1+\frac{\mathrm{Pe}^2}{210})$	**Numerical error**	**Convergence time** $(t_{disp})(\Delta t)$
14.7	2.0215	2.021	0.024%	1.2×10^5
29.41	5.1105	5.12	0.14%	1.4×10^5
50	12.90	12.894	0.122%	1.54×10^5
100	48.63	48.60	0.0704%	1.74×10^5
200	191.55	191.42	0.071%	3.45×10^5
300	429.75	429.44	0.073%	5.41×10^5
400	763.22	762.64	0.077%	6.98×10^5

Table 2: Comparison between analytical and numerical effective dispersion coefficients for different Peclet numbers (parallel plate geometry).

Displacement distributions and propagators

The propagators $P(\delta x,t)$, which correspond to the displacement distributions, represent the probability of the tracer to be displaced from a position x_0 to a position $x=x_0+\delta x$ over the time t. They can be written as follows:

$$P(x-x_0,t)=\alpha\sum_y\sum_q g_q(x,y,t);$$
$$\text{with}\sum_{\delta x}P(\delta x,t)=1\implies\alpha=\frac{1}{\sum_{\delta x}\sum_y\sum_q g_q(x_0+\delta x,y,t)}$$

which yields:

$$P(x-x_0,t)=\frac{1}{\sum_{\delta x}\sum_y\sum_q g_q(x_0+\delta x,y,t)}\sum_y\sum_q g_q(x,y,t); \tag{II .23}$$

In what follows, we present the normalized propagator defined using a normalized x-axis to account for fluid advection along the x direction. This propagator $P[(x-x_0)/Ut,t]$ is defined as:

$$P\left(\frac{x-x_0}{Ut},t\right)=\frac{Ut}{\sum_{\delta x}\sum_y\sum_q g_q(x_0+\delta x,y,t)}\sum_y g_q\left(\frac{x}{Ut},y,t\right) \tag{II .24}$$

The derivation of Eq. (II .24) is presented in Appendix B.3.

The normalized propagators $P[(x-x_0)/Ut,t]$ obtained for the two plate geometry considered with $\mathrm{Pe}=50$ are presented in Fig. 18(b). Note that accordingly the x-axis is normalized/shifted to display $(x-x_0)/Ut$ instead of x. To monitor the dispersion, the normalized propagators are plotted at different times t. At short time t_1 (black curve), the shape of the propagator is quasi-Gaussian; this indicates that the distance traveled by the tracer by diffusion is greater than the

distance traveled by advection (diffusive regime). We notice that a non-negligible proportion of tracers show negative displacements ($(x-x_0)/Ut < 0$); this confirms the key role played by diffusion at short time which transport tracers in the opposite direction to the advective flow. For $t_2 = 10^4 \Delta t$ (red curve), the propagator is strongly influenced by the velocity profile; this corresponds to the advection-dominated regime (the data obtained at t_3 correspond to a timestep where this transient regime is about to end). Once the Taylor dispersive regime is reached (at large times such as for $t = t_4$ and t_5), the propagators display a nearly perfect Gaussian shape. These results shed light on the transport mechanisms that give rise to the different regimes discussed in Fig. 18(a).

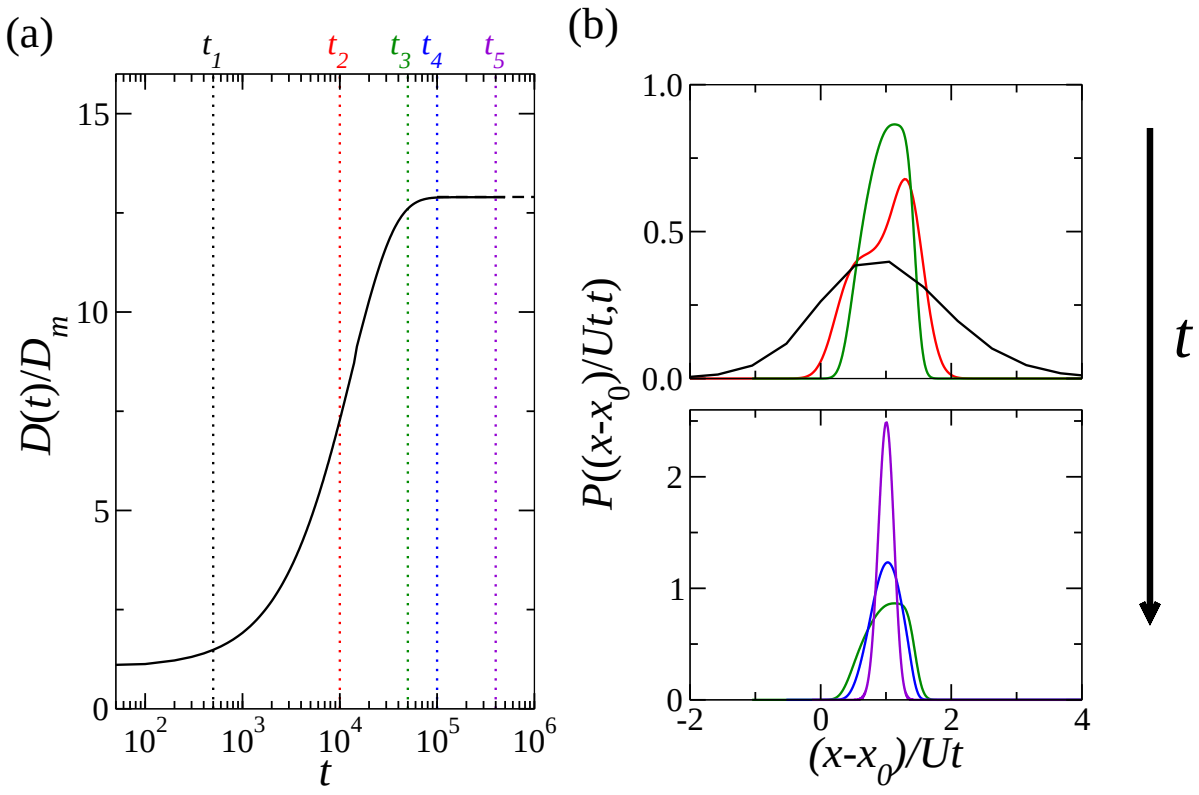

Figure 18: (a) Temporal evolution of the time derivative of the displacement variance for advection/diffusion flow. These data were obtained for Pe = 50. (b) Normalized propagators $P((x-x_0)/Ut,t)$ at different times t for a Peclet number Pe = 50.

2.4. Numerical resolution/accuracy

Like for Stokes flow, we performed simulations with different node numbers to study the numerical error expected when addressing advection/diffusion problems with the Lattice Boltzmann approach (we recall that we use the TRT scheme throughout this study). Table 3 shows the

different node numbers that were used to map a simple channel geometry of a width L_y. As expected, our results show that the numerical error decreases with increasing the node number. Even for small node numbers, the numerical error is acceptable. All the values presented in this table were obtained in the stationary dispersive regime.

Nodes number	**9**	**21**	**41**	**81**	**101**	**151**
Pe	100	100	100	100	100	100
$\lim_{t\to\infty} \frac{D(t)}{D_m}$	47.559	48.4797	48.6022	48.6249	48.6285	48.6303
Error	2.2153%	0.3222%	0.0704%	0.0236%	0.0163%	0.0125%
Convergence time (t_{disp})	7.86×10^5	6.87×10^5	1.64×10^5	1.75×10^5	1.74×10^5	1.47×10^5

Table 3: Impact of node number on the numerical accuracy of dispersion simulations conducting using the Lattice Boltzmann approach within the two relaxation time scheme.

Chapter Conclusion

In this chapter, we presented the Lattice Boltzmann Two Relaxation Time scheme. We highlight its fundamentals and importance as a numerical method as well as the main steps in the LBM-TRT algorithm: the propagation and the collision steps. We figured out that to solve different problems the key difference lies in the definition of the collision operator. Then, we presented the different equations needed to solve the Stokes equation with the appropriate boundary as well as the one used to solve the advection diffusion equation, which allows to study the dispersion of a passive tracer. Furthermore, we validated the implemented equations by performing simulation in parallel plates geometry. We were able to obtain the appropriate Poiseuille profile for the Stokes simulations. In addition, we performed the transport of passive tracer simulation, we proved the mass conservation of the molecules and we visualized the different transport quantities (normalized propagators and the concentration distribution) at the diffusive, advective and dispersive regime. This model delivers values consistent with the effective dispersion coefficients that characterize the Taylor dispersion regime. Furthermore, the results for different Peclet numbers were also verified. Finally, we validated the ability of the method to give accurate results with a minimum number of nodes for both the Stokes and the ADE simulations.

Chapter III

Cooperative surfactant adsorption

Contents

Surfactant adsorption in porous media remains poorly understood as the microscopic cooperative behavior of these amphiphilic molecules lead to non-conventional adsorption phenomena with complex underlying kinetics/structural organization. Here, we develop a simple thermodynamic model which captures this rich behavior by including cooperative effects – i.e. lateral interactions between adsorbed molecules and formation of ordered or disordered self-assemblies. More in detail, this model relies on a kinetic approach involving adsorption/desorption rates that are dependent on the surfactant surface concentration to account for facilitated or hindered adsorption at different adsorption stages. Using experimental data for different surfactants/porous solids, adsorption on both strongly and weakly adsorbing surfaces are found to be accurately described with model parameters that are readily estimated from experimentally available adsorption isotherms. The validity of our physical approach is confirmed by showing that the inferred adsorption/desorption rates obey the quasi-chemical approximation for lateral adsorbate interactions. Such cooperative effects are shown to lead to adsorption kinetics that drastically depart from conventional frameworks (Henry, Langmuir and Sips models).

This chapter is divided into three sections. In the first section, the adsorption of surfactants will be briefly discussed. The concept of cooperative adsorption effects as well as surface aggregation will be introduced followed by a short discussion on adsorption models – including their limitations – available in the literature. The second section is devoted to the development of a novel adsorption model that accounts for cooperative adsorption and surface aggregation. We will first present the basic assumptions and hypotheses at the root of this model. Then, we will provide a rigorous thermodynamic and kinetic derivation before comparing the model against relevant experimental data taken from the literature. More in detail, two experimental data sets are considered as they involve two different surfactants and two different mineral surfaces. In the third section, we will present some physical insights that can be derived from this cooperative adsorption model. First, we will show that this model is consistent with the quasi-chemical approximation which allows including lateral interactions in statistical physics of adsorption. Then, we will study the impact of cooperative effects and surface aggregation on adsorption kinetics. This third section ends with some conclusions and perspectives.

A. Surfactant adsorption

1. Adsorption and surface aggregation

The rich thermodynamic behavior of surfactants results from competing molecular interactions between the different – hydrophobic and hydrophilic – groups which combine with large entropy effects for such molecules [126]. Yet, despite such an intrinsic complexity, the phase behavior of bulk surfactants is reasonably well understood with available tools and formalisms to describe phenomena such as self-assembly and phase separation/transition but also non-intuitive temperature effect on liquid immiscibility, solubility, and micellization [127, 128, 129]. In contrast, the physical behavior of surfactants confined in porous materials or close to solid surfaces still challenges existing frameworks [130]. Adding free energy contributions corresponding to the head/surface and tail/surface intermolecular interactions lead to intriguing effects such as inverse temperature adsorption phenomena but also surface transitions between disordered and/or ordered mesoscopic assemblies (e.g. bilayers, hemi-micelles, vesicles, elongated micelles) [127, 131, 132, 133]. The situation is even more puzzling as the type of surfactant adsorption phenomena observed depends specifically on the solid chemistry (surface affinity/groups with possible amphoretic charges), surfactant molecule (apolar/polar, cationic/anionic) but also the thermodynamic/solution conditions (concentration, temperature, presence of an electrolyte, etc.). [3, 134, 135, 136]

As a result of this complexity, most of the experimental literature on surfactant adsorption focuses on a given family of surfaces or surfactants. In particular, significant research effort has been devoted to unraveling the structural mechanisms followed upon adsorption at increasing concentrations [137, 138, 139, 140, 141]. By combining thermodynamic measurements with structural analysis, some authors proposed advanced scenarios to rationalize step-adsorption and/or S-shaped adsorption isotherms observed experimentally [142, 143]. As illustrated in Fig. 19(b), such mechanisms often assume the adsorption of isolated monomers followed by the formation of a monolayer which eventually transforms into more complex structures (e.g. bilayer, hemimicelle, vesicle) upon increasing the surfactant concentration. [2] However, while such combined structural/thermodynamical studies provide an accurate and robust description

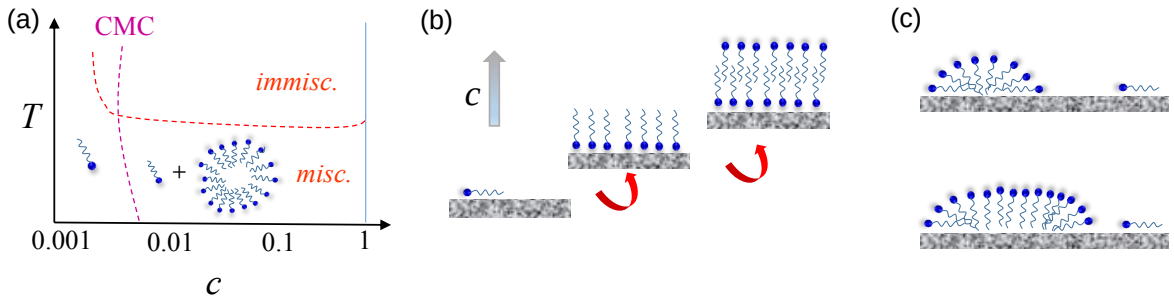

Figure 19: (a) Temperature-concentration (T,c) phase diagram of bulk surfactant solutions. The surfactant monomer is pictured as a hydrophilic head (blue sphere) combined with a hydrophobic chain (grey segment). A miscibility gap separates the high/low T regions with solvent/surfactant miscibility only observed at low T and c. In the miscibility range, for c smaller than the so-called critical micelle concentration (CMC), the monomers are solubilized in the solvent phase. For $c >$ CMC, the monomers coexist with micelles. (b,c) illustrates the orientation of surfactant molecules and possible surface aggregates obtained at a solid surface. (b) corresponds to the stepped Langmuir adsorption isotherm with the formation of a monomer adsorbed layer followed by film reorientation and growth. (c) illustrates other ordered or disordered self-assemblies coexisting with isolated adsorbed monomers.

for a broad class of solid/surfactant situations, there is a number of systems that lead to more complex data departing from such a picture [144, 145]. In particular, data for surfactants in various silica-based porous materials display complex adsorption mechanisms and kinetics with underlying mechanisms involving the formation of elongated/distorted micelles or vesicles [as illustrated in Fig. 19(c)] that cannot be captured using currently available models. Such complex effects arise from the heterogeneity in the solid surface chemistry and disordered morphology/topology of the host confining material.

2. Available modeling strategies

From a theoretical viewpoint, statistical physics is a powerful framework to predict the complex behavior of surfactants in bulk solution (including anomalous temperature effects on self-assembly for instance). In particular, extended lattice gas theory for monomers including a supra-lattice for the formation of micelles was shown to capture most of the physical phenomena involved in the phase diagram of these complex objects [146]. This method was extended later by Bock et al. [147] to account for surface adsorption through the use of surface interaction terms in the lattice gas Hamiltonian [146]. From a thermodynamic viewpoint, several models

such as those described hereafter have been proposed to describe surfactant adsorption on solid surfaces. Empirical models have been proposed to describe in an effective fashion S-shaped adsorption isotherms. This is the essence of the Sips model [148] which corresponds to the Langmuir model with the pressure raised to an empirical power α. The Toth model falls in the same category as it consists of accounting empirically for surface heterogeneity through a stretched Langmuir adsorption isotherm [149]. Other empirical approaches in this field consist of combining different physical models such as Henry, Langmuir, and BET adsorption isotherms to account for non-conventional surfactant adsorption isotherms [50]. More physical pictures have been proposed such as the model by Zhu and Gu in which adsorption is seen as a two-step process with two underlying equilibrium conditions (adsorption of a single monomer and recombination with already adsorbed monomers to form self-assemblies) [54, 55]. Other physical models such as those proposed by Tempkin [150] and Reed-Ehrlich [151] rely on the quasi-chemical approximation to account for lateral interactions within the adsorbed layer. This approximation is an extension of the Bragg-Williams approximation in which the Langmuir model is augmented by including a mean-field description of the lateral interactions between adsorbed molecules [152].

B. A simple model for cooperative adsorption

1. Basic assumptions

In spite of their physical basis, the models described above do not provide a general formalism for surfactant adsorption as they address different aspects (lateral interaction or self-assembly). In other words, a reliable thermodynamic description of the behavior of surfactants at surfactant/surface interfaces that includes both lateral interactions and transitions from adsorbed monomers to self-assembled objects is still missing. This task is complex but also crucially needed as the specific adsorption isotherm shape observed experimentally depends on many parameters (surfactant type, surface chemistry, presence of electrolytes/other fluid components, etc.). Here, we intend to fill this gap by providing a generic theoretical picture of surfactant adsorption through a phenomenological model based on simple thermodynamic ingredients. More in detail, this physical model is obtained by including physical cooperative effects through

both lateral interactions between adsorbed molecules and the possibility to form self-assembled structures at the solid surface using an occupancy parameter that can be larger than unity. It is important to note here that simply accounting for lateral interactions in adsorption models is not sufficient to describe the adsorption of mesoscopic objects at the solid surface. Indeed, even if such lateral interactions are physically needed to account for self-assembly, only a model including both lateral interactions and an occupancy larger than one can describe the adsorption/formation of supramolecular structures.

In practice, this model is derived by writing the underlying kinetic equation involving adsorption/desorption rates that are dependent on the surface concentration of surfactant to account for facilitated or hindered adsorption. Using experimental data for two surfactants on two mineral surfaces, this simple yet realistic model is shown to capture different surfactant adsorption types as observed upon varying the surfactant affinity towards the surface. We note that the present model can be extended to almost any surfactant adsorption/porous surface type as it has its roots in generic thermodynamic concepts (fluid/surface affinity, occupancy/packing, fluid/fluid interactions, etc.). The cooperative effects invoked in our model to capture the complex adsorption phenomena occurring at the surfactant/surface interface are believed to be physically relevant as they can be rationalized using a simple quasi-chemical adsorption model (which can be seen as a Langmuir model in which interactions between adjacent adsorbed molecules are treated in a mean-field approximation). It is also shown that the adsorption kinetics is drastically affected by such cooperative effects, therefore offering an additional mean to understand the physics of surfactant adsorption (role of lateral interactions and self-assembly).

2. Thermodynamic and kinetic derivation

To derive our model, let us consider the situation depicted in Fig. 20 with a solid surface made up of adsorption sites denoted s. Each site s can adsorb a single monomer m (blue sphere) or $n = 1/\beta$ aggregated monomers m' (red sphere) where n can be seen as the packing efficiency of aggregated monomers. $\beta \in]0,1]$ is a key ingredient which renders our model versatile as it allows describing very different physical situations. $\beta = 1/n$ describes the physical situation previously considered by Zhu and Gu [54] where a single monomer is used to aggregate with

$n-1$ other monomers to form a column on a single solid site s. In contrast, $\beta \to 1$ corresponds to very weakly aggregated object where each monomer m' lies at a solid site s. Therefore, as will be illustrated in the present chapter, defining β as a variable allows reproducing – at least in an effective fashion – almost any aggregation type without having to assume a given shape (micelle, hemi-micelle, vesicle, disordered aggregate, etc.). In particular, the combined use of a packing efficiency and surface-concentration adsorption constants allow describing both the adsorption of aggregated monomers forming at the pore surface (below and above CMC) and the direct adsorption of micelles formed in the bulk solution (above CMC).

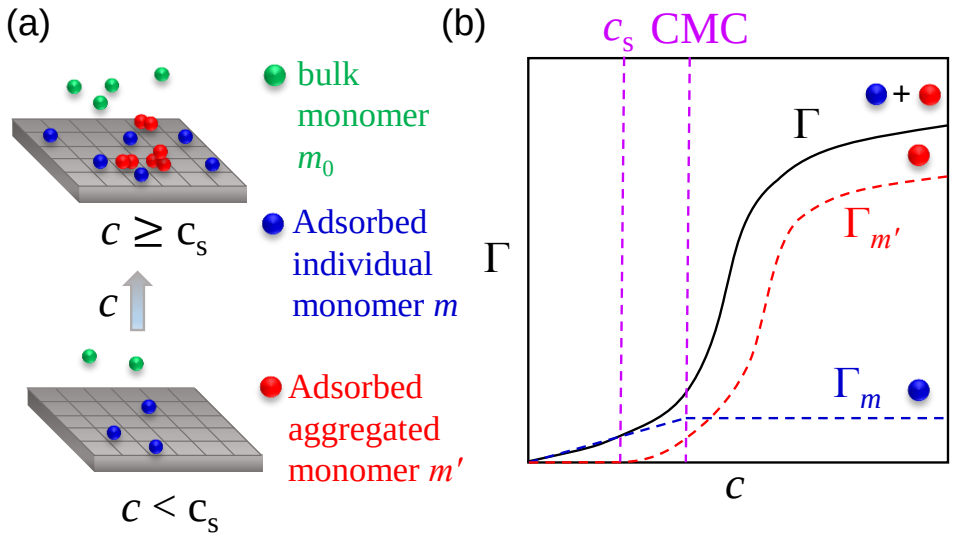

Figure 20: (a) Thermodynamic model of surfactant adsorption onto a solid surface in which the surface concentration Γ as a function of the bulk concentration c is the sum of a contribution Γ_m corresponding to adsorbed individual monomers m and a contribution $\Gamma_{m'}$ corresponding to aggregated monomers m'. (b) Adsorption isotherm corresponding to the model shown in (a). The black line is the total surface concentration Γ while the blue and red lines correspond to Γ_m and $\Gamma_{m'}$, respectively. For bulk concentration c smaller than the critical surface concentration c_s, only isolated monomers m get adsorbed at the surface – here following a Henry adsorption isotherm $\Gamma_m \sim c$ but any other adsorption regime can be considered. Beyond $c >$ CMC, Γ_m plateaus as the bulk concentration of isolated monomers remains constant. For $c_s < c <$ CMC, both isolated monomers m and monomers in aggregated objects m' adsorb at the surface.

Having introduced the fundamental ingredients of our model, its constitutive equations for adsorption equilibrium and kinetics can be derived by writing simple mass balance equations between the free monomers m_0 (green sphere) in solution $c = c[m_0]$, the solid surface sites s, the adsorbed individual monomers m and the adsorbed aggregated monomers m'. While such conditions can be written formally, rendering our model tractable requires an additional assump-

tion as follows. We introduce a surface critical concentration c_s below which only adsorption of individual monomers m occurs – this critical concentration can be seen as a minimum concentration to observe the formation of aggregated (self-assembled) structures at the solid surface, i.e. above c_s, both the individual monomers m and the aggregated monomers m' are adsorbed to the surface sites s.

Below the surface critical concentration $c < c_s$

The surface phase equilibrium can be expressed as $s + m_0 \rightleftharpoons m$ with an underlying first order kinetic equilibrium given by:

$$\frac{\partial \Gamma_m(c,t)}{\partial t} = k_A c \left[\Gamma^\infty - \Gamma_m(c,t)\right] - k_D \Gamma_m(c,t) \tag{III .1}$$

where $\Gamma_m(c,t)$ is the surface concentration of individual adsorbed monomers m and Γ^∞ is the surface site concentration in which individual adsorbed monomers m can be adsorbed. The first and right terms in the above equation account for the adsorption/desorption contributions over a time ∂t (k_A and k_D are the adsorption and desorption rates, respectively). The solution to this well-known mass balance condition corresponds to the Langmuir kinetic equation (with $k = k_A/k_D$):

$$\Gamma_m(c,t) = \frac{\Gamma^\infty ck}{1+ck}\left[1 - e^{-(1+k)k_D t}\right] \tag{III .2}$$

which converges in the stationary regime ($t \to \infty$) towards the Langmuir model $\Gamma_m(c,\infty) = \Gamma^\infty ck/(1+ck)$. In passing, we note that taking the limit $\Gamma^\infty >> \Gamma_m(c,\infty)$ allows recovering the Henry regime as usually observed at very low concentrations c: $\Gamma_m(c,t) = \Gamma^\infty ck[1 - e^{-k_D t}]$ with the long-time limit $\Gamma_m(c,\infty) = \Gamma^\infty ck$.

Above the surface critical concentration $c \geq c_s$

For $c \geq c_s$, both the individual monomers m and aggregated monomers m' get adsorbed in the surface sites s. As already mentioned, by using the concept of aggregated monomers, we encompass into the same contribution both the adsorption and recombination of adsorbed surfactants into mesoscopic assemblies (for $c > c_s$) and the direct adsorption of micelles formed in the bulk onto the solid surface (for $c >$ CMC $> c_s$). This is a specificity of our model in which the use of surface concentration-dependent adsorption/desorption rates allows treating in an ef-

fective yet physical fashion these complex adsorption phenomena. Here, as a simplification that allows straightforward comparison with experimental data without changing fundamentally the physical basis of our model, we assume that the adsorption of individual monomers occurs on a much shorter timescale than the adsorption of aggregated monomers. This implies that in the following kinetic equation, $\Gamma_m(c,t) \sim \Gamma_m(c,\infty)\ \forall t$. Moreover, each surface site is assumed to adsorb $n = 1/\beta$ aggregated monomers where the packing efficiency n allows accounting for nearly almost self-assembled object.

With these approximations, surface phase equilibrium for $c \geq c_s$ can be expressed as $s^* + m_0 \rightleftharpoons m'$ where the $*$ in s^* indicates that only the surface sites that remain available for aggregated monomers are considered. The corresponding first order kinetic equation for the adsorption/desorption of the aggregated monomers in such a process can be expressed as:

$$\frac{\partial \Gamma_{m'}(c,t)}{\partial t} = k'_A(\Gamma_{m'})\, c \times [\Gamma^{\infty} - \Gamma_m(c,\infty) - \beta\Gamma_{m'}(c,t)] - k'_D(\Gamma_{m'})\,\Gamma_{m'}(c,t) \qquad \text{(III .3)}$$

where $\Gamma_{m'}(c,t)$ is the surface concentration in aggregated monomers m' while β accounts for the fact that the adsorption of a single monomer in aggregated objects only occupies a fraction β of the surface site (therefore, with these definitions, $\beta\Gamma_{m'}(c,t)$ is the number of such mesoscopic i.e. aggregated objects). Moreover, to account for lateral interactions between monomers in aggregated objects, we make the adsorption and desorption rates k'_A and k'_D in the above equation explicitly dependent on the surface concentration $\Gamma_{m'}$. At equilibrium (i.e. in the stationary regime $\partial\Gamma_{m'}/\partial t = 0$), for a bulk concentration c, this kinetic equation leads to the following solution:

$$\Gamma_{m'}(c,\infty) = [\Gamma^{\infty} - \Gamma_m(c,\infty)] \times \frac{k'(\Gamma_{m'})c}{[1+\beta c k'(\Gamma_{m'})]} \qquad \text{(III .4)}$$

where $k'(\Gamma_{m'}) = k'_A(\Gamma_{m'})/k'_D(\Gamma_{m'})$.

In summary, this model allows introducing a required degree of complexity through collective effects in surfactant adsorption that manifest themselves into two factors. First, while isolated monomers are assumed to adsorb independently of each other, lateral interactions between monomers adsorbing into self-assemblies must be included. Second, the formation of

either ordered (e.g. hemimicelle, vesicle) or distorted (e.g. elongated micelle) mesoscopic assemblies is included in an effective fashion through the use of a packing efficiency n. This generic model relies on a limited yet important set of assumptions: namely, superimposition of isolated and aggregated monomer adsorption, fast isolated monomer adsorption, description of self-assemblies through an effective parameter n. However, despite these assumptions, as illustrated in the remaining of this chapter, this model allows deriving fundamental insights into the thermodynamics and kinetics of surfactant adsorption from simple experimental data. In particular, as shown below, a merit of this model is that the adsorption-dependent dynamical coefficients governing the adsorption kinetics of isolated and aggregated monomers can be estimated from static adsorption data (since the adsorption/desorption rates k'_A and k'_D depend only explicitly on $\Gamma_{m'}$). Moreover, this versatile model can be applied with almost no restriction regarding the type of surfactants, surfaces, self-assemblies, etc.

3. Parameterization against experimental data

To test our model, we consider two sets of experimental data which are representative of different surfactant adsorption behaviors. More in detail, we use the data by Denoyel and coworkers who considered the adsorption at room temperature of two polar (non-ionic) surfactants onto silica-based surfaces (TX100 onto silica and TX 165 onto kaolinite clay) [138].

As shown in Fig. 21, for both systems, the adsorption isotherms exhibit two regimes which correspond to monomer adsorption at low concentration c followed by a rapid increase in the surface concentration corresponding to surface self-assembly at concentrations around the CMC. However, a major difference between the two data sets lies in the monomer adsorption regime in the low concentration range with a slow – Henry-like – regime for Fig. 21(a) and a rapid – Langmuir-like – regime for Fig. 21(b) (we note that, in general, a Langmuir model can be assumed by default as Henry law is simply its asymptotic limit). Since the two surfactants considered here are similar non-polar molecules with an OH group at their end, the origin of this difference has to be found in the surface chemistry of the different surfaces. Typically, for the kaolin sample, as discussed by Denoyel and coworkers [138], the observed strong adsorption phenomenon is thought to occur on a basal plane – more exactly, the basal plane made up of

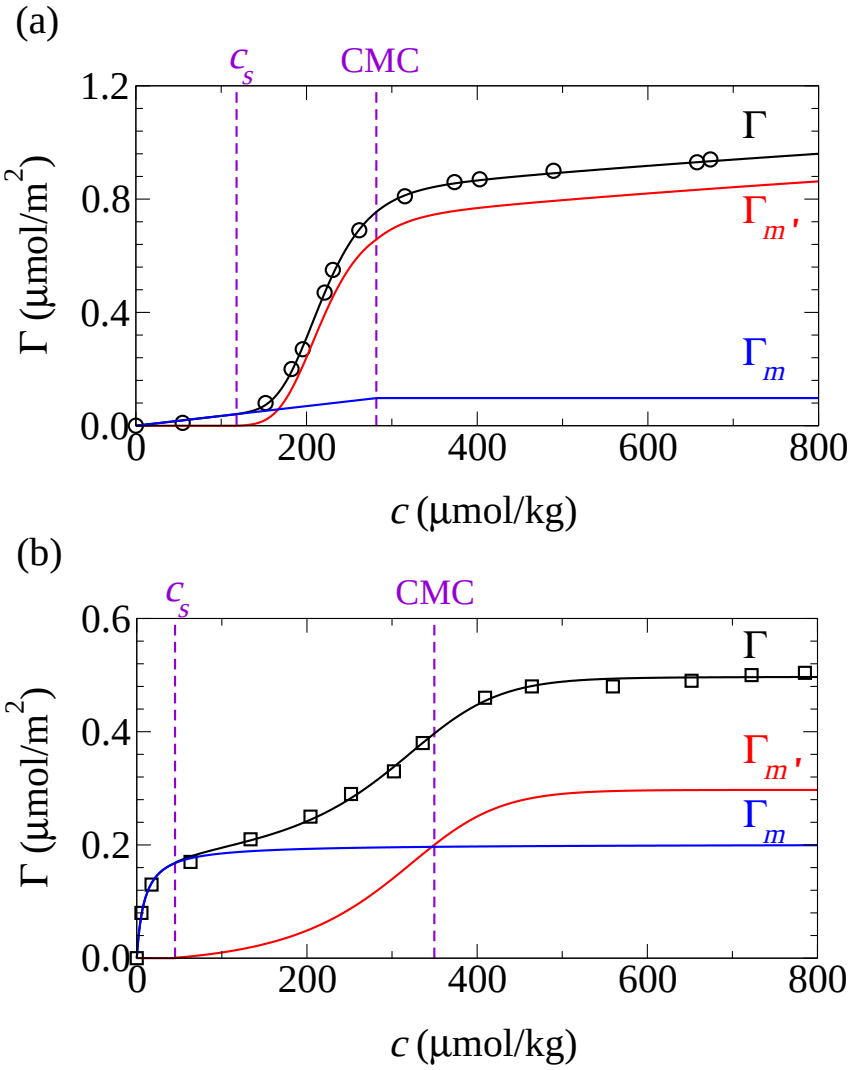

Figure 21: Surfactant adsorption isotherms at $T = 298$ K showing the surface concentration of surfactants Γ onto a silica-based surface as a function of the bulk concentration c: (a) TX100 surfactant on quartz silica and (b) TX165 surfactant on kaolin. The black symbols are the experimental data taken from Denoyel et al. with the black line corresponding to smoothed interpolation data. For both systems, the blue and red lines show the predictions of our model for the adsorption of isolated and aggregated monomers, respectively (by construction, the sum of these two contributions is equal to the experimental data). A Henry law and a Langmuir law were used to describe the isolated monomer adsorption in (a) and (b), respectively. The vertical dashed lines indicate the critical surface concentration c_s and critical micelle concentration CMC.

aluminol sites as the surface concentrations were found to be pH independent (adsorption sites on this basal plane do not form amphoteric charges with pH). [138] In contrast, because the weak adsorption phenomenon displayed in Fig. 21 for silica is found to be pH-sensitive, it is assumed to occur on neutral adsorption sites that become charged upon increasing the pH.

We use the following procedure to apply our model to the experimental data $\Gamma^{\exp}(c)$ shown in Fig. 21.

- First, to define the surface critical concentration c_s, the interpolated experimental data are fitted against a Langmuir adsorption isotherm over a concentration range $[0, c_{\max}]$. While the fit is very good for small $c_{\max}$, the fit does not provide satisfactory results for large $c_{\max}$ (since a simple Langmuir or Henry adsorption isotherm cannot describe the raw experimental adsorption data over a large concentration range). At this stage, it is decided to define c_s as the maximum value $c_{\max}$ for which a correlation coefficient of $R^2 = 0.99$ is obtained. While the specific cutoff value used is arbitrary, it should be emphasized here that slightly different values would lead to very similar predictions (in practice, with variations in the degree of agreement with experimental data that falls within the experimental error bar). This allows us to have a good approximation to describe the monomer surface concentration $\Gamma_m(c,\infty)$ for $c < c_s$.

- Second, having a fitted model for $\Gamma_m(c,\infty)$, one can estimate the contribution corresponding to the adsorbed aggregated monomers $\Gamma_{m'}(c,\infty)$ by subtracting $\Gamma_m(c,\infty)$ from $\Gamma^{\exp}(c)$, i.e. $\Gamma_{m'}(c,\infty) = \Gamma^{\exp}(c) - \Gamma_m(c,\infty)$.

- Third, $k'(\Gamma_{m'})$ can be readily estimated from $\Gamma_{m'}(c,\infty)$ by inverting Eq. (III .4):

$$k'(\Gamma_{m'}) = \frac{\Gamma_{m'}(c,\infty)}{c[\Gamma^{\infty} - \Gamma_m(c,\infty) - \beta\Gamma_{m'}(c,\infty)]} \tag{III .5}$$

As shown in Fig. 21, for both systems, the model including cooperative effects applies accurately to the experimental data.

Fig. 22 shows $k'(\Gamma_{m'})$ as a function of $\Gamma_{m'}$ for the two systems considered here (TX100 on quartz silica and TX165 on kaolin). It should be noted that the model applied to the isothermal adsorption data does not allow estimating β. This is a drawback of our model but β can be estimated independently of $k'(\Gamma_{m'})$ from adsorption kinetics data as shown in the last section of this chapter Fig. 22 shows that $k'(\Gamma_{m'})$ increases with increasing $\Gamma_{m'}$ for a given β, therefore pointing to the existence of collective, i.e. cooperative, effects in surfactant adsorption (otherwise $k'(\Gamma_{m'})$ would remain constant). Physically, this behavior indicates that cooperative effects lead

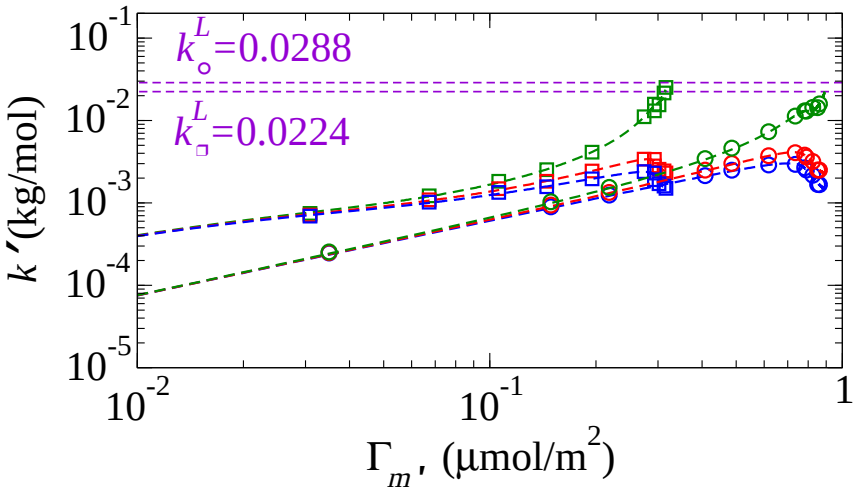

Figure 22: Adsorption constant $k'(\Gamma_{m'})$ for the aggregated monomers m' as a function of their surface concentration $\Gamma_{m'}$ as extracted from the experimental adsorption data shown in Fig. 21. The circles are for TX100 adsorption on quartz silica while the squares are for TX165 on kaolin. For each system, the blue, red, and green data denote data obtained for $\beta = 0.2$, $\beta = 0.5$ and $\beta = 1.0$, respectively. The two horizontal dashed lines in purple indicate the Langmuir adsorption constants that best match the experimental adsorption isotherms in the high concentration range $c > c_s$.

to enhanced adsorption with already adsorbed molecules facilitating adsorption of additional monomers either in the same adsorption sites (when $\beta \neq 1$) and/or in neighboring adsorption sites ($\beta = 1$). As expected from Eq. (III .5), upon decreasing β, the fraction of available sites to adsorb aggregated monomers increases so that $k'(\Gamma_{m'})$ decreases. This is due to the fact that $k'(\Gamma_{m'})$ is an effective adsorption constant so that low β corresponds to systems that tend to self-assemble easily (therefore not requiring large adsorption constants to pack efficiently at the solid surface). Fig. 22 also shows for the two systems considered here the Langmuir adsorption constant $k^L = k_A/k_D$ which was estimated by fitting the concentration range beyond the critical surface concentration $c > c_s$. More in detail, by restricting the fitting procedure to the region where the surface concentration increases rapidly with concentration, it is possible to describe semi-quantitatively the data using a simple Langmuir model. As shown in Fig. 22, except for large surface concentrations $\Gamma_{m'}$, regardless of the system considered, the Langmuir constant k^L overestimates the adsorption constant $k'(\Gamma_{m'})$ predicted using our model. This result is due to the fact that the Langmuir model does not describe cooperative adsorption so that a larger effective constant is needed to capture the increasing adsorption rate upon increasing the surface concentration.

C. Cooperative effects in physical adsorption/aggregation

For a given surfactant/surface couple, the parameters involved in the present model are derived from available experimental data. To assess the physical validity and robustness of our model, it is important to connect its underlying parameters to existing theoretical frameworks. We can refer to the quasi-chemical adsorption model (which can be considered as a Langmuir model in which the interactions between adjacent adsorbed molecules are treated in a mean-field approximation). Moreover, adsorption kinetics will be studied, as they are significantly affected by the cooperative effects, which is going to provide an additional means of understanding of the physics of surfactant adsorption (role of lateral interactions and self-assembly).

1. Consistency with the quasi-chemical approximation

The quasi-chemical approximation allows deriving a simple expression for the surface concentration that accounts for lateral interactions between adsorbed monomers. In the first paragraph, we provide the main thermodynamic ingredients of this important model and give the exact derivation of the chemical potential. Then, in the second paragraph, we will use the resulting expression and compare it to the respective chemical potential obtained using our model, for the two experimental data sets.

1.1. Formal derivation

Let us consider a solid surface made up of M adsorption sites occupied by N fluid molecules. For such a surface lattice having a connectivity z_0 ($z_0 = 4$ for a simple square lattice as each site is connected to 4 nearest neighbors), the total number of pairs is $z_0 M/2$ since each of the M sites is paired with z_0 sites but each site pair is double counted $[(i,j) = (j,i)]$. Each neighboring site pair can be occupied as follows: (1) both sites are empty, (2) one site is empty while the other one is occupied, (3) both sites are occupied. Let us denote N_{00}, N_{01}, and N_{11} the number of pairs corresponding to these three configurations (the subscripts '0' and '1' therefore refer to an unoccupied site and an occupied site in the considered pair). N_{00}, N_{01}, and N_{11} necessarily obey the following normalization rules: (1) $z_0 N = 2N_{11} + N_{01}$ and (2) $z_0(M-N) = 2N_{00} + N_{01}$.

These two rules can be understood as follows. Each isolated molecule corresponds to one of the N adsorbed molecules and generates $z_0 N_{01}$ pairs but each neighboring molecule pair removes two pairs of type N_{01}. The same reasoning applies for the second rule but with the unoccupied sites.

In what follows, the canonical partition functions of an individual adsorbed molecule and of the whole system made of M sites occupied by N molecules at the temperature T are denoted q and $Q(N,M,T)$, respectively. By noting w the energy of a given pair of neighboring adsorbed molecules, the lateral interaction energy between adsorbed molecules writes $N_{11}w = z_0 Nw/2 - N_{01}w/2$. This allows writing the total partition function as:

$$Q(N,M,T) = q^N \sum_{N_{01}} g(N,M,N_{01}) e^{-N_{11}w/k_B T} = q^N e^{-z_0 Nw/2k_B T} \sum_{N_{01}} g(N,M,N_{01}) e^{N_{01}w/2k_B T} \tag{III .6}$$

where $g(N,M,N_{01})$ corresponds to the number of ways the N adsorbed molecules can be distributed among the M solid sites while leading to N_{01} occupied/unoccupied site pairs. To determine $g(N,M,N_{01})$, we first consider the number of ways $\omega(N,M,N_{01})$ each site pair can be assigned to N_{00}, N_{01}, and N_{11} without considering whether these configurations are actually possible or not [$\omega(N,M,N_{01}) \geq g(N,M,N_{01})$]:

$$\omega(N,M,N_{01}) = \frac{[z_0 M/2]!}{[z_0 N/2 - N_{01}/2]![z_0(M-N)/2 - N_{01}/2]![N_{01}/2]!^2} \tag{III .7}$$

Following the approach by Hill [152], to correct $\omega(N,M,N_{01})$ for impossible configurations and estimate $g(N,M,N_{01})$, we write that $g(N,M,N_{01}) = C(N,M)\omega(N,M,N_{01})$ where $C(N,M)$ is the correction factor that needs to be determined. After noting that $\sum_{N_{01}} g(N,M,N_{01}) = M!/[N!(M-N)!]$, $C(N,M)$ can be determined by writing:

$$\sum_{N_{01}} g(N,M,N_{01}) = C(N,M) \sum_{N_{01}} \omega(N,M,N_{01}) = \frac{M!}{N!(M-N)!} \tag{III .8}$$

Then, we use the maximum term method which consists of approximating the sum over N_{01} by its maximum contribution obtained for N_{01}^*. In practice, N_{01}^* is determined by maximizing ω,

i.e. $\partial \ln \omega / \partial N_{01} = 0$ for $N_{01} = N_{01}^*$. This leads to $N_{01}^* = z_0 N(M-N)/M$ with[1]:

$$\omega(N,M,N_{01}^*) = \left[\frac{M!}{N!(M-N)!}\right]^{z_0} \tag{III .9}$$

and, therefore, the following expression:

$$C(N,M) = \left[\frac{M!}{N!(M-N)!}\right]^{1-z_0} \tag{III .10}$$

By introducing $t(N,M,N_{01}) = g(N,M,N_{01})e^{N_{01}w/2k_BT} = C(N,M)\omega(N,M,N_{01})e^{N_{01}w/2k_BT}$, the partition function in Eq. (III .6) can be expressed as:

$$Q(N,M,T) = q^N e^{-z_0 Nw/2k_BT} \sum_{N_{01}} t(N,M,N_{01}) \sim q^N e^{-z_0 Nw/2k_BT} t(N,M,N_{01}^*) \tag{III .11}$$

where the last expression is obtained by replacing the sum over N_{01} by its maximum contribution (maximum term method); i.e. $\partial \ln t(N,M,N_{01})/\partial N_{01} = 0$ for $N_{01} = N_{01}^*$. From the expression of $t(N,M,N_{01})$, this last optimization condition leads to

$\partial \ln t(N,M,N_{01})/\partial N_{01} = \partial \ln \omega(N,M,N_{01})/\partial N_{01} + w/2k_BT = 0$. After a little algebra[2], it is possible to show that $\partial \ln \omega / \partial N_{01} = 1/2 \ln[(\theta-\alpha)(1-\theta-\alpha)/\alpha^2]$ where $\theta = N/M$ is the occupancy rate and $\alpha = N_{01}/z_0 M$. Using this expression in the condition $\partial \ln t(N,M,N_{01})/\partial N_{01} = 0$ leads to:

$$\frac{(\theta-\alpha)(1-\theta-\alpha)}{\alpha^2} = e^{-w/k_BT} \tag{III .12}$$

The last expression is a second degree equation in α which admits as solutions:

$$\alpha = \frac{N_{01}^*}{z_0 M} = \frac{2\theta(1-\theta)}{\gamma+1} \tag{III .13}$$

with $\gamma = [1 - 4\theta(1-\theta)(1-\exp(-w/k_BT))]^{1/2}$ (among the two solutions admitted by this quadratic equation, only the one leading to the correct solution $\alpha = \theta(1-\theta)$ for $w = 0$ i.e. $\gamma = 1$ is kept).

[1] Using Stirling formula, $\ln N! \sim N\ln N - N$, we obtain $\partial \ln N!/\partial N = \ln N$. Applying this formula to $\partial \ln \omega / \partial N_{01} = 0$ for $N_{01} = N_{01}^*$, we obtain $\partial \ln \omega / \partial N_{01} = 1/2 \ln[z_0 N/2 - N_{01}^*/2] + 1/2 \ln[z_0(M-N)/2 - N_{01}^*/2] - \ln[N_{01}^*/2] = 0$ which can be recast as $[z_0 N - N_{01}^*][z_0(M-N) - N_{01}^*] = {N_{01}^*}^2$ and, hence, $N_{01}^* = z_0 N(M-N)/M$.

[2] Let us start from the expression derived in footnote 1: $\partial \ln \omega / \partial N_{01} = 1/2 \ln[z_0 N/2 - N_{01}/2] + 1/2 \ln[z_0(M-N)/2 - N_{01}/2] - \ln[N_{01}/2]$ which can be recast as $\partial \ln \omega / \partial N_{01} = 1/2 \ln[(z_0 N/2 - N_{01}/2)(z_0(M-N)/2 - N_{01}/2)/(N_{01}/2)^2]$. We then factorize the numerator and denominator by $z_0^2 M^2$ and introduce the variables θ and α.

Going back to the approximate partition function given in Eq. (III .11), it can be recast as:

$$\ln Q(N,M,T) = N\ln[qe^{-z_0 w/2k_BT}] + \ln t(N,M,N_{01}^*) \tag{III .14}$$

which leads to the following chemical potential expression:

$$-\frac{\mu}{k_BT} = \left(\frac{\partial \ln Q}{\partial N}\right)_{M,T} = \ln[qe^{-z_0 w/2k_BT}] + \left(\frac{\partial \ln t}{\partial N}\right)_{N_{01}^*,M,T} + \left(\frac{\partial \ln t}{\partial N_{01}^*}\right)_{N,M,T}\left(\frac{\partial N_{01}^*}{\partial N}\right)_{M,T}$$

$$= \ln[qe^{-z_0 w/2k_BT}] + \left(\frac{\partial \ln t}{\partial N}\right)_{N_{01}^*,M,T} \tag{III .15}$$

where the last expression is obtained by noting that $\partial \ln t/\partial N_{01}^* = 0$ since N_{01}^* is the value that maximizes t at given N,M,T conditions. Using the definition $t(N,M,N_{01}) = C(N,M) \times \omega(N,M,N_{01})e^{N_{01}w/2k_BT}$, we arrive at: $\partial \ln t/\partial N = \partial \ln C(N,M)/\partial N + \partial \ln \omega(N,M,N_{01}^*)/\partial N$ which leads to:

$$\begin{aligned}\left(\frac{\partial \ln t}{\partial N}\right)_{N_{01}^*,M,T} &= -(1-z_0)[\ln N - \ln(M-N)] \\ &\quad - \frac{z_0}{2}\left[\ln\left(\frac{z_0 N}{2} - \frac{N_{01}^*}{2}\right) - \ln\left(\frac{z_0(M-N)}{2} - \frac{N_{01}^*}{2}\right)\right]\end{aligned} \tag{III .16}$$

where the first term corresponds to the derivation of $C(N,M)$ given in Eq. (III .10) while the last two terms corresponds to the derivation of $\omega(N,M,N_{01}^*)$ given in Eq. (III .7). Using $\theta = N/M$ and $\alpha = N_{01}^*/z_0 M$, Eq. (III .16) can be recast as:

$$\left(\frac{\partial \ln t}{\partial N}\right)_{N_{01}^*,M,T} = \ln\left[\left(\frac{\theta}{1-\theta}\right)^{z_0-1}\left(\frac{1-\theta-\alpha}{\theta-\alpha}\right)^{z_0/2}\right] \tag{III .17}$$

Inserting this expression into Eq. (III .15) yields the following expression:

$$\frac{\mu}{k_BT} = -\ln[qe^{-z_0 w/2k_BT}] + \ln\left[\left(\frac{1-\theta}{\theta}\right)^{z_0-1}\left(\frac{\theta-\alpha}{1-\theta-\alpha}\right)^{z_0/2}\right] \tag{III .18}$$

Using the relation between α and γ (see above) and introducing the energy of a single adsorbed molecule ε_0 so that $q = \exp[-\varepsilon_0/k_BT]$, the latter equation can be recast as:

$$\frac{\mu}{k_BT} = \frac{(z_0 w + 2\varepsilon_0)}{2k_BT} + \ln\left[\frac{(\gamma - 1 + 2\theta)(1-\theta)}{(\gamma + 1 - 2\theta)\theta}\right]^{z_0/2} + \ln\left[\frac{\theta}{1-\theta}\right] \tag{III .19}$$

which is the formula we will use for our comparison in the next paragraph.

1.2. Comparison

Phase equilibrium between the adsorbed monomers and the free monomers in solution at a temperature T implies that the chemical potential is equal in the two phases, i.e. $\mu = \mu_b$ (the subscript b refers to the bulk solution). Using the quasi-chemical approximation, the chemical potential of the adsorbed phase from Eq. (III .19) becomes:

$$\mu = \mu_0 + k_B T \ln\left[\frac{\theta}{1-\theta}\right] + z_0 \frac{k_B T}{2} \ln\left[\frac{(\gamma - 1 + 2\theta)(1-\theta)}{\theta(\gamma + 1 - 2\theta}\right]$$

In this expression, the reference chemical potential $\mu_0 = [z_0 w/2 + \varepsilon_0]/k_B T$ corresponds to the energy of an adsorbed monomer at full saturation (which includes an energy contribution with the surface $\sim \varepsilon_0$ and an energy contribution with all neighboring adsorbed monomers $\sim z_0 w/2$), with w is the interaction with a single neighbor. we recall that $\theta \in [0,1]$ is the site average occupancy, z_0 is the number of neighboring sites ($z_0 = 4$ for a surface) and $\gamma = [1 - 4\theta(1-\theta)(1-\eta)]^{1/2}$ (with $\eta = \exp[-w/k_B T]$).

By noting that $\theta = \beta\Gamma_{m'}/(\Gamma^\infty - \Gamma_m)$ and $1 - \theta = (\Gamma^\infty - \Gamma_m - \beta\Gamma_{m'})/(\Gamma^\infty - \Gamma_m)$, the previous expression leads to the following expression for $\Delta\mu = \mu - \mu_0$:

$$\begin{aligned}\frac{\Delta\mu}{k_B T} =& \ln\left[\frac{\beta\Gamma_{m'}}{\Gamma^\infty - \Gamma_m - \beta\Gamma_{m'}}\right] + \frac{z_0}{2}\ln\left[\frac{\Gamma^\infty - \Gamma_m - \beta\Gamma_{m'}}{\beta\Gamma_{m'}}\right] \\ &+ \frac{z_0}{2}\ln\left[\frac{(\gamma-1)(\Gamma^\infty - \Gamma_m) + 2\beta\Gamma_{m'}}{(\gamma+1)(\Gamma^\infty - \Gamma_m) - 2\beta\Gamma_{m'}}\right]\end{aligned} \tag{III .20}$$

Taking the bulk concentration $c = c_0$ as the concentration at the reference point μ_0 and assuming that the concentration remains low enough, we can write $\Delta\mu$ for the bulk phase as $\Delta\mu_b = k_B T \ln c/c_0$. By inverting Eq. (III .5), we obtain $c = 1/k'(\Gamma_{m'}) \times \Gamma_{m'}/[\Gamma^\infty - \Gamma_m - \beta\Gamma_{m'}]$ which leads to the following expression upon insertion in $\Delta\mu_b$:

$$\frac{\Delta\mu_b}{k_B T} = \ln\left[\frac{\beta\Gamma_{m'}}{\Gamma^\infty - \Gamma_m - \beta\Gamma_{m'}}\right] - \ln\left[\frac{c_0 \times k'(\Gamma_{m'})}{\beta}\right] \tag{III .21}$$

To verify that our model of cooperative adsorption is consistent with a description of interacting adsorbed species using the quasi-chemical approximation, we can check whether our model verifies the chemical potential equality as defined in the quasi-chemical approximation.

To do so, by noting that the first term on the right hand side, $\mu^\star = k_B T \ln[\beta\Gamma_{m'}/(\Gamma^\infty - \Gamma_m - \beta\Gamma_{m'})]$ is identical in Eqs. (III .20) and (III .21) we can assess the model by comparing $\Delta\mu - \mu^\star$ and $\Delta\mu_b - \mu^\star$.

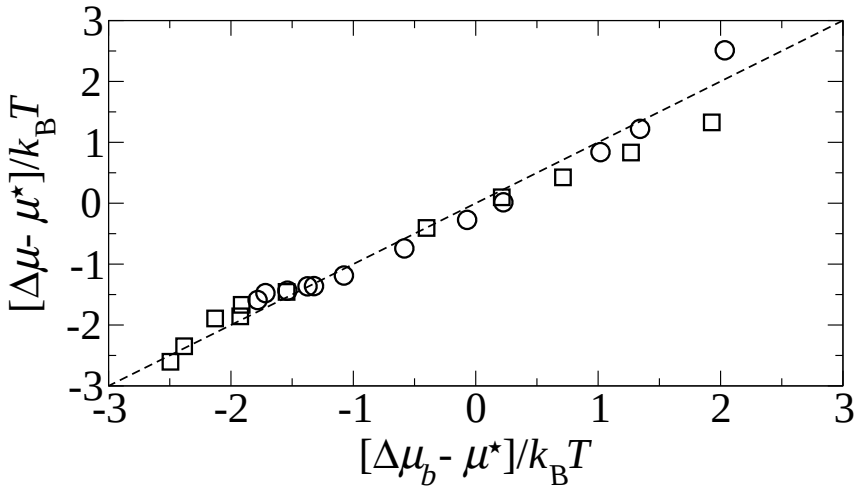

Figure 23: Comparison between the chemical potential shift for bulk and adsorbed surfactants as predicted within the quasi-chemical approximation using the data derived from our model. The circles and squares refer to the data for TX100 on quartz silica and TX165 on kaolin, respectively. The dashed line is a guide to the eye which indicates chemical potential equality between the bulk and adsorbed phases.

As shown in Fig. 23, when using the values for k' in Fig. 22, good agreement is obtained between the two chemical potentials for both TX100 on quartz silica and TX165 on kaolin. When establishing such a comparison, $\eta = \exp[-w/k_B T]$ and c_0 were used as adjustable parameters but we note that they are the only fitting variables – we found $\eta \sim 3.3$ for TX100 on silica and $\eta \sim 4.0$ for TX165 on kaolinite. More importantly, it was verified *a posteriori* that these values for η, which lead to $w \sim -1.2 k_B T$ for TX100 on silica and $w \sim -1.4 k_B T$ for TX165 on kaolinite, are physically relevant as discussed in what follows. First, as expected for cooperative effects leading to facilitated adsorption, w is negative so that it corresponds to attractive lateral interactions between neighbors. Second, w is of the order of $k_B T$ as required to observe cooperative adsorption (indeed, for lower i.e. less negative lateral interactions, thermal motion and therefore desorption would prevail). Third, the stronger attractive interaction w for TX165 is consistent with the fact that this molecule is similar to TX100 but with a longer alkyl chain – 16 versus 9-10 carbon groups. In practice, the two data sets used are for different surfaces –

which could affect the comparison made here – but we recall that η is related to the interaction between two adsorbed molecules and can, therefore, be considered mostly dependent on their molecular nature/chemistry.

2. Surfactant adsorption kinetics

As will be shown here, the present model has strong implications in terms of surfactant adsorption/desorption kinetics on surfaces. In particular, changes in the adsorption/desorption rates induce drastic variations in the characteristic time corresponding to the transient regime leading to thermodynamic equilibrium. While this feature is not specific to our model (since underlying kinetics in the Langmuir and Henry models also depend on the adsorption/desorption constant rates), the introduced concept of $\Gamma_{m'}$-dependence of k_A and k_D leads to rich and complex kinetics. In this respect, it should be emphasized that only such a level of complexity allows capturing the intriguing adsorption kinetics observed experimentally for surfactant adsorption. In particular, all typical non-Langmuirian adsorption dynamics observed in transient adsorption experiments but also in breakthrough curves, which resist available modeling frameworks, point to the existence of cooperative adsorption effects and, more generally, complex collective phenomena [3].

To illustrate the influence of cooperative effects on adsorption kinetics, the dynamical equation given in Eq. (III .3) was solved numerically for different bulk concentrations c. For TX100 adsorption on silica, this leads to the time-evolution shown in Fig. 24 and for TX165 on kaolinite, the results are shown in Fig. 25. Many choices can be made for $k'_A(\Gamma_{m'})$ and $k'_D(\Gamma_{m'})$ because static adsorption data only provide information on $k'(\Gamma_{m'}) = k'_A(\Gamma_{m'})/k'_D(\Gamma_{m'})$. Two illustrative situations were considered.

(1) $k'_A \sim \nu_0 k'(\Gamma_{m'})$ and $k'_D \sim \nu_0$

(2) $k'_A \sim \nu_0/c$ and $k'_D \sim \nu_0/k'(\Gamma_{m'})c$

where ν_0 is a characteristic constant in s^{-1} that sets the typical time scale (since it is used as a constant throughout this study, it does not affect the discussion below). We emphasize that

the two cases considered here are asymptotic limits as both k'_A and k'_D should depend on k' and hence $\Gamma_{m'}$ in general. For each situation, we also consider the effect of the aggregation parameter β which is varied between $\beta = 0.2$ and 1 ($n = 1/\beta$ is the number of aggregated monomer that can be packed into a single adsorption site). Fig. 24 and Fig. 25 also show for each situation the kinetics obtained using the Langmuir kinetic model with (1) $k_A^L \sim \nu_0 k^L$ and $k_D^L \sim \nu_0$ and (2) $k_A^L \sim \nu_0/c$ and $k_D^L \sim \nu_0/k^L c$ where k^L is the Langmuir adsorption constant that best matches the experimental adsorption isotherm in the high concentration range $c > c_s$ (see Fig. 22 and its caption).

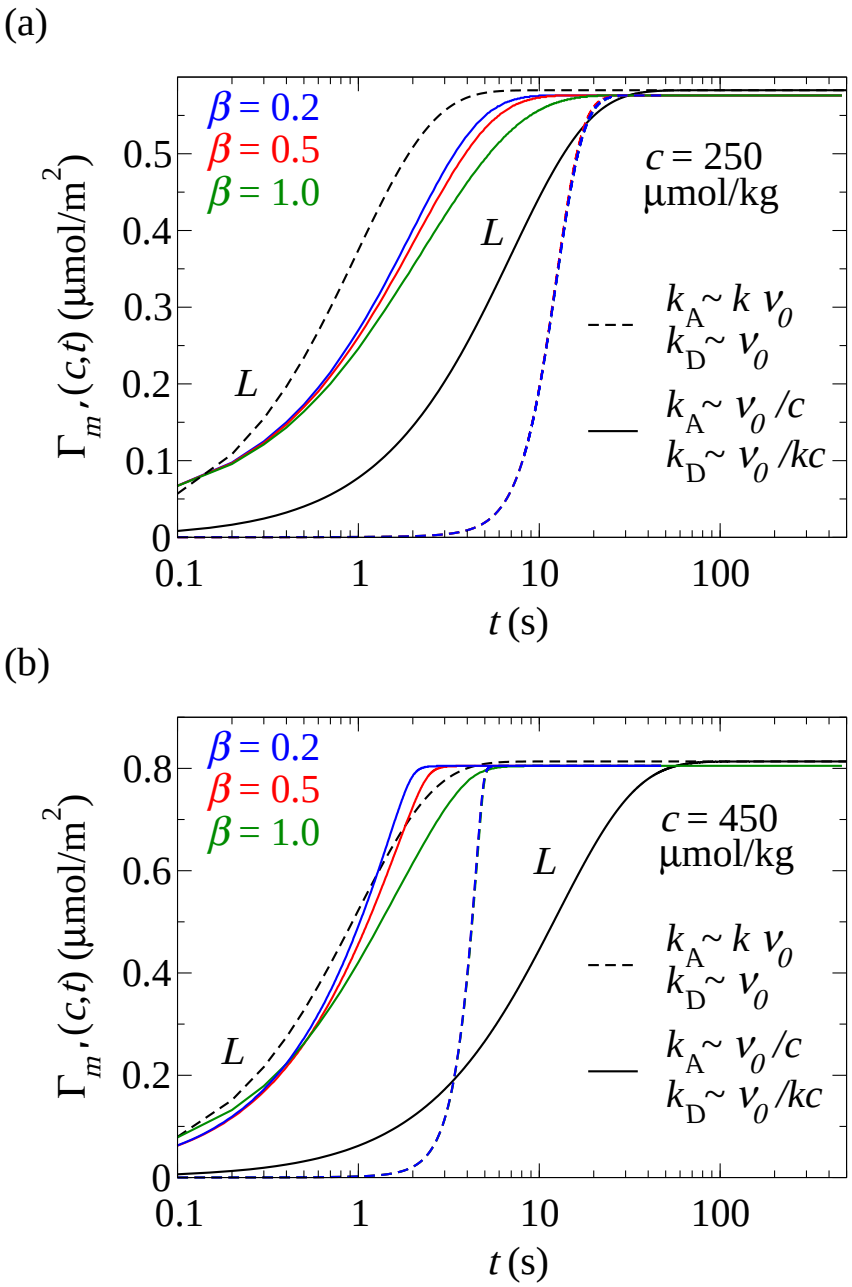

Figure 24: Adsorption kinetics as determined by solving numerically Eq. (III .3) showing $\Gamma_{m'}$ as a function of time t for TX100 on silica for two bulk concentrations: (a) $c = 250$ μmol/kg and (b) $c = 450$ μmol/kg. The color lines denote the data obtained using the cooperative model with $\beta = 0.2$ (blue), $\beta = 0.5$ (red), and $\beta = 1.0$ (green) while the black lines correspond to kinetics predicted using the Langmuir kinetic model with an adsorption/desorption constant k^L that best matches the experimental adsorption isotherm (see text). In each case, the dashed lines correspond to the case $k_A \sim \nu_0 k$ and $k_D \sim \nu_0$ while the solid lines correspond to $k_A \sim \nu_0/c$ and $k_D \sim \nu_0/kc$. Note that our model predicts that the color dashed lines (i.e. $k_A \sim k$ and k_D constant) are superimposed.

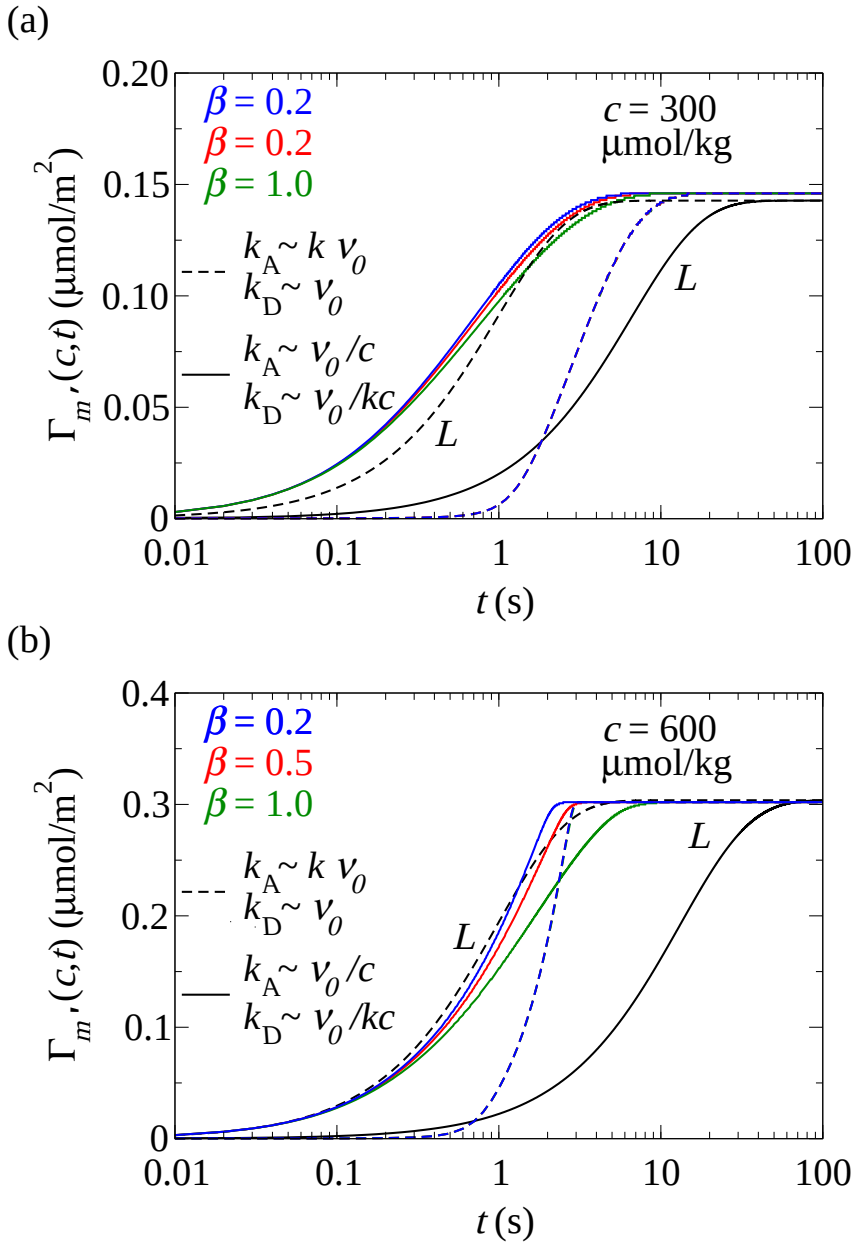

Figure 25: Adsorption kinetics showing $\Gamma_{m'}$ as a function of time t for TX165 surfactant on kaolinite clay for two bulk concentrations: (a) $c = 300$ μmol/kg and (b) $c = 600$ μmol/kg. The color lines denote the data obtained using the cooperative model with $\beta = 0.2$ (blue), $\beta = 0.5$ (red), and $\beta = 1.0$ (green) while the black lines correspond to kinetics predicted using the Langmuir kinetic model with an adsorption/desorption constant k^L that best matches the experimental adsorption isotherm (see text). In each case, the dashed lines correspond to the case $k_A \sim \nu_0 k$ and $k_D \sim \nu_0$ while the solid lines correspond to $k_A \sim \nu_0/c$ and $k_D \sim \nu_0/kc$. Note that our model predicts that the color dashed lines (i.e. $k_A \sim k$ and k_D constant) are superimposed.

Examining in details the two situations considered here allow gaining insights into the role of cooperative effects on surfactant adsorption/desorption kinetics in porous media. In particular, this illustrates how application of the present model to experimental adsorption kinetics data could be used to probe adsorption and desorption properties including the aggregation constantβ.

• Case $[k'_A \sim k'$ while $k'_D \sim$ constant$]$. With these assumptions, inserting the expression for k' given in Eq. (III .10) into the kinetics described by Eq. (III .3) shows that the adsorption rate k'_A is constant (i.e., independent of β). Therefore, in that case, both k'_A and k'_D are constant so that the adsorption kinetics is independent of the aggregation parameter β for all concentrations c (see color dashed lines in Fig. 24 and Fig. 25). Moreover, comparison with the ideal Langmuir model for this case indicates that our cooperative model predicts a much slower kinetics as $k' \lesssim k^L$ for all c (as shown in Fig. 22). Indeed, at constant desorption rate, the kinetics becomes faster with increasing the adsorption rate.

• Case $[k'_A \sim$ constant while $k'_D \sim 1/k']$. With these assumptions, β significantly affects the observed adsorption kinetics. As can be inferred from Eq. (III .10), k' increases with β so that $k'_D \sim 1/k'$ decreases. As can be directly illustrated using a simple Langmuir kinetic equation, the adsorption kinetics becomes slower with decreasing the desorption constant k_D while maintaining k_A constant. This interpretation is consistent with the data shown in Fig. 22 for $k'_D \sim 1/k'$ and k_A constant where it is observed that the adsorption kinetics becomes slower with increasing β. Finally, for a given concentration with $k_D \sim 1/k'$ and k_A constant, we observe that the simple Langmuir kinetics is significantly slower than that observed with cooperative effects. This result is consistent with our previous explanation on the role of the desorption rate at constant k_A since $k^L > k'$ for all c leads to $k^L_D < k'_D$ and therefore a slower kinetics for the Langmuir model.

Chapter Conclusion

In conclusion, we developed a simple physical model of the thermodynamics and kinetics of surfactant adsorption onto surfaces that accounts for cooperative effects inherent to such complex objects. By cooperative effects, we refer here to strong lateral interactions between adsorbed surfactants but also intramolecular and intermolecular interactions responsible for their propensity to form mesoscopic (supramolecular) structures. With this model, important collective driving forces that cannot be ignored for such self-assembling molecules are taken into account to describe the non-conventional static and dynamic adsorption behavior observed experimentally when surfactant solutions are set in contact with solid surfaces. In practice, this model involves a simple kinetic formalism involving adsorption/desorption rates that vary with the surfactant surface concentration. Such formalism can be extended to any class of objects that is expected to involve adsorption cooperative effects such as ionic liquids [153], long chain molecules (e.g. normal alkanes) [154], etc. Moreover, while all cases treated here involved a surface concentration c_s lower than the CMC, our model also deals without any further development to non-wetting situations where surface aggregation occurs beyond its bulk counterpart.

Once applied to available experimental data, this framework provides a valuable tool to infer key quantities that govern the microscopic behavior of any adsorbed surfactant onto various solid surfaces including surface self-assembly into ordered or disordered. More generally, this robust and versatile model, which is found to be consistent with rigorous microscopic treatments such as the quasi-chemical approximation in statistical physics of surface adsorption, can be extended in principle to surfactant adsorption but also transport in porous materials. Beyond immediate practical implications, the results reported here about the non-standard surfactant adsorption thermodynamics and kinetics in porous materials also raises new challenging questions. In particular, owing to cooperative effects in surfactant adsorption, strong departure from the adsorption/dynamics interplay observed for more classical fluids is to be expected in agreement with experimental observations in breakthrough or injection experiments. The present work offers a well-grounded thermodynamic basis to address such questions.

Chapter IV

Lattice Boltzmann-based method for adsorption

Contents

In this chapter, we report on a novel method based on the Lattice Boltzmann approach which extends the description of adsorption phenomena to dynamical conditions. By dynamical conditions, it is meant here that we explicitly account for both adsorption and transport kinetics. Other Lattice Boltzmann-based methods including adsorption, probe dispersion and diffusion constants under stationary conditions. Despite the effectiveness of this approach, the development of such a simple tool that includes kinetic aspects is important as it allows treating real engineering conditions such as molecule injection (e.g. surfactants) at a given time and for a given period of time in a flowing liquid in models representing mineral rocks or materials. In particular, this allows assessing the coupled dynamics of advection/diffusion/adsorption in pores not only in static conditions but also under dynamical conditions. The development of such an approach is important as it provides a simple mean to determine the impact of adsorption kinetics on molecule flow and dispersion (and vice-versa). Moreover, the use of a Lattice Boltzmann-based approach is important in this context as it allows considering porous media of any morphology and topology. Finally, owing to its versatility, the present approach provides a mean to consider different adsorption regimes (e.g. Henry, Langmuir, adsorption with cooperative effects, etc.) with more or less complex underlying kinetics that is specific to a class of adsorbate objects and/or porous solids. For these reasons, the method derived in this Chapter complements already available approaches – either based on a theoretical (i.e. statistical physics) or a numerical (i.e. Lattice Boltzmann) ground – which were reported in pioneering works (see for instance Refs. [115, 116, 65, 155, 117]).

In brief, the extended Lattice Boltzmann method reported here relies on the formal treatment of the advection/diffusion phenomenon which is augmented to include adsorption. For this reason, the approach derived in this chapter is formally equivalent to solving the diffusion/advection/adsorption equation but using a Lattice Boltzmann technique. In practice, the advection/diffusion part is solved using an already available Lattice Boltzmann technique used at IFPEN which consists of performing a collision step followed by a propagation step of the molecules within the flowing liquid (see validation in Chapter 2). Adsorption is included within this formalism by adding a third intermediate step – between the collision and propagation steps – which consists of updating the free tracer and adsorbed tracer concentrations using a given adsorption kinetics

equation. As with other Lattice Boltzmann methods, the Stokes flow is pre-calculated and assumed to remain unaffected as adsorption proceeds. As already stated, the use of this generic and versatile approach allows considering any adsorption mechanisms from well known regimes such as Henry, Langmuir or Sips adsorption isotherms to more complex behaviors such as those described in Chapter 3 of this thesis.

The remainder of this Chapter is organized as follows. In Section 1, we report the extended Lattice Boltzmann method that accounts for adsorption thermodynamics and kinetics. After providing the key ingredients and steps of this extended approach, we write formally the resulting equations to be solved numerically for different adsorption regimes: Langmuir adsorption (which includes Henry adsorption regime as it corresponds to an asymptotic limit of the Langmuir model) and the cooperative model that was derived in Chapter 3. In this first section, we also provide details about the simulation set-up and procedure as well as a flow chart to illustrate how the simulation is conducted. In section 2, we validate our approach by considering the adsorption kinetics under no flow conditions for different regimes: Henry, Langmuir, and cooperative adsorption. For different concentrations, using a simple slit pore geometry, we show that our method provides an exact description of the known solution to these problems (as theoretical treatments are available for such simple adsorption examples in ideal pore geometries). In section 3, we extend this validation part by considering more complex situations where adsorption equilibration proceeds from a starting injection configuration within the flowing liquid (a slice of adsorbate molecules is injected for a given time period). It is shown that the solution obtained using our method matches the exact solution proposed by Levesque et al. [65].

A. Extended Lattice Boltzmann method

1. Kinetics implementation

1.1. Problem statement

Let us consider a discretized porous material made up of solid sites coexisting with porous sites that are accessible to carrying fluid molecules and tracer molecules (Fig. 26). All fluid sites adjacent to a solid site adsorb tracer molecules. In what follows, two populations will be considered: free and adsorbed tracers with the corresponding concentrations – $c(\mathbf{r},t)$ and $c_a(\mathbf{r},t)$ – at a time t and position $\mathbf{r}$. The concentration of adsorbed tracer molecules in porous sites not in contact with the solid phase is assumed to be zero (physically, this approximation is justified by the fact that the mesoscopic lattice spacing used in Lattice Boltzmann extends far beyond the typical range of intermolecular forces responsible for adsorption). For the sake of simplicity, throughout this Chapter, a simple slit pore geometry is considered but the method derived here can be extended to any pore geometry (as will be done in Chapter 5 where realistic micromodels from IFPEN will be used). Moreover, as already mentioned, all Lattice Boltzmann simulations reported in this thesis are performed for 2D systems to ensure that the computational burden remains reasonable. In practice, this means that the porous system shown in Fig. 26 corresponds to a slice of a slit pore (no infinite extension in the y direction).

The porous system depicted in Fig. 26(a) is subjected to a liquid stationary, laminar flow – the so-called carrying fluid – which is assumed to be entirely described through its Stokes velocity field $U(\mathbf{r})$. The latter is pre-calculated using regular Lattice Boltzmann simulations which do not account for the presence and, *a fortiori*, for adsorption of the tracer molecules. In practice, the resulting Stokes flow is assumed to remain constant/independent upon subsequent injection, diffusion, and adsorption of the tracer molecules. As shown in Fig. 26(b), at a given time $t = 0$, the free tracer molecules are injected for a given time Δt_0 which can be varied from a single to several time steps $\Delta t_0 = n\Delta t$ (with n an integer defined strictly positive and Δt the Lattice Boltzmann integration timestep). As shown in Fig. 26(c), different spatial distributions can be injected during the injection time Δt_0: either as a homogeneous distribution $c(\mathbf{r}) = c_0$, $\forall \mathbf{r}$ or as a heterogeneous distribution such as a concentration slice $c(\mathbf{r}_0) = c_0$ with $\mathbf{r}_0 = (x_0, y)$ such that

x_0 is a given lateral position within the slit pore.

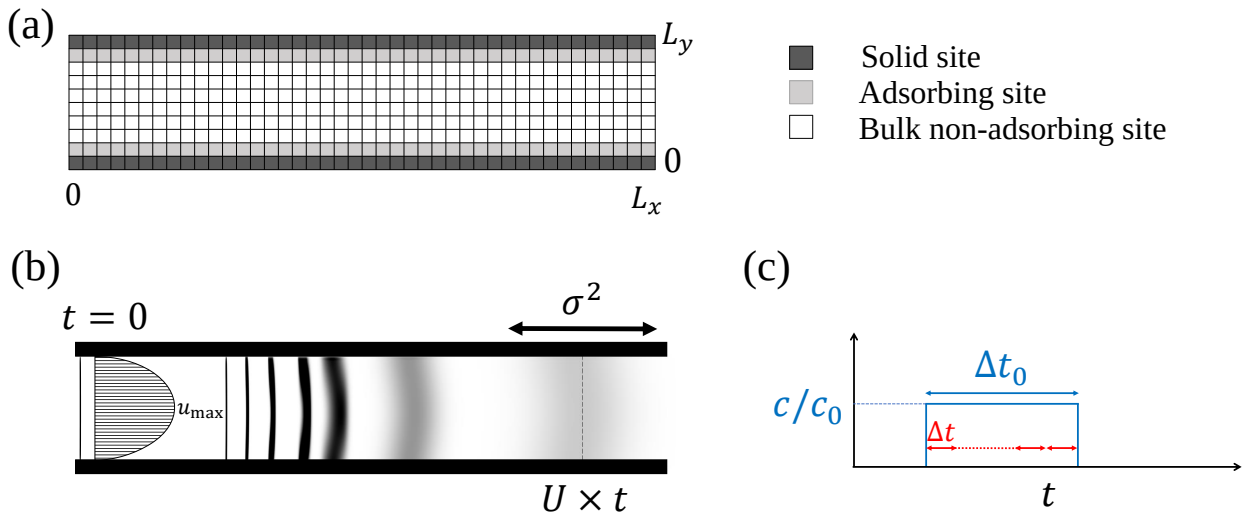

Figure 26: Schematic representation of the simulation set up used in our Lattice Boltzmann calculations. (a) A slit pore having a length L_x and a width L_y is used as a simple reference system to validate our Lattice Boltzmann method. The geometry mesh is shown where each site is either a fluid site (white) or a solid site (black). Fluid sites directly in contact with a solid site adsorb tracer molecules (grey). (b) The molecule concentration within the geometry is monitored as a function of time. Starting from a concentration peak injected at a given time $t = 0$ in a slice located in x, the density broadens as molecular diffusion disperses the tracers within the pore. Moreover, under laminar flow condition, in addition to such diffusion-induced broadening, the concentration distribution takes the shape of a Poiseuille profile in the long time limit. In this long time regime, Taylor dispersion is observed as the dispersion of the molecules leads to a molecule distribution with a Gaussian shape. (c) Different initial conditions are considered for the Lattice Boltzmann simulations. At a time t_0 (taken as the time origin $t_0 = 0$), a concentration step $c = c_0$ is injected for a time period Δt_0.

As described in more detail below, the coupled dynamics resulting from advection, diffusion, and adsorption can be determined by following the evolution in time of the free and adsorbed tracer distributions. On the one hand, the variance $\sigma_x^2(t)$ of the free tracer distribution $c(\mathbf{r},t)$ along the direction x provides a direct measurement of the dispersion coefficient $D(t) \sim d\sigma_x^2(t)/2dt$. On the other hand, the evolution in time of the adsorbed tracer distribution $c_a(\mathbf{r},t)$ allows determining the resulting adsorption kinetics $c(\mathbf{r},t) \sim f(t)$. In practice, while our Lattice Boltzmann calculations are performed using local volume concentrations $c(\mathbf{r},t)$ and $c_a(\mathbf{r},t)$, most of our results in Chapters 4 and 5 will report adsorbed quantities expressed as surface concentrations $\Gamma(\mathbf{r},t)$. Considering that $\Gamma(\mathbf{r},t) = c_a(\mathbf{r},t)\Delta x$ where Δx is the lattice spacing used in the Lattice Boltzmann calculations, the two quantities are strictly equivalent. In

particular, when expressed in Lattice Boltzmann units $\Delta x = 1$, the surface and bulk concentrations in adsorbed tracers follow the same evolution $\Gamma(\mathbf{r},t) \sim c_a(\mathbf{r},t)$ (for the sake of clarity, in what follows, the different evolution equations are reported using bulk concentrations $c(\mathbf{r},t)$ and $c_a(\mathbf{r},t)$).

1.2. Algorithm and flow chart

Fig. 27 shows a flow chart presenting the algorithm corresponding to our extended Lattice Boltzmann approach. Once the pore geometry has been defined, the Stokes flow of the carrying fluid is calculated using an independent Lattice Boltzmann calculation. The presentation of this first step will be skipped here as it corresponds to conventional Lattice Boltzmann simulations for Stokes flow that have been discussed in Chapter 2. Once the Stokes field has been determined, the tracer molecules are injected at a time $t = 0$ according to a well-defined time and space distribution as shown in Fig. 26(c). For a given Stokes flow, starting from such initial conditions, the dispersion and adsorption kinetics of the free and adsorbed tracer molecules are computed by incrementing the time t in a discretized manner $t \rightarrow t + \Delta t$. Each time increment Δt involves three intermediate steps corresponding to molecule redistribution – including free and adsorbed tracers – due to collision, adsorption, and propagation. On the one hand, the collision and propagation steps, which are identical to those used in conventional Lattice Boltzmann calculations, only apply to the free tracer distribution $c(\mathbf{r},t)$. On the other hand, the adsorption step applies to both the free and adsorbed tracer molecules as it corresponds to a kinetic equation that redistributes molecules between $c(\mathbf{r},t)$ and $c_a(\mathbf{r},t)$. In practice, as described hereafter for each step, these different intermediate steps apply to the free molecule sub-distribution $g_q(\mathbf{r},t)$ which corresponds to the density of free tracer molecules having a velocity along the direction q at a position $\mathbf{r}$ and time t ($\mathbf{v}_q$). To avoid any ambiguity, such distributions are denoted using the letter g as the letter f was already used in Chapter 2 to denote the molecule distribution of the carrying fluid.

Let us introduce the different free tracer molecule distributions $\tilde{g}_q(\mathbf{r},t)$, $\tilde{\tilde{g}}_q(\mathbf{r},t)$, and $g_q(\mathbf{r},t+1)$ obtained after the the collision, adsorption, and propagation steps, respectively. Because these

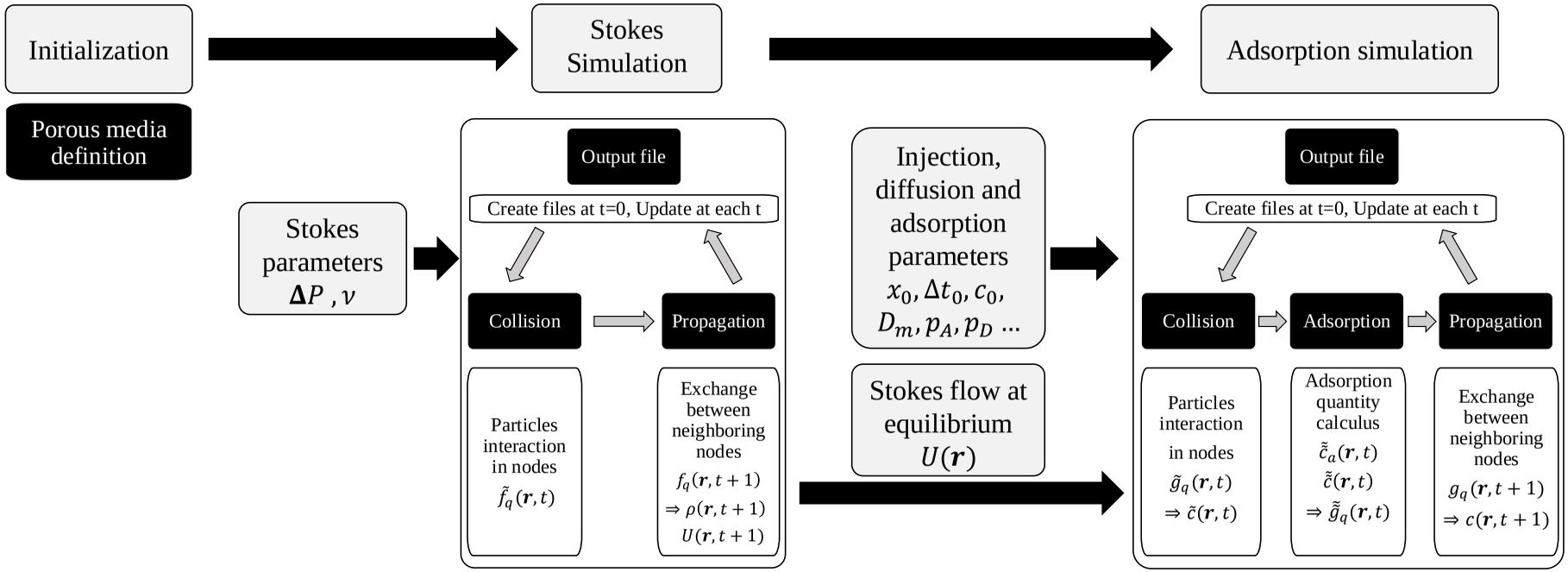

Figure 27: Description of the different algorithm steps used in the Lattice-Boltzmann simulation for adsorption. There are three main steps with different intermediate steps. The first step consists of defining the pore geometry. The second step involves the calculation of the Stokes flow using the LBM-Stokes algorithm (explained in detail in chapter 2). The third step is the Lattice Boltzmann simulation of advection/diffusion/adsorption processes. More precisely, once the geometry is defined, the Stokes simulation is performed to obtain the Stokes flow field at equilibrium. Such velocity field is then used as input for the third step. At this point, the different inputs for the adsorption simulation are defined: the molecular diffusion coefficient, the adsorption/desorption rates, and the Stokes flow. Using these data, free tracer molecules are injected into the pore geometry according to a well-defined time and space distribution as shown in Fig. 26(c) (i.e. an initial concentration c_0 is injected at a given lateral position x_0). Using these initial conditions, the dispersion and adsorption kinetics of free and adsorbed tracer molecules is monitored by incrementing the time t in a discrete fashion $t \rightarrow t + \Delta t$. The time increment Δt involves three intermediate steps which redistribute the free and adsorbed tracer molecules due to collision, adsorption and propagation.

different functions are normalized, the concentrations in free tracer molecules after the collision, adsorption, and propagation steps are readily obtained as $\tilde{c}(\mathbf{r},t) = \sum_q \tilde{g}_q(\mathbf{r},t)$, $\tilde{\tilde{c}}(\mathbf{r},t) = \sum_q \tilde{\tilde{g}}_q(\mathbf{r},t)$, and $c(\mathbf{r},t+1) = \sum_q g_q(\mathbf{r},t+1)$. For reasons that will become clearer when introducing the different intermediate steps below, we do not need to introduce the molecule distributions for the adsorbed tracer molecules (for these molecules, we only consider the total concentration c_a which is directly linked to c because of overall density conservation). Moreover, while the q-components $g_q(\mathbf{r},t)$ of the distribution $g(\mathbf{r},t)$ are redistributed during the collision/propagation steps (as physically expected), their fraction $\tilde{x}_q(\mathbf{r},t) = \tilde{g}_q(\mathbf{r},t)/\tilde{c}(\mathbf{r},t) = \tilde{g}_q(\mathbf{r},t)/\sum_q \tilde{g}_q(\mathbf{r},t)$ remain unaffected during the adsorption step ($\tilde{x}_q(\mathbf{r},t) = \tilde{\tilde{x}}_q(\mathbf{r},t)$). This approximation consists of assuming that the velocity distribution among the different velocity components q are not changed during the adsorption step despite the change in the total number of free tracers within the time step Δt, i.e. $\Delta c(\mathbf{r},t) = -\Delta c_a(\mathbf{r},t)$ (where the symbol Δ indicates that the difference is taken between the collision step $\tilde{}$ and the adsorption step $\tilde{\tilde{}}$). This approximation can be also introduced by invoking that, regardless of their velocity, all molecules get adsorbed with the same adsorption rate. Reciprocally, this also implies that all desorbing molecules are reintroduced in the free tracer population according to a velocity distribution that verifies the current q-component distribution.

• **Collision**. At a given time step t, the components $g_q(\mathbf{r},t)$ at each site $\mathbf{r}$ are redistributed among the site populations to mimic molecule collisions:

$$\tilde{g}_q(\mathbf{r},t) = \Omega[g(\mathbf{r},t)]_q \tag{IV .1}$$

where $g(\mathbf{r},t)$ denotes the set of q-components $g_q(\mathbf{r},t)$ and $\Omega[g(\mathbf{r},t)]_q$ the collision operator which transfers momentum between the different q-components. The same equation/operator is used in the Lattice Boltzmann calculations for advection/diffusion phenomena without adsorption. For the sake of brevity, further details will not be provided here as they can be found in Chapter 2 where we introduced such conventional calculations. At the end of this collision step, the local free tracer molecule concentration is readily obtained as $\tilde{c}(\mathbf{r},t) = \sum_q \tilde{g}_q(\mathbf{r},t)$.

• **Adsorption**. The treatment used for the adsorption step depends on the exact adsorption

mechanism and underlying kinetics considered. The different regimes considered in this thesis – Henry, Langmuir, and cooperative adsorption – will be described specifically in the following section. Here, for the sake of clarity, we consider the Henry adsorption isotherm as a simple yet representative example to introduce the key ingredients used in the adsorption step (the use of this simple formalism remains general enough to be extended later to other regimes). The adsorption step simply follows the first order kinetic equation which leads to the Henry adsorption isotherm. Starting from the free and adsorbed tracer molecule concentrations obtained after the collision step – $\tilde{c}(\mathbf{r},t)$ and $\tilde{c}_a(\mathbf{r},t)$ – the adsorption kinetics can be written as:

$$\tilde{\tilde{c}}_a(\mathbf{r},t) = p_A\tilde{c}(\mathbf{r},t) + [1-p_D]\tilde{c}_a(\mathbf{r},t) \tag{IV .2}$$

$$\tilde{\tilde{c}}(\mathbf{r},t) = \tilde{c}(\mathbf{r},t) - p_A\tilde{c}(\mathbf{r},t) + p_D\tilde{c}_a(\mathbf{r},t) \tag{IV .3}$$

where p_A and p_D are the adsorption and desorption rates in Lattice Boltzmann units. Physical values for p_A and p_D can be obtained from the comparison with the physical kinetic equation, i.e. $\partial\Gamma(\mathbf{r},t)/\partial t = k_A c(\mathbf{r},t) - k_D\Gamma(\mathbf{r},t)$ (with the surface concentration readily obtained from the adsorbed tracer concentration, i.e. $\Gamma(\mathbf{r},t) = c_a(\mathbf{r},t)\Delta x$). Considering that k_A is in m.s^{-1} and k_D in s^{-1}, such a comparison shows that $p_A = k_A\Delta t/\Delta x$ and $p_D = k_D\Delta t$. As mentioned earlier, the distribution ratio $\tilde{\tilde{x}}_q$ between the different q-components is assumed to be unaffected during the adsorption step. Using the concentration definition, i.e. $\tilde{\tilde{c}}(\mathbf{r},t) = \sum_q \tilde{\tilde{g}}_q(\mathbf{r},t)$, we choose to redistribute the variation ($\Delta c(\mathbf{r},t) = \tilde{\tilde{c}}(\mathbf{r},t) - \tilde{c}(\mathbf{r},t)$) between the different $\tilde{\tilde{g}}_q$ components in a homogeneous and proportional manner, which implies $\tilde{\tilde{g}}_q(\mathbf{r},t) = \tilde{g}_q(\mathbf{r},t) - \tilde{x}_q(\mathbf{r},t)(\tilde{\tilde{c}}(\mathbf{r},t) - \tilde{c}(\mathbf{r},t))$. The latter gives that the molecule distributions $\tilde{\tilde{g}}_q(\mathbf{r},t)$ after the adsorption step obey the following evolution equations:

$$\tilde{\tilde{g}}_q(\mathbf{r},t) = \tilde{g}_q(\mathbf{r},t) - \tilde{x}_q(\mathbf{r},t)\Big[p_A\tilde{c}(\mathbf{r},t) - p_D\tilde{c}_a(\mathbf{r},t)\Big] \tag{IV .4}$$

where $\tilde{x}_q(\mathbf{r},t) = \tilde{g}_q(\mathbf{r},t)/\tilde{c}(\mathbf{r},t)$ is the fraction of molecules having a velocity $\mathbf{v}_q$ at time t and position $\mathbf{r}$.

• **Propagation**. At a given time step t, after the collision/adsorption intermediate steps described above, the distribution components $g_q(\mathbf{r},t)$ at each site $\mathbf{r}$ are redistributed among the neighboring sites. The change induced by this propagation intermediate step in the free tracer

distribution between t and $t+\Delta t$ can be expressed as:

$$g_q(\mathbf{r}+\mathbf{v}_q\Delta t, t+\Delta t) = \tilde{\tilde{g}}_q(\mathbf{r},t) \tag{IV .5}$$

This simple propagation scheme consists of displacing the molecule distribution $g_q(\mathbf{r},t)$ using the velocity set $\{\mathbf{v}_q\}$. More in detail, the molecules still located at node $\mathbf{r}$ at time t after the collision and the adsorption steps are transferred to node $\mathbf{r}+\mathbf{v}_q\Delta t$ at the end of each iteration. For more details, the reader is referred to the description of the propagation intermediate step in Chapter 2.

1.3. Adsorption mechanisms and kinetics

Adsorption kinetics is known to significantly impact the transport of molecules in porous media. Here, in an attempt to shed light on the interplay of adsorption and transport of tracer molecules, we employ the Lattice Boltzmann approach introduced above to consider different adsorption models. More in detail, we consider the Henry regime, the Langmuir regime and the cooperative model which was developed in the frame of this thesis (Chapter 3). While the Henry adsorption isotherm is effective in the low concentration range, the Langmuir adsorption isotherm accounts for site saturation as the surface concentration of adsorbed tracer molecules increases. The cooperative model, introduced in Chapter 3, allows accounting for adsorbate molecule interactions as well as for possible cooperative effects on adsorption thermodynamics and kinetics. In what follows, considering that the Henry regime was addressed in the previous section, we only treat the Langmuir and cooperative models (moreover, we recall that the Henry regime is the asymptotic limit of the Langmuir model in the low concentration range).

Surface saturation. The Langmuir adsorption model is a simple non-linear equation which accounts for surface saturation upon adsorption; the adsorbed tracer molecule concentration $c_a(\mathbf{r},t)$ cannot exceed the value c_a^∞. Adsorption increases rapidly with concentration in the low concentration range and then reaches a plateau asymptotically as the surface sites become saturated with already adsorbed molecules. Implementing the Langmuir model in our Lattice Boltzmann approach simply requires to modify Eqs. (IV .2) and (IV .3) to account for surface

saturation:

$$\tilde{\tilde{c}}_a(\mathbf{r},t) = p_A \tilde{c}(\mathbf{r},t)\left[1 - \frac{\tilde{c}_a(\mathbf{r},t)}{c_a^\infty}\right] + (1-p_D)\tilde{c}_a(\mathbf{r},t) \tag{IV .6}$$

$$\tilde{\tilde{c}}(\mathbf{r},t) = \tilde{c}(\mathbf{r},t) - p_A \tilde{c}(\mathbf{r},t)\left[1 - \frac{\tilde{c}_a(\mathbf{r},t)}{c_a^\infty}\right] + p_D \tilde{c}_a(\mathbf{r},t) \tag{IV .7}$$

where $c(\mathbf{r},t)$ and $c_a(\mathbf{r},t)$ denote the free and adsorbed tracer concentrations. The symbols $\tilde{}$ and $\tilde{\tilde{}}$ indicate quantities obtained after the intermediate collision and adsorption steps, respectively. Like for the Henry regime, the adsorption parameters p_A, p_D and c_a^∞ can be derived by formally writing the analogy with the Langmuir adsorption kinetics $\partial\Gamma(\mathbf{r},t)/\partial t = [1-\Gamma(\mathbf{r},t)/\Gamma^\infty]k_A c(\mathbf{r},t) - k_D\Gamma(\mathbf{r},t)$ (where the maximum surface concentration is defined as $\Gamma^\infty = c_a^\infty \times \Delta x$). This leads to the same definition for p_A and p_D as with the Henry model: $p_A = k_A \times \Delta t/\Delta x$ and $p_D = k_D \times \Delta t$. Moreover, due to mass balance condition, the free tracer distribution q-components $\tilde{\tilde{g}}_q(\mathbf{r},t)$ after the adsorption intermediate step are defined by modifying Eq. (IV .4) as follows:

$$\tilde{\tilde{g}}_q(\mathbf{r},t) = \tilde{g}_q(\mathbf{r},t) - \tilde{x}_q(\mathbf{r},t)\left(p_A \tilde{c}(\mathbf{r},t)\left[1 - \frac{\tilde{c}_a(\mathbf{r},t)}{c_a^\infty}\right] - p_D \tilde{c}_a(\mathbf{r},t)\right) \tag{IV .8}$$

Cooperative adsorption. To implement our cooperative adsorption model into the Lattice Boltzmann approach introduced above, we distinguish two adsorbed concentrations: the concentration of adsorbed isolated monomers $c_{a,m}(\mathbf{r},t)$ and the concentration of adsorbed aggregated monomers $c_{a,m'}(\mathbf{r},t)$. As introduced in Chapter 3, only isolated monomers get adsorbed below the surface concentration c_s. On the other hand, above c_s, both isolated and aggregated monomers get adsorbed at the solid surface. The total surface concentration of adsorbed monomers is simply the sum of the two concentrations: $c_a(\mathbf{r},t) = c_{a,m}(\mathbf{r},t) + c_{a,m'}(\mathbf{r},t)$. For $c < c_s$, the situation is simple as only isolated monomers get adsorbed so that the interplay of adsorption kinetics and molecule transport can be described using the Lattice Boltzmann approach above (using either the Henry or Langmuir regime depending on the type of adsorption isotherm observed). In contrast, for $c(\mathbf{r},t) \geq c_s$, both the adsorption of individual and aggregated monomers must be considered.

As in Chapter 3, with the aim to keep things as simple as possible, we assume that the adsorption of isolated monomers is an instantaneous process: $c_{a,m}(\mathbf{r},t) = c_{a,m}(\mathbf{r},\infty)\ \forall t$. Within this approximation, we use the normalized adsorption kinetics given by (See Chapter 3, for the original expression): $\partial\Gamma_{m'}(\mathbf{r},t)/\partial t = [1-(\beta\Gamma_{m'}(\mathbf{r},t)+\Gamma_m(\mathbf{r},\infty))/\Gamma^\infty]\,k'_A c(\mathbf{r},t) - k'_D\Gamma_{m'}(\mathbf{r},t)$ where the adsorption and desorption rates k'_A and k'_D depend on the adsorbed amount $\Gamma_{m'}(\mathbf{r},t) = c_{a,m'}(\mathbf{r},t)\Delta x$. As for the parameter β, we recall that it denotes the packing fraction of the aggregated monomers within the adsorbing sites. In practice, assuming $\beta = 1$ and constant adsorption/desorption rates k'_A and k'_D allows recovering the Langmuir adsorption model. This cooperative model can be implemented in our Lattice Boltzmann approach by modifying the kinetic evolution described in Eqs. (IV .2) and (IV .3) as follows:

$$\tilde{\tilde{c}}_{a,m'}(\mathbf{r},t) = p'_A\tilde{c}(\mathbf{r},t)\left[1-\frac{\beta\tilde{c}_{a,m'}(\mathbf{r},t)+c_{a,m}(\mathbf{r},\infty)}{c_a^\infty}\right]+(1-p'_D)\tilde{c}_{a,m'}(\mathbf{r},t) \tag{IV .9}$$

$$\tilde{\tilde{c}}(\mathbf{r},t) = \tilde{c}(\mathbf{r},t) - p'_A\tilde{c}(\mathbf{r},t)\left[1-\frac{\beta\tilde{c}_{a,m'}(\mathbf{r},t)+c_{a,m}(\mathbf{r},\infty)}{c_a^\infty}\right]+p'_D\tilde{c}_{a,m'}(\mathbf{r},t) \tag{IV .10}$$

where $c_a^\infty = \Gamma^\infty\Delta x$, $p'_A = k'_A\Delta t/\Delta x$ and $p'_D = k'_D\times\Delta t$. Finally, at the end of the adsorption intermediate step, the total adsorbed amount is simply obtained as $\tilde{\tilde{c}}_a(\mathbf{r},t) = c_{a,m}(\mathbf{r},\infty)+\tilde{\tilde{c}}_{a,m'}(\mathbf{r},t)$ with the underlying tracer sub-distributions given by:

$$\tilde{\tilde{g}}_q(\mathbf{r},t) = \tilde{g}_q(\mathbf{r},t) - \tilde{x}_q(\mathbf{r},t)\left(p'_A\tilde{c}(\mathbf{r},t)\left[1-\frac{\beta\tilde{c}_{a,m'}(\mathbf{r},t)+c_{a,m}(\mathbf{r},\infty)}{c_a^\infty}\right]-p'_D\tilde{c}_{a,m'}(\mathbf{r},t)\right) \tag{IV .11}$$

B. Adsorption kinetics under no flow conditions

In this section, we present the results from our Lattice Boltzmann approach for different adsorption models (Henry, Langmuir, and cooperative model). We consider here static conditions, i.e. under no flow condition, as we first aim at validating the correct adsorption kinetics implementation for each model. More in detail, we use the Lattice Boltzmann approach as introduced above to check that it correctly generates the different adsorption isotherms $\Gamma(c,\infty)$ as well as the underlying adsorption kinetics $\Gamma(c,t)$. In practice, for such simulations performed in the absence of any liquid flow, each fluid node is filled at a time $t = 0$ with a concentration c_0 (i.e.

$c(\mathbf{r},t=0)=c_0;\ \forall\mathbf{r})$. The evolution of the surface concentration Γ as a function time t is then monitored together with the asymptotic value of $\Gamma(c,\infty)$ at infinite time as a function of the remaining free tracer concentration c. At first, the influence of the initial concentration c_0 on the adsorption behavior is considered. The numerical adsorption kinetics is then compared with the analytical solution of the kinetics equation. Adsorption is only considered at an adsorbing site located far from the pore entrance/exit to avoid numerical instabilities. Typically, for the slit pore considered here having a length $L_x = 1000\Delta x$ (site number parallel to the pore wall), the adsorbed amount in the slice located at $x = 200$ is monitored.

1. Henry adsorption

As mentioned earlier, the Henry regime accurately describes adsorption in the low concentration range. This model simply predicts a linear relationship between the adsorbed amount Γ and the concentration of free tracer c as shown in Fig. 28. In this figure, we present the numerical results obtained for an Henry adsorption isotherm with $p_A = 0.0005$ and $p_D = 0.05$ ($k_H = 0.01$). Starting from different initial concentrations c_0, our Lattice Boltzmann approach converges towards a final solution that perfectly matches the theoretical prediction corresponding to the solid black line. For each initial concentration c_0, the dashed line indicates the time evolution of the adsorbed amount which eventually reaches the equilibrium value. Such time evolution indicates that the adsorption kinetics follows nearly a vertical line (i.e. at constant bulk concentration c) even if a small inflection towards the adsorption isotherm is observed when reaching equilibrium. This result can be explained by the fact that the adsorption/desorption ratio $k_H = 0.01$ chosen here is very low; therefore, the bulk concentration in such static simulations - does not change much since the adsorbed concentration corresponds to a very small contribution of the overall bulk concentration, $c_a \sim k_H c$. Yet, close inspection of the time evolution of the bulk concentration c (i.e. open circles) reveals an interesting behavior. Starting from the initial concentration c_0 at $t = 0$, the bulk concentration c slightly decreases in the first time steps due to rapid adsorption in the adsorbing sites. However, after a number of iterations (i.e. timesteps), the bulk concentration c increases as chemical adsorption/desorption equilibrium is reached (where, as expected, the final bulk concentration is only slightly smaller than the initial value

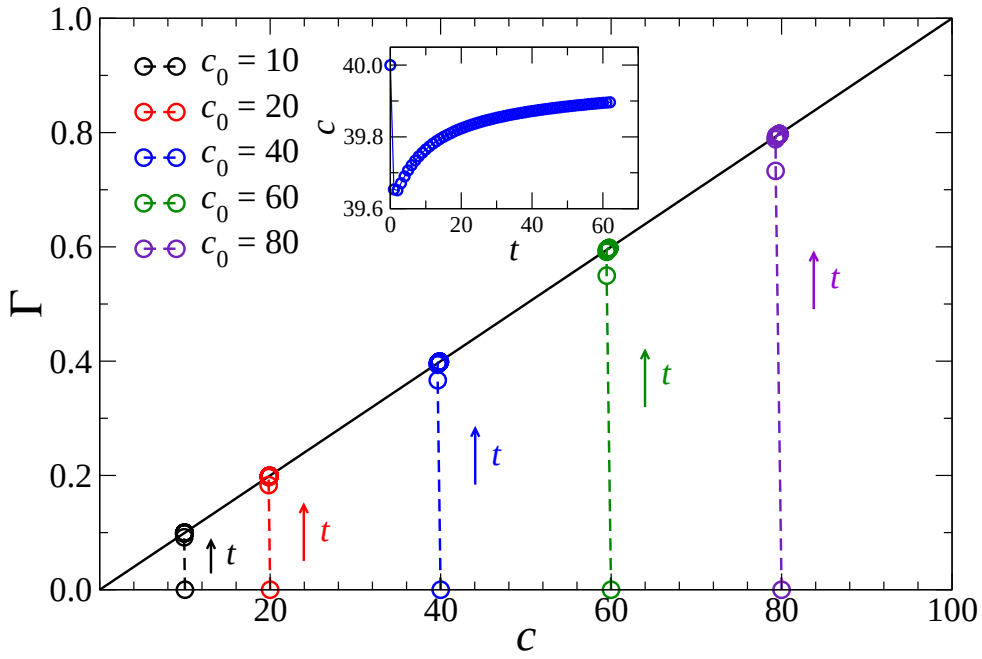

Figure 28: Henry adsorption isotherm $\Gamma(c)$ for $k_H = p_A/p_D = 0.01$ with $p_A = 0.0005$ and $p_D = 0.05$. The adsorbed amount corresponds to the surface concentration Γ given as a function of the bulk concentration c. The black solid line is the theoretical prediction $\Gamma = k_H c$ while the open circles are the results from the Lattice Boltzmann calculations. Each color corresponds to a given initial concentration c_0 as indicated in the graph. For each color, the dashed line presents the time evolution of the adsorbed amount $\Gamma(t)$.

c_0 due to the large reservoir size in the considered pore geometry). Overall, the results above indicate that the Henry adsorption isotherm as implemented in our LBM-adsorption scheme allows reproducing the thermodynamic equilibrium described using this canonical model.

Let us now consider more specifically the adsorption kinetics as predicted using the Lattice Boltzmann approach including adsorption/desorption. Again, we consider the case where adsorption corresponds to a Henry adsorption isotherm with $k_H = 0.01$ ($p_A = 0.0005$, $p_D = 0.05$). Also, as a benchmark case, we still consider the simple situation where the solvent is at rest (i.e. no flow condition). Fig. 29 compares the adsorption kinetics obtained using the Lattice Boltzmann calculations with the known analytical solution corresponding to Eq. (IV .12) (the initial concentration is $c_0 = 10$). More in detail, theoretically, the adsorption kinetics for such Henry regime – which corresponds to the dashed line in Fig. 29 – is given by:

$$\Gamma(t) = (1 - e^{-P_D t}) k_H c_0 \qquad \text{(IV .12)}$$

As shown in Fig. 29, the Lattice Boltzmann approach including adsorption describes within

numerical errors the theoretical prediction for such a simple adsorption regime. This result further validates our model by showing that it provides an accurate and reliable description of the Henry adsorption kinetics.

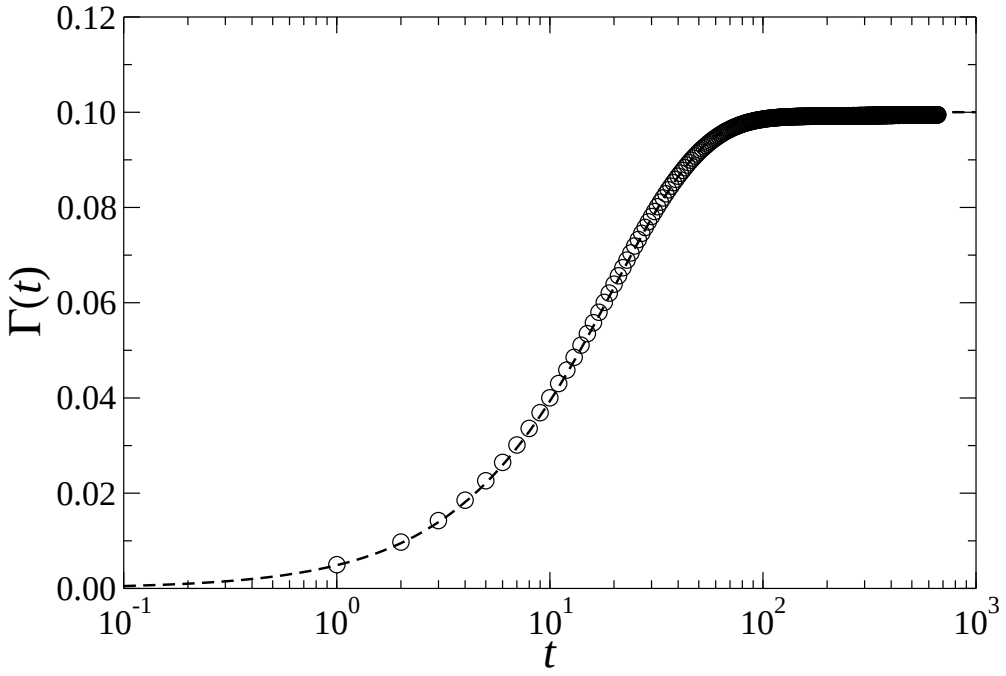

Figure 29: Comparison between the adsorption kinetics $\Gamma(t)$ predicted using Lattice Boltzmann simulations and the analytical expression for the Henry adsorption regime. These data are obtained for an adsorption isotherm corresponding to the Henry regime with $k_H = 0.01$ ($p_A = 0.0005$ and $p_D = 0.05$). The initial concentration is $c_0 = 10$. The open symbols correspond to the numerical solution using the Lattice Boltzmann model while the dashed line indicates the analytical expression for Henry kinetics as described in Eq. (IV .12).

2. Langmuir adsorption

In the previous section, we demonstrated the ability of our Lattice Boltzmann/adsorption method to accurately describe the thermodynamics and kinetics of the Henry adsorption regime. We now turn to a more complicated regime which corresponds to the Langmuir adsorption model. By accounting for surface saturation occurring upon adsorption, the Langmuir model is suitable to describe isothermal adsorption over a broader concentration range. In particular, despite its very simple underlying formalism, this model is known to capture experimental data for a very large set of adsorbate/adsorbent couples.

To validate our Lattice Boltzmann approach when combined with a Langmuir adsorption isotherm, we first check its ability to generate the associated Langmuir adsorption isotherm: $\Gamma = \Gamma^{\infty} k_L c/[1+k_L c]$. Fig.30 shows the adsorbed amount Γ as a function of the bulk concentration c as predicted using our Lattice Boltzmann calculations (such data are obtained for a maximum surface concentration $\Gamma^{\infty} = 1$ and adsorption/desorption rates $p_A = 0.005$ and $p_D = 0.05$). For different different initial concentration, the Lattice Boltzmann calculations reach an equi-

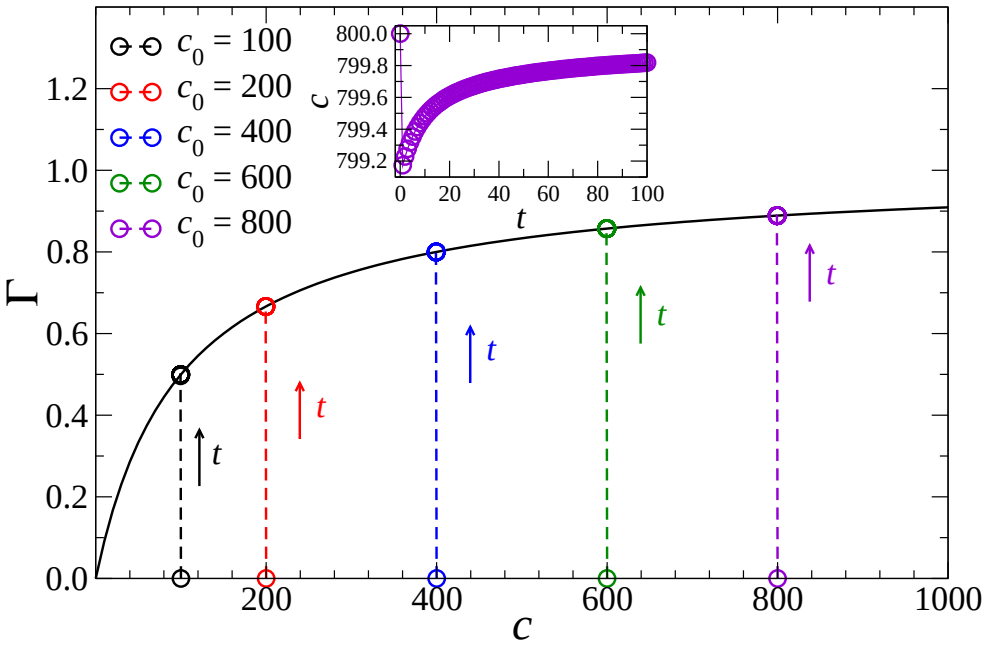

Figure 30: Langmuir adsorption isotherm $\Gamma(c)$ for $k_L = p_A/p_D = 0.01$ with $p_A = 0.0005$ and $p_D = 0.05$ (the maximum surface concentration is $\Gamma^{\infty} = 1$). The adsorbed amount is expressed as the surface concentration $\Gamma(c)$ as a function of the bulk concentration c. The black solid line denotes the theoretical Langmuir isotherm with $\Gamma = \Gamma^{\infty} k_L c/[1+k_L c]$ while the open circles are the results from the Lattice Boltzmann calculations. Each color corresponds to a given initial concentration c_0 as indicated in the graph. For each color, the dashed line presents the time evolution of the adsorbed amount $\Gamma(t)$.

librium value which corresponds exactly to the analytical solution (displayed as the black solid line in the figure). Moreover, for each initial concentration c_0, the corresponding colored dashed lines shows the time evolution. While this time evolution suggests a nearly vertical variation (i.e. at constant bulk concentration), a more careful analysis reveals that the bulk concentration does evolve as adsorption occurs. Such a small change in the bulk concentration is due to the small Langmuir adsorption rate considered here which leads to small adsorbed amounts (and hence small changes in the bulk concentration). More in detail, as with the Henry regime considered above, the bulk concentration first decreases in the very short time range due to

very rapid adsorption. Then, after a few timesteps, the overall concentration in the reservoir increases as adsorption/desorption equilibrium is attained (with a final bulk concentration slightly smaller than the initial bulk concentration c_0 due to adsorption). Overall, the data shown in Fig.30 establishes the ability of our Lattice Boltzmann model for adsorption to mimic Langmuir adsorption in porous media.

In a second step, we also investigated the Langmuir adsorption kinetics as obtained from the equations implemented in the lattice Boltzmann method. Under no flow conditions, we studied the Langmuir adsorption kinetics for the same adsorption system as in the previous paragraph – i.e. with $k_L = 0.01$ corresponding to $p_A = 0.0005$ and $p_D = 0.05$ and with $\Gamma^{\infty} = 1$. Fig. 31 compares the predictions from the Langmuir kinetic equation given in Eq. (IV .13) and the results obtained using our Lattice Boltzmann calculations (all these data were obtained for an initial concentration $c_0 = 100$). As a reminder, we recall that the Langmuir kinetic equations

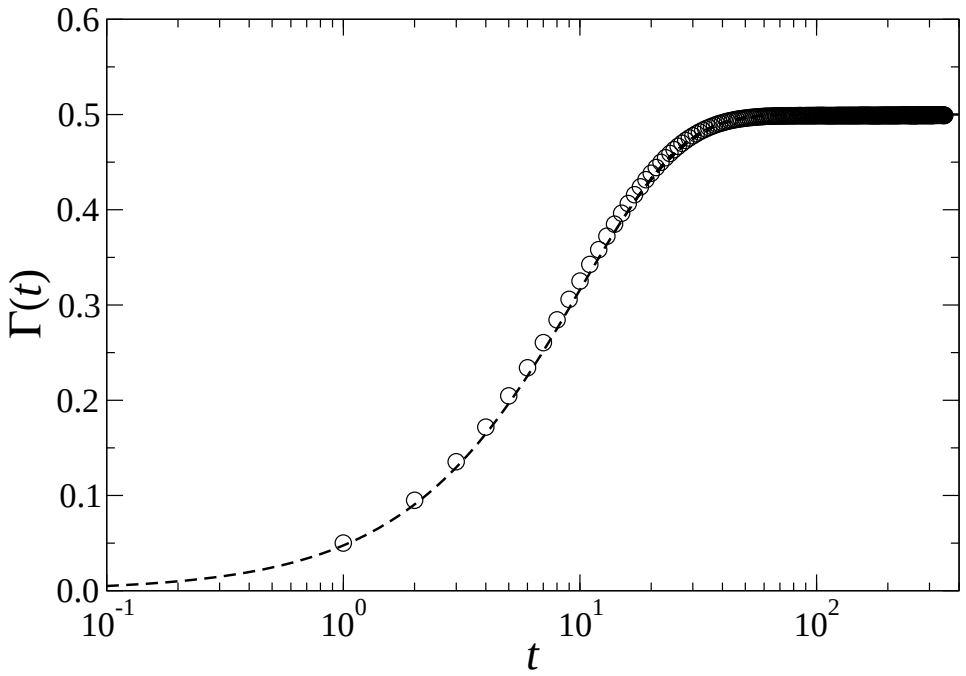

Figure 31: Comparison between the adsorption kinetics predicted using the lattice Boltzmann simulations and the analytical expression for the Langmuir adsorption isotherm. For such simulations under no flow conditions, the initial concentration is set to $c_0 = 100$ and the Langmuir adsorption isotherm is defined using the following constants: $k_L = 0.01$ with $p_A = 0.0005$, $p_D = 0.05$ (the maximum surface concentration is $\Gamma^{\infty} = 1$). The dashed line indicates the analytical solution for the Langmuir kinetics as given in Eq. (IV .13). The open symbols correspond to the numerical solution using the lattice Boltzmann model including adsorption.

writes:

$$\Gamma(t) = \left(1 - e^{-p_D t(1+k_L c_0))}\right) \frac{\Gamma^{\infty} k_L c_0}{1 + k_L c_0} \tag{IV .13}$$

As illustrated in Fig. 31, the simulation data perfectly match the theoretical prediction. This result demonstrates the ability of our Lattice Boltzmann approach to capture/describe the thermodynamics and kinetics of Langmuir adsorption in porous media.

3. Cooperative Langmuir adsorption

To validate the efficiency and robustness of the implemented lattice Boltzmann approach when combined with the cooperative model introduced in Chapter 3, we first introduce the data set against which our analysis will rely. We refer to the data reported in Chapter 3 for the adsorption of the TX100 surfactants in porous silica. To make our validation as complete as possible, the following packing fractions β will be considered: $\beta = 0.2$, 0.5, and 1.

We proceed by first testing the ability of our Lattice Boltzmann approach to generate the adsorption isotherms obtained using the cooperative adsorption model. As with the Henry and Langmuir regimes above, this test is performed for a system taken under no flow conditions. The specificity of the cooperative adsorption model lies in its ability to describe collective effects induced by lateral surface interactions and surface aggregation. As already discussed, in our model, such cooperative effects only manifest themselves for bulk concentrations above the so-called critical surface concentration c_s (below this value, our model simply assumes that isolated monomer adsorption follows a Henry or Langmuir adsorption isotherm). As a first validation test, we aim at verifying the ability of the Lattice Boltzmann approach for adsorption to accurately predict the total adsorbed amount $\Gamma(c) = \Gamma_m(c) + \Gamma'_m(c)$ in equilibrium with a bulk concentration c. Fig. 32 shows the adsorbed amount $\Gamma(c)$ as a function of the bulk concentration c. Both the results obtained using our Lattice Boltzmann approach and the predictions of our thermodynamic model are shown. In this figure, the colored dashed lines indicate the time evolution of the adsorbed amount $\Gamma(c,t)$. For different initial concentrations varying between $c_0 = 50$ to $c_0 = 700$, the results of the Lattice Boltzmann calculations are in perfect agreement with the theoretical predictions. As discussed above for the Henry and Langmuir regimes, the time evolution seems to follow a nearly vertical line – i.e. at constant bulk concentration – due

to the very large reservoir size with respect to the number of adsorbing sites. Indeed, typically, with the cooperative model, using the data shown in Fig. 22 in Chapter 3, the adsorption constant $k' < 0.02$ so that the the overall adsorbed amount represents a very small fraction of the total bulk concentration. The blue, red and green colors in Fig. 32 correspond to different aggregation numbers/packing fractions β. The influence of this important parameter was tested for the same initial concentration. More in detail, two examples were considered: $c_0 = 100$ and $c_0 = 200$ which are respectively below and above the critical surface concentration $c_s \sim 115$. The results in Fig. 32 show that, regardless of the aggregation number considered, the Lattice Boltzmann model accurately predicts the adsorbed amount derived using the cooperative adsorption model.

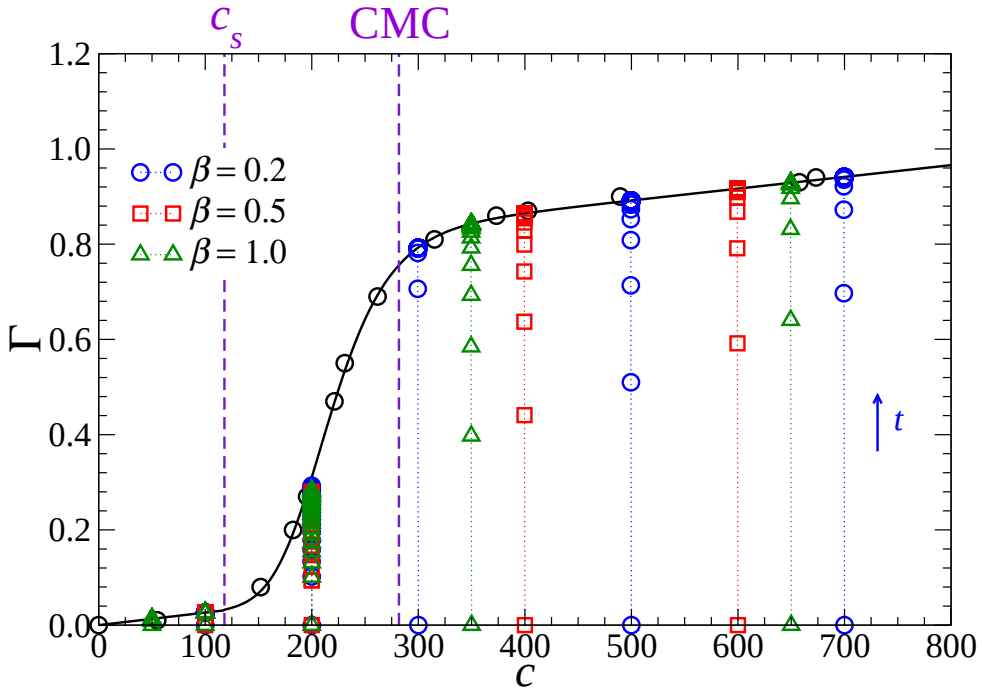

Figure 32: Cooperative adsorption model for the adsorption of TX100 onto silica (see details in Chapter3). The adsorbed amount is expressed as the surface concentration Γ as a function of the bulk concentration c. The black solid line denotes the theoretical adsorption isotherm as predicted using the cooperative model while the open circles correspond to the results obtained using the Lattice Boltzmann calculations. The colors denote the results of the cooperative model with different aggregation constant $\beta = 0.2$ (blue), $\beta = 0.5$ (red), and $\beta = 1.0$ (green). The black circles denote the experimental data. Each dotted line indicates the time evolution of the adsorbed amount $\Gamma(t)$ for a specific aggregation constant β and an initial concentration c_0. c_s is the surface aggregation concentration while CMC is the critical micelle concentration.

To study the kinetics of the cooperative model using the Lattice Boltzmann model, we follow the time evolution of the amount of adsorbed aggregated monomers $\Gamma_{m'}$ (in fact, this is the

only relevant choice that can be made since the adsorption kinetics for individual adsorbed monomers is assumed to be instantaneous in the cooperative adsorption model). Using the same data set discussed in the previous paragraph, an initial concentration c_0 larger than the critical surface concentration c_s is considered (typically, $c_0 = 250$). As discussed in Chapter 3, the cooperative adsorption model is a simple – versatile and adjustable – model since various adsorption kinetics can be described depending on the value used for p'_A and p'_D (and hence k'). In the frame of this cooperative adsorption model, we validate in what follows the kinetics described by the Lattice Boltzmann approach by selecting the two following situations – as in Chapter 3: (1) a constant adsorption rate $p'_A \sim \nu_1$ [Fig. 33(a)] and a constant desorption rate $p'_D \sim \nu_0$ [Fig. 33(b)]. The dashed lines in Fig. 33 present the analytical kinetics as predicted using the cooperative adsorption model while the solid lines correspond to the data obtained using the Lattice Boltzmann calculations. Such a comparison indicates that the results from the analytical kinetic equation are correctly reproduced by the Lattice Boltzmann model.

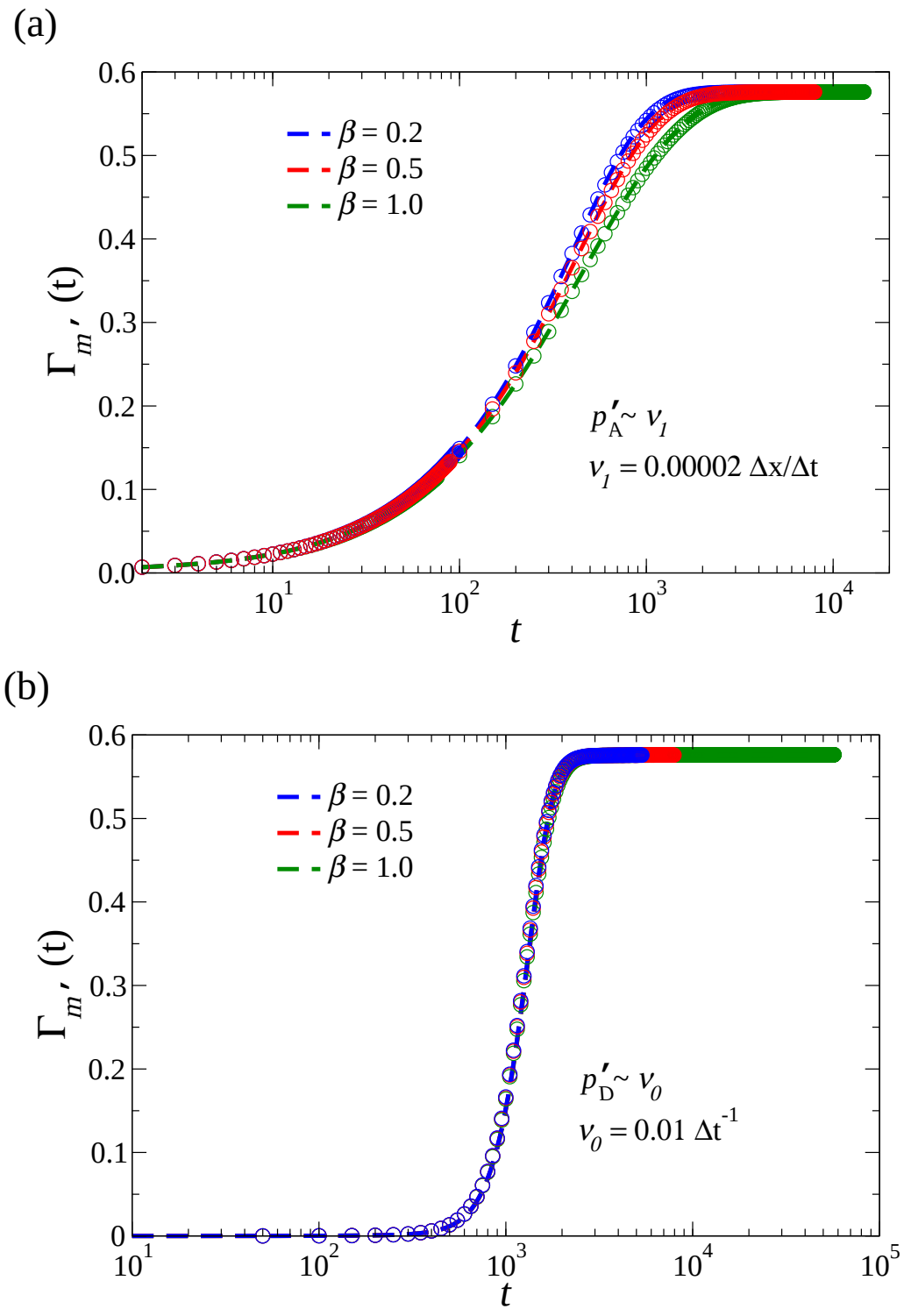

Figure 33: Comparison between the adsorption kinetics predicted using the lattice Boltzmann simulations and the analytical expression of the cooperative adsorption model for TX100 on silica for an initial concentration $c_0 = 250$. The dashed lines denote the adsorption kinetics as determined by solving numerically Eq. (III .3). More in detail, these data show $\Gamma_{m'}$ as a function of time t. The open symbols correspond to the numerical results obtained using the lattice Boltzmann model. For each dataset, the colors denote the results from the cooperative model with different aggregation constants: $\beta = 0.2$ (blue), $\beta = 0.5$ (red), and $\beta = 1.0$ (green). Panel (a) corresponds to data with $p'_A \sim \nu_1$ and $p'_D \sim \nu_1/k'$ while panel (b) corresponds to data with $p'_A \sim \nu_0 k'$ and $p'_D \sim \nu_0$.

C. Adsorption kinetics under flow conditions

As introduced in the first section of this Chapter, our Lattice Boltzmann approach enables us to study the transport of adsorbing molecules under dynamical conditions. More in detail, in the presence of a flowing liquid characterized by a given Stokes flow, the LBM-TRT simulations using the adsorption scheme above allows investigating the adsorption kinetics under flow conditions. The interplay between molecule adsorption and their advective/diffusive transport can be described analytically using the classical advection-diffusion-adsorption equation which we copy here again for the sake of clarity (see Chapter 1 for details):

$$\frac{\partial c(\mathbf{r},t)}{\partial t} + \boldsymbol{U} \cdot \nabla c(\mathbf{r},t) - \nabla \cdot [D_m \nabla c(\mathbf{r},t)] + \frac{\partial c_a(\mathbf{r},t)}{\partial t} = 0 \qquad \text{(IV .14)}$$

where $c(\mathbf{r},t)$ and $c_a(\mathbf{r},t)$ are the free and adsorbed tracer concentrations, respectively. $\boldsymbol{U}$ is the Stokes flow velocity while D_m is the molecular self-diffusion coefficient of the free tracers.

In what follows, the latter equation will be used under simple, specific adsorption conditions – namely, Henry regime – to validate the ability of our Lattice Boltzmann approach for adsorption to describe adsorption under flow conditions. As in the rest of this Chapter, a simple slit pore geometry is used with a length $L_x = 10000\Delta x$ and a width $L_y = 41\Delta x$. Moreover, the Lattice Boltzmann simulations are also performed by monitoring the evolution of the free and adsorbed tracer concentrations after injecting a pulse. More in detail, within the flowing fluid, we inject for a given time $\Delta t_0 = \Delta t$ an initial concentration c_0 in all sites located at an arbitrary lateral position x_0 (i.e. $c(\mathbf{r}_0,t) = c_0; \forall \mathbf{r}_0 = (x_0, y)$). After such injection, we monitor the dispersion of this concentration pulse in the pore geometry while imposing adsorbing conditions corresponding to the Henry regime. Such a simple adsorption model was chosen as it will provide reference data when studying more complex adsorption kinetics.

1. Dispersion coefficient of adsorbing molecules

Adding adsorbing surface conditions to the problem of tracer dispersion in a flowing fluid drastically affects the Taylor dispersion regime. In particular, the resulting – effective – dispersion coefficient is influenced by the adsorption kinetics. Several studies have reported observations

on the dispersive regime in the transport of adsorbing tracer molecules [110, 113, 115, 117]. Some of these works provide details on the impact of adsorption in a slit pore geometry on the Taylor regime [117]. However, these studies did not consider the transient phase where adsorption kinetics is coupled with (advective) transport effects before reaching the dispersive limit.

In a first step, the validity of our Lattice Boltzmann approach for adsorption will be verified for an analytically known situation. More precisely, in what follows, we consider the dispersion of tracer molecules in a slit pore geometry where adsorption proceeds through a simple Henry model. Formally, this problem was addressed in detail using a statistical physics approach by Levesque et al. [65]. Using a stochastic treatment, these authors were able to derive an analytical expression for the effective dispersion coefficient for such an ideal yet complex problem. More in detail, in the long time limit, for a Henry adsorption isotherm with adsorption/desorption constants p_A, p_D (corresponding to a Henry constant $k_H = p_A/p_D$), the effective dispersion coefficient is given by:

$$\frac{D_{eff}^{ads}}{D_m} = 1 + \frac{1}{D_m}\left(\frac{1}{210}\frac{L_y^2 U^2}{D_m}\frac{102 L_y {k_H}^2 + 18 L_y^2 k_H + L_y^3}{(L_y + \frac{2p_A}{p_D})^3} + \frac{U^2}{p_D}\frac{2L_y^2 k_H}{(L_y + 2k_H)^3}\right) \qquad \text{(IV .15)}$$

where D_m is the molecular diffusion coefficient, L_y the characteristic channel, and U the flow velocity. We recall that this equation was outlined in Chapter 1 with all details given in Appendix A.

Fig. 34 compares the results from our Lattice Boltzmann approach with the theoretical predictions obtained using Eq.(IV .15). The data are compared for different Peclet numbers $\mathrm{Pe} = UL_y/D_m$ but also for various Henry constants k_H. While the solid lines correspond to the predictions using the analytical expression by Levesque et al., the symbols denote our simulation results. As can be seen in Fig. 34, the Lattice Boltzmann simulations yield numerical predictions that are in very good agreement with the analytical solution for the effective dispersion coefficient D_{eff}^{ads}/D_m. More in detail, while the agreement is excellent for all Pe numbers when k_H is small, we notice a small departure between the two data sets at high Pe numbers when k_H is large (with the Lattice Boltzmann calculations slightly underestimating the effective dispersion coefficient). This difference can be assigned to different effects. First, Levesque et

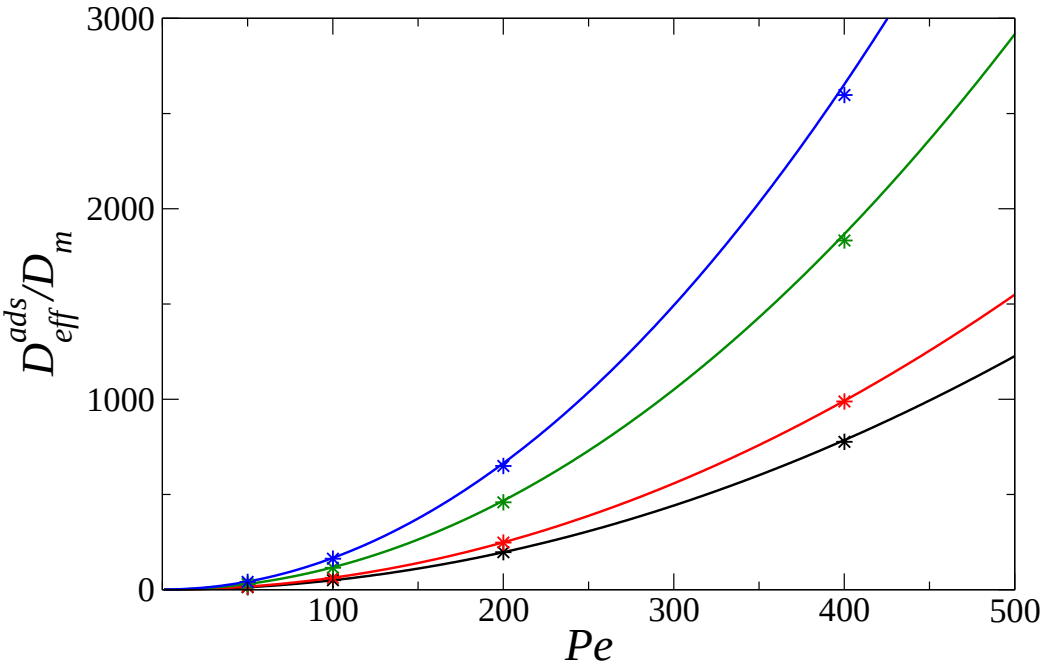

Figure 34: Normalized dispersion coefficient for adsorbing molecules carried in a slit pore geometry by a liquid flow (obeying a simple Poiseuille flow). The data are presented as a function of the Peclet number which characterizes the diffusion/advection rate. Adsorption is described using a simple Henry law with different Henry constants k_H. The symbols correspond to the results from the Lattice Boltzmann calculations using the adsorption scheme proposed in this thesis. The data show $D_{eff}^{ads}/D_m = D(t \to \infty)/D_m$ with $D(t)$ corresponds to the derivative of the displacement variance with respect to time. The lines correspond to the analytical expression for D_{eff}^{ads}/D_m as derived by Levesque et al. (see Eq (IV .15) in the text). Different k_H are considered but, in all cases, a fixed desorption rate $p_D = 0.01$ is used. The red, black, green and blue symbols denote data obtained for $k_H = 0.1$, 1, 5 and 10, respectively.

al. considered a different situation as these authors account only for a system in the asymptotic dispersive regime (i.e. no transient regime is given as only the stationary regime is taken into account). Second, we note that the Lattice Boltzmann approach used here is also prone to numerical errors. To investigate such possible numerical errors, the influence of the mesh resolution used in the Lattice Boltzmann calculations on the accuracy of the predictions was checked. In particular, the same simulation was conducted with different node numbers to describe the slit pore width L_y – typically, different node numbers from 9 to 151 was considered. Fig. 35 shows the difference obtained between the dispersion coefficient obtained by means of Lattice Boltzmann calculations and the analytical expression given in Eq. (IV .15) (Pe $= 100$ and $k_H = 1$ were used). This comparison shows that the difference decreases with increasing the node number. In all cases, such differences remain within a few % at most. Typically, the difference is less that 1% provided the node number > 20.

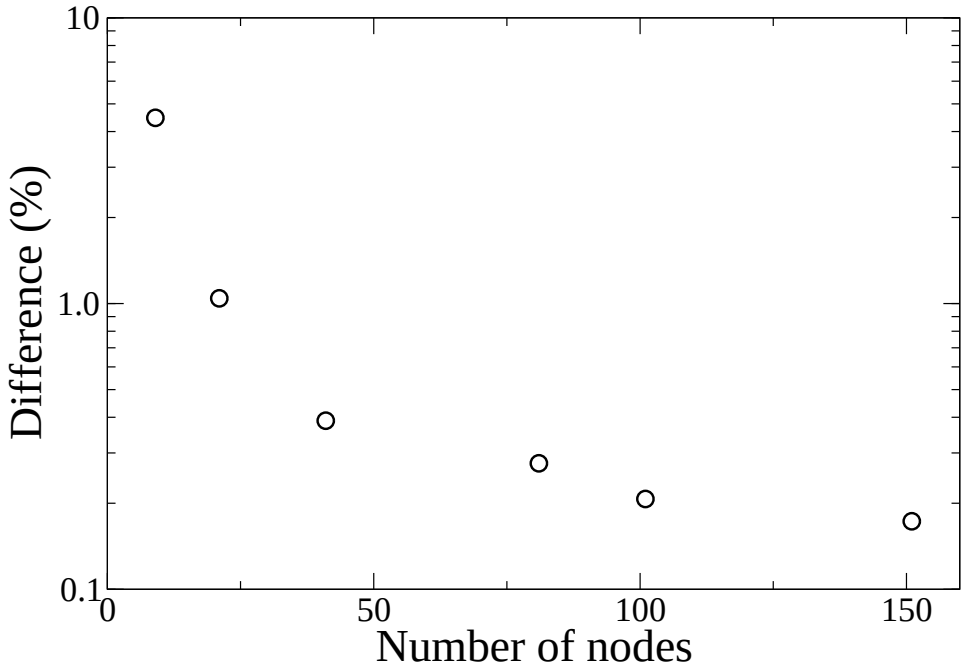

Figure 35: Difference in % between the analytical expression and the simulation results for the dispersion coefficient as a function of the node number. These results are for tracer molecules that adsorb according to a simple Henry model while being dispersed in a flowing liquid. The flow and adsorption characteristics are such that Pe $= 100$ and $k_H = 1$ ($p_A = p_D = 0.05$).

2. Transport in adsorption/desorption conditions

As mentioned in the previous section, available studies accounting for surface adsorption in the presence of a flowing fluid considered the dispersive limit – especially the influence of such adsorption conditions on the resulting Taylor dispersion coefficient. Here, we intend to use the Lattice Boltzmann scheme proposed in this thesis to investigate the interplay between the adsorption kinetics and the advective/dispersive transport. While such a study will be presented in depth in Chapter 5, we wish to conclude this section by illustrating how the interplay between adsorption and transport can be investigated using our approach. As shown in Fig. 36, the transient regime where adsorption kinetics and advective/diffusive transport are coupled can be investigated by probing the variance of the tracer molecules displacement as a function of time after injection at a given time $t = 0$ and location $x = x_0$. While the adsorption kinetics is found to drastically affect the dispersion coefficients at every timestep, the typical evolution shown in Fig. 36 remains identical to the non-adsorbing situation. The different transition regimes between molecular diffusion, advection dominated flow, and dispersion are still

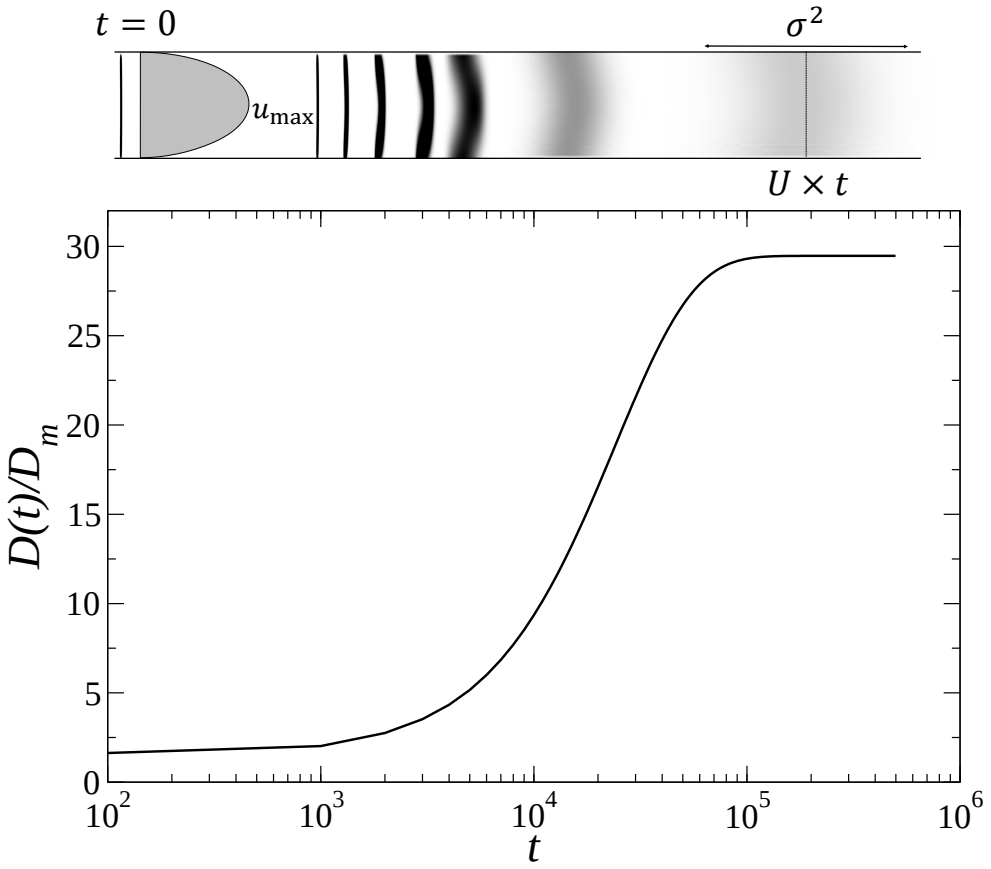

Figure 36: Temporal evolution of the time derivative of the displacement variance $D(t)$ for adsorbing molecules in a slit pore geometry. $D(t)$ is normalized to the molecular diffusion coefficient D_m of the free tracer molecules. The molecules adsorb according to a simple Henry adsorption isotherm with $k_H = 5$ ($p_A = 0.05$ and $p_D = 0.01$) while being carried by a flowing liquid described through its Stokes flow. The system is characterized by its Peclet number Pe = 100 and an initial concentration $c_0 = 20$. The different transport regimes – molecular diffusion, advection-dominated transport and dispersion – are observed in the short, intermediate, and long time ranges, respectively.

observed. In the short time range, a first plateau is observed as the molecules get dispersed through molecular diffusion. In the intermediate time range, a transitory regime is observed as the dispersion coefficient rapidly increases with time. This transient regime corresponds to the so-called advection-dominated flow where the flowing liquid involves a heterogeneous – i.e. position dependent – velocity distribution which increases the dispersion of the tracer molecules. Finally, in the long time range, a second plateau is observed as the system reaches the Taylor dispersive regime for the adsorbing tracer molecules. The asymptotic value obtained at infinite time provides the effective dispersion coefficient D_{eff}^{ads}/D_m. In the next chapter, we will study in detail typical data like those shown in Fig. 36 to gain insights into the role played by adsorption. More in detail, results for non-adsorbing and adsorbing tracers will be compared

while considering different adsorption regimes as well as adsorption/desorption rates.

Chapter Conclusion

In this chapter, we introduced our approach to extend the LBM-TRT to consider the adsorption kinetics. We added an intermediate adsorption step between the collision and propagation step of the LBM-TRT algorithm. The adsorption occurs at each fluid site adjacent to a solid surface where two populations are considered: the free tracer and the adsorbed tracer. At each iteration, the adsorption kinetics is applied to both the concentration of the free tracer $c(\mathbf{r},t)$ and the concentration of the adsorbed tracer $c_a(\mathbf{r},t)$. This approach has the advantage that it allows the use of different adsorption kinetics: the Henry as the linear adsorption kinetics, the Langmuir kinetics to consider the surface saturation and the cooperative model introduced in Chapter 3 to account for the cooperative effects due to the lateral interactions and surface aggregation. At a second step, we validated this algorithm in the slit pore geometry at static and dynamic conditions. At static condition, we obtained a good accordance with theoretical representation of the different adsorption models where we were able to present the adsorption isotherms $\Gamma(c)$ as well as the adsorption kinetics $\Gamma(t)$. Under dynamic conditions, in the presence of flowing liquid, the accuracy of this method was demonstrated as we obtained dispersion coefficients in accordance with the analytical definition proposed in the literature; we also measured the influence of the resolution on the accuracy of this result. This approach allows us to study the effects of adsorption on the transient phase. Therefore, we have carried out simulations of Dirac injection to follow the dispersion of molecules where we have illustrated the different transport regimes involved: diffusion, advection and dispersion.

Chapter V

Adsorption and pore morphology effects on the transport of adsorbing molecules

Contents

In this chapter, using the Lattice Boltzmann approach for adsorption/transport introduced in the previous chapter, we study the influence of adsorption kinetics on the transport of surfactants at the presence flowing liquid. We recall that the ability of this novel Lattice Boltzmann scheme to reproduce the thermodynamics and kinetics of adsorption under no flow conditions was verified in the previous chapter. This important validation step showed that this numerical strategy is efficient as it provides dispersion coefficients in very good agreement with theoretical treatments (only available in a few well-defined situations). To gain insights into the interplay of adsorption kinetics and transport, we consider in this chapter the influence of different parameters such as adsorption/desorption constants, adsorption regimes, flow rate, Peclet number, etc. In addition to different adsorption regimes, we also investigate the effect of the pore morphology by considering both simple and complex porous geometries.

The remainder of this chapter is organized as follows. In the first section, we study the transport of adsorbing molecules confined between two parallel plates. As already mentioned at the end of the previous chapter, adsorption and transport can be studied by monitoring the time evolution of the free tracer concentration distribution through its displacement variance $\sigma_x^2(t)$ along the flow direction x. Such a statistical quantity provides a direct measurement of $D(t) = d\sigma_x^2(t)/2dt$. We first focus on the difference between the transport of passive tracer (non-adsorbing molecules) and adsorbing molecules where adsorption obeys a simple Henry regime. In particular, we investigate the effect of adsorption on the molecule displacement but also the influence of the adsorption/desorption ratio k_H. We also study the contribution of the adsorbed tracer distribution $c_a(\mathbf{r},t)$ and its influence on $D(t)$ as well as on the normalized propagators. In a second step, we study the influence of site saturation by considering the Langmuir adsorption isotherm as a more refined model to describe adsorption in a broader condition set. The results obtained for this model are compared with those obtained for the Henry regime. Finally, we also perform a similar study using the cooperative model which was derived in Chapter 3 to capture complex collective adsorption effects and surface aggregation observed in surfactant adsorption. In the second section of this chapter, we study the transport in a realistic porous medium by considering a micromodel used at IFPEN. This model provides a simple yet representative microstructure of a complex, real medium with disordered

pore morphology/topology. Comparing data for such a material with those obtained for the parallel plates geometry allows considering the impact of confinement/pore disorder on surfactant adsorption/transport. More in detail, in this second section, we first present the main characteristics of this micromodel and the Stokes flow obtained for the flowing liquid using conventional Lattice Boltzmann calculations. We then compare the transport of the non-adsorbing molecules (reference) and adsorbing molecules using different adsorption and transport conditions.

A. Adsorption thermodynamics and kinetics

1. Henry adsorption

As shown at the end of Chapter 4, when adding adsorbing conditions at the solid/fluid interface, the same three transport regimes are observed in the dispersion of molecules in a flowing liquid: molecular diffusion, advection-dominated flow, and Taylor-like dispersion. This result was established by considering a simple adsorption mechanism where the molecules adsorb according to a Henry law. Yet, as will be shown below, even with such simple adsorbing conditions, marked quantitative differences are observed between adsorbing and non-adsorbing molecules. In what follows, the different input parameters will be varied to study in detail the impact of adsorbing surfaces and adsorption kinetics on the transport and the distribution of free and adsorbed tracer molecules.

1.1. Influence of adsorption on transport

In this section, we first compare the dispersion of non-adsorbing molecules with the dispersion of adsorbing molecules in a carrying fluid flowing through the porosity formed by two parallel plates. Fig. 37 compares the results obtained for these two systems characterized by Peclet number Pe $= 100$. The adsorbing conditions are imposed using a Henry model with $k_H = 1$ where $p_A = p_D = 0.001$ and an initial concentration $c_0 = 10$. In agreement with our previous conclusion (see Chapter 4), the results for adsorbing/non-adsorbing molecules display different transport regimes corresponding to the short, intermediate, and long time regions: diffusion, advection, and dispersion. Quantitatively, from this comparison, we conclude that the adsorp-

tion of molecules increases the effective dispersion coefficient measured in the long time limit. This result can be explained by the increase in the spreading of the free molecules as some of them get adsorbed and then desorbed due to adsorption. More precisely, upon adsorption at the liquid/solid interface, a significant number of molecules are held back for a short yet non-negligible time – the characteristic adsorption residence time – while other molecules are carried away through the flowing liquid. As a result, on average, the variance of displacement of the entire set of tracer molecules increases upon adsorption conditions.

To shed more light into the effect of adsorption on the dispersion of adsorbing molecules, Fig. 38 shows the time evolution of two important transport quantities: the normalized propagator and the concentration distribution of the free tracer molecules. More in detail, Fig. 38(a) shows the time evolution of the free tracer concentration distribution in the slit pore geometry. These results are presented using a normalized x-axis $(x-x_0)/Ut$ where x_0 is the lateral position for the initial concentration injection at $t=0$ and U is the mean velocity of the flowing fluid. Both the data for non-adsorbing molecules (top figure) and adsorbing molecules (bottom figure) are shown. In the latter case, adsorption corresponds to a Henry regime with an adsorption/desorption ratio $k_H = 1$ ($p_A = p_D = 0.001$) and an initial concentration $c_0 = 10$ injected at the lateral position $x_0 = 200$. The comparison between the time evolution for these two systems reveals that the main difference occurs in the advective regime – i.e. in the intermediate time range. For the adsorbing molecules, at $t_3 = 3\times 10^4$, the concentration in free molecules is smaller than its counterpart observed for the non-adsorbing molecules (in the latter case, the concentration is both larger and more homogeneous). This result is due to adsorption as part of the free molecules are adsorbed so that they do not contribute to the free tracer concentration profile (the Lattice Boltzmann approach obeys mass conservation). In the long time limit – t_4 and t_7 – the adsorbing and non-adsorbing systems reach the dispersive regime where the concentration distribution is homogeneous. Close inspection of the data reveals that the dispersion of the molecules is more important for the system subjected to adsorption. As a result, in agreement with the data shown in Fig. 37, the dispersion coefficient $D(t\to\infty)$ is larger for the adsorbing system than for the non-adsorbing.

Fig. 38(b) compares the normalized propagators $P[(x-x_0)/Ut,t]$ for the adsorbing and non-

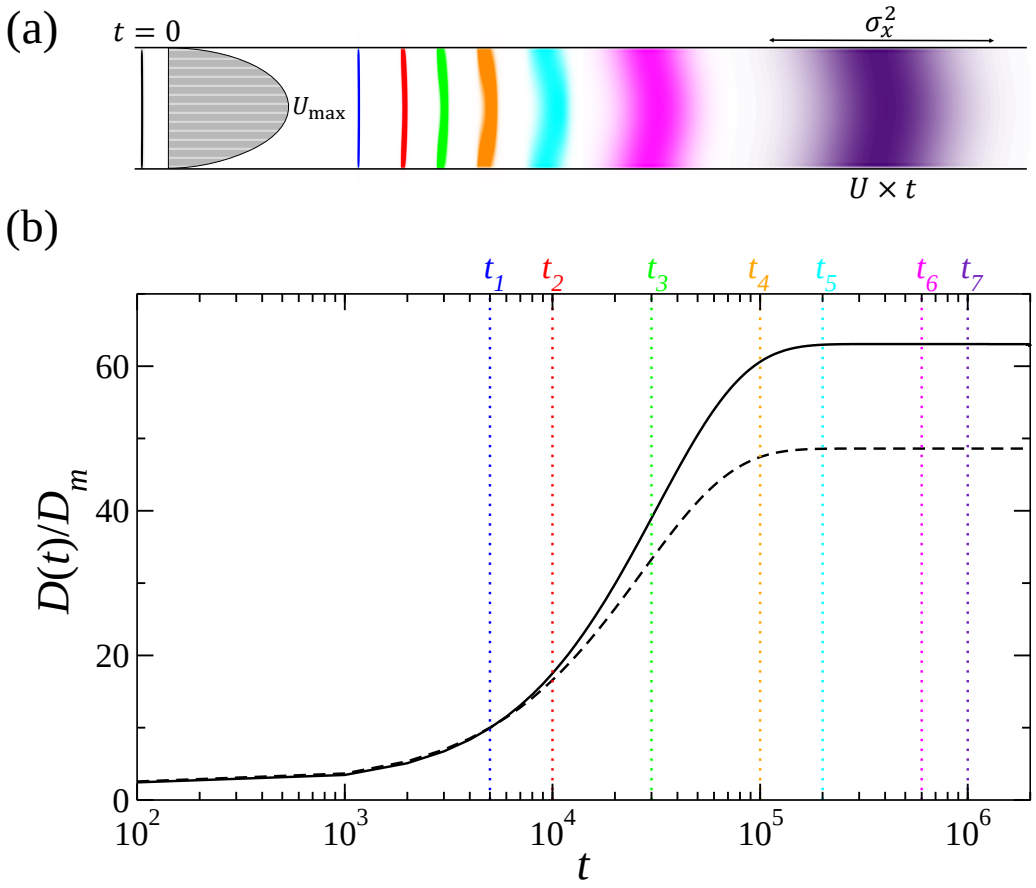

Figure 37: (a) Using a slit pore geometry, the displacement of adsorbing molecules within a carrying fluid is assessed by monitoring the concentration profile at different times. In this figure, the adsorbing conditions correspond to a Henry regime with the parameters described in the main text. These molecules are carried along the pore direction by a flowing liquid described through its Stokes flow (corresponding for this simple pore geometry to a Poiseuille velocity profile with a maximum velocity U_{max}). The different colors denote different times t_n which increase from left to right as the carrying fluid is transported along this direction). (b) Temporal evolution of the time derivative of the displacement variance $D(t)$. $D(t)$ is normalized to the molecular diffusion coefficient D_m of the free tracer molecules. The dashed line denotes the non-adsorbing molecules while the solid black line corresponds to the data for molecules that adsorb according to the Henry adsorption isotherm with $k_H = 1$ ($p_A = p_D = 0.001$). The system is characterized by a Peclet number $\mathrm{Pe} = 100$ and an initial concentration $c_0 = 10$. The vertical dotted lines denote the different times t_n for which the corresponding concentration profile is shown in the top figure.

adsorbing systems. For t_1, the most significant difference between the two data sets is observed for $(x - x_0)/Ut = 0$. This result is dues to the fact that most molecules are still near the injection slice x_0, and this is where adsorption is the most important. More in detail, for t_1, most molecules initially injected at x_0 have remained close to the injection point so that the local concentration $c(\mathbf{r},t)$ is high. In turn, according to Henry's law, such a large local concentration leads to a large adsorbed concentration $c_a(\mathbf{r},t)$. At $t = t_3$ (advective regime), the molecules

are now distributed more homogeneously in the pore space due to advection. As a result, in sites located far from the injection point x_0, the adsorbed tracer concentration $c_a(\mathbf{r},t)$ increases compared to the value obtained at earlier times. According to Henry's law, such a concentration increase leads to an increase in the adsorbed concentration so that the effect of adsorption becomes more pronounced. At $t = t_1$, the system reaches the end of the diffusion-dominated regime to enter the advection-dominated regime. In this transient regime, the dashed and solid lines corresponding to the adsorbing and non-adsorbing tracer concentrations nearly overlap. This result indicates that there is no significant adsorption effect in the short time interval corresponding to the transition zone. However, at large times, at $t = t_3$, as molecules travel over long distances and explore the whole porosity/interface, a larger number of molecules get affected by adsorption so that more pronounced differences are observed between adsorbing and non-adsorbing conditions. At even larger times – i.e. t_4 – transport becomes dispersive since both the non-adsorbing and adsorbing tracer molecules get displaced according to propagators with a shape different but close to Gaussian. For $t = t_7$, the shape of the propagators for both systems is perfectly Gaussian as expected for molecules in the dispersion regime. As an important consistency check, we also notice that the position of the peak center in the Gaussian profile for the passive i.e. non-adsorbing tracer is located at $(x - x_0)/Ut = 1$. While this corresponds to an expected result for Taylor dispersion, the peak center for the adsorbing particles is located at a position < 1 using such units. This result confirms that adsorption decreases the particle displacement velocity of the free molecules.

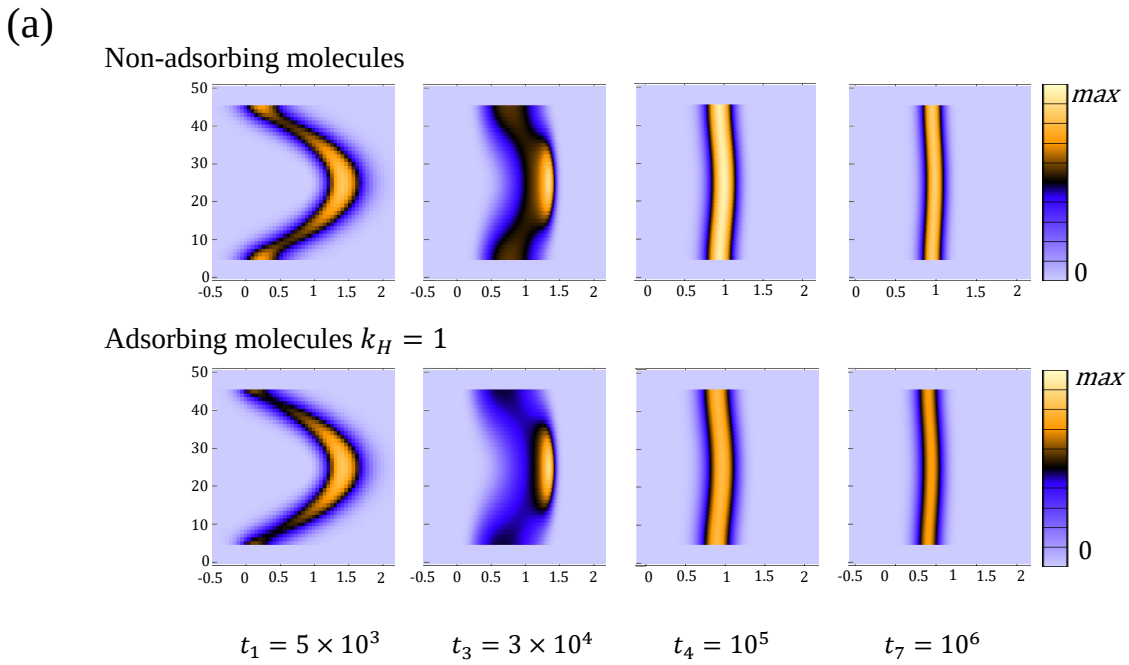

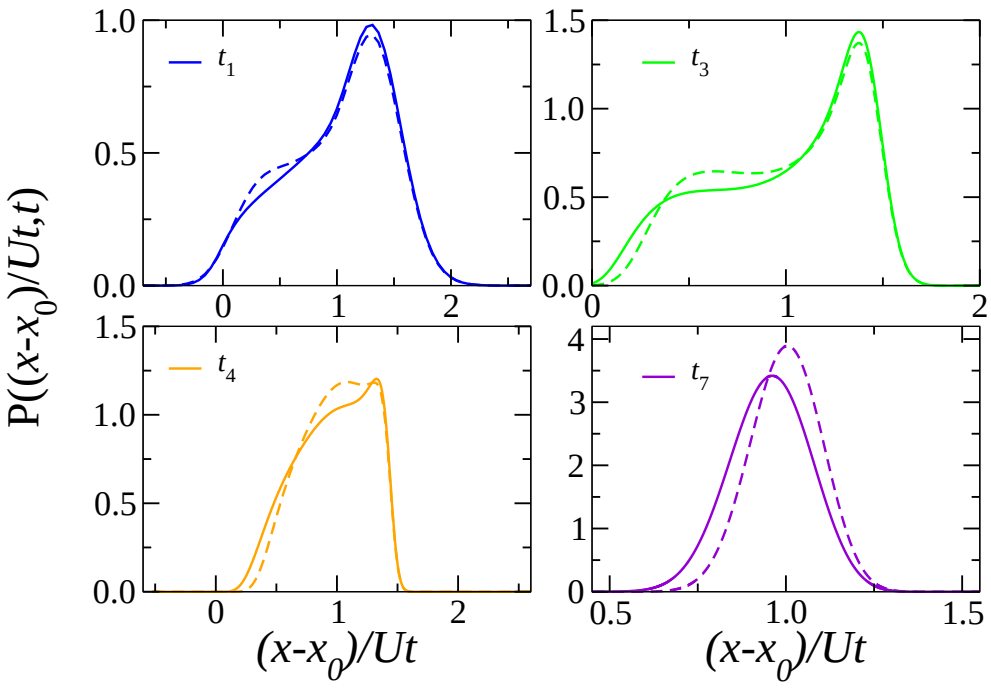

Figure 38: (a) Concentration profile observed at different times t_n along the advective and dispersive regimes. The top data are for non-adsorbing tracer molecules dispersion while the bottom data are for adsorbing tracer molecules (adsorption corresponds to a Henry regime with $k_H = 1$ as described in the main text). The abscissas are plotted in units of $(x - x_0)/Ut$ where x_0 is the lateral injection position and U the mean velocity. These results are obtained for systems characterized by Peclet number $\mathrm{Pe} = 100$ with an initial tracer concentration per site $c_0 = 10$. (b) Normalized propagator $P((x - x_0)/Ut, t)$ observed at different times t_n – similar to those shown in panel (a). The dashed lines denote the results for non-adsorbing tracer while the solid lines corresponds to the results for the adsorbing tracer. The same flow and adsorption conditions as in (a) were considered.

1.2. Influence of adsorption/desorption coefficient

In this section, we investigate the influence of the adsorption/desorption ratio on the transport of molecules which are subjected to adsorbing conditions. The flowing i.e. carrying fluid is characterized by its Peclet number set to Pe = 100. We use a Henry's law with a constant initial concentration $c_0 = 10$ while varying the adsorption/desorption coefficient k_H via the adsorption rate parameter p_A (i.e. at constant p_D). More in detail, a constant desorption rate $p_D = 0.001$ is used and we select $k_H = 10$, 40, 100 (which correspond to $p_A = 0.01$, 0.04, 0.1, respectively). We first present in Fig. 39 the normalized time derivative of the displacement variance as a function of time $D(t)/D_m$. Upon increasing k_H, a maximum appears in $D(t)/D_m$ at a time which roughly corresponds to the time domain prior to the dispersive regime ($D(t)/D_m$ is constant in the latter). However, regardless of the adsorption/desorption ratio, the three main transport regimes are still observed: diffusion, advection, and dispersion. The maximum observed in the time evolution of $D(t)/D_m$ is specific to the use of adsorbing conditions as it is not observed when non-adsorbing conditions are used (this is confirmed by the fact that its amplitude increases with increasing k_H). This adsorption-specific effect can be explained by the fact that adsorption is a much faster process than desorption (i.e. the adsorption rate is larger than the desorption one). As a result, the adsorption process leads to adsorbed amounts that are larger than the value reached in the long time limit (equilibrium). In turn, such an overestimated adsorbed amount leads to a large value of $D(t)/D_m$ since a large number of molecules stick to the surface while most of the free molecules are carried away with the flowing liquid. Then, as the time increases, this transient situation disappears since the adsorbed amount reaches the equilibrium state/value with a large number of molecules desorbing from the surface. In this asymptotic (long-time) limit, $D(t)/D_m$ decreases and eventually reaches the plateau value that characterizes the dispersive regime.

Fig. 40 shows the normalized propagators $P[(x-x_0)/Ut,t]$ for the different systems considered above taken at different times t_n. At $t = t_2$, the system is at the onset of the advective regime where the concentration has been displaced by a small amount x only. Therefore, in this short time regime, the influence of the adsorption ratio k_H is not pronounced as most of the molecules are still located near the injection position x_0. In the advection dominated regime, i.e. for $t = t_3$,

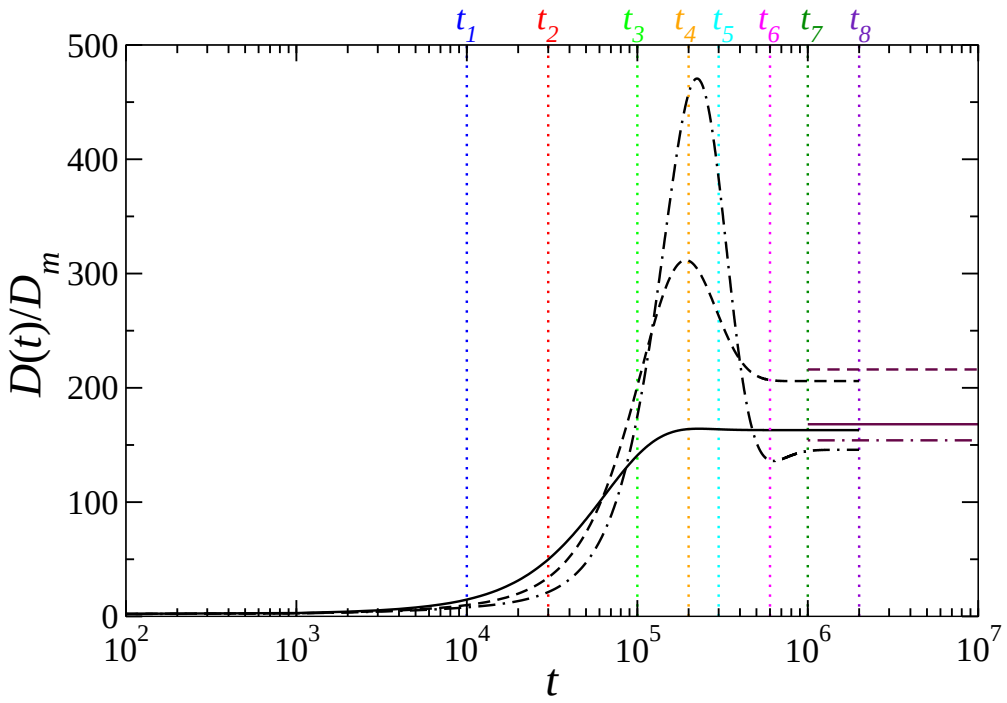

Figure 39: Temporal evolution of the time derivative of the displacement variance $D(t)$. $D(t)$ is normalized to the molecular diffusion coefficient D_m of the free i.e. non-adsorbing tracer. Molecules adsorb to the pore surface according to a Henry adsorption model with different adsorption/desorption rates k_H (varied by changing p_A while keeping p_D equal to 0.001). The solid, dashed and dotted-dashed lines denote $k_H = 10$, 40 and 100, respectively. The dashed horizontal lines denote the analytical values of D_{eff}^{ads}/D_m while the vertical dotted lines denote different times t_n. The system is characterized by Pe = 100 and an initial concentration $c_0 = 10$.

$t = t_4$ and $t = t_5$, the different data sets exhibit more pronounced differences when varying k_H as most molecules get adsorbed at the pore surfaces (therefore, as expected, k_H significantly affects the tracer dispersion). The propagators display a plateau in the region $x \sim x_0$ which reflects the significant concentration of molecules that get adsorbed near the injection point (so that they are not dispersed as much as the rest of the tracer molecules which are carried along the flow). For $t = t_4$, the propagators obtained with $k_H = 10$ start to approach a quasi-Gaussian shape, which suggests that the end of the advection-dominated regime is reached. However, for the adsorbing systems with $k_H = 40$ and $k_H = 100$, $D(t)/D_m$ is maximum at $t = t_4$ with a pronounced adsorption effect on the normalized propagators. In this case, the advection-dominated regime ends at a larger time – typically about $t \sim t_5$. For $t = t_6$, the data for $k_H = 10$ correspond to a propagator that has a nearly Gaussian shape. In contrast, owing to more significant adsorption effects, the data for $k_H = 40$ and 100 correspond to an asymmetric propagator which is not Gaussian in shape. For $t = t_7$, all propagators become closer to ideal Gaussian distributions but the differ-

ences observed between the different data reflect the effect of the adsorption/desorption ratio k_H. The Gaussian curve is shifted to the left along the x-axis with a shift that increases upon increasing the adsorption/desorption ratio. This result indicates that adsorption drastically delays the dispersion of the tracer. As already mentioned, this is due to the fact that molecules get adsorbed in an intermittent fashion (adsorption/desorption) with adsorption sequences/times that do not contribute to the dispersion of the tracer within the porosity. In other words, adsorption processes decrease the overall particle displacement velocity with a velocity decrease proportional to the adsorption/desorption ratio k_H.

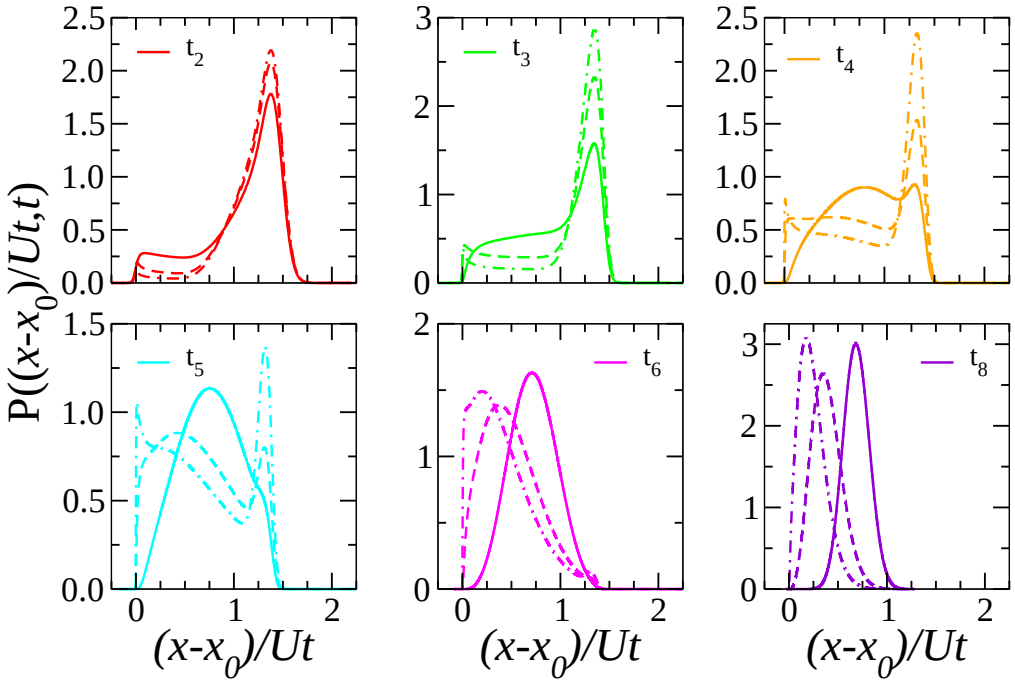

Figure 40: Normalized Propagator $P((x-x_0)/Ut,t)$ observed at different times t_n – as shown in Fig. 39. These data illustrate the dispersion for molecules that adsorb according to a Henry adsorption isotherm with different constants k_H (obtained by varying p_A while keeping $p_D = 0.001$). The solid, dashed and dotted-dashed lines denote $k_H = 10$, 40 and 100, respectively. The system considered here is characterized by Pe $= 100$ and initial concentration $c_0 = 10$.

To better understand the effect of the adsorption/desorption ratio on the time evolution of the free tracer, we show in Fig. 41 the tracer concentration distributions for different adsorbing conditions. When $k_H = 10$, the data obtained at $t = t_2$ indicate that the tracer molecules are distributed according to the Poiseuille velocity profile. These data are characteristic of the advection-dominated regime. However, for $t = t_4$, one can observe that adsorption hinders the transport of the free tracer molecules with non-negligible tracer redistribution. At larger

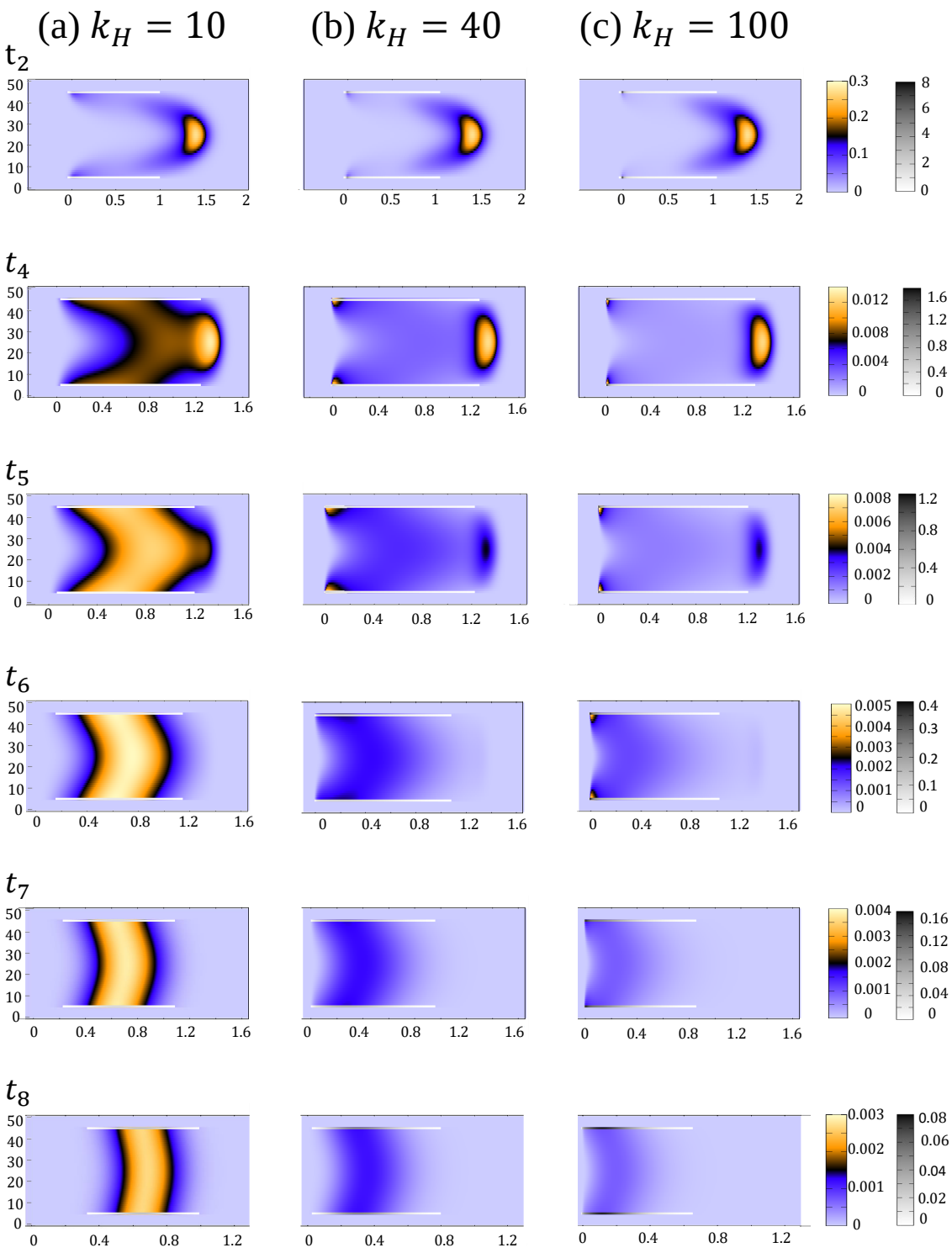

Figure 41: Tracer concentration profile observed at different times t_n along the advective and dispersive regimes. The results are for the dispersion of molecules that adsorb according to an Henry adsorption isotherm with different k_H (as obtained by varying p_A while keeping $p_D = 0.001$). The panels (a), (b) and (c) present the dispersion for $k_H = 10$, $k_H = 40$ and $k_H = 100$, respectively. The abscissas are plotted in unit of $(x - x_0)/Ut$ where x_0 is the lateral injection position and U is the mean flow velocity. The systems considered here are characterized by a Peclet number $\mathrm{Pe} = 100$ with an initial concentration $c_0 = 10$. The concentration profile for the adsorbed tracer molecules is presented using a black-and-white toned scale at the interface of the parallel plates geometry for the different systems.

times, i.e. for $t = t_5$, $t = t_6$ and $t = t_7$, the tracer concentration distribution becomes more homogeneous, which characterizes the beginning of the dispersion regime. Comparing the different columns in Fig. 41 allows probing the effect of the adsorption/desorption ratio k_H. In the advection-dominated regime (t_4 and t_5), two pore regions with large concentrations compared to the average concentration are observed. These two marked concentration regions correspond to molecules that are carried by the Stokes flow and molecules adsorbed at the surface near the injection slice x_0, respectively (note that x_0 corresponds the abscissa 0 in the figure). We note that this effect is more pronounced as k_H increases as the impact of adsorption is more important. At larger times, $t = t_6$, $t = t_7$ and $t = t_8$, the contrast between the two regions fades out and the concentration in free molecules becomes more homogeneous within the geometry (the dispersion regime is reached).

Influence of the adsorbed tracers

In the previous section, transport quantities such as the dispersion coefficient were assessed by accounting for the free tracer concentration only, i.e. $c(\mathbf{r},t)$. In this paragraph, we consider the total concentration $c(\mathbf{r},t)+c_a(\mathbf{r},t)$ as this is expected to lead to different time evolution for the dispersion coefficient $D(t)/D_m$ and the corresponding normalized propagator. We define $D_{total}(t)$ (resp. $D_{free}(t)$) as the time derivative of the displacement variance when considering the free and adsorbed molecules (resp. only the free molecules). Similarly, P_{total} (resp. P_{free}) are the normalized propagators when considering the total molecule concentration (resp. only the free molecule concentration).

Fig. 42 presents the results obtained for the dispersion of molecules adsorbing according to the Henry adsorption model with $k_H = 40$ (the stokes flow is characterized by Pe $= 100$). Fig. 42(a) compares $D_{total}(t)/D_m$ and $D_{free}(t)/D_m$. These results show that both data sets present the three transport regimes: diffusion, advection, and dispersion. The main difference between the two curves is observed in the advection-dominated regime. At the onset of this regime, for $t = t_1$ and $t = t_2$, $D_{total}(t) > D_{free}(t)$, which reflects the importance of the adsorbed molecule contribution on the total displacement/dispersion in the short time regime (such adsorbed molecules which are mostly located near $x \sim x_0$ contribute significantly to the overall

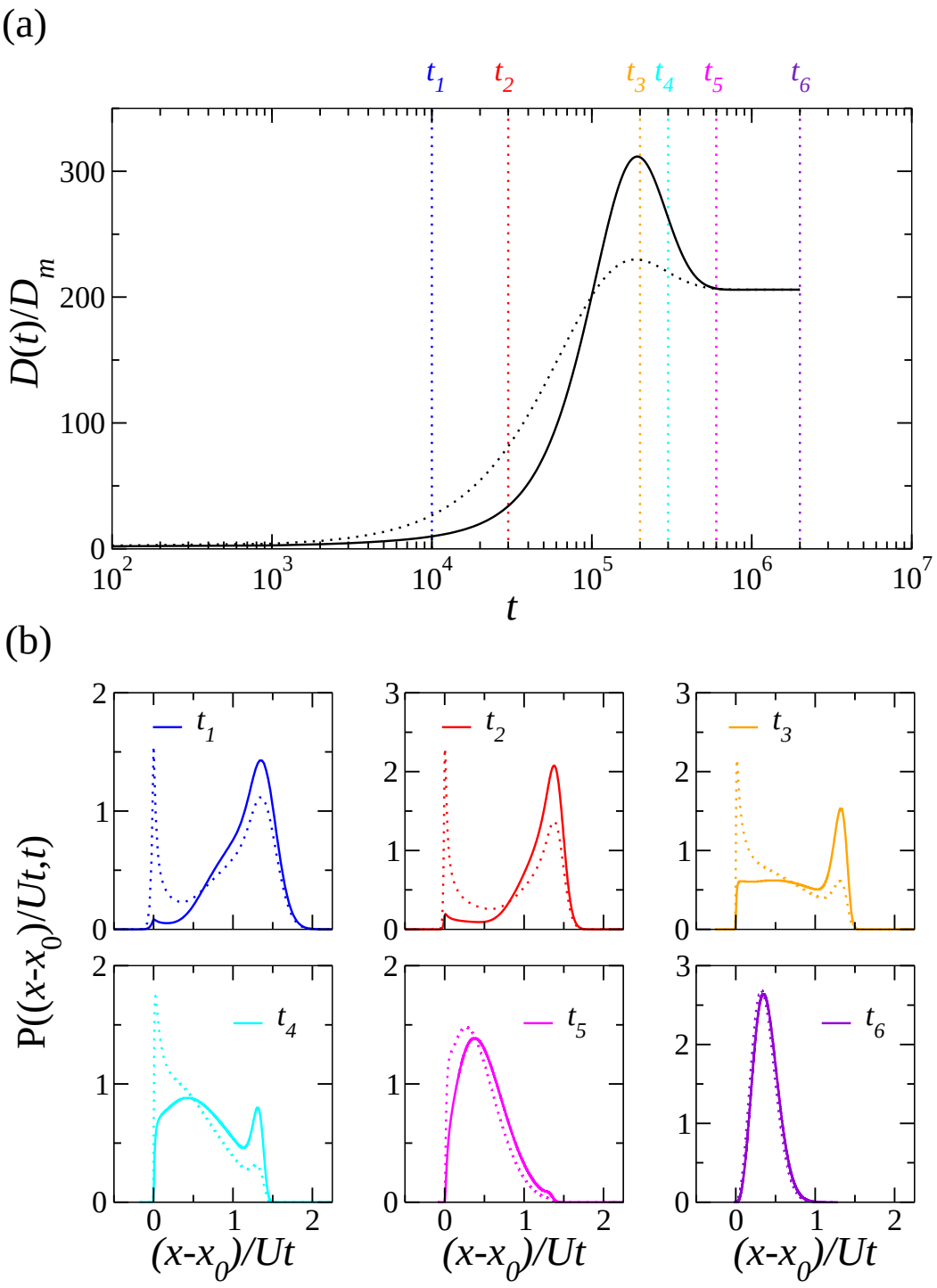

Figure 42: (a) Temporal evolution of the time derivative of the displacement variance $D(t)$. $D(t)$ is normalized to the molecular diffusion coefficient D_m of the free tracers. The system corresponds to the data for molecules that adsorb according to a Henry adsorption isotherm with $k_H = 40$ ($p_A = 0.04$, $p_D = 0.001$). The solid line corresponds to $D_{free}(t)/D_m$, the system when accounting only for the free tracer concentration $c(\mathbf{r},t)$. The dashed line denotes $D_{total}(t)/D_m$, the system when considering the total concentration $c(\mathbf{r},t) + c_a(\mathbf{r},t)$. The simulation set considered here is characterized by a Peclet number $\mathrm{Pe} = 100$ with an initial concentration $c_0 = 10$. (b) Normalized propagators at different times t_n - shown in panel (a). The solid lines denote the normalized propagator P_{free} for the free tracer concentration while the dotted lines correspond to the normalized propagator P_{total} for the adsorbed and free tracer concentrations.

dispersion because of their small variance). However, at the end of the advective regime, for $t = t_3$ and $t = t_4$, the adsorbed molecules are transported in the channel by the flowing liquid but to a smaller extent – as a result, the overall molecule displacement is less important than when only considering the non-adsorbed i.e. free molecules – $D_{total}(t) < D_{free}(t)$. In the dispersive regime, for $t = t_5$ and $t = t_6$, the contribution of $c_a(\mathbf{r},t)$ does not change the effective dispersion coefficient since we get $D_{total}(t \to \infty) \sim D_{free}(t \to \infty)$. This result proves that the molecules are displaced in a homogeneous manner and the adsorption at this level has no influence since the different molecule contributions have reached equilibrium.

Fig. 42(b) presents the time evolution of the normalized propagators $P_{free}((x-x_0)/Ut,t)$ and $P_{total}((x-x_0)/Ut,t)$. In the advective regime, for $t \in [t_1,t_4]$, we notice the presence of two peaks in $P_{total}((x-x_0)/Ut,t)$. This result confirms the existence of two regions. The first region corresponds to the adsorbed molecules at the pore surface near the injection point $x \sim x_0$. The second region corresponds to the free molecules carried along the Stokes flow. At larger times, the influence of the adsorbed molecules is less pronounced as the normalized propagators P_{free} and P_{total} nearly overlap. We performed the same comparison for $k_H = 1$; the results show that $c_a(\mathbf{r},t)$ does not impact the different transport quantities (see Appendix C.1.). In conclusion, the contribution $c_a(\mathbf{r},t)$ is important when using large adsorption/desorption ratios only.

Adsorbing molecules dispersion

The results in Fig. 39 show a non-linear variation of $D(t \to \infty)/D_m$ as a function of the adsorption/desorption ratio k_H. In order to understand this behavior, i.e. the influence of the adsorption/desorption ratio on the dispersion coefficient for Henry adsorbing molecules $D(t \to \infty)$, we study the evolution of the analytical expression for D_{eff}^{ads}/D_m as a function of k_H. We recall the analytic expression of D_{eff}^{ads}/D_m which was introduced in Eq. (I .32) in Chapter 1:

$$\frac{D_{eff}^{ads}}{D_m} = 1 + \frac{K_v^{Pois}}{D_m} = 1 + \frac{1}{210}\frac{L_y^2U^2}{D_m^2}\frac{102L_yk_H^2 + 18L_y^2k_H + L_y^3}{(L_y+2k_H)^3} + \frac{U^2}{D_mk_D}\frac{2L_y^2k_H}{(L_y+2k_H)^3} \qquad \text{(V .1)}$$

where L_y is the pore width, U is the average velocity of the flowing fluid, and D_m is the bulk molecular diffusion coefficient. It is straightforward to show that the derivative of Eq. (V .1)

with respect to k_H leads to:

$$\frac{\partial}{\partial k_H}\frac{D_{eff}^{ads}}{D_m} = \frac{2L_y^2U^2\left(35D_m(L_y-4k_H)+L_yk_D\left(L_y^2+11L_yk_H-17k_H^2\right)\right)}{35D_m^3k_D(L_y+2k_H)^4} \tag{V .2}$$

As expected, the latter quantity is a function of the characteristic length L_y. We plot in Fig. 43 Eq. (V .2) as a function of k_H for two systems characterized by $L_y = 41\Delta x$ and $L_y = 10\Delta x$. For $L_y = 41\Delta x$ (the pore width used throughout our study), the derivative is strictly positive for $0 < k_H < 30$ which indicates that the dispersion coefficient increases with the adsorption desorption ratio k_H. On the other hand, for $k_H > 30$, the derivative is negative as the dispersion coefficient decreases with k_H (this corresponds to the data obtained for $k_H = 40$ and $k_H = 100$ which indeed show the decrease of D_{eff}^{ads} with k_H). The same trend is observed for $L_y = 10\Delta x$ but the range of k_H where the derivative is positive is smaller $0 < k_H < 7$. This result can be explained by the dependence of the roots of the derivative with the width of the channel (one is always negative and the second is positive but decreases with the width of the channel; for rigorous derivation see Appendix C.2.). This indicates that increasing the adsorption/desorption ratio k_H yields lower dispersion coefficient as adsorption is too strong to allow significant re-distribution between adsorbed and free molecules.

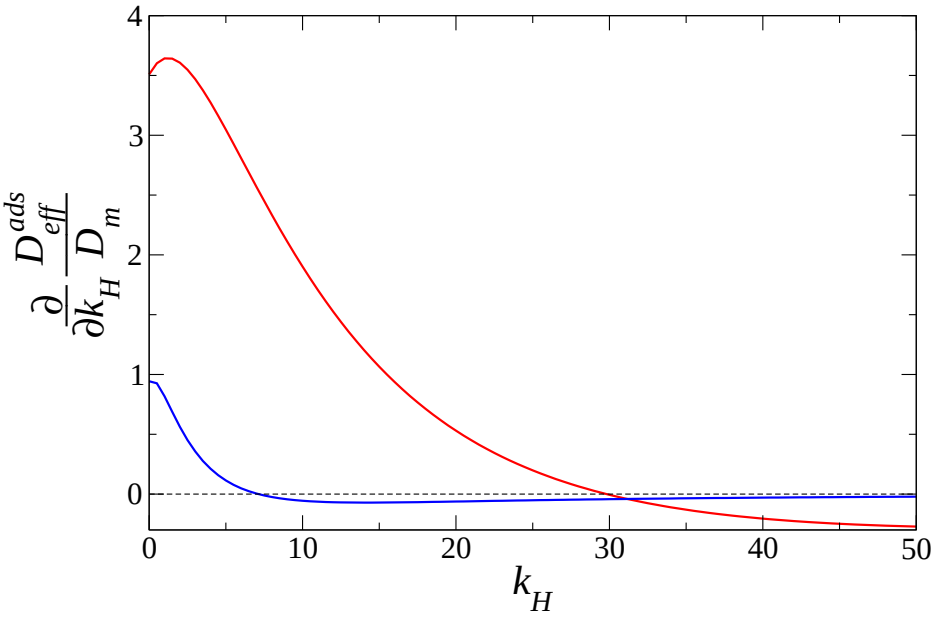

Figure 43: Effect of the adsorption/desorption ratio k_H on the dispersion coefficient D_{eff}^{ads}/D_m (note that to highlight this effect, we plot the derivative of the dispersion coefficient with respect to k_H). The systems considered here correspond to the slit pore geometry with different characteristic lengths L_y (defined as the width between the two parallel plates). The data are for systems with a mean velocity U and a molecular diffusion coefficient D_m. The red and blue colors denote data obtained for $L_y = 41\Delta x$ and $L_y = 10\Delta x$, respectively.

1.3. Slug injection

We perform simulations for continuous "slug" injection of the molecules adsorbing according to the Henry law with an initial concentration $c_0 = 1$ (injected at $x_0 = 1$). The injection time varies from $\Delta t_0 = 2 \times 10^6$ (see Fig. 26(c) in Chapter 4). Fig. 44 compares the simulation results for adsorbing and non-adsorbing molecules dispersed within a carrying fluid characterized by Pe $= 10$. We present in Fig. 44(a) the distribution of free molecules in the slit pore geometry (the adsorption data are obtained for the Henry model with $k_H = 5$ corresponding to $p_a = 0.05$ and $p_d = 0.01$). For the adsorbing molecules, the spreading of the concentration is delayed compared to the concentration for the passive tracer (i.e. non-adsorbing molecules); this result indicates that the molecules get dispersed through the geometry over a longer time due to adsorption at the pore surface. This result highlights the fact that adsorption decreases the characteristic displacement/motion in confinement. Fig. 44(b) shows the evolution in time of the free molecule concentration profile $c_l(x,t)$ at different lateral positions x (as obtained in the course of the Lattice Boltzmann simulations). We recall that $c_l(x,t) = 1/L_y \times \sum_y c(\mathbf{r},t)$ is the normalized concentration at a lateral position x within the pore. These data correspond to

molecules adsorbing according to Henry's law with $k_H = 1$ and $k_H = 5$. The different systems reach the same values as the concentration of the adsorbed tracers is very small compared to the concentration of the free tracers. When comparing the difference between the adsorbing and non-adsorbing systems, we observe that the distribution of the adsorbing molecules display a slower time evolution. This result confirms that adsorption decreases molecular dispersion within the pore by inducing non-negligible residence times at the pore surface. This is confirmed by the results for the adsorbing systems with $k_H = 1$ and $k_H = 5$ which indicate that increasing the adsorption/desorption coefficient leads to slower dispersion.

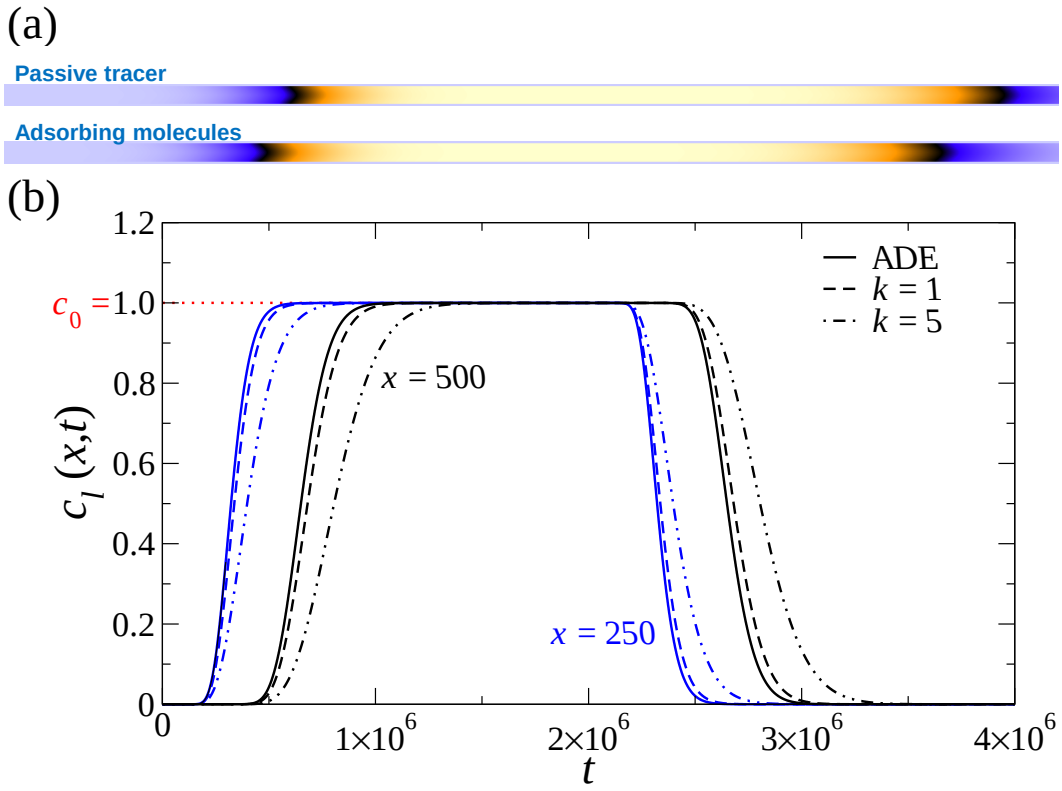

Figure 44: (a) Concentration profile observed at $t = 2 \times 10^6$ for tracer molecules transported in a slit pore geometry. The top data are for non-adsorbing molecules (passive tracer) while the bottom data are for adsorbing molecules (the adsorption corresponds to a Henry regime with $k_H = 5$). (b) Time evolution of the normalized concentration $c_l(x,t)$ at different lateral positions in the two parallel plates geometry for non-adsorbing and adsorbing molecules. The solid lines correspond to results obtained for non-adsorbing molecules. The dashed lines present the results for a Henry adsorption isotherm with $k_H = 1$ ($p_A = p_D = 0.01$) while the dashed-dotted lines correspond to $k_H = 5$ ($p_A = 0.05$, $p_D = 0.01$). The blue and black colors indicate the results obtained at a lateral position $x = 250$ and $x = 500$, respectively.

2. Langmuir adsorption

In this section, we investigate the influence of site saturation on the transport of adsorbing tracers. We perform numerical simulations to model the dispersion of molecules adsorbing according to the Langmuir adsorption model. Different adsorption/desorption ratios k_L and initial concentrations c_0 are considered. The results will be compared with the data obtained in the previous section where Henry adsorption was considered. As will be shown in the following paragraphs, the value of c_0 is an important parameter so that a section is dedicated to determine its impact.

2.1. Influence of the adsorption/desorption ratio

In order to understand the influence of the adsorption/desorption ratio, we perform the Dirac injection at the lateral position $x_0 = 200$ in the parallel plate geometry for a system characterized by $\mathrm{Pe} = 25$. We consider different adsorbing ratios $k \in \{0.1, 0.5, 1, 5, 10\}$. For each k, we perform Langmuir simulations for different initial concentration $c_0 \in \{10, 20, 30\}$. We also present the corresponding results for the Henry adsorbing system. However, for the Henry adsorption simulations, varying the initial concentration was found to have no influence on the displacement variance (or, equivalently, the corresponding normalized propagators). Therefore, for the Henry adsorption conditions, we present the results for only one initial concentration $c_0 = 10$. Fig. 45 shows the time evolution of $D(t)/D_m$ for the different systems. The dispersion of the molecules following the Langmuir model displays the three typical transport regimes: diffusion, advection and dispersion regimes. On the other hand, the comparison of the different data reveals various important differences. First, for small adsorption/desorption ratios $k \in \{0.1, 0.5\}$, the results for the Langmuir model – for the different initial concentrations c_0 – overlap with those obtained for the Henry model. As established in the previous section, in this k-range, the molecules adsorbing according to Henry's law display the same time evolution for $D(t)/D_m$ as that obtained for the non-adsorbing molecules. Thus, we conclude that the Langmuir adsorption model for small k has no significant influence on $D(t)/D_m$. Second, for large k, the difference between the Langmuir and Henry models becomes more important. Moreover, the influence of c_0 becomes more pronounced. Hence, the influence of c_0 increases upon increasing the adsorption/desorption ratio k. Third, for $k = 10$, the dispersive regime for

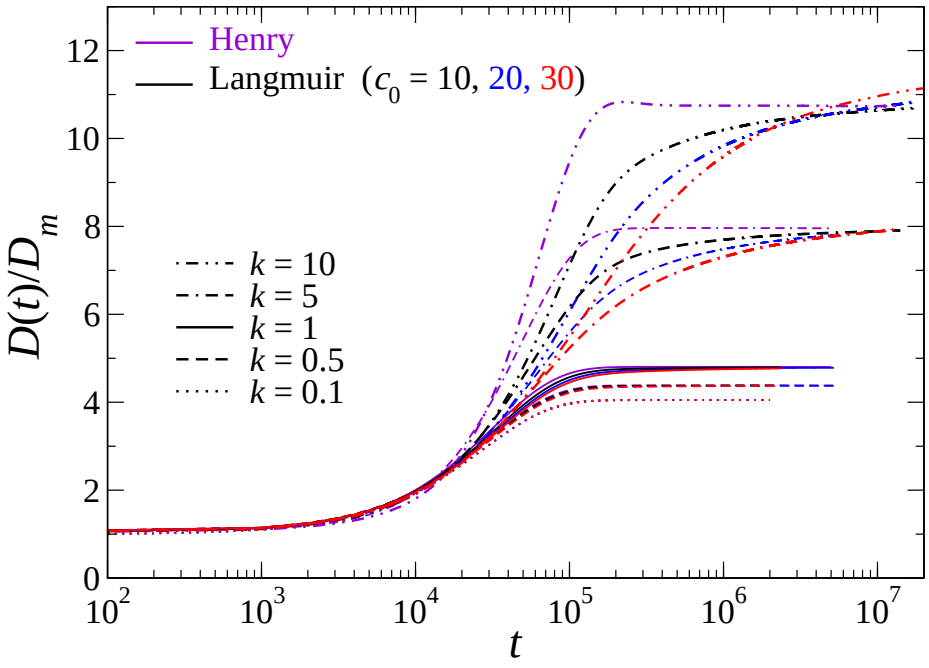

Figure 45: Temporal evolution of the time derivative of the displacement variance $D(t)$. $D(t)$ is normalized to the molecular diffusion coefficient D_m for the free tracer molecules. We consider the dispersion of molecules that obey different adsorption models. The black, blue and red colors denote Langmuir adsorption isotherm for different initial concentrations ($c_0 = 10$, $c_0 = 20$, $c_0 = 30$). The violet color denotes Henry adsorption isotherm for $c_0 = 10$. The lines (dotted, dashed, solid, dashed-dotted, double-dashed-dotted and dashed-double-dotted) denote different values of $k = k_L = k_H$ (0.1, 0.5, 1, 5 and 10, respectively). The system is characterized by Pe = 25.

$c_0 = 30$ corresponds to a larger dispersion coefficient than the one obtained at lower concentrations – with the latter corresponding to the dispersive coefficient obtained for the Henry model. Thus, the effective dispersion coefficient for the Langmuir model is concentration-dependent and not equal to the value obtained for Henry's model. In order to investigate the influence of the initial concentration c_0 on the effect of k, we normalize $D(t)$ with respect to its value in the infinite time limit $D(t \to \infty)$. We present its temporal evolution in Fig. 46 for the data obtained with $k = 0.5$ and $k = 1$. These results indicate that the difference between the Henry model and the different Langmuir adsorption models is more pronounced for $k = 1$ than for $k = 0.5$ – therefore, suggesting that the effect of the initial concentration c_0 on the Langmuir adsorption is more pronounced when using a higher adsorption/desorption ratio k.

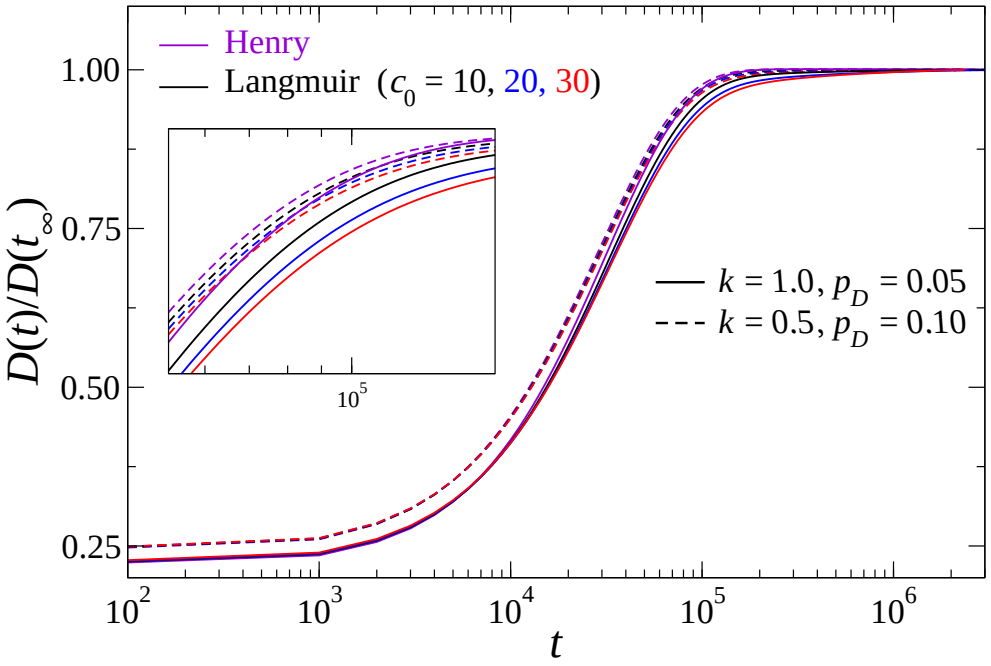

Figure 46: Temporal evolution of the time derivative of the displacement variance $D(t)$. $D(t)$ is normalized to the effective dispersion coefficient $D(t \to \infty)$. We consider the dispersion of molecules that follow different adsorption models. The solid and dashed lines represent data obtained for adsorption/desorption ratios $k = 1$ and $k = 0.5$. The black, blue and red colors denote Langmuir adsorption configuration for $c_0 = 10$, $c_0 = 20$ and $c_0 = 30$, respectively. The violet curves are for Henry adsorption configuration for $c_0 = 10$. The flowing liquid considered here is characterized by Pe $= 25$.

2.2. Influence of initial concentration c_0

In this paragraph, we assess the influence of the initial concentration c_0 on the dispersion of molecules adsorbing according to the Langmuir adsorption model (with $k_L = 10$). We vary c_0 from 10 to 1000 to study its influence on the temporal evolution of $D(t)/D_m$, the concentration of free molecules distribution, and the associated propagator. The considered systems are characterized by a Peclet number Pe $= 25$. Fig. 47 presents the time evolution of $D(t)/D_m$. For low concentrations, i.e. $c_0 \in [10, 100]$, the typical transport regimes are observed. At short times, the diffusion-dominated regime is observed followed by the advection-dominated regime. At long times, the dispersion regime is reached. Upon increasing the initial concentration, i.e. for $c_0 = 75$ and $c_0 = 100$, the advective regime extends over a longer time so that the time required to reach dispersion becomes longer. This effect is due to the influence of the adsorbed molecules on the displacement of the free molecules. The time required to re-distribute the adsorbed concentration increases and so does the advective regime. For systems obtained for larger initial concentration, i.e. for $c_0 > 200$, the temporal evolution of $D(t)/D_m$ is different. We notice that

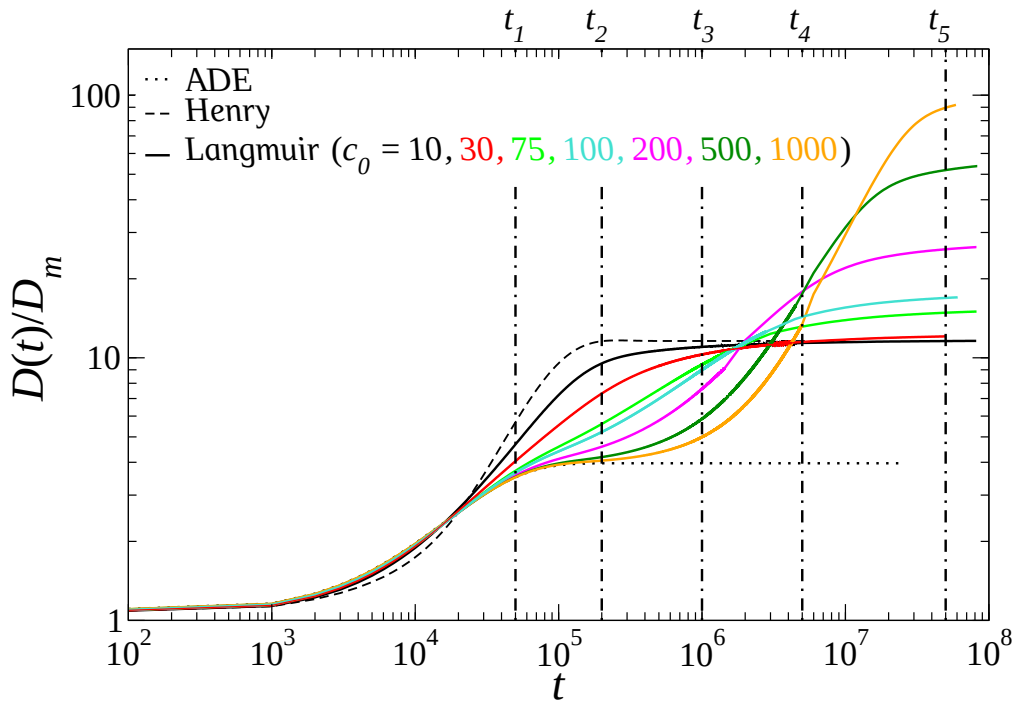

Figure 47: Temporal evolution of the time derivative of the displacement variance $D(t)$. $D(t)$ is normalized to the molecular diffusion coefficient D_m of the free tracer molecules. We consider the dispersion of molecules that obey different adsorption models with an adsorption/desorption ratio $k = 10$. The dotted, dashed and solid lines correspond to the dispersion of non-adsorbing molecules, molecules following the Henry law and molecules following the Langmuir model, respectively. The black color corresponds to data for systems with an initial concentration $c_0 = 10$. The systems considered here are characterized by $\mathrm{Pe} = 25$.

the advective regime is divided into two stages which are separated by an additional stationary regime. The latter regime corresponds to the Taylor dispersion regime (the limit of the passive tracer transport). The reason for the appearance of this plateau is as follows. In this time range, the impact of adsorption kinetics on the dispersion of free molecules at the solid interface is considerable. However, this influence is negligible for the free molecules in the bulk. More in detail, in this time range, the free molecules concentration is important since c_0 is large. On the other hand, $\Gamma^{\infty} = 1$ so that the variance on the adsorbed molecules concentration, i.e. $\Delta c_a(\mathrm{r},t)$, is too small to impact the overall variance. Therefore, in this time range, the displacement variance is not affected by adsorption equilibrium at the surface. In other words, the free molecules get dispersed in the channel as if $k_L = 0$ (i.e. as in the normal Taylor dispersion regime). At larger times, the free molecules gets dispersed in the channel and their concentration becomes comparable to that for the adsorbed molecules. As a result, the adsorption effect is important and $D(t)/D_m$ increases until reaching the asymptotic dispersion regime that is characteristic of

this system obeying the Langmuir adsorption model.

In order to validate the above explanation, we present in Fig. 48 the time evolution of the different transport quantities for the dispersion of molecules (adsorbing according to the Langmuir adsorption model for initial concentrations $c_0 \in \{10, 30, 500\}$). We study the time evolution during both the advective and dispersive regimes. Fig. 48(a) shows the temporal evolution of the free molecule concentration along the normalized x-axis $(x-x_0)/Ut$. At $t = t_1$ and $t = t_2$, the results for the small initial concentrations c_0 show a concentration distribution that is affected by the velocity profile. These results provide evidence for the adsorption effect since the dispersion of the free molecules is delayed due to surface adsorption. However, for $c_0 = 500$, we observe at $t = t_1$ a homogeneous distribution for the free molecules which is influenced only by the velocity profile (no adsorption effect at the surface is noticed). For $t = t_2$, the concentration becomes more homogeneous, which corroborates the plateau observed in the time evolution in $D(t)D_m$ (as already explained, this plateau corresponds to the Taylor dispersion regime as the adsorbed molecules do not impact significantly the overall concentration distribution). For $t = t_4$, in the case of low initial concentrations, the dispersion regime is reached as the molecule concentration is redistributed homogeneously. However, for large initial concentration c_0, we notice that the free molecules concentration starts to spread over smaller $(x-x_0)/Ut$ positions. The latter corresponds to a less concentrated region, which characterizes the contribution of the adsorbed molecules on the free molecule distribution after equilibrium. This effect is less pronounced for $t = t_5$ where the distribution becomes more homogeneous, therefore reflecting the beginning of the dispersive regime for our adsorbing system ($c_0 = 500$).

To shed more light into the impact of the initial concentration c_0, Fig. 48(b) shows the normalized propagators $P((x-x_0)/Ut, t)$ obtained at different times along the advective and dispersive regimes. Inspection of the different curves for the different systems confirms our previous explanation. For $t = t_1$, we observe the advective regime for the different systems as confirmed by the non-Gaussian form of the propagators. For $t = t_2$, the propagators have a quasi-Gaussian shape, therefore confirming that the onset of the dispersion regime is reached. For larger times, i.e. $t = t_3$, we see that for $c_0 = 10$ and $c_0 = 30$ the Gaussian propagator is shifted due to adsorption. However, for $c_0 = 500$, the center of the Gaussian curve is located at 1, which corresponds to the

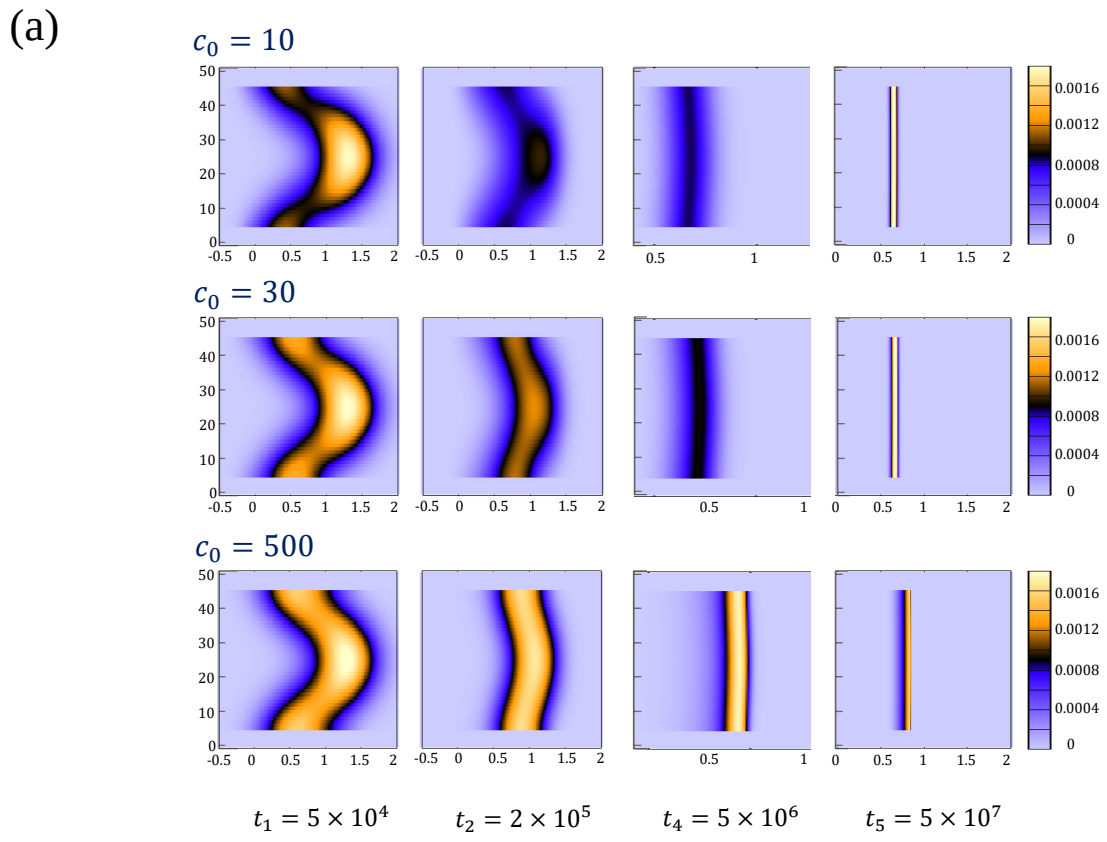

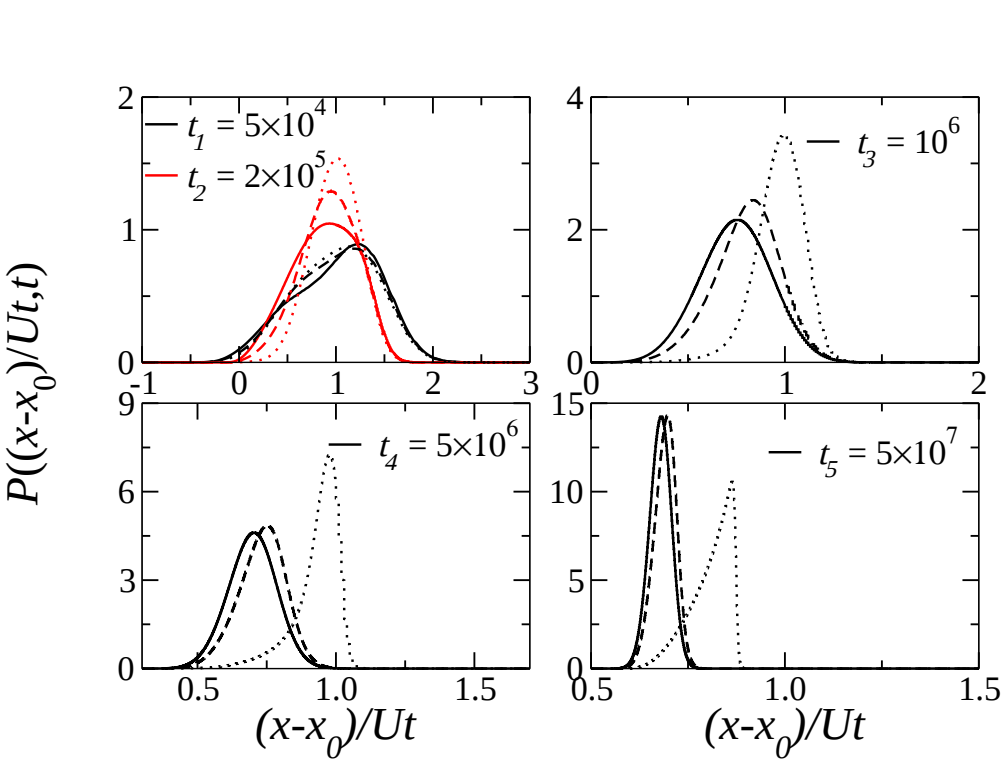

Figure 48: (a) Concentration profile observed at different times t_n along the advective and dispersive regimes. The top, middle and bottom data are for $c_0 = 10$, 30 and 500, respectively. The abscissas are plotted in units of $(x-x_0)/Ut$. The results correspond to the dispersion of molecules obeying a Langmuir adsorption isotherm with $k_L = 10$. The systems considered here are characterized by Peclet number Pe $= 25$. (b) Normalized propagator $P((x-x_0)/Ut,t)$ observed at different times t_n. The solid, dashed and dotted lines correspond to data obtained for the Langmuir adsorption model with an initial concentrations $c_0 = 10$, 30 and 500, respectively. The same configuration and adsorbing conditions as in (a) are used.

Gaussian curve of the normalized propagator in the Taylor dispersive regime. At large times, the propagators for the small initial concentration are Gaussian unlike for $c_0 = 500$ (where a tail appears). These results indicate that increasing the initial concentration changes the different transport regimes. In particular, for some concentration ranges, a additional stationary regime is observed.

3. Cooperative Langmuir adsorption

In this section, after considering Henry and Langmuir adsorbing models above, we study the impact of cooperative adsorption on the transport of adsorbing molecules. With this goal, we will use the model validated in Chapter 3 that describes the adsorption of surfactants on silica. More in detail, we recall that the adsorbing system is described as follows. The adsorption of individual monomers is defined by a Henry adsorption model with an adsorption desorption ratio k_H which is valid until the concentration reaches the critical micellar concentration CMC. Above the so-called critical surface concentration c_s, aggregated monomers adsorb at the pore surface by using a surface concentration-dependent adsorption/desorption ratio $k'(\Gamma_{m'})$. First, we perform numerical simulations using a simple set-up where the adsorbing molecules are injected using a Dirac injection peak. The results will be compared to the same dispersion data obtained when adsorption is described using Henry's law. Then, in order to better understand the impact of cooperative adsorption, we perform continuous injection simulations. The latter allow us to determine the evolution of the individual adsorbed monomers Γ_m as well as the evolution of the aggregated adsorbed monomers $\Gamma_{m'}$. In the last paragraph of this section, we perform the same simulations for adsorbing molecules according to the Henry, Langmuir and Henry-Langmuir models. The Henry-Langmuir model provides a representation of the adsorption of the individual monomers as well as of the aggregated monomers. Individual monomers adsorb according to the Henry model for a concentration below c_s while the adsorption of the aggregated monomers is represented by the Langmuir model ($c > c_s$). These results will be compared with the cooperative model in order to identify differences between these models.

3.1. Dirac versus slug injection

In this paragraph, we consider Dirac injection in the two parallel plates geometry for an initial concentration $c_0 = 1000$ (injection is performed at the lateral position $x_0 = 200$). The system

is characterized by Peclet number Pe = 100. The adsorbing configuration is as follows: we use adsorption/desorption ratios (k_H , k') – this indicates that the adsorption of individual monomers is characterized by a Henry constant k_H while the adsorption of aggregated monomers is characterized by the concentration dependent adsorption/desorption ratio k'. We compare the results obtained for the dispersion of molecules adsorbing according to the Henry adsorption model (with the same adsorption/desorption ratio k_H). Fig. 49 shows the time evolution of $D(t)/D_m$. These data show that the two curves perfectly overlap as no difference is noticeable between the two systems (i.e. no adsorption impact). Such a behavior can be explained as follows. After injection, a rapid decrease of the bulk concentration is observed so that the initial injected concentration, $c(\mathbf{r},0)$, disperses in the geometry to reach a free molecule concentration smaller than c_s (where the cooperative model is strictly equivalent to the Henry model). This is due to the fact that the adsorption/desorption ratios used in these simulations are too small ($k_H \sim 10^{-3}$, $k' \sim 10^{-3}$). We performed the same comparison with larger adsorption rates (Fig. 49) but again

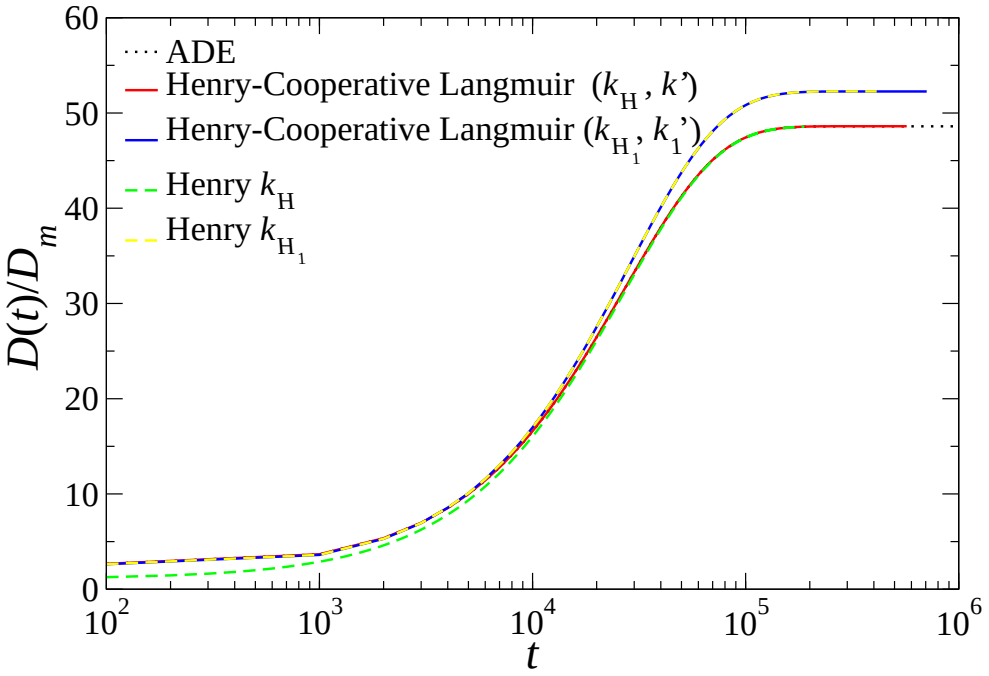

Figure 49: Temporal evolution of the time derivative of the displacement variance $D(t)$. $D(t)$ is normalized to the molecular diffusion coefficient D_m for the free tracer molecules. The dotted, solid and dashed lines denote the dispersion data for non-adsorbing molecules, molecules obeying the Henry-Cooperative Langmuir adsorption model and molecules obeying the Henry adsorption model. The blue and red colors denote the adsorption configuration with a nominal set (k_H, k') and ($k_{H_1} = 10^3\ k_H$, $k'_1 = 10^3\ k'$), respectively. The green and yellow colors denote systems with k_H and $k_{H_1} = 10^3\ k_H$, respectively. The systems considered are characterized by Peclet number Pe = 100 with an initial concentration $c_0 = 1000$.

the two data sets overlap. In conclusion, for a system with a Dirac injection, the initial injected concentrations decrease rapidly to a value lower than the critical surface concentration c_s.

In order to circumvent this issue, we perform a continuous injection with an initial concentration $c_0 = 1000$ at $x = x_0 = 1$. We carry out the injection over a period of time $\Delta t_0 = 10^6$ (see Fig. 26(c) in Chapter 4). Fig. 50 shows the evolution at $t = 2 \times 10^6$ of the different adsorbed quantities: the total adsorbed quantity Γ, the individual adsorbed monomers Γ_m and the aggregated adsorbed monomers $\Gamma_{m'}$. We also plot the surface concentration profile. These results allow validating the accuracy of the model; for small surface concentrations $c_{surf} < c_s$, only adsorption of individual monomers occurs so that we reach $\Gamma_m \sim k_H c_{surf}$. As expected, such

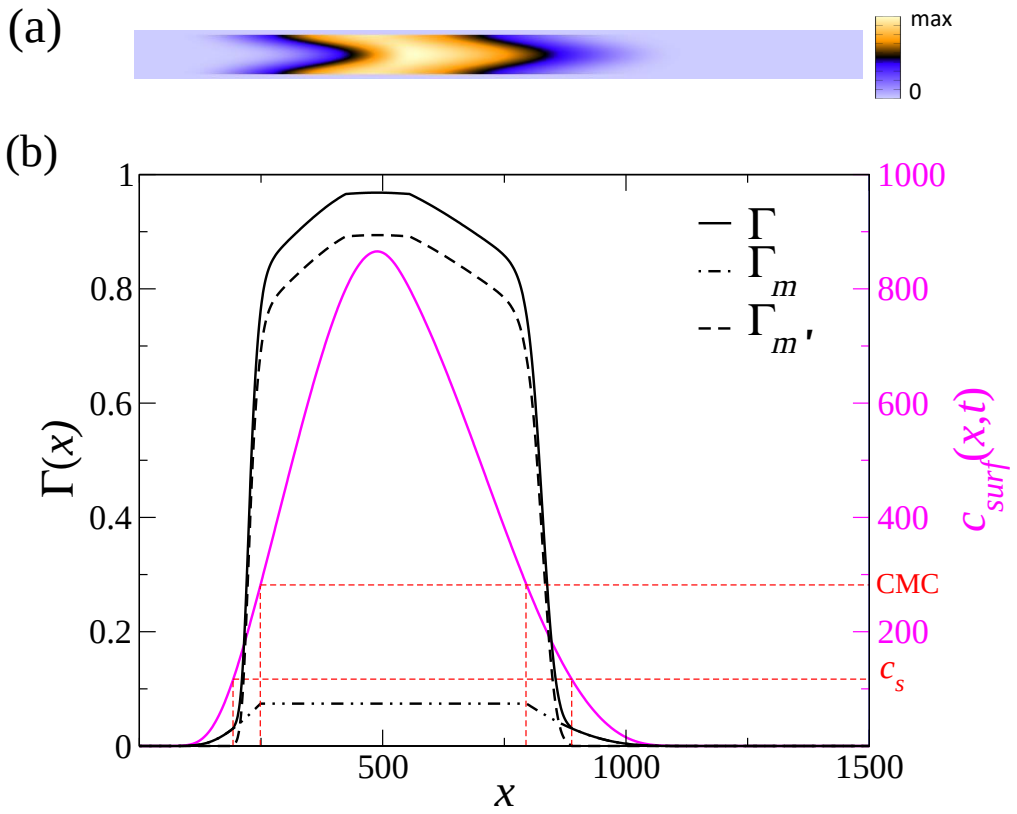

Figure 50: (a) Concentration profile for the free i.e. non-adsorbed molecules in a pore corresponding to a two parallel plates geometry. The molecules adsorb to the pore surface according to a Henry-Cooperative Langmuir adsorption isotherm. The date are take at a time $t = 2 \times 10^5$. (b) Adsorbed amount distribution for the Henry-Cooperative Langmuir adsorbing system taken at a time $t = 2 \times 10^5$. The black solid, dashed and dashed-dotted lines denote the total adsorbed amount Γ, the adsorbed amount of aggregated monomers $\Gamma_{m'}$ and the adsorbed amount of individual monomers Γ_m, respectively. The pink solid line indicates the surface concentration distribution. The system considered is characterized by Peclet number Pe = 100 and initial concentration $c_0 = 1000$.

adsorption saturates – i.e. becomes constant – for concentrations above CMC ($\Gamma_m \sim k_H$CMC). For $c_{surf} > c_s$, the adsorption of aggregated monomers occurs. Upon increasing the surface concentration, c_{surf} close to 800, $\Gamma_{m'}$ starts to reach a plateau (as the adsorbing surface becomes saturated with both adsorbed individual and aggregated monomers).

3.2. Comparison with other adsorption models

In this paragraph, we study the difference between the various adsorption models when using a continuous injection situation. Our geometry is exposed to a fluid flow that obeys Stokes flow with an average flow rate U. The Peclet number takes Pe $= 100$, we inject an initial concentration $c_0 = 1000$ at a lateral position $x_0 = 1$ over a time period $\Delta t_0 = 10^6 \Delta t$. We consider the following adsorption models: an ideal Henry model, a Langmuir model, a Henry-Langmuir model and the cooperative adsorption model. For the Henry model, we use the adsorption/desorption ratio k_H which characterizes the adsorption of individual monomers in the cooperative model. For the Langmuir model, we use the value k_L that best fits the aggregated monomer adsorption from TX100 adsorption on silica (presented in Fig. 21(a) in Chapter 3). For the Henry-Langmuir model, we associate the ideal Henry with the ideal Langmuir with adsorption-desorption ratios noted as (k_H, k_L). With this combined model, the adsorption of individual monomers is described using a Henry constant k_H while that of aggregated monomers is described using a Langmuir model with constant k_L. Finally, we use the cooperative model using the adsorption/desorption ratios (k_H, k'). We present the comparison of $\Gamma(x)$ for the different adsorption models in Fig. 51. For the Henry adsorption model, obviously, $\Gamma(x)$ is a linear function of the surface concentration $c_{surf}(x)$. For the Langmuir model, Γ increases with increasing concentration but reaches asymptotically the maximum adsorption capacity of the model. When using the combined models, i.e. Henry-cooperative Langmuir model and the Henry-Langmuir model, we found that for a concentration below the critical surface concentration c_s, it is similar to the Henry model since, only the adsorption of individual monomers is considered. On the other hand, at higher concentrations, we get different patterns/results. When using the Langmuir model, $\Gamma(x)$ increases significantly, which is not realistic. However, for the cooperative model, thanks to the variation in the adsorption/desorption ratio k' with concentration, $\Gamma(x)$ varies grad-

ually with the concentration and then reaches a plateau (surface saturation).

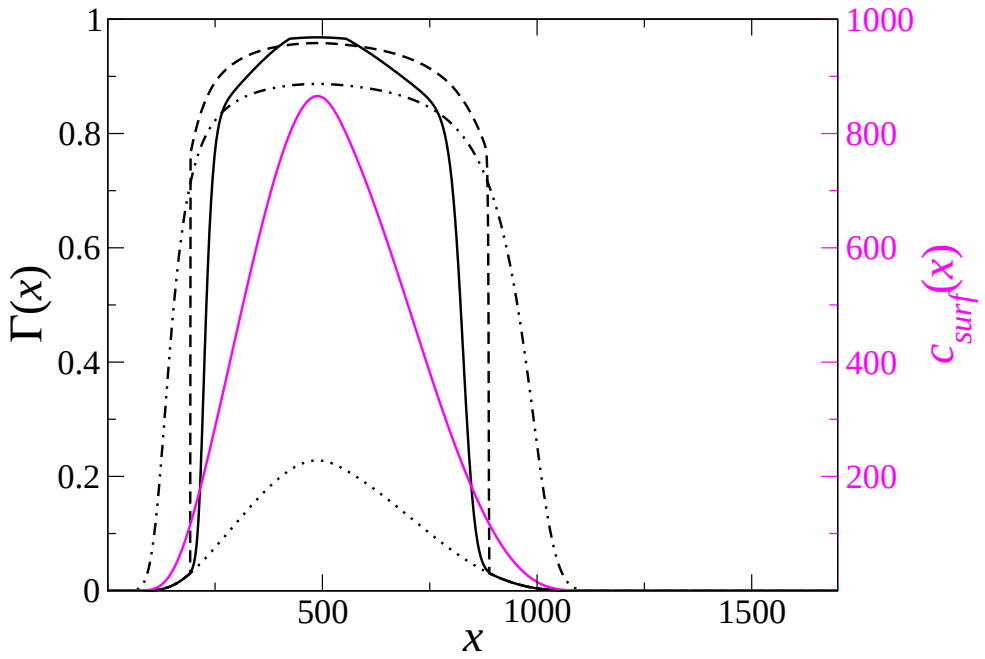

Figure 51: Concentration distribution along the x-axis for different adsorption conditions. The black color denotes the concentration distribution for the adsorbed tracers. The dotted, dashed-dotted, dashed, and solid black lines denote the adsorbed amount $\Gamma(x)$ for the Henry, Langmuir, Henry-Langmuir and Henry-Cooperative Langmuir adsorption models, respectively. The pink solid line corresponds to the surface concentration distribution along the x-axis. The systems considered are characterized by Peclet number $\mathrm{Pe} = 100$ and initial concentration $c_0 = 1000$.

In this paragraph, we study the time evolution of the free and adsorbed concentrations in the slit pore geometry for the cooperative adsorption model. Fig. 52(a), which shows the free concentration distributions, indicates that the concentration in the channel increases for $t \leq \Delta t_0$ (where Δt_0 is the end of the injecting step). Then at longer times, i.e. $t = 2 \times 10^6$ and $t = 4 \times 10^6$, the free molecules are more homogeneously distributed within the pore geometry with smaller local concentrations. Due to the small adsorption/desorption ratios (k_H, k') considered here, the influence of adsorption on the free concentration distribution is negligible. We also looked at the distribution of adsorbed molecules $\Gamma(x)$ along the x-axis as well as the normalized concentration $c_l(x,t)$ for these adsorbing conditions. We also compare these results with those obtained with the Henry-Langmuir model in Fig.52(b). The two data sets perfectly overlap – see data for $c_l(x,t)$ – at the different times, therefore confirming that the difference between the two models is insignificant when examining the free molecule concentration (particularly in the case of small adsorption/desorption ratios). Nonetheless, the comparison of $\Gamma(x,t)$ re-

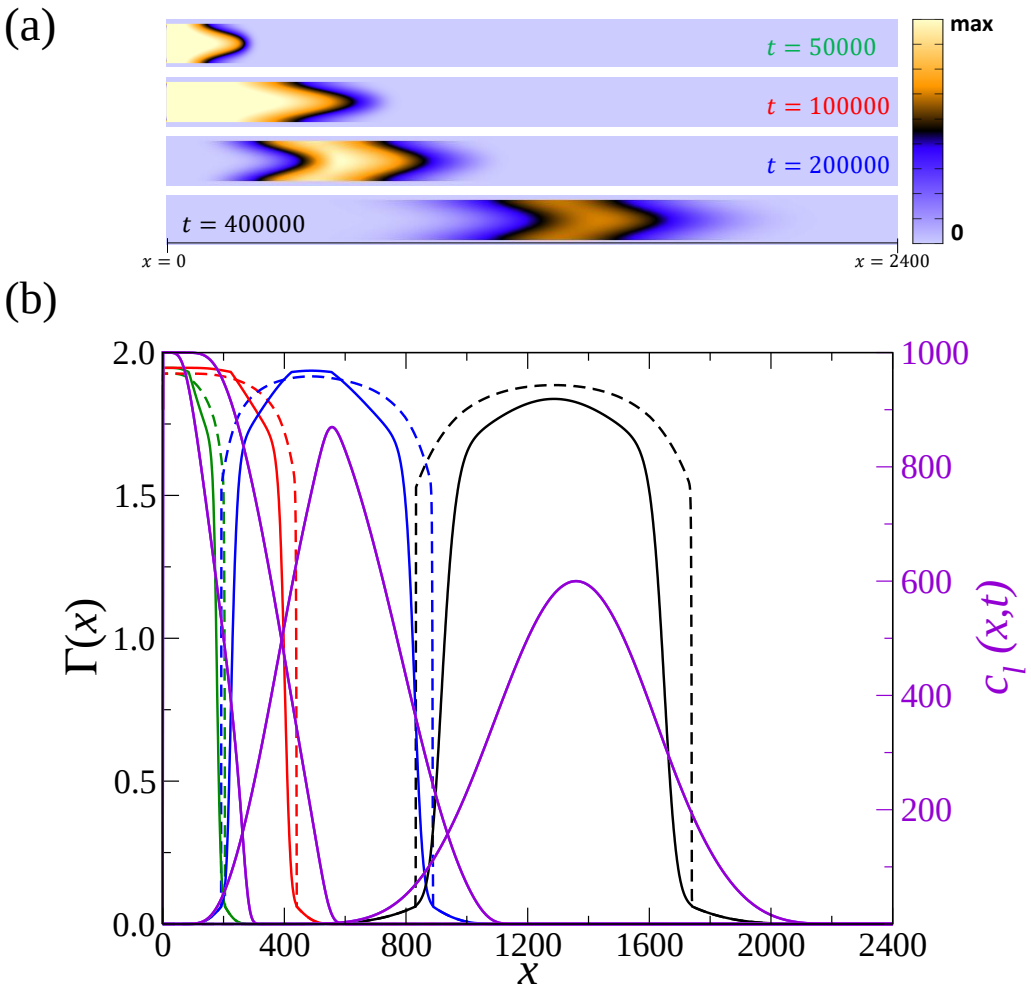

Figure 52: (a) Concentration distribution for the free tracer dispersion in a pore corresponding to a two parallel plates geometry and for molecules adsorbing according to the Henry-Cooperative Langmuir adsorption isotherm at different times. (b) Concentration distribution along the x-axis. The concentration of the adsorbing tracers Γ corresponds to the solid lines for the Henry-Cooperative Langmuir adsorption isotherm while the dashed lines correspond to the same system but for a Henry-Langmuir adsorption isotherm. The green, red, blue and black colors denote the following times: $t = 5 \times 10^4$, $t = 10^5$, $t = 2 \times 10^5$, and $t = 4 \times 10^5$. The normalized concentration distributions at a lateral position are shown as violet solid lines. The system corresponds to a flowing liquid in which continuous injection at $x_0 = 1$ of an initial concentration $c_0 = 1000$ is performed over a time period $\Delta t_0 = 10^5 \Delta t$ (Pe = 100).

veals remarkable differences which can be seen when considering the adsorption of aggregated monomers. In addition, one notices that $\Gamma(x)$ reaches its maximum value for the two systems at times shorter than Δt_0, i.e. $t = 5 \times 10^4$ and $t = 10^5$. This result is due to the fact that, before the end of the injection stage, the surface concentration is important near the channel inlet so that the maximum adsorption capacity is reached. However, at longer times, the free tracer concentration is more dispersed/homogeneous (lower local concentration at the pore surface) so that the adsorbed quantity decreases.

B. Transport in porous media: impact of pore geometry

As outlined in the introduction, one of the main objectives of this work is to investigate the influence of structural heterogeneity of porous media on transport and the associated impact on adsorption in this type of containment. To this end, in this section we examine the influence of complex pore geometries on the displacement and the concentration field of the molecules. We consider a 2D porous medium based on a realistic porous structure developed at IFPEN. The results will be compared and contrasted to those obtained with a parallel plates geometry. This section will be divided into 4 parts. First, we will characterize the porous medium; secondly, simulations will be carried out to generate Stokes flow in the structure. Afterwards, we will study the transport of non-adsorbing molecules and finally we will consider the transport of adsorbing molecules. As far as adsorption is concerned, we will examine Henry and Langmuir's models. Since we use the Dirac injection configuration, we will not examine the cooperative adsorption model. Indeed, as indicated in the previous section, for this configuration, the bulk concentrations are very low, which characterizes the individual monomers that follow Henry's adsorption model. Therefore, the study of the cooperative model will give the same outcome as Henry adsorption model.

1. Porous medium: 2D micromodel

1.1. Micromodel manufacturing

A micromodel is an idealized, two-dimensional representation of a porous medium: a network of connected pores, through which fluids flow and solutes spread. Micromodels used at IFPEN are manufactured using a chemical etching technique called "wet etching". They consist of a first transparent glass plate, on which is engraved a set of intersecting channels forming a network, and a second transparent glass plate installed on the engraved face of the first glass plate. The glass has more affinity with water, thus it is considered as water wet. The micromodel is based on a 2D slice of rock obtained by X-ray tomography. In order to obtain better percolation, the X-ray image was slightly modified.

1.2. Micromodel for LBM simulation

We use the 2D porous geometry shown in Fig. 53.a. Each pixel from the micromodel image is considered as one lattice, i.e. 1 pixel $= \Delta x$. The micromodel has dimensions $L_x = 4000\Delta x$ and $L_y = 2300\Delta x$, and its porosity is $\phi = 49.47\%$, the porosity per slice varies between 35% and 65% as illustrated in Fig. 53.b.

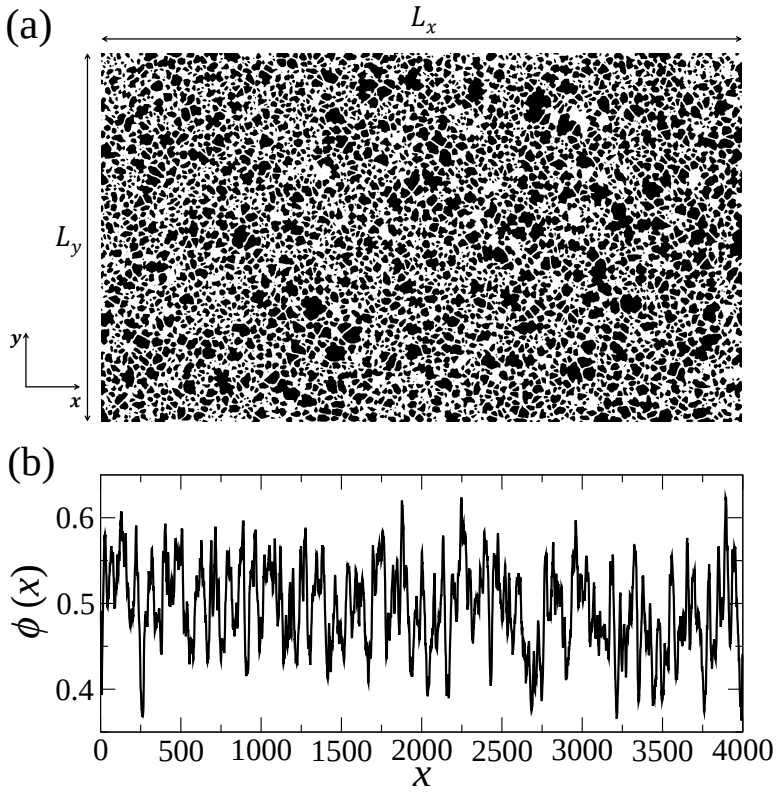

Figure 53: (a) Micromodel image with width L_x and length L_y, the color black presents the solid and the white stands for the pore volume. (b) Porosity distribution across lateral positions x in the geometry of the micromodel, i.e. the fraction of pore volume relative to total volume – pore and solid – for each x, where x is in Lattice Boltzmann length unit (Δx).

2. Stokes Simulation results

We used the Lattice Boltzmann method to solve the steady-state Stokes equation for water flow in the micromodel. In the 2D porous medium, fluid velocities are small (i.e., Re $<<$ 1), justifying the use of the Stokes equation to obtain the velocity field at the pore scale. Along the $y = 0$ and $y = L_y$ boundaries of the 2D domain, no-slip boundary conditions were imposed. A fixed pressure difference was applied between the inlet ($x = 0$) and the outlet ($x = L_x$) in accordance with the definition provided in Eq. (II .6) in chapter 2. We present the resulting velocity field

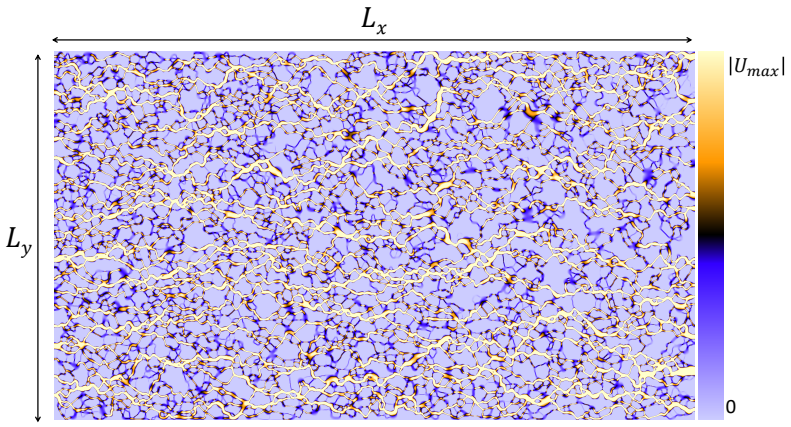

Figure 54: Velocity field obtained by solving Stokes equation using LBM-TRT in the micro-model ($L_x = 4000$ and $L_y = 2300$).

in Fig. 54. The flow goes from the left inlet to the right outlet, and it shows a complex pattern. Various variations in the velocity field due to the heterogeneity of the porous medium can be observed, leading to some preferential paths.

3. Transport of passive tracer

In this paragraph, we simulate passive tracer (non-adsorbing molecules) transport in the micro-model. We consider the simulation process illustrated in Fig. 26.c in chapter 4. Our geometry is exposed to a fluid flow that obeys Stokes flow with an average flow rate U.We impose an initial concentration c_0 at each fluid site placed at the lateral injection position x_0. As illustrated in Fig. 55, for a bulk position $\mathbf{r}_0 = (x_0, y)$, we apply $c(\mathbf{r}_0) = c_0$ within $\Delta t_0 = \Delta t$ (Dirac injection). For our system, we apply initial concentration $c_0 = 10$ at lateral injection position $x_0 = 200$. This system is characterized by Peclet number $\mathrm{Pe} = 100$.

In Fig. 56, we present the normalized evolution of the derivative of the displacement variance over time, defined as $D(t)/D_m = \frac{1}{2D_m}\frac{\partial \sigma_x^2(t)}{\partial t}$, with σ_x^2 being the variance of the displacement distribution in the x-direction. It shows different regimes: at the beginning, a diffusive regime, where the values of $D(t)/D_m$ are almost constant, $D(t) \sim D_m$. Then, we have a transient regime: the advection-dominated regime where $D(t)/D_m$ increases significantly. In the interval $[t_3, t_5]$, we have a plateau-like pattern with oscillating values. For higher time intervals, $D(t)/D_m$ in-

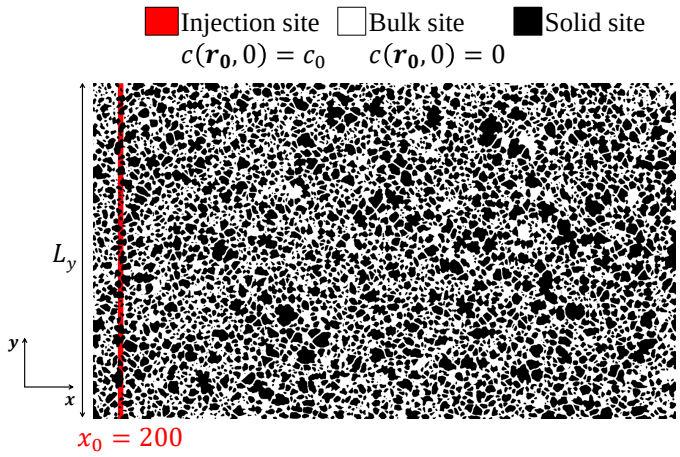

Figure 55: Initialization ($t = 0$) of the tracer concentration in the micromodel geometry.

creases. This behavior can be attributed to the influence of the no-slip boundary condition applied at $y = 0$ an $y = L_y$ and to the heterogeneity of the porous medium that affect the velocity field. Consequently, the transport becomes very complex in this situation. The sinusoidal behavior and the following increase in $D(t)/D_m$ should therefore be further analyzed. It is actually attributed to the insufficient size of the micromodel in comparison to its heterogeneity and the boundary effects. An in-depth discussion to explain these effects is presented in Appendix D.

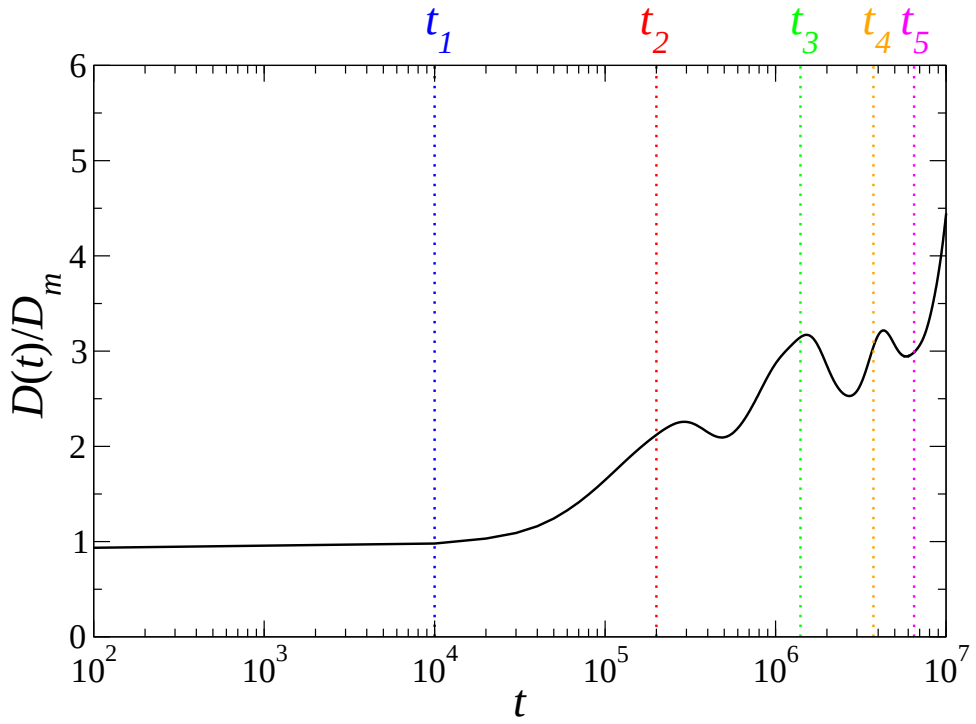

Figure 56: Temporal evolution of the time derivative of the displacement variance $D(t) = d\sigma_x^2(t)/2dt$ in the micromodel geometry for the transport of the passive tracer. $D(t)$ is normalized by the molecular diffusion coefficient D_m of the free tracer molecules. The system is characterized by Pe = 100.

In order to better understand the transport in the 2D porous medium, we study the normalized propagators $P((x-x_0)/Ut,t)$ as well as the concentration distributions at different time intervals in the geometry. The propagators are presented in Fig. 57. For each propagator, we plot the corresponding concentration distribution. The concentration distribution shows the spreading of the molecules in the geometry over time. The different panels denote the diffusion, the advection and the dispersive regime, respectively. The tracer molecules passe through the pores of the micromodel and they disperse gradually. The distribution is affected by the heterogeneity of the structure. Moreover, the dispersed front is delayed along the y-axis boundary, which

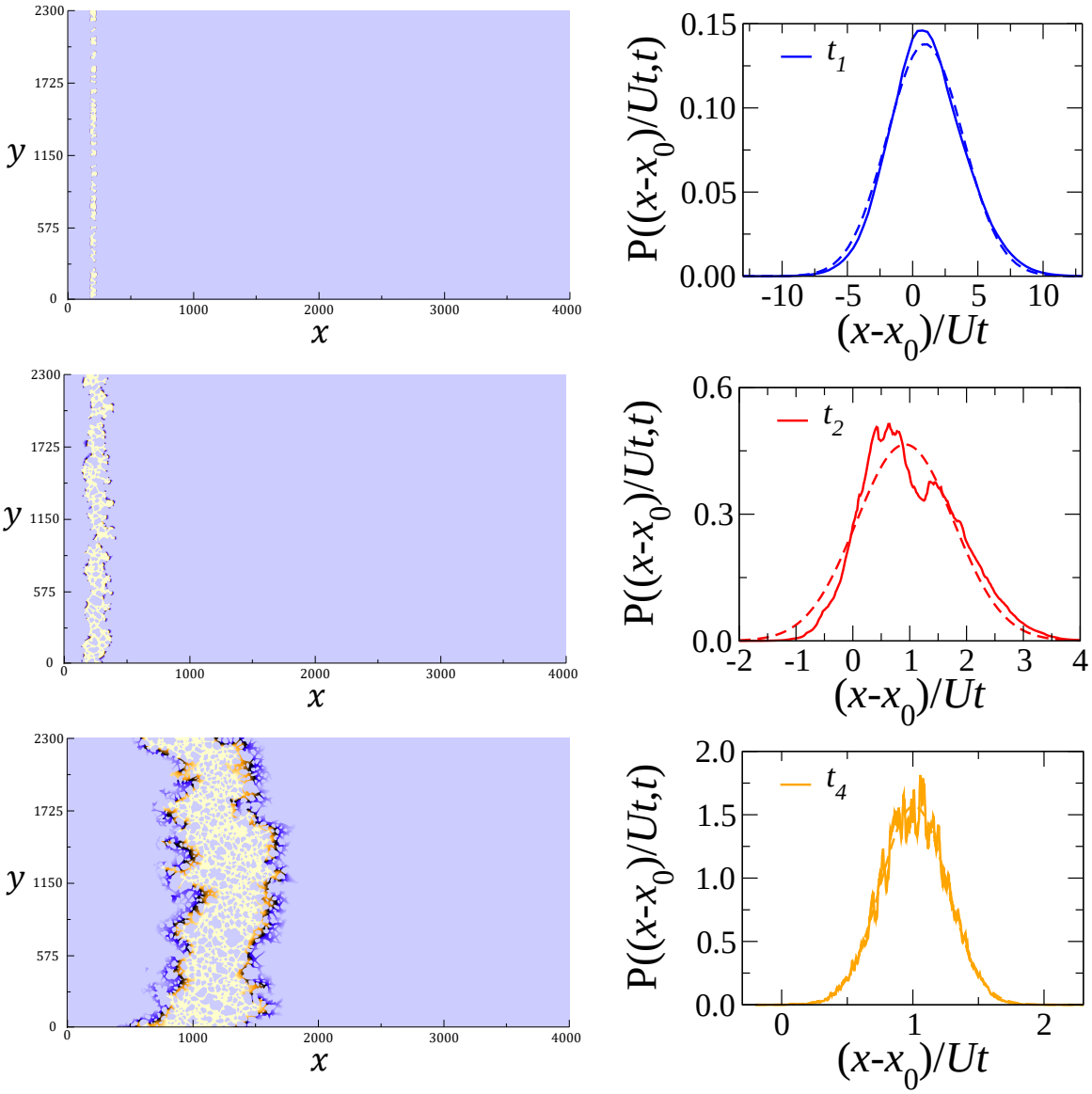

Figure 57: Normalized propagators $P((x-x_0)/Ut,t)$ for different time intervals as well as the respective concentration distributions for the passive tracer transport in the micromodel ($P_e = 100$). The solid lines stand for the simulation results and the dashed lines represent the corresponding Gaussian fit.

is due the no-slip boundary condition applied to the Stokes flow. The normalized propagator $P((x-x_0)/Ut,t)$ varies between two limiting behaviors in the short and long time range: in the short term (t_1), molecular diffusion predominates over advection. At long term (t_4), molecules have sampled a representative part of the velocity field, resulting in effective dispersion. In both cases, the shape of the propagators is similar to a Gaussian curve. We fit these propagators using the Gaussian equation, which is shown with the dashed lines. These propagators have a maximum moving on the x-axis with a mean velocity. For the diffusion dominated regime (t_1), the mean velocity is close to zero. For a pure diffusive regime the mean velocity equals zero, however we don't have access to these data since the pure diffusive regime ends after an extremely short time interval. Considering the dispersive regime (t_4), the data are well adjusted with the Gaussian equation, and the mean velocity is $U = 1$. At intermediate time intervals (t_2) in the so-called advective regime, displacements due to the velocity are dominant and the propagator is different from the Gaussian curve. We justify the noisy form of the propagators particularly at large time intervals by the influence of the heterogeneity of the porous medium.

4. Transport of adsorbing molecules

In this paragraph, we consider the transport of adsorbing molecules. To this goal, we use the Henry and the Langmuir adsorption model. We first study the influence of the adsorption desorption ratio on the transport of molecules following the Henry adsorption model and then we investigate the difference between these results and those obtained with the Langmuir model.

4.1. Henry adsorption

In a first step, we simulate the transport of molecules following Henry's adsorption model with different values of the adsorption parameter k_H. We perform the same Dirac injection configuration as the one used for the transport of the passive tracer (non-adsorbing molecules). An initial concentration $c_0 = 10$ is injected at the lateral position $x_0 = 200$. The Peclet number is $\mathrm{Pe} = 100$. Simulations with the following value of k_H are performed: $k_H \in \{0.1, 1, 5, 10\}$. More in detail, a constant adsorption rate $p_A = 0.05$ is used and the desorption rates correspond to $p_D = 0.5$, 0.05, 0.01, 0.005 respectively). The results are compared to those obtained for the passive tracer and to those obtained in the parallel plates geometry.

We present in Fig. 58, the evolution of $D(t)/D_m$ of the transport of adsorbing molecules following Henry's model. The result shows that the temporal evolution of $D(t)/D_m$ for these adsorbing molecules is similar to the one of the non-adsorbing molecules. For a short period, diffusion dominates, characterized by the initial plateau. Then $D(t)/D_m$ increases, which indicates the advective regime. For longer time intervals, a slight stabilization of $D(t)/D_m$ might be observed. For $k_H = 0.1$, we obtain the same result as for the non-adsorbing molecules, which is justified by the fact that the adsorbed quantity is too small to influence the behavior of the molecules in the bulk. It can be noticed that $D(t)/D_m$ decreases with increasing the values of k_H.

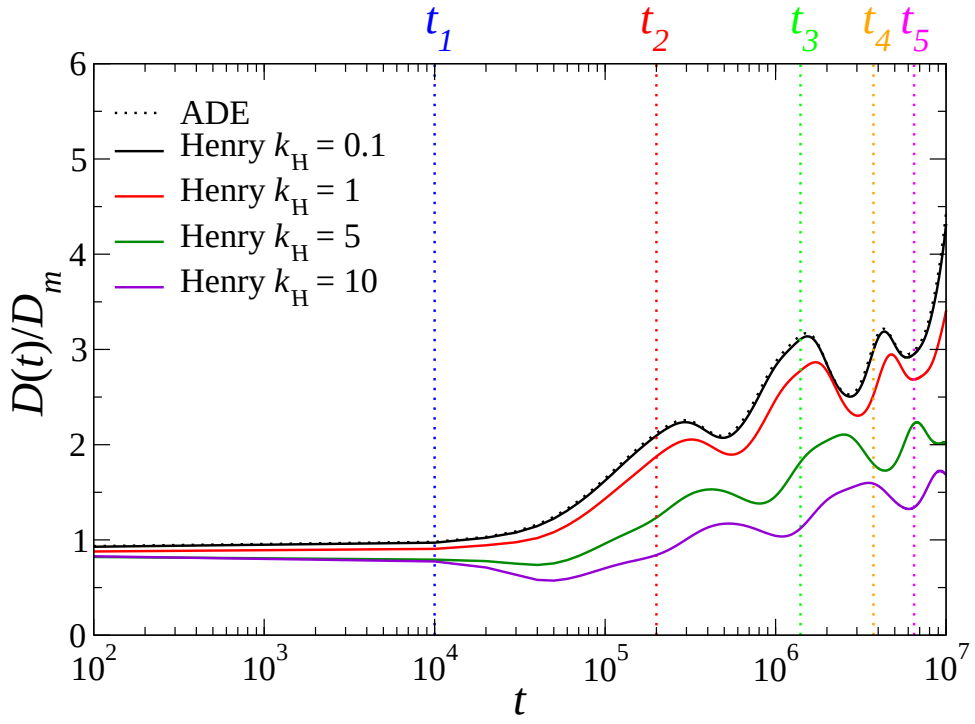

Figure 58: Temporal evolution of the time derivative of the displacement variance $D(t)$ in the micromodel geometry for the transport of molecules following the Henry adsorption model (Pe = 100). $D(t)$ is normalized to the molecular diffusion coefficient D_m of the free tracer molecules. The dotted line denotes the non-adsorbing molecules and the solid lines denote the molecules following the Henry adsorption model. The black, red, green and violet colors denote respectively $k_H = 0.1$; $k_H = 1$; $k_H = 5$ and $k_H = 10$.

This result is justified by the study we made in the two parallel plates geometry where we also investigated the evolution of $D_{eff}^{ads}/D_m = \lim_{t\to\infty} D(t)/D_m$ as a function of k_H (see section.. A.1.2. and Fig. 43). The study showed that the result depends on the channel width. By decreasing the distance between the two parallel plates, the range of k_H where $\frac{\partial}{\partial k_H}\frac{D_{eff}^{ads}}{D_m} < 0$ becomes larger. In this range D_{eff}^{ads}/D_m decreases as function of k_H. For the structure of the micro-

model, the characteristic channel width of the pores ranges from $2\Delta x$ to $20\Delta x$ with a mean value of $10\Delta x$. Using the exact value of U and D_m ($U = 2.915\ 10^{-4}\Delta x/\Delta t$; $D_m = 3.125\ 10^{-3}\Delta x^2/\Delta t$), the result gives a strictly negative derivative and therefore $D(t)/D_m$ decreases as a function of k_H. By comparing the result of the micromodel with the result of the parallel plates, a second effect can be detected contributing to the decrease of $D(t)/D_m$ with increasing k_H in the porous structure. Indeed, adsorption on solid surfaces perpendicular to the flow might hinder the transport and the spreading of the molecules and thus reduce the displacement variance σ_x^2. This is not the case for parallel plates where there are no surfaces to adsorb in this direction.

We present in Fig. 59, the temporal evolution of the total concentration distribution, i.e. $c(\mathbf{r},t) + c_a(\mathbf{r},t)$ in the micromodel geometry for different adsorption rates: $k_H \in \{0.1, 1, 10\}$. We recall that $c(\mathbf{r},t)$ is the free tracer concentration distribution and $c_a(\mathbf{r},t)$ is the adsorbed tracer distribution. For $k_H = 0.1$, the transport is only slightly different from the transport of non-adsorbing molecules. However, a strong influence of the adsorption on the transport can be seen for $k_H = 5$ and particularly for $k_H = 10$. Several differences can be observed:

• First of all, we find that stronger adsorbing molecules lead to a slower mean displacement of the molecules compared to weaker adsorbing molecules. Therefore, the increase in the value of k_H yields a lower propagation rate.

• Then, the comparison of the concentration distribution of the free molecules of the passive tracer with that of the adsorbing molecules shows that adsorption leads to a narrower distribution. Furthermore, this distribution becomes narrower with the increase of k_H. This is consistent with the evolution of $D(t)/D_m$, where the plateaus become lower for higher k_H.

• Third, we note that increasing k_H increases the amount of adsorbed molecules. To better visualize the difference in the amount of adsorbed molecules at the fluid-solid interface, we show in Fig. 60, a zoom on the concentration distribution. For $k_H = 0.1$, the adsorbed quantity is too small to be correctly visualized. For $k_H = 1$, it is of the same range as the concentration of the free molecules. Here, the adsorbed quantity can be seen lining the solid/liquid interface. For $k_H = 10$, with regard to the scale of concentration, we can see that the concentration of the adsorbed molecules is higher than the concentration of the molecules in the bulk. This result is due to the definition of Henry's model, which leads to an adsorbed quantity equal to $k_H c(\mathbf{r},t)$

without maximal surface saturation, and thus $c_a(\mathbf{r},t)$ is not limited by a maximum adsorption value.

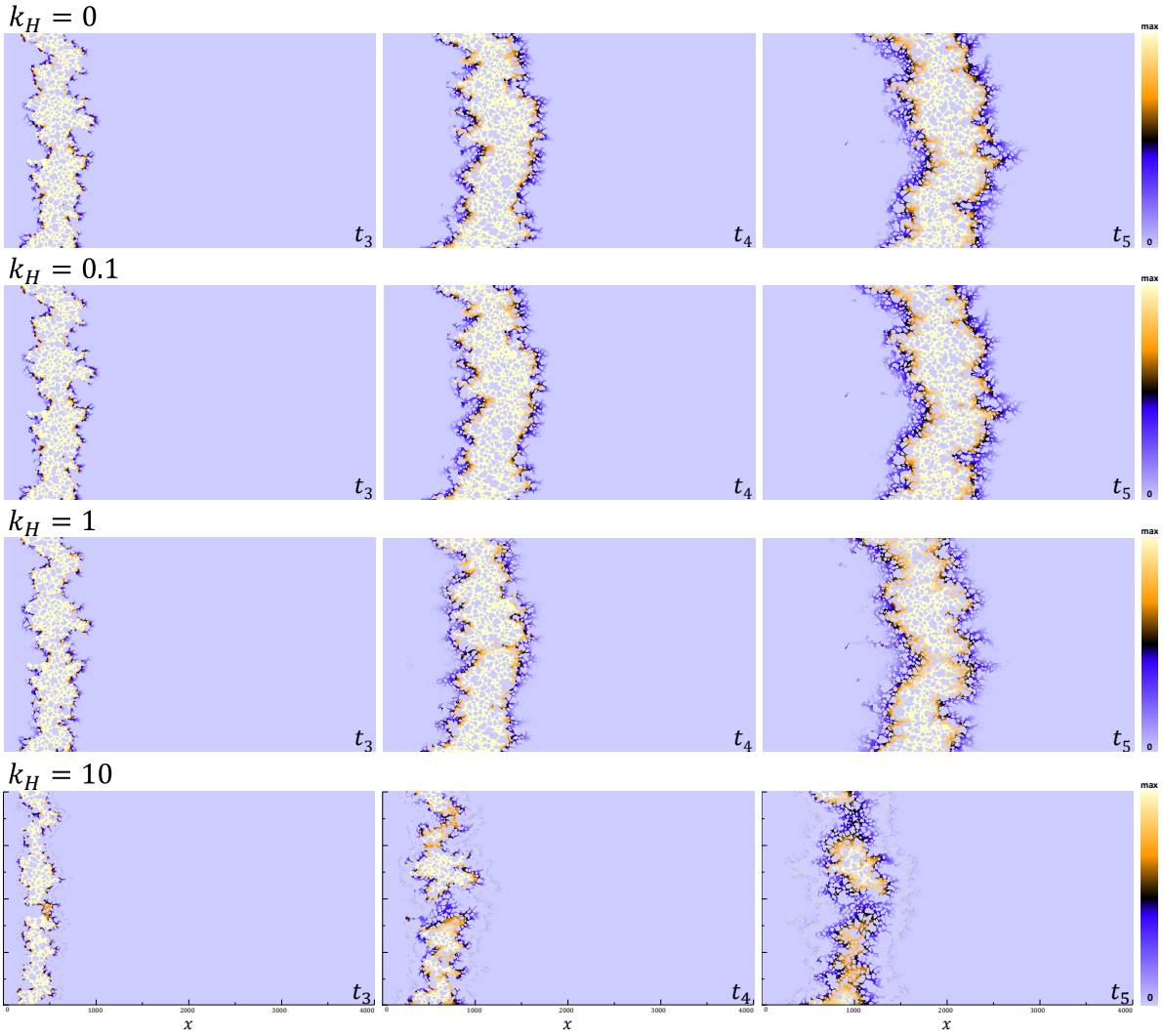

Figure 59: Concentration distribution of free and adsorbed molecules in the micromodel geometry for different time intervals (t_3; t_4 and t_5) with Pe $= 100$ for different adsorption desorption ratio $k_H = 0.1$, 1 and 10 in comparison to the non-adsorbing molecules.

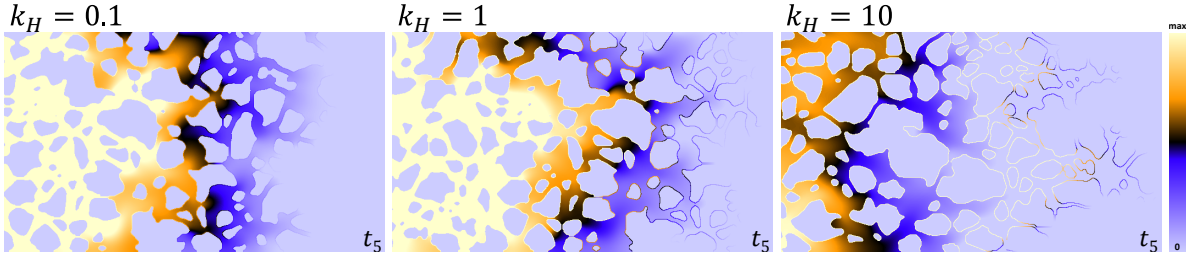

Figure 60: Zoom on the concentration of free and adsorbed molecules in the geometry of the micromodel for t_5, for different adsorption-desorption ratios $k_H = 0.1$, 1 and 10 (Pe $= 100$). The adsorbed concentrations are located at the solid/fluid interface. They are clearly identifiable for $k_H = 1$ and $k_H = 10$, however for $k_H = 0.1$, the adsorbed quantity is very small and therefore difficult to visualize.

We present in Fig. 61, the normalized propagators of the transport of molecules following the Henry adsorption model for $k_H = 10$ and compare the results with the simulation of non-adsorbing molecules transport. In this paragraph, we refer to the propagators for the free molecules in the bulk by P_{free} (presented with the colored solid lines) and by P_{total}, the propagators for all molecules (free and adsorbed), presented by the colored dashed-dotted lines. For small time t_1, the shape of the propagators P_{free} is relatively close to the Gaussian curve, which

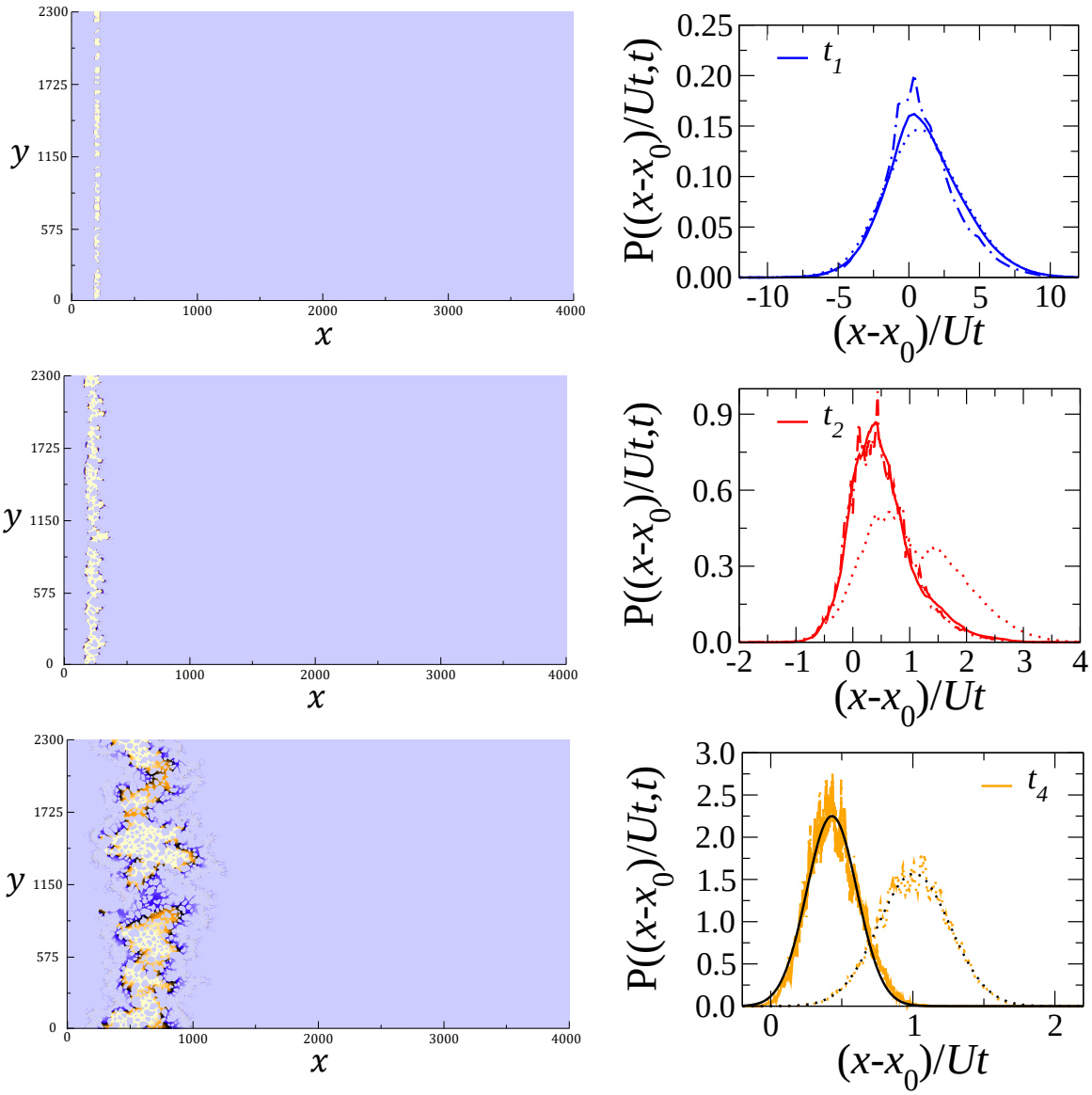

Figure 61: Normalized propagators $P((x-x_0)/Ut,t)$ at different times as well as the respective concentration distribution for the Henry adsorbing molecules ($k_H = 10$) and for $P_e = 100$. The colored dotted line denotes the non-adsorbing molecules result and the colored solid line denotes the result for the Henry adsorbing model when considering the free tracers P_{free} and the colored dashed-dotted line is for the Henry adsorbing model when considering all the molecules (free and adsorbed) P_{total}. The black color denote the Gaussian fit of the propagators (non-adsorbing molecules and adsorbing molecules) at the dispersive regime.

characterizes the end of the diffusion dominated regime. However, the shape of P_{total} is different. For the intermediate time t_2, P_{free} and P_{total} are both different from the Gaussian curve. For t_4, P_{free} and P_{total} have a quasi-Gaussian profile and the curves overlap. This can be explained by the fact that all molecules have sampled a representative volume of the porous medium and almost all molecules have been adsorbed and desorbed on the surfaces. By comparing the propagators of the non-adsorbing molecules with the propagators of the adsorbing molecules, the latter give curves of the same form, i.e. having a Gaussian profile, which characterizes the dispersion regime for the adsorbing molecules. In addition, this propagator has a delay on the x-axis which proves that adsorption delays the transport of the molecules.

4.2. Langmuir adsorption

In this paragraph we consider the transport of adsorbing molecules following the Langmuir model. We concluded in the first section of this chapter that in order to have a difference between the transport of the Langmuir and Henry adsorbing molecules, a high adsorption-desorption ratio should be considered. Therefore, we study the transport of the Langmuir adsorbing molecules with two adsorption-desorption ratios: $k_L = 0.1$ and $k_L = 10$. More in detail, we use a constant adsorption rate $p_A = 0.05$ and the desorption rates correspond to $p_D = 0.5$ and $p_D = 0.005$, respectively. We perform the same simulation as in the previous paragraph using the Dirac injection where we inject an initial concentration $c_0 = 10$ at the lateral position $x_0 = 200$.

We present in Fig. 62, the normalized derivative of the displacement variance over time $D(t)/D_m$ for different adsorption desorption ratio for the Henry and Langmuir adsorption models and compare the results with the non-adsorbing molecules results. As can be seen, for $k = 0.1$, the results for the transport of the molecules following the Langmuir and Henry adsorption models are very similar and the curves of $D(t)/D_m$ overlap the curve of the non-adsorbing molecules. It demonstrates that for a low adsorption/desorption ratio, the effect of adsorption is very small and does not affect transport in the bulk. However, for $k = 10$, $D(t)/D_m$ of the molecules following the Langmuir adsorption model is higher than $D(t)/D_m$ obtained with the

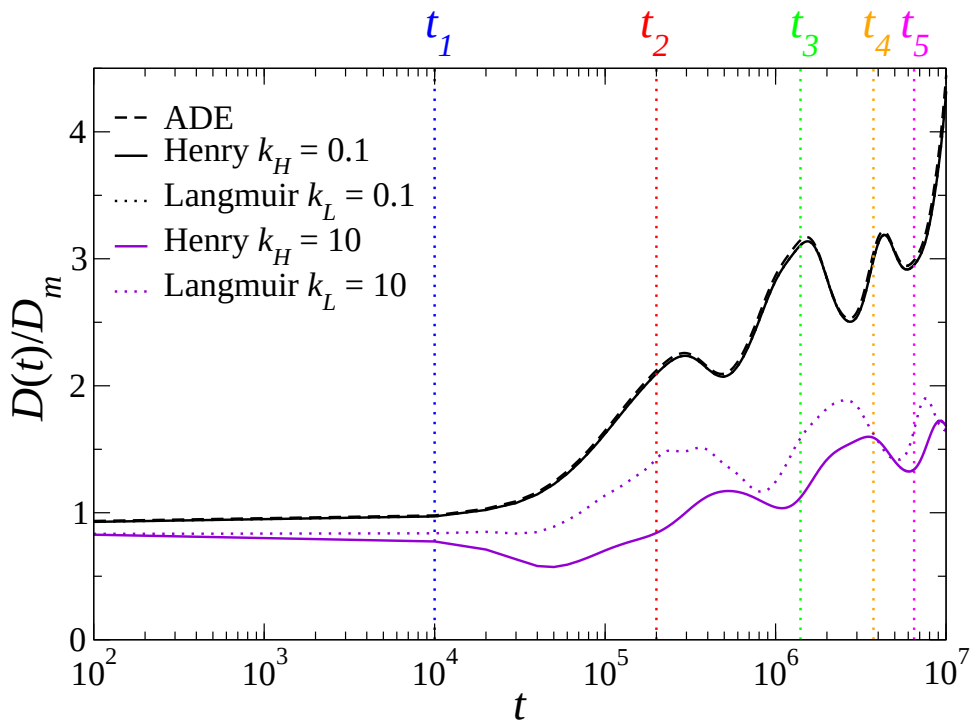

Figure 62: Time evolution of the time derivative of the displacement variance $D(t)$ for Pe $= 100$ in the micromodel. $D(t)$ is normalized to the molecular diffusion coefficient D_m of the free tracer molecules. The dashed lines denote the non-adsorbing molecules, while the dotted and the solid lines present respectively the Langmuir adsorbing molecules, and the Henry adsorbing molecules. The colors black and violet denote respectively ($k = 0.1$ and $k = 10$).

Henry model. This reflects that the molecules obeying the Langmuir adsorption model are more dispersed than those obeying the Henry adsorption model. This result is due to the the surface saturation feature of the Langmuir adsorption model ($\Gamma^{\infty} = 1$). Therefore, the concentration of the adsorbed tracer $c_a(\mathbf{r},t) = \Delta x \Gamma(\mathrm{r},t)$ is limited whereas Henry adsorption model does not present a maximum surface saturation, and we have $c_a(\mathbf{r},t)$ proportional to $k_H c(\mathbf{r},t)$. For $k_H = 10$, this leads to a higher concentration of the free molecules following Langmuir adsorption model compared to those following Henry adsorption model and consequently higher value of $D(t)/D_m$.

In order to better understand the transport of the molecules following the Langmuir adsorption model, we present in Fig. 63, the normalized propagators $P((x-x_0)/Ut,t)$ at different time intervals and the corresponding total concentration distribution $(c_a(\mathbf{r},t)+c(\mathbf{r},t))$ in the micromodel geometry. We present the propagators using the free tracer concentration $c(\mathbf{r},t)$, namely P_{free} and compare the results to those obtained with the Henry's adsorption model for

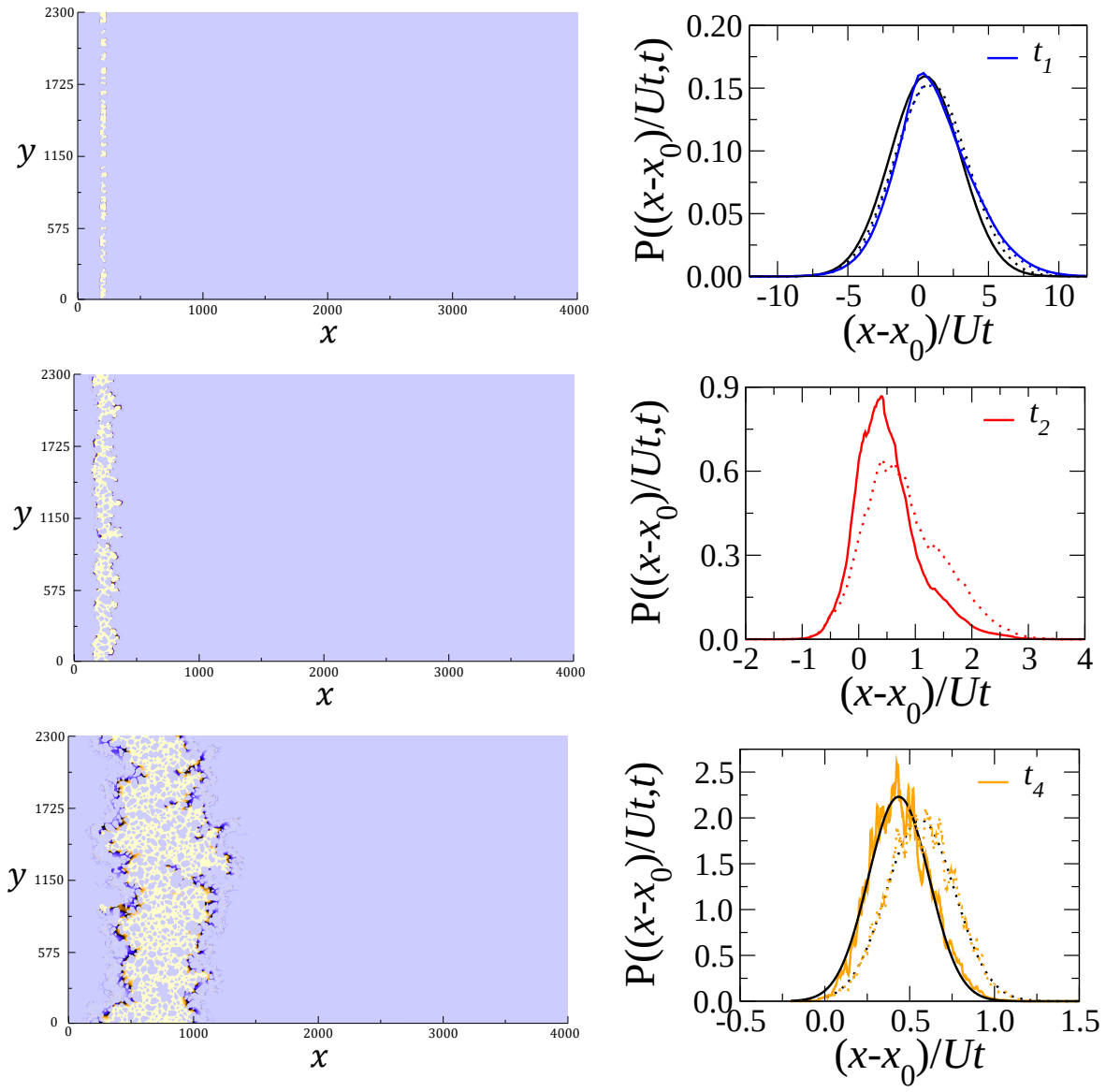

Figure 63: Normalized propagators $P((x-x_0)/Ut,t)$ for the free tracer concentration $c(\mathbf{r},t)$ at different times as well as the respective concentration distribution for the Langmuir adsorbing molecules ($k = 10$) and for Peclet number $P_e = 100$. The colored solid and dotted lines denote the molecules following respectively the Henry and the Langmuir adsorption models. The black color denotes the Gaussian fit at the diffusive and dispersive regimes.

$k_H = 10$. The results show the typical transport regimes. At small and large time intervals, we have a nearly Gaussian profile, which characterizes the diffusive and dispersive regimes. For the dispersive regime, t_6, we present in the black color the Gaussian fit of the propagators to confirm the results. For intermediate time intervals, we have a non-Gaussian profile, which characterizes the advective regime. When we compare the propagator profiles obtained with the Henry and Langmuir models, the main difference lies in the advective and the dispersive regimes. For the advection-dominated regime, at t_2, we notice that the curve of the propagator

obtained with the Langmuir adsorption model is larger and the peak is lower. This reflects that the molecules in the bulk, following the Langmuir adsorption model, have higher concentration compared to those obtained following the Henry adsorption model. In the dispersive regime, the propagator corresponding to the Langmuir model has a lower peak. We also note that the mean displacement velocity is higher, i.e. the displacement of molecules for the Langmuir model are dispersed at a faster rate compared to the molecules following the Henry adsorption model. This is caused by the difference in the maximum adsorbed quantity. The Langmuir model has a limit of Γ^{∞}, while the Henry model gives an adsorbed concentration that is proportional to $k_H c(\mathbf{r},t)$. The initial concentration injected at t_0 is the same for both systems as well as the adsorption ratio $k_H = k_L = 10$. However, the Langmuir model has a maximum surface saturation defined by $\Gamma^{\infty} = 1$. The Langmuir adsorption leads to lower adsorbed quantity and thus higher bulk molecules compared to the result of the Henry model. Accordingly, the displacement of molecules in bulk for the Langmuir model is widespread.

To better visualize the difference between the two adsorption models, we present in Fig. 64 the evolution over time of the total concentration distribution $(c_a(\mathbf{r},t)+c(\mathbf{r},t))$ in the dispersive regime (in the time interval $[t_3,t_5]$). The comparative study shows that molecules in the bulk are more dispersed using Langmuir's model than by using Henry's model. Moreover, it can

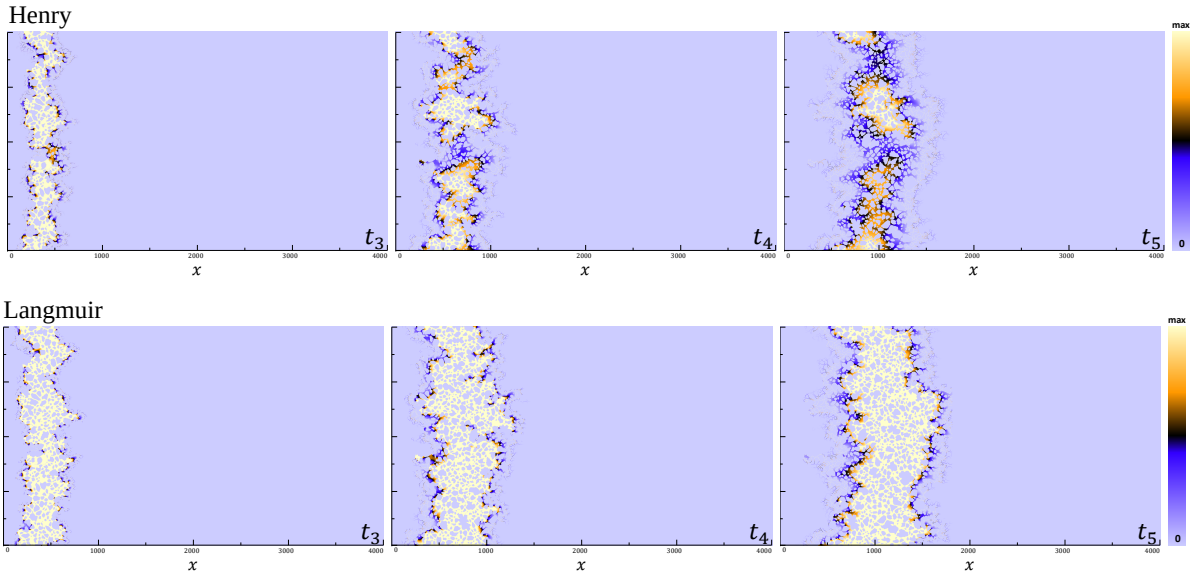

Figure 64: Concentration fields in the porous geometry at different time slots (t_3; t_4 and t_5) for $\mathrm{Pe} = 100$.

be observed that the concentration of the adsorbed tracer, at the solid/fluid interface, is higher in the Henry adsorption model than in the Langmuir model. This result is consistent with the comparison we have carried out for normalized propagators.

Chapter Conclusion

In this chapter, we have studied the influence of adsorption kinetics on tracer transport. The results of the parallel plate geometry showed that when the adsorption-desorption ratio is low, the adsorption has an insignificant effect on the transport. However, when using a higher value, it modifies the transport behavior. For the Henry's adsorption mechanism, a high value of the adsorption-desorption ratio k_H, causes a larger displacement and leads to over-adsorption (a peak on the curve of $D(t)/D_m$). For the Langmuir model, the results showed the importance of the initial concentration value. A high initial concentration value modifies the transport regimes, where the advection regime occurs in two steps which are separated by an additional stationary regime: Taylor dispersion regime. Considering the results of the micromodel geometry, they showed that the transport in this porous structure is strongly affected by the heterogeneity of the structure, it highlights a sinusoidal dispersive regime. Regarding the adsorption simulations, the adsorption reduces the displacement variance since the latter is hindered by the adsorption in the small pores. The displacement variance decreases with increasing the values of the adsorption desorption ratio. This result goes along with the analytical studies available, where the range in which $\frac{\partial}{\partial k_H}\frac{D(t\to\infty)}{D_m}$ is negative, becomes larger when considering smaller channel width. For our case, the characteristic channel width of the pores in the micromodel has a mean value of $10\Delta x$, which leads to strictly negative derivative and therefore $D(t)/D_m$ decreases as a function of k_H. For the Langmuir adsorption model, where a maximum surface saturation is defined, the transport leads to a more important molecule spreading compared to the transport of molecules following the Henry adsorption model.

General conclusion

Surfactant adsorption is a complex process involving different phenomena that resist existing frameworks. In particular, typical surfactant adsorption isotherms – like for other complex fluids – display features that cannot be described using simple thermodynamic models (e. g. Henry, Langmuir). Therefore, novel adsorption modeling that captures surfactant adsorption processes, including monomer adsorption and surface aggregation, from liquid solutions must be established. From a practical viewpoint, surfactant adsorption processes in industry are mostly used in in-flow applications. Understanding the interplay between surfactant transport and adsorption is therefore of utmost importance. In order to address these important issues, the present manuscript reports different elements. First, we derive a simple phenomenological adsorption model which accounts for adsorption cooperative effects (from lateral interactions between adsorbed monomers to surface self-assembly into ordered or disordered mesoscopic objects). Second, we perform numerical simulations that provide key insights into the coupling between transport and adsorption kinetics of molecules in different pore geometries.

The Henry and Langmuir adsorption models are robust equations to describe a broad class of adsorbate/adsorbent systems. However, the adsorption of surfactants in a porous material leads to complex adsorption behavior such as the formation of micelles or vesicles. These effects are augmented by the heterogeneity of the surface which combines with cooperative effects that are inherent to such complex molecules. These rich phenomena are not captured using most available thermodynamic models. It is possible to model this complex adsorption behavior using effective approaches such as the stepped adsorption isotherm or the S-shaped adsorption isotherm. Yet, these simple models portray the adsorption of individual monomers that have accumulated to form a monolayer that eventually transforms into a more complex structure at the pore surface. As a result, they do not properly take into account the self-assembly

and lateral interactions that are inherent to surfactant adsorption. Although other models exist, they address each of these aspects individually. Within this thesis, we propose a cooperative adsorption model; it consists of a thermodynamic model that captures the collective behavior leading to complex kinetics and structural (re)arrangement upon surfactant adsorption. It takes into account both the lateral interactions between adsorbed surfactants and possible transitions between individual adsorbed monomers and self-assembled objects (i.e. ordered and disordered self-assemblies). Our model is therefore generic as it allows describing surfactant adsorption based on simple thermodynamic ingredients. More in detail, our model is based on two main ingredients. First, we use an occupancy parameter greater than one, which allows taking into account self-assembled objects. Second, both the adsorption and desorption coefficients depend on surface concentrations to account for the role of lateral interactions as a function of surface concentration. This allows accounting for either hindered or facilitated adsorption. The validity of this versatile model – which can be easily extended to any other complex fluids – is checked against available experimental data. Using this general approach, additional important information can be gained such as regarding the adsorption kinetics. In turn, such key insights allow better understanding the physics of surfactant adsorption. In particular, the exact dependence of adsorption and desorption rates on surface concentration allow unraveling the rich and complex kinetics observed in experimental results.

As for the second objective of this work, we investigate the interplay between surfactant adsorption kinetics and transport using the Lattice Boltzmann method within the Two Relaxation Time approach. This method ensures that accurate results are obtained for molecule transport in simple and complex pore geometries. We first demonstrate the numerical accuracy of this numerical framework by testing the influence of the number of nodes on the precision of the results for the transport of passive i.e. non adsorbing tracers. Then, to investigate the interplay between advection, diffusion and adsorption, we extend this numerical Lattice Boltzmann method to include tracer adsorption at the pore surface. In practice, this is achieved by adding a third step in the numerical algorithm; this additional step corresponds to a simple mass balance equation between the free and adsorbed tracer concentrations – with a detailed balance condition that is specific to the selected adsorption model. In our work, we specifically considered

the Henry and Langmuir adsorption isotherms but also the cooperative model developed in this thesis. The kinetics implementation is shown to verify ideal solutions such as those described using the Henry and Langmuir models (as it correctly predicts the adsorption isotherm $\Gamma(c)$ and its underlying adsorption kinetics $\Gamma(t)$). As an important extension, other simulations are carried out to study adsorption under dynamic conditions – i.e. under a flowing fluid. We evaluate the impact of adsorption on the free tracer propagators distribution by studying the displacement variance $\sigma_x^2(t)$ along the flow direction x. The latter measurement provides a direct estimate of the effective dispersion coefficient $D(t \to \infty)$ with $D(t) \sim d\sigma_x^2(t)/2dt$. In practice, we investigate the effect of the adsorption/desorption ratio k as well as that of the initial concentration c_0.

In the pore geometry, the dispersion of adsorbing molecules that obey the Henry adsorption model follows the same evolution for $D(t)/D_m$ as that for the non-adsorbing tracers. More in detail, the three following regimes are observed: diffusion, advection-dominated, and dispersion. Interestingly, the transport of adsorbing molecules leads to a dispersive regime with an effective dispersion coefficient that is larger than that for the non-adsorbing molecules. This is due to adsorption conditions at the surface of the parallel plate geometry which leads to an increase in the displacement variance $\sigma_x^2(t)$ in the x-direction (the flow direction). This result is in agreement with available analytical expressions – which can be derived for the Henry model – for the dependence of the dispersion coefficient on the adsorption/desorption ratio k_H. Moreover, k_H is found to significantly affect the observed transport regimes since large k_H yields an over-adsorption effect near the lateral injection position. The corresponding large adsorbed amount remains trapped at the surface over long residence times. In practice, this leads to the appearance of an additional step during the advection-dominated regime: the increase in the displacement variance $D(t)/D_m$ reaches a maximum before decreasing to its asymptotic value as adsorbed and free molecules get redistributed. To study the influence of surface saturation, we model the transport of molecules following the Langmuir adsorption model. The results show that the initial concentration c_0 has an important effect on the transport regimes. Moreover, we also found that this dependence on initial concentration is more pronounced as the adsorption/desorption ratio k increases. This effect arises during the advection regime, which extends over longer times with an increase in the value of the effective dispersion coefficient.

Using large $c_0 > 200$, the advection regime consists of two stages which are connected by a stationary regime. During the first stage, the distribution of free molecules is not affected by adsorption as we reach an intermediate stationary regime for $D(t)/D_m$; this regime corresponds to the Taylor dispersion regime. Then during the second stage, $D(t)/D_m$ increases until it reaches the dispersion regime with a value characteristic of the transport of the molecules adsorbing according to the Langmuir adsorption model. This effect is due to the strong contrast between the concentration of the adsorbed and free molecules. Overall, the number of free molecules is large compared to the number of adsorbed molecules (as the latter is limited to the value imposed by the maximum surface concentration $\Gamma^{\infty} = 1$). This adsorbed concentration does not affect the dispersion of the free molecules. However, at longer times, due to advection, the concentration of free molecules decreases so that the impact of adsorption kinetics becomes more important. The adsorbed molecules get redistributed by exchanging/desorbing with the free tracers until the dispersive regime for the transport of adsorbing molecules is attained. Using the cooperative adsorption model developed in this thesis, we also studied the influence of such a collective behavior at concentrations larger than the critical surface concentration c_s. Even for a large initial concentration c_0, with such cooperative adsorption, the bulk concentration decreases quickly after injection so that the surface concentration is always in the Henry regime (where only monomer adsorption occurs). To circumvent this issue, we perform simulations with continuous concentration injection. By monitoring the evolution of the different adsorbed amounts (isolated versus aggregated monomers) – $\Gamma_m(x,t)$ and $\Gamma_{m'}(x,t)$ –, we checked the accuracy/validity of of the kinetics implementation of the cooperative adsorption model in the LBM-TRT algorithm.

In the last part of this thesis, we performed Lattice Boltzmann simulations in a 2D porous medium to study the influence of structure heterogeneity on surfactant transport and adsorption. For such disordered materials, the Stokes flow simulation generates a complex velocity field exhibiting preferential paths. As for the surfactant transport, we first studied the dispersion of non-adsorbing tracers. The corresponding results do not reach a stationary regime even in the long time limit as a sinusoidal function is obtained for $D(t)/D_m$. Despite this variation, the propagator in this long time limit is close to Gaussian so that the dispersive regime can be characterized. As for the adsorption simulations, the transport of adsorbing molecules according to

the Henry and Langmuir adsorption models were performed. The normalized dispersion coefficient $D(t)/D_m$ for the two models resembles that obtained when considering transport for the passive i.e. non-adsorbing tracers. However, in contrast to adsorption in a simple parallel plate geometry, adsorption in realistic porous media leads to a decrease in $D(t)/D_m$ compared to its counterpart for the passive tracers. This result can be explained by the fact that adsorption in porous media also occurs in the x-direction (in contrast to the slit pore geometry where flowing molecules never encounter the pore surface in this direction). Such "additional" adsorption reduces the dispersion of the molecules in this flowing direction. As a result, we obtain smaller displacements variance σ_x^2 (i.e. smaller $D(t)/D_m$). In addition, increasing the adsorption desorption ratio, leads to smaller $D(t)/D_m$. This result goes along with the analytical study of the evolution of $\frac{\partial}{\partial k_H}\frac{D(t\to\infty)}{D_m}$. For our case, since the characteristic channel width of the pores is too small, we have $\frac{\partial}{\partial k_H}\frac{D(t\to\infty)}{D_m} < 0$ and therefore $D(t)/D_m$ decreases as a function of k_H. When comparing results obtained with the Henry and Langmuir adsorption models, no difference is observed for low adsorption coefficients. Moreover, the results are very close to those obtained for non-adsorbing tracers. On the other hand, for large adsorption coefficients, the molecules following the Langmuir adsorption model are more dispersed than the molecules following the Henry adsorption model (when comparing data taken at the same time step). This result highlights the key-role played by surface saturation at the pore surface.

The absence of the stationary regime for the dispersion simulation in the porous geometry should be further investigated. This result can be caused by the complex pattern of the Stokes flow. To address this issue, we also considered porous systems with a more homogeneous geometry. As shown in the appendix, an oscillatory behavior exists but is slightly attenuated compared to the results for the realistic micromodel geometry. However, $D(t)/D_m$ is still increasing with time. Our proposition is to remove the no-slip boundary condition implemented along the $y-axis$ limits so that periodic boundary conditions can be used. In so doing, the Stokes flow pattern would become homogeneous. As a second option, simulations could be performed for larger geometries to avoid finite size effects including such heterogeneity effects.

Appendices

A. Dispersion coefficient calculus for adsorbing molecules

In the article by Levesque et al. they develop a theoretical analysis of Taylor dispersion under adsorption conditions.They use a stochastic approach to derive the dispersion coefficient for Poiseuille flow in simple geometries: planar and cylindrical.

In this paragraph, we follow the exact approach to derive the dispersion coefficient. As cited in the article [65], they define the longitudinal dynamics of Brownian particle in a flow of velocity using following Langevin equation:

$$\dot{x}(t) = v(y(t),t) + \mathbb{1}_b(y(t))\eta_b(t) + \mathbb{1}_s(y(t))\eta_s(t) \tag{3}$$

where $r = (x,y)$ is the position of the particle, $y(t)$ is the position at the transverse direction. $\mathbb{1}_b(y(t))$ is the indicator function of bulk b and it takes into account the bulk diffusion which is characterized by the diffusion coefficient D_m. $\mathbb{1}_s(y(t))$ is the indicator function of surface s and it is associated with surface diffusion related to the diffusion coefficient D_s.

They also introduce the independent Gaussian white noise related to the bulk η_b and to the surface η_s using the correlation functions:

$$\begin{aligned} \langle \eta_b(t) \rangle &= \langle \eta_s(t) \rangle = 0, \\ \langle \eta_b(t)\eta_b(t') \rangle &= 2D_m\delta(t-t'), \\ \langle \eta_s(t)\eta_s(t') \rangle &= 2D_s\delta(t-t'). \end{aligned} \tag{4}$$

The system considered corresponds to an adsorbing system with k_A and k_D as the adsorption and the desorption rates. We introduce P the propagators at equilibrium of the free molecules and Γ the propagator of the adsorbed molecules at equilibrium (i.e. on the surface). The particle at $t = 0$ starts from $x = 0$ and the transverse diffusion equation is given as follows:

$$\partial_t P(y,t|y',0) = D_m \nabla^2 P(y,t|y',0) \qquad \forall y \in b \tag{5}$$

$$\begin{aligned} \partial_t \Gamma(y,t|y',0) &= -k_D\Gamma(y,t|y',0) + k_A P(y,t|y',0) \\ &= D_m \partial_n P(y,t|y',0) \end{aligned} \qquad \forall y \in s \tag{6}$$

where ∂_n stands for the normal derivative. The process $y(t)$ is considered stationary and it is described by the stationary distribution $P_{stat}(y)$ that is homogeneous in each phase (bulk or the

surface). The transition probability between y and y' is defined as $P(y,t|y',t') \equiv P(y,t-t'|y',0)$. In this paragraph, we aim to compute the variance of $x(t)$ to infer the dispersion coefficient with adsorption at stationary state.

In the case of a stationary velocity field $v(y,t) \equiv v(y)$, the large time limit of the variance of the displacement $M(t) = \langle x^2(t)\rangle - \langle x(t)\rangle^2$ is given by:

$$\lim_{t\to\infty} M(t) = 2Kt \tag{7}$$

where K is the dispersion coefficient.

Calculus of the dispersion coefficient K

In this paragraph, in order to compute K, we first determine the displacement variance $M(t)$. To this goal, we define the first and the second moment of $x(t)$ where we use the cross section in the bulk b as the spatial integration domain so:

$$\begin{aligned} \langle x(t)\rangle &= \int_b dy\, x(t) P_{stat}(y) \\ \langle x^2(t)\rangle &= \int_0^t dt' \int_0^t dt'' \langle \dot{x}(y(t'),t'), \dot{x}(y(t'),t'')\rangle \end{aligned} \tag{8}$$

Calculus of $\langle x(t)\rangle$ using eq (3)

$$\begin{aligned} \langle x(t)\rangle &= \int_b dy\, x(t) P_{stat}(y) \\ &= \int_b \int_0^t dy\, \dot{x}(t') dt' P_{stat}(y) \\ &= \int_0^t dt' \int_b dy\, v(y(t'),t') P_{stat}(y) \\ &+ \int_0^t dt' \int_b dy\, \mathbb{1}_b(y(t'))\eta_b(t') P_{stat}(y) \\ &+ \int_0^t dt' \int_b dy\, \mathbb{1}_s(y(t'))\eta_s(t') P_{stat}(y) \\ &= \int_0^t dt' \int_b dy\, v(y(t'),t') P_{stat}(y) + \int_0^t dt' \langle \eta_b(t')\rangle + \int_0^t dt' \langle \eta_s(t')\rangle \\ \langle x(t)\rangle &= \int_0^t dt' \int_b dy\, v(y(t'),t') P_{stat}(y) \end{aligned} \tag{9}$$

Calculus of $\langle x^2(t)\rangle$

$$\begin{aligned}
\langle x^2(t)\rangle &= \int_0^t dt' \int_0^t dt'' \langle \dot{x}(y(t'),t')\dot{x}(y(t''),t'')\rangle \\
&= \int_0^t dt' \int_0^t dt'' \langle v(y(t'),t')v(y(t''),t'')\rangle + \int_0^t dt' \int_0^t dt'' \langle \eta_b(t')\eta_b(t'')\rangle \\
&\quad + 2\int_0^t dt' \int_0^t dt'' \langle \eta_s(t')\eta_s(t'')\rangle + 2\int_0^t dt' \int_0^t dt'' \langle \eta_b(t')\eta_s(t'')\rangle \\
&\quad + \int_0^t dt' \int_0^t dt'' \langle v(y(t'),t')\eta_b(t'')\rangle + \int_0^t dt' \int_0^t dt'' \langle v(y(t'),t')\eta_s(t'')\rangle \\
&\quad + \int_0^t dt' \int_0^t dt'' \langle \eta_b(t')v(y(t''),t'')\rangle + \int_0^t dt' \int_0^t dt'' \langle \eta_s(t')v(y(t''),t'')\rangle \\
\langle x^2(t)\rangle &= \int_0^t dt' \int_0^t dt'' \langle v(y(t'),t')v(y(t''),t'')\rangle + 2D_m\langle T_b(t)\rangle + 2D_s\langle T_s(t)\rangle
\end{aligned}$$

where $T_b(t)$ (resp. $T_s(t)$) is the cumulative time spent in the bulk (resp. on the surface) up to time t.

We define I as $I = \langle x^2(t)\rangle - 2D_m\langle T_b(t)\rangle - 2D_s\langle T_s(t)\rangle$

$$\begin{aligned}
I &= \langle x^2(t)\rangle - 2D_m\langle T_b(t)\rangle - 2D_s\langle T_s(t)\rangle \\
&= \int_0^t dt' \int_0^t dt'' \langle v(y(t'),t')v(y(t''),t'')\rangle \\
&= \underbrace{\int_0^t dt'' \int_0^{t''} dt' \langle v(y(t''),t'')v(y(t'),t')\rangle}_{I_1} \\
&\quad + \underbrace{\int_0^t dt'' \int_{t''}^t dt' \langle v(y(t''),t'')v(y(t'),t')\rangle}_{I_2}
\end{aligned} \tag{10}$$

In order to determine I_2, we will be using the Fubini's theorem

$$I_2 = \int_0^t dt'' \int_{t''}^t dt' \int_b dy_1 \int_b dy_2 \; v(y_2,t'')v(y_1,t')P_{stat}(y_2) \times P_{stat}(y_1,t'|y_2,t'')$$

for

$$\begin{cases} t'' \le t' \le t \\ 0 \le t'' \le t \end{cases} \Longrightarrow \begin{cases} 0 \le t'' \le t' \\ 0 \le t' \le t \end{cases}$$

we get:

$$I_2 = \int_0^t dt' \int_0^{t'} dt'' \int_b dy_1 \int_b dy_2 \; v(y_2,t'')v(y_1,t')P_{stat}(y_2) \times P_{stat}(y_1,t'|y_2,t'')$$

we set $t'' = t' - \tau$

$$I_2 = -\int_0^t dt' \int_{t'}^0 d\tau \int_b dy_1 \int_b dy_2 \; v(y_2,t'-\tau)v(y_1,t')P_{stat}(y_2) \times P_{stat}(y_1,t'|y_2,t'-\tau)$$
$$= \int_0^t dt' \int_0^{t'} d\tau \int_b dy_1 \int_b dy_2 \; v(y_2,t'-\tau)v(y_1,t')P_{stat}(y_2) \times P_{stat}(y_1,\tau|y_2,0)$$

since the transition probability $P_{stat}(y_1,t'|y_2,t'-\tau) = P_{stat}(y_1,\tau|y_2,0)$

$$\begin{cases} 0 \le \tau \le t' \\ 0 \le t' \le t \end{cases} \Longrightarrow \begin{cases} \tau \le t' \le t \\ 0 \le \tau \le t \end{cases}$$

$$I_2 = \int_0^t d\tau \int_\tau^t dt' \int_b dy_1 \int_b dy_2 \; v(y_2,t'-\tau)v(y_1,t')P_{stat}(y_2) \times P_{stat}(y_1,\tau|y_2,0)$$

Calculus of I_1

$$I_1 = \int_0^t dt'' \int_0^{t''} dt' \langle v(y_1,t')v(y_2,t'')\rangle$$
$$= \int_0^t dt'' \int_0^{t''} dt' \int_b dy_1 \int_b dy_2 \; v(y_1,t')v(y_2,t'')P_{stat}(y_1) \times P_{stat}(y_2,t''|y_1,t')$$

we set $t' = t'' - \tau$

$$I_1 = -\int_0^t dt'' \int_{t''}^0 d\tau \int_b dy_1 \int_b dy_2 \; v(y_1,t''-\tau)v(y_2,t'')P_{stat}(y_1) \times P_{stat}(y_2,t''|y_1,t''-\tau)$$

since the transition probability $P_{stat}(y_2,t''|y_1,t''-\tau) = P_{stat}(y_2,\tau|y_1,0)$

$$I_1 = \int_0^t dt'' \int_0^{t''} d\tau \int_b dy_1 \int_b dy_2 \; v(y_1,t''-\tau)v(y_2,t'')P_{stat}(y_1) \times P_{stat}(y_2,\tau|y_1,0)$$

$$\begin{cases} 0 \le \tau \le t'' \\ 0 \le t'' \le t \end{cases} \Longrightarrow \begin{cases} \tau \le t'' \le t \\ 0 \le \tau \le t \end{cases}$$

$$I_1 = \int_0^t d\tau \int_\tau^t dt'' \int_b dy_1 \int_b dy_2 \; v(y_1,t''-\tau)v(y_2,t'')P_{stat}(y_1) \times P_{stat}(y_2,\tau|y_1,0)$$

since y_1 and y_2 are dummy variables they can be exchanged and then we get :

$$I_1 = \int_0^t d\tau \int_\tau^t dt'' \int_b dy_2 \int_b dy_1 \; v(y_2,t''-\tau)v(y_1,t'')P_{stat}(y_2) \times P_{stat}(y_1,\tau|y_2,0)$$

so then $I_1 = I_2$ and Eq. (10) becomes

$$I = 2\int_0^t d\tau \int_\tau^t dt' \int_b dy_1 \int_b dy_2 v(y_2,t'-\tau)v(y_1,t')P_{stat}(y_2) \times P_{stat}(y_1,\tau|y_2,0) \tag{11}$$

on the other hand

$$\langle x(t)\rangle^2 = \left(\int_0^t dt' \int_b dy P_{stat}(y) \times v(y,t')\right)^2$$
$$= \int_0^t dt' \int_0^t dt' \int_b dy_1 \int_b dy_2 v(y_2,t'')v(y_1,t')P_{stat}(y_2)P_{stat}(y_1))$$

And following the calculus of I we get

$$\langle x(t)\rangle^2 = 2\int_0^t d\tau \int_\tau^t dt' \int_b dy_1 \int_b dy_2 v(y_2,t'-\tau)v(y_1,t')P_{stat}(y_2)\times P_{stat}(y_1) \tag{12}$$

So using eqs. (11) and (12), we get

$$\begin{aligned} &\langle x^2(t)\rangle - \langle x(t)\rangle^2 - 2D_m\langle T_b(t)\rangle - 2D_s\langle T_s(t)\rangle = f(t) \\ &f(t) = 2\int_0^t d\tau \int_\tau^t dt' \int_b dy_1 \int_b dy_2 v(y_2,t'-\tau)v(y_1,t') \\ &\times P_{stat}(y_2)\times (P_{stat}(y_1,\tau|y_2,0) - P_{stat}(y_1) \end{aligned} \tag{13}$$

So as defined in Eq. (7), the large time limit of the variance of the displacement $M(t) = \langle x^2(t)\rangle - \langle x(t)\rangle^2$, helps to get the dispersion coefficient K, and through Eq (13), it becomes:

$$K = P_{stat}(b)D_m + P_{stat}(s)D_s + K_v$$

where $P_{stat}(b)$ and $P_{stat}(s)$ are the stationary probability to be in the bulk or to be adsorbed on the surface. We introduce k_v as the velocity-dependent part.

$$\begin{aligned} &K_v = \int_b dy_1 \int_b dy_2 v(y_1)v(y_2)\times P_{stat}(y_2)h(y_1|y_2) \\ &\text{with } h(y_1|y_2) = \int_0^\infty [P(y_1,t|y_2,0) - P_{stat}(y_1)]dt. \end{aligned} \tag{14}$$

Calculus of the stationary probability limit $P_{stat}(\alpha)$

Let $N = N_s + N_b$ with N denote the number of all particles in the system. N_b (resp. N_s) corresponds to the number of particle in the bulk (resp. adsorbed on surface).

The bulk volume corresponds to $V = L^3$ and the total adsorption surface is $S = 2L^2$.

$$\begin{aligned} P_{stat}(b) &= \frac{N_v}{NL} \\ P_{stat}(s) &= \frac{N_s}{2N} \end{aligned}$$

As the system considered is in equilibrium state, we have:

$$\frac{N_s}{S} = \frac{k_A}{k_D}\frac{N_v}{V} \Rightarrow N_s = 2\frac{k_A}{k_D}\frac{N_v}{L}$$

Which gives

$$N_v = N\frac{k_D L}{L(k_D L + 2k_A)}$$
$$\Rightarrow P_{stat}(b) = \frac{N_v}{NL} = \frac{k_D}{k_D L + 2k_A}$$

$$N_s = N - N_v = N\left(1 - \frac{k_D L}{k_D L + 2k_A}\right) = N\frac{2k_A}{k_D L + 2k_A}$$
$$\Rightarrow P_{stat}(s) = \frac{N_s}{2N} = \frac{k_A}{k_D L + 2k_A}$$

Calculus of $h(y_1|y_2)$

In order to determine $h(y_1|y_2)$ (pseudo-Green's function), Levesque et Al. propose the use of the first Laplace an to transform Eq. (5) and Eq. (6). Once the Laplace transform is performed, they pass to the small Laplace variable limit.

After determination of the pseudo-green function, Eq. (14) gives a generic expression of the Taylor dispersion coefficient in the presence of adsorption and desorption conditions. In the case of a planar system, i.e. two parallel plates having a poiseuille flow with the velocity field $v(y) = 6\bar{v}\frac{y}{L}(1 - \frac{y}{L})$, where $\bar{v}$ represents the velocity averaged over a cross-section L and $y \in [0, L]$). We obtain the following expression:

$$\begin{aligned} h^{plan}(y_1|y_2) = & \frac{\frac{1}{2}y_1^2 + \frac{k_A}{k_D}y_1 + \frac{1}{2}y_2^2 - y_2(L + \frac{k_A}{k_D})}{D_m(L + \frac{2k_A}{k_D})} \\ & + \frac{\frac{1}{3}L^3 + \frac{2D_m k_A}{k_D^2} + \frac{k_A L^2}{k_D} + \frac{Lk_A^2}{k_D^2}}{D_m(L + \frac{2k_A}{k_D})^2} \end{aligned} \tag{15}$$

And thus, k_v the velocity-dependent part of the dispersion coefficients takes:

$$K_v^{Pois} = \alpha\frac{L^2\bar{v}^2}{D_m}\frac{\beta L\frac{k_A}{k_D}^2 + \gamma L^2\frac{k_A}{k_D} + L^3}{(L + \frac{2k_A}{k_D})^3} + \frac{\bar{v}^2}{k_D}\frac{2L^2\frac{k_A}{k_D}}{(L + \frac{2k_A}{k_D})^3}$$

with $\alpha = 1/210$, $\beta = 102$ and $\gamma = 18$.

B. LBM results in 2D geometry

1. Stokes TRT equations

The equations we used are from the article of Ginzburg[121]. She introduces the equilibrium components $e_q^{\pm}$ used to solve the Navier-Stokes equations and presents the required approximations to solve the Stokes problem. The initial form of the equilibrium components equations is as follows:

$$\begin{cases} e_q^+(\mathbf{r},t) = \bar{D}(s(\mathbf{r},t))E_q(\mathbf{r},t) \\ e_q^-(\mathbf{r},t) = t_q^*(\mathbf{j}(\mathbf{r},t).\mathbf{v}_q) \\ e_0^+(\mathbf{r},t) = e_0 = s(\mathbf{r},t) - \sum_{q=1}^{Q_m} e_q^+(\mathbf{r},t) \\ e_0^- = 0 \end{cases} \tag{16}$$

with $s(\mathbf{r},t) = \rho(\mathbf{r},t)$, and $\bar{D}(s(\mathbf{r},t)) = P(\rho(\mathbf{r},t)) = v_s^2\rho(\mathbf{r},t)$. E_q is defined by $E_q = t_q^*\left[1 + (1/v_s^2)E_q^{(u)}(\boldsymbol{U})\right]$. For the Stokes problem, the non-linear term $E_q^{(u)}(\boldsymbol{U}) = 0$, then we obtain the following equations:

$$\begin{cases} e_q^+(\mathbf{r},t) = v_s^2\rho(\mathbf{r},t)t_q^* \\ e_q^-(\mathbf{r},t) = t_q^*(\mathbf{j}(\mathbf{r},t).\mathbf{v}_q) \\ e_0^+(\mathbf{r},t) = \rho(\mathbf{r},t) - \sum_{q=1}^{Q_m} e_q^+(\mathbf{r},t) \\ e_0^- = 0 \end{cases} \tag{17}$$

2. ADE TRT equations

To derive the equilibrium components for the ADE equation, we used the definitions introduced in the work of Ginzburg[99].

$$\begin{cases} E_q^+ = E_q^{(m)} + g^{(u)}E_q^{(u)}(\boldsymbol{U}); \\ E_q^- = t_q^{(a)}(\boldsymbol{U}.\mathbf{v}_q) \\ E_0 = \left(1 - \sum_{q=1}^{Q_m} E_q^+(\mathbf{r},t)\right) \end{cases} \tag{18}$$

to derive E_q^+, we have to determine $E_q^{(m)}$, $g^{(u)}$ and $E_q^{(u)}$. For our case, we cancel the numer-

ical diffusion, so we have $g^{(u)} = 1$. Then to determine $E_q^{(m)}$, we have [99]:

$$E_q^{(m)} = t_q^{(m)} v_e + E_q^{(a)}$$
$$\text{with } E_q^{(a)} = \frac{D_{xx} - D_{yy}}{4} P_q^{xx} + \frac{D_{xy}}{4} P_q^{xy}$$

with P_q^{xx} and P_q^{xy} defined using the velocity vector $\mathbf{v}_q$ by $P_q^{xx} = v_{qx}^2 - v_{qy}^2$ and $P_q^{xy} = v_{qx} v_{qy}$. D_{xx}, D_{yy} and D_{xy} are the diagonal (x and y axis) and off-diagonal (xy) diffusion coefficients. We have an isotropic diffusion, therefore $D_{xy} = 0$ and the diffusion coefficients are $D_{xx} = D_{yy}$. This gives:

$$E_q^{(a)} = 0$$
$$E_q^{(m)} = t_q^{(m)} v_e.$$

Since we have isotropic diffusion, to determine $E_q^{(u)}$, we use $E_q^{(u)}(\boldsymbol{U}) = E_q^*(\boldsymbol{U})$ [99] defined as:

$$E_q^*(\boldsymbol{U}) = \frac{t_q^*}{2}(3(\boldsymbol{U}.\mathbf{v}_q)^2 - \boldsymbol{U}^2)$$

with $\boldsymbol{U} = \{U_x, U_y\}$ is the advective velocity and $\boldsymbol{U}^2 = U_x^2 + U_y^2$. t_q^* are the isotropic weights. The weights families $t_q^{(m)}$ and $t_q^{(a)}$ become $t_q^{(m)} = t_q^{(a)} = t_q^* = \left\{\frac{1}{3}; \frac{1}{12}\right\}$[99]. Then we get the following equations:

$$\begin{cases} E_q^+ = t_q^* v_e + \dfrac{t_q^*}{2}(3(\boldsymbol{U}.\mathbf{v}_q)^2 - \boldsymbol{U}^2) \\ E_q^- = t_q^*(\boldsymbol{U}.\mathbf{v}_q) \\ E_0 = \left(1 - \displaystyle\sum_{q=1}^{Q_m} E_q^+(\mathbf{r},t)\right) \end{cases} \tag{19}$$

3. Normalized propagator computation

The propagators distribution is defined for $\delta x = x - x_0$ by:

$$P(\delta x, t) = \frac{1}{\sum_{\delta x'} \sum_y \sum_q g_q(\delta x', y, t)} \sum_y \sum_q g_q(\delta x, y, t); \tag{20}$$

In order to compute the normalized propagators $P(x - x_0/Ut, t)$, we substitute δx by $(x - x_0)/Ut$, so we have the following expression:

$$P\left(\frac{x - x_0}{Ut}, t\right) = \underbrace{\frac{1}{\sum_{\delta x'} \sum_y \sum_q g_q\left(\frac{\delta x'}{Ut}, y, t\right)}}_{(1)} \sum_y g_q\left(\frac{x - x_0}{Ut}, y, t\right) \tag{21}$$

The term (1) is defined as:

$$\frac{1}{\sum_{\delta x'}\sum_y\sum_q g_q\left(\frac{\delta x'}{Ut},y,t\right)} = \frac{Ut}{\sum_{\delta x'}\sum_y\sum_q g_q(\delta x',y,t)}$$

Therefore Eq.(21) becomes:

$$P\left(\frac{x-x_0}{Ut},t\right) = \frac{Ut}{\sum_{\delta x'}\sum_y\sum_q g_q(\delta x',y,t)}\sum_y g_q\left(\frac{x-x_0}{Ut},y,t\right) \tag{22}$$

4. Results in parallel plates geometry

Comparison with analytical tracer concentration profile

For initial and boundary conditions that insure a slug injection, we have the analytical solution proposed by Van Genuchten and Alves for 1D system at a lateral position x, defined by $c_{l,analyt}(x,t)$ [156]:

$$c_{l,analyt}(x,t) = \begin{cases} c_0 A(x,t) & 0 < t < t_0 \\ c_0 A(x,t) - c_0 A(x,t-t_0) & t > t_0 \end{cases} \tag{23}$$

where

$$A(x,t) = \frac{1}{2}erfc\left[\frac{x-Ut}{2(Dt)^{\frac{1}{2}}}\right] + \frac{1}{2}exp(\frac{x}{D})erfc\left[\frac{x+Ut}{2(Dt)^{\frac{1}{2}}}\right]$$

with c_0 being the initial concentration, D is the coefficient of diffusion, and U is the average velocity from the Stokes simulations.

In Fig. 65, we compared the evolution of the concentration in time at a position x, obtained by simulation $c_l(x,t) = \frac{1}{L_y}\sum_y c(\mathbf{r},t)$ with the analytical solution $c_{l,analyt}(x,t)$ in Eq. (23) at different positions in the channel. We can deduce from the comparison at different abscissa that the analytical and simulation curves overlap for abscissa close to the channel entrance. But we see a slight difference for large x. This difference can be related to the difference between the system studied by the analytical solution and by our LBM simulations: the analytical solution is defined for a $1D$ system and our simulations represent a $2D$ system. Furthermore, such a difference might be attributed to the accumulation of numerical errors in the simulation.

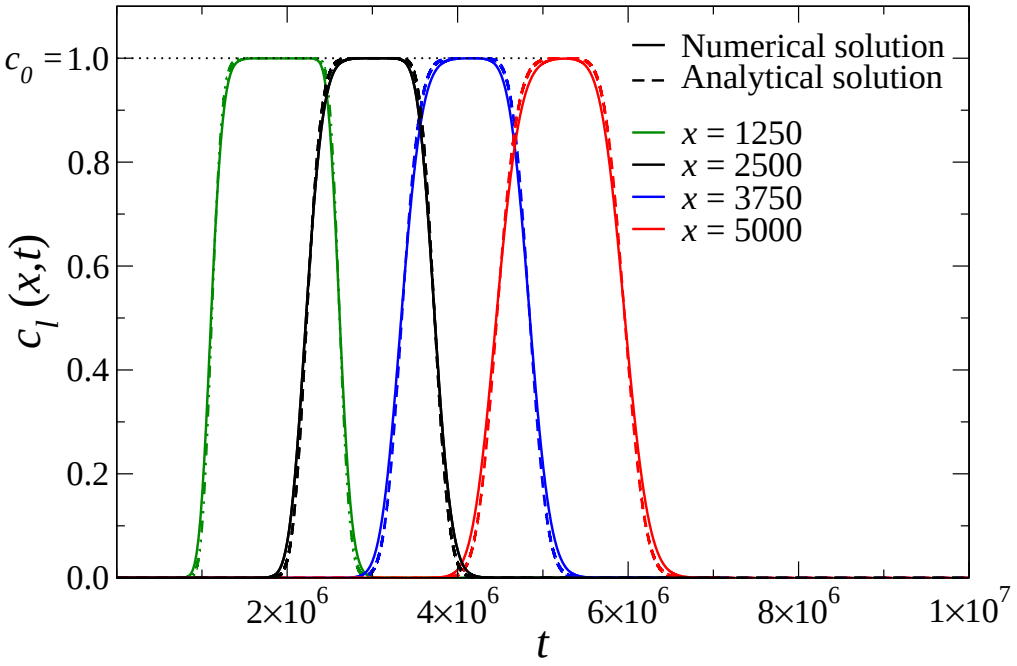

Figure 65: Comparing analytical solution with simulation results of the evolution of the concentration in time for the the parallel plates geometry for $Pe = 9.2$. Straight lines denote the simulation results and the dashed lines present the analytical solution

5. Results in complex regular 2D geometry

In order to consider more complex geometries, we created crenelations and sinusoids on the parallel plates and used them as our geometries.

5.1. Stokes flow

Fig. 66 presents the results of the Stokes flow simulation in different geometries. As we can see, near the restriction of the geometry, we have a variation of the average velocity. It presents the shear effect caused by the shape of the geometries: the no-slip boundary condition dictates that the velocity of the fluid at the boundary is zero. Furthermore, the flow rate is constant throughout the geometry so the velocity is greater in the restrictions and lower in the wider sections.

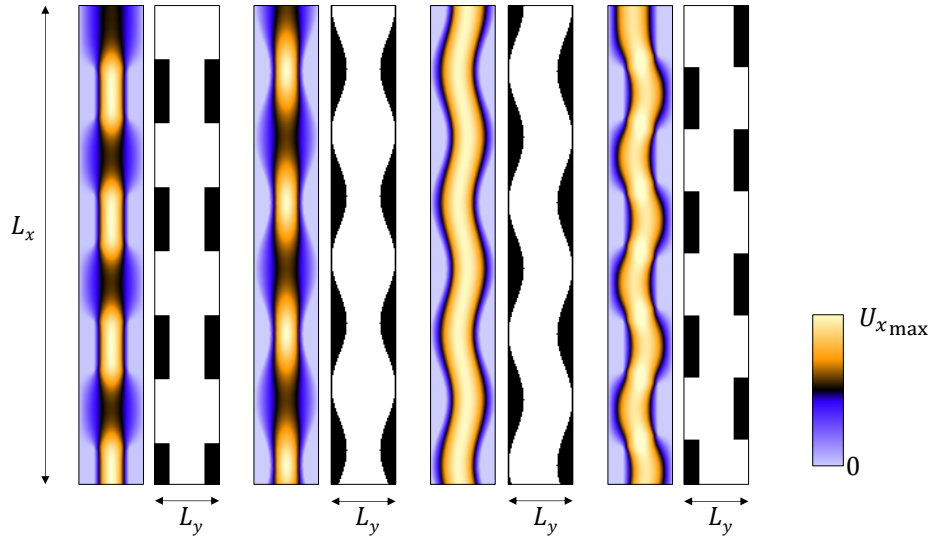

Figure 66: flow in the x-direction in periodic geometries: sinusoids, crenelatations with $L_x = 2000$ and $L_y = 41$

The flow shows that the sinusoids and crenelations have a relatively small effect on most of the flow but cause a strong deceleration of the fluid near to the boundary since we have the no slip boundary condition. A complex interaction exists between fluid flow and convective particles transfer. Therefore, the changes we see here will affect the transport of the tracer simulations.

5.2. Passive tracer dispersion

In this section, we performed tracer dispersion simulation for a crenelated geometry. Propagators at different times are plotted in Fig. 67 (passive tracer was injected for this simulation at $x_0 = 150$). For small times t, the shape of the propagator is quasi-Gaussian but for higher times the distribution of the propagators is not Gaussian. We therefore, conclude that the changes in the geometry affects the dispersion of the tracer, since it becomes non-Gaussian in the crenelated geometry.

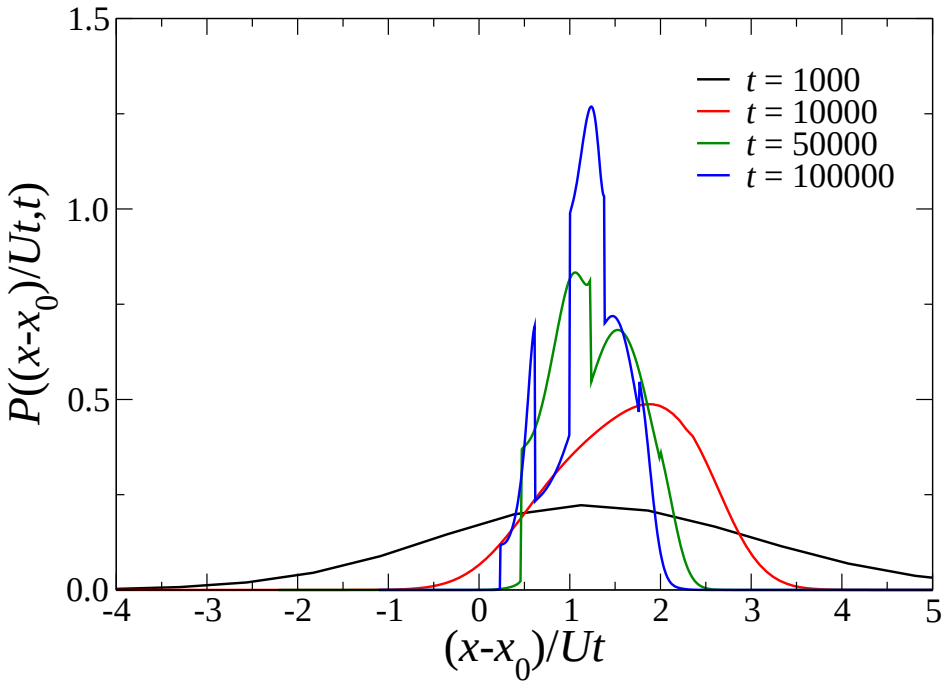

Figure 67: Propagators $P((x-x_0)/Ut,t)$ at time t in the crenelated geometry

C. LBM transport of adsorbing molecules in parallel plates geometry

1. Influence of the adsorbed tracer for Henry $k_H = 1$

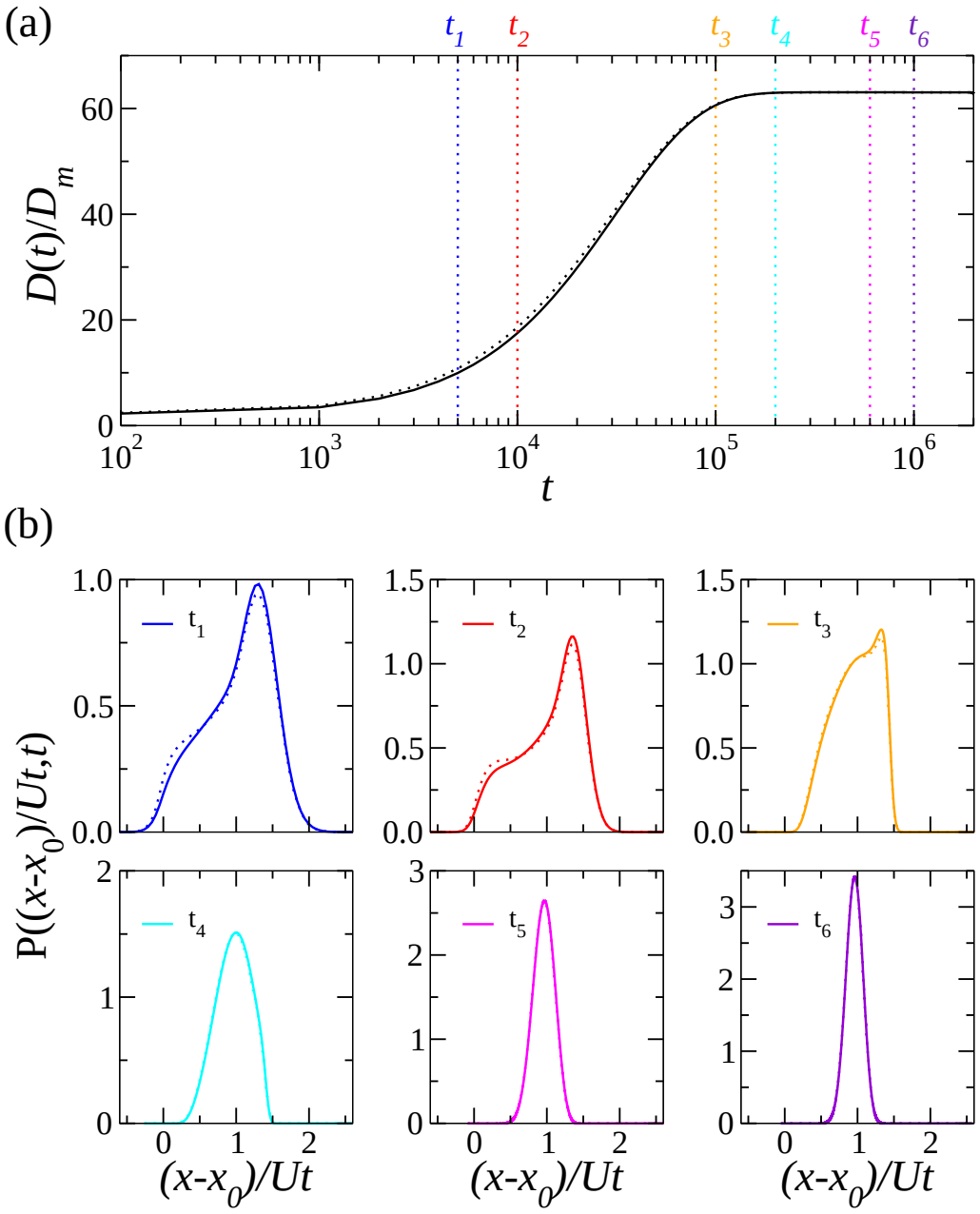

Figure 68: LBM simulation results of the transport of Henry adsorbing molecules with adsorption desorption coefficient $k_H = 1$ and $p_D = 0.001$; the solid and dashed lines denote respectively. The simulations are for $Pe = 100$ and initial concentration per site $c_0 = 10$. (a) Normalized evolution of the derivative of the displacement variance over time. The dashed lines denote the analytical values of D_{eff}^{ads}/D_m. (b) Normalized propagators at the different time slots.

2. Evolution of the dispersion coefficient

The derivative of the dispersion coefficient for adsorbing molecules:

$$\frac{\partial}{\partial k_H}\frac{D_{eff}^{ads}}{D_m} = \frac{2L_y^2U^2\left(35D_m(L_y-4k_H)+L_yk_D\left(L_y^2+11L_yk_H-17k_H^2\right)\right)}{35D_m^2k_D(L_y+2k_H)^4} \tag{24}$$

The roots of Eq. (24) are as follows:

$$k_1 = \frac{\sqrt{7}\sqrt{2800D_m^2-100D_mL^2k_D+27L^4k_D^2}-140D_m+11L^2k_D}{34Lk_D}$$

$$k_2 = \frac{-\sqrt{7}\sqrt{2800D_m^2-100D_mL^2k_D+27L^4k_D^2}-140D_m+11L^2k_D}{34Lk_D}$$

D. LBM transport of passive tracer in realistic media

1. Concentration distribution in micromodel geometry

In order to better understand the increasing value of $D(t)/D_m$ for a large time intervals shown in Fig. 56, we present in Fig. 69, the temporal evolution of the concentration distribution in the micromdel for larger time intervals. We observe that the tracer passes gradually through

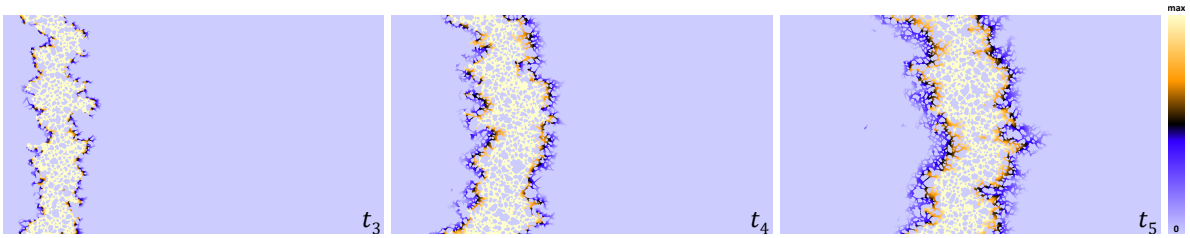

Figure 69: Concentration of the molecules distribution in the micromdel geometry at different time slots (t_3; t_4 and t_5) under a flowing fluid with peclet number Pe $= 100$.

the porous medium and that it disperses adequately. However, in contrast to the dispersion in the parallel plates geometry, in the heterogeneous micro-structure, the dispersion front is more heterogeneous. More important, we notice that the transport along the boundaries $y = 0$ and $y = L_y$ is delayed and this influences the displacement of the front. The reason for this is due to the porous structure and the resulting heterogeneity in the flow field in combination with the no-slip boundary condition. To control this behavior, we should consider a larger structure or a periodic boundary condition instead of the no-slip boundary condition, so that the macroscopic flow along the x-direction becomes more homogeneous in this geometry.

2. Transport of passive tracer in regular geometry

In this paragraph, we perform the transport simulation of passive tracer in a regular geometry shown in Fig.70. It is a regular stacking of 2D spheres with $L_x = 4000$ and $L_y = 2300$, the porosity of this geometry is 46%

The result in Fig.71, presents the temporal evolution of the normalized derivative over time $D(t)/D_m$. It shows a more homogeneous result than the result in the micromodel, but the increasing value behavior for $D(t)$ is still present. The sinusoidal form of the curve is less apparent than in the micromodel simulation. One difference is at the beginning and the end of the advective regime, for the regular geometry, we get a decrease of $D(t)$ and it is smaller than

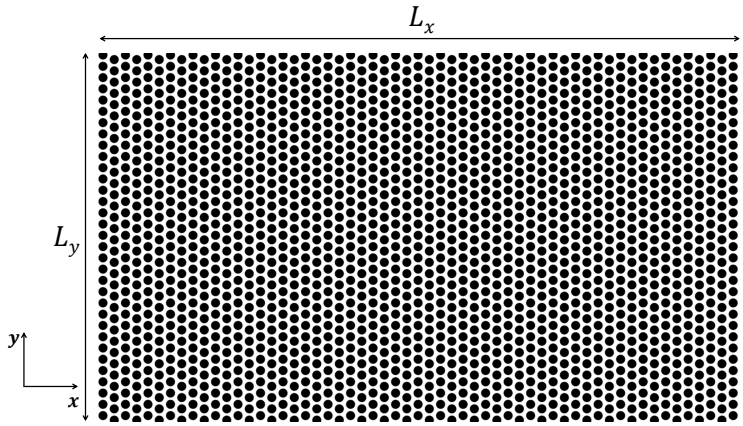

Figure 70: Regular Geometry image with width L_x and length L_y, the color black presents the solid and the white stands for the pore volume.

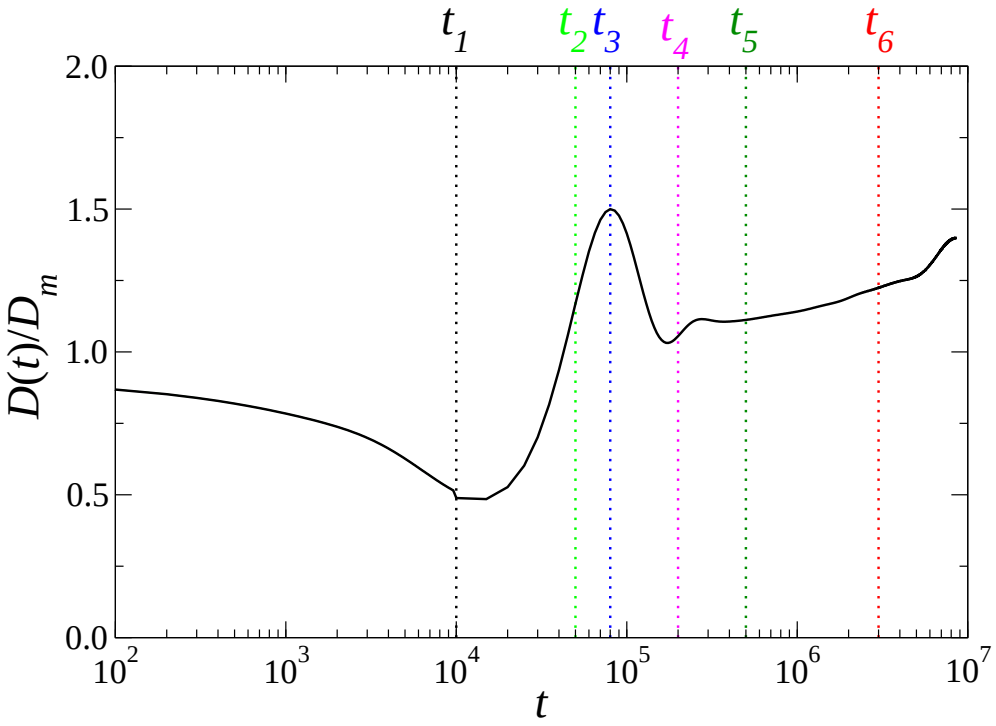

Figure 71: Normalized evolution of the derivative of the displacement variance over time $\frac{D(t)}{D_m} = \frac{1}{2D_m}\frac{\partial\sigma_x^2(t)}{\partial t}$ in the micromdel geometry for the transport of the passive tracer under flowing fluid for Pe $= 100$.

the molecular diffusion coefficient D_m. So the change of the geometry allowed to reduce the sinusoidal behavior but not the increasing value of $D(t)$.

In Fig. 72, we present temporal evolution for the normalized propagators in the geometry. The results are in accordance with the existence for the advective regime, between t_1 and $t4$, where the form of the propagators is altered due to advection as well as for the dispersive regime, for t_5 and t_6, we have the form of the geometry that changes the propagators but it as

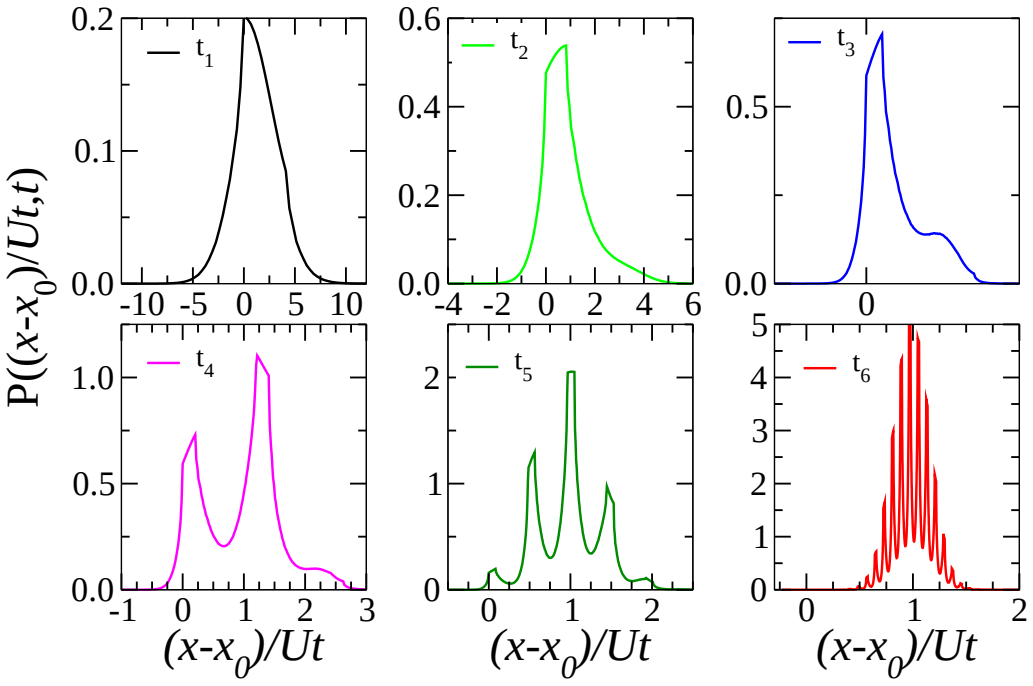

Figure 72: Normalized propagators in the regular geometry for the transport of the passive tracer for Pe = 100.

nearly a Gaussian shape. For small time intervals, we don't get the Gaussian shape of the propagators, which can be explained that it modified due to the spheres in the geometry.

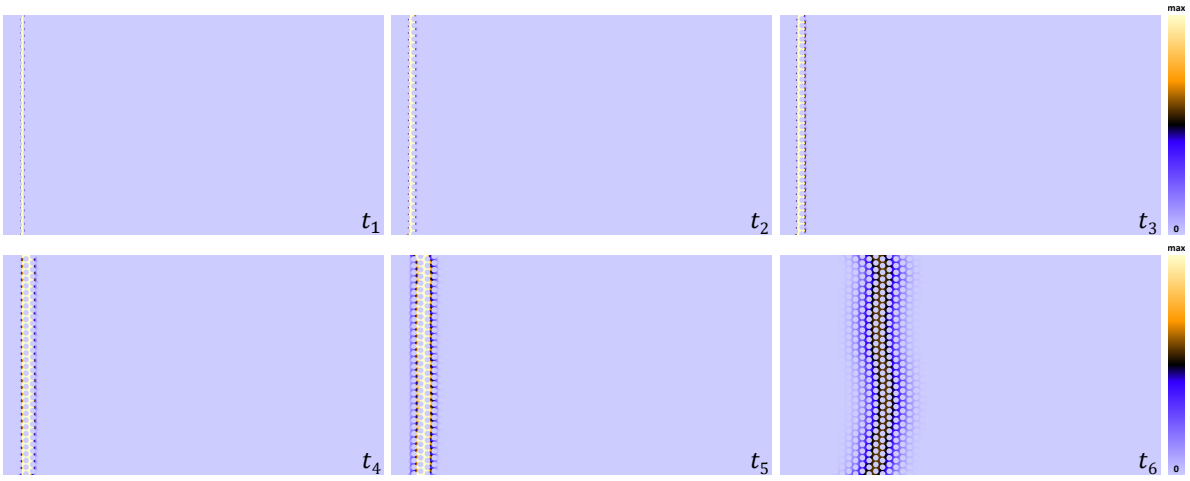

Figure 73: Concentration of the molecules distribution in the regular geometry at different time slots under a flowing fluid with Peclet number Pe = 100.

The concentration distribution is presented in Fig. 73. It shows that for large time interval, at t_6, the concentration distribution have a wavy form, that we assume is caused by the form of the geometry. Therefore, we concluded that using a more homogeneous geometry, does not change the non uniform behavior of the concentration distribution and thus the main reason

behind this effect is the no-slip boundary condition combined with the geometry heterogeneity and one option to solve this is to use periodic boundary condition at the y-axis boundary.

Bibliography

[1] Géraud Delport. *Non-convalent functionalization of carbon nanotubes : From the organization of surfactants to the self-assembly ofporphyrins.* PhD thesis, 12 2016.

[2] Kunio Esumi and Minoru Ueno. *Structure-performance relationships in surfactants*, volume 112. CRC Press, 2003.

[3] W Kwok, HA Nasr-El-Din, RE Hayes, and D Sethi. Static and dynamic adsorption of a non-ionic surfactant on berea sandstone. *Colloids and Surfaces A: Physicochemical and Engineering Aspects*, 78:193–209, 1993.

[4] Ridha Djebali, Mohamed Ammar Abbassi, and Abdallah Jaouabi. A lattice boltzmann model for the simulation of flows and heat transfer at very high temperature: a dynamic framework of conversion to physical space with test cases. In *Thermo-Mechanics Applications and Engineering Technology*, pages 151–169. Springer, 2018.

[5] Oualid Hamdaoui and Emmanuel Naffrechoux. Modeling of adsorption isotherms of phenol and chlorophenols onto granular activated carbon: Part i. two-parameter models and equations allowing determination of thermodynamic parameters. *Journal of Hazardous materials*, 147(1-2):381–394, 2007.

[6] Patrizio Raffa, Diego Armando Zakarias Wever, Francesco Picchioni, and Antonius A Broekhuis. Polymeric surfactants: synthesis, properties, and links to applications. *Chemical reviews*, 115(16):8504–8563, 2015.

[7] MJ Ruiz-Angel, Samuel Carda-Broch, José Ramón Torres-Lapasió, and MC García-Álvarez-Coque. Retention mechanisms in micellar liquid chromatography. *Journal of Chromatography A*, 1216(10):1798–1814, 2009.

[8] Ewa Olkowska, Zaneta Polkowska, and Jacek Namiesnik. Analytics of surfactants in the environment: problems and challenges. *Chemical reviews*, 111(9):5667–5700, 2011.

[9] Valipuram S Manoranjan and Thomas B Stauffer. Exact solution for contaminant transport with kinetic langmuir sorption. *Water Resources Research*, 32(3):749–752, 1996.

[10] AR Appadu. Comparative study of three numerical schemes for contaminant transport with kinetic langmuir sorption. In *AIP Conference Proceedings*, volume 1738, page 030021. AIP Publishing LLC, 2016.

[11] Jacob Bear. *Modeling phenomena of flow and transport in porous media*, volume 31. Springer, 2018.

[12] B-L Su, Clément Sanchez, and Xiao-Yu Yang. *Hierarchically structured porous materials: from nanoscience to catalysis, separation, optics, energy, and life science*. John Wiley & Sons, 2012.

[13] Kozo Ishizaki, Sridhar Komarneni, and Makoto Nanko. *Porous Materials: Process technology and applications*, volume 4. Springer science & business media, 2013.

[14] Don Kulasiri and Wynand Verwoerd. *Stochastic Dynamics. Modeling Solute Transport in Porous Media*. Elsevier, 2002.

[15] Davood Domairry Ganji and Sayyid Habibollah Hashemi Kachapi. *Application of nonlinear systems in nanomechanics and nanofluids: analytical methods and applications*. William Andrew, 2015.

[16] Zhengwen Zeng and Reid Grigg. A criterion for non-darcy flow in porous media. *Transport in porous media*, 63(1):57–69, 2006.

[17] I.L. Mostinsky. Diffusion.

[18] Jean J Fried. *Groundwater pollution*. Elsevier, 1975.

[19] Fred C Payne, Joseph A Quinnan, and Scott T Potter. *Remediation hydraulics*. CRC Press, 2008.

[20] CW Fetter. Applied hydrogeology: Macmillan college publishing company. *New York New York*, 1994.

[21] R Dewey and Paul J Sullivan. Longitudinal dispersion in flows that are homogeneous in the streamwise direction. *Zeitschrift für angewandte Mathematik und Physik ZAMP*, 30(4):601–613, 1979.

[22] P Somasundaran and Joy T Kunjappu. In-situ investigation of adsorbed surfactants and polymers on solids in solution. *Colloids and Surfaces*, 37:245–268, 1989.

[23] A Dabrowski. Adsorption—from theory to practice. *Advances in colloid and interface science*, 93(1-3):135–224, 2001.

[24] Milton J Rosen and Joy T Kunjappu. *Surfactants and interfacial phenomena*. John Wiley & Sons, 2012.

[25] Kurt W Kolasinski. *Surface science: foundations of catalysis and nanoscience*. John Wiley & Sons, 2012.

[26] A Dabrowski and M Jaroniec. Theoretical foundations of physical adsorption from binary non-electrolytic liquid mixtures on solid surfaces: present and future. *Advances in Colloid and Interface Science*, 27(3-4):211–283, 1987.

[27] A Dabrowski, M Jaroniec, and J Oscik. Surface and colloid science vol. 14, 1987.

[28] Herbert Freundlich. *Kapillarchemie*. Akademische Verlagsgesellschaft, 1922.

[29] James William McBain. The sorption of gases and vapours by solids. *The Journal of Physical Chemistry*, 37(1):149–150, 1933.

[30] A Eucken. Verh. dtsch. phys. *Ges. 16*, 345, 1914.

[31] Michael Polanyi. Adsorption from the point of view of the third law of thermodynamics. *Verh. Deut. Phys. Ges*, 16:1012–1016, 1914.

[32] Michael Polanyi. Adsorption von gasen (dampfen) durch ein festes nichtfluchtiges adsorbens. *Verhandlungen der Deutschen Physekalischen Gesellschaft*, 18:55–80, 1916.

[33] Irving Langmuir. The adsorption of gases on plane surfaces of glass, mica and platinum. *Journal of the American Chemical society*, 40(9):1361–1403, 1918.

[34] GS Rushbrooke and CA Coulson. The thermodynamic derivation of langmuir's isotherm. In *Mathematical Proceedings of the Cambridge Philosophical Society*, volume 36, pages 248–251. Cambridge University Press, 1940.

[35] Stephen Brunauer, Paul Hugh Emmett, and Edward Teller. Adsorption of gases in multimolecular layers. *Journal of the American chemical society*, 60(2):309–319, 1938.

[36] Stephen Brunauer and Paul H Emmett. The use of van der waals adsorption isotherms in determining the surface area of iron synthetic ammonia catalysts. *Journal of the American Chemical Society*, 57(9):1754–1755, 1935.

[37] Stephen Brunauer and Paul H Emmett. The use of low temperature van der waals adsorption isotherms in determining the surface areas of various adsorbents. *Journal of the American Chemical Society*, 59(12):2682–2689, 1937.

[38] Filip Ambroz, Thomas J Macdonald, Vladimir Martis, and Ivan P Parkin. Evaluation of the bet theory for the characterization of meso and microporous mofs. *Small Methods*, 2(11):1800173, 2018.

[39] Kenneth SW Sing. Adsorption methods for the characterization of porous materials. *Advances in colloid and interface science*, 76:3–11, 1998.

[40] J Frenkel. Kinetic theory of liquids' clarendon press, 1946.

[41] David Matheson Young and Albert Dary Crowell. Physical adsorption of gases. Technical report, Butterworths,, 1962.

[42] Robert Aveyard and Denis Arthur Haydon. *An introduction to the principles of surface chemistry*. CUP Archive, 1973.

[43] Ondřej Kadlec. The history and present state of dubinin's theory of adsorption of vapours and gases on microporous solids. *Adsorption Science & Technology*, 19(1):1–24, 2001.

[44] Hans-Jürgen Butt, Karlheinz Graf, and Michael Kappl. *Physics and chemistry of interfaces*. John Wiley & Sons, 2013.

[45] Cary T Chiou. Fundamentals of the adsorption theory. *Partition and Adsorption of Organic*, 2002.

[46] MM Dubinin. Adsorbtsiya gazov i parov i struktura adsorbentov. *Uspekhi Khimii*, 21(5):513, 1952.

[47] Fritz Stoeckli, A Lavanchy, and Deirdre Hugi-Cleary. Dubinin's theory: a versatile tool in adsorption science. In *Fundamentals of adsorption*, volume 6, pages 75–80. Elsevier, 1998.

[48] AW House and DH Everett. en:"specialist periodical reports", vol. 4. *Editor: DH Everett. Chemical Society, London*, 1979.

[49] M Jaroniec, J Choma, and PA Thrower. Chemistry and physics of carbon, vol. 22, 1989.

[50] OJDL Redlich and D L Peterson. A useful adsorption isotherm. *Journal of Physical Chemistry*, 63(6):1024–1024, 1959.

[51] Robert Sips. On the structure of a catalyst surface. *The Journal of Chemical Physics*, 16(5):490–495, 1948.

[52] H Magdi Selim. Modeling the kinetics of heavy metals reactivity in soils. In *Fate and transport of heavy metals in the vadose zone*. Lewis Publishers Boca-Raton, FL, USA, 1999.

[53] CH Giles and TH MacEwan. S. n. nakhwa, and d. smith. *J. Chem. Soc*, 3973, 1960.

[54] Bu-Yao Zhu, Tiren Gu, and Xiaolin Zhao. General isotherm equation for adsorption of surfactants at solid/liquid interfaces. part 2. applications. *Journal of the Chemical Society, Faraday Transactions 1: Physical Chemistry in Condensed Phases*, 85(11):3819–3824, 1989.

[55] Bu-Yao Zhu and Tiren Gu. Surfactant adsorption at solid-liquid interfaces. *Advances in colloid and interface science*, 37(1-2):1–32, 1991.

[56] LUUK K Koopal. Modeling association and adsorption of surfactants. *Surfactant science series*, pages 111–196, 2003.

[57] Jacob Israelachvili. Self-assembly in two dimensions: surface micelles and domain formation in monolayers. *Langmuir*, 10(10):3774–3781, 1994.

[58] P Levitz. Aggregative adsorption of nonionic surfactants onto hydrophilic solid/water interface. relation with bulk micellization. *Langmuir*, 7(8):1595–1608, 1991.

[59] L Lajtar, J Narkiewicz-Michalek, W Rudzinski, and S Partyka. A new theoretical approach to adsorption of ionic surfactants at water/oxide interfaces: effect of oxide surface heterogeneity. *Langmuir*, 9(11):3174–3190, 1993.

[60] L Lajtar, J Narkiewicz-Michalek, W Rudzinski, and S Partyka. A new theoretical approach to adsorption of ionic surfactants at water/oxide interfaces: studies of the mechanism of cationic surfactant adsorption. *Langmuir*, 10(10):3754–3764, 1994.

[61] Mateusz Drach, Jolanta Narkiewicz-Michałek, Władysław Rudziński, Gerhard H Findenegg, and Zoltán Király. Calorimetric study of adsorption of non-ionic surfactants on silica gels: Estimating the role of lateral interactions between surface aggregates. *Physical Chemistry Chemical Physics*, 4(11):2307–2319, 2002.

[62] A Andrzejewska, M Drach, and J Narkiewicz-Michałek. Theoretical description of surfactant aggregation at the solid/liquid interface–comparative study. *Annales universitatis Mariae Curie-Sklodowska (Maria Curie-Skłodowska University-UMCS): Lublin-Polonia*, 61, 2006.

[63] W Kwok, RE Hayes, and HA Nasr-El-Din. Modelling dynamic adsorption of an anionic surfactant on berea sandstone with radial flow. *Chemical engineering science*, 50(5):769–783, 1995.

[64] Alexander M Berezhkovskii and Alexei T Skvortsov. Aris-taylor dispersion with drift and diffusion of particles on the tube wall. *The Journal of chemical physics*, 139(8):084101, 2013.

[65] Maximilien Levesque, Olivier Bénichou, Raphaël Voituriez, and Benjamin Rotenberg. Taylor dispersion with adsorption and desorption. *Physical Review E*, 86(3):036316, 2012.

[66] J Calvin Giddings and Henry Byring. A molecular dynamic theory of chromatography. *The Journal of Physical Chemistry*, 59(5):416–421, 1955.

[67] David A Edward and AMJ Davis. Diffusion and convective dispersion through arrays of spheres with surface adsorption, diffusion, and unequal solute partitioning. *Chemical engineering science*, 50(9):1441–1454, 1995.

[68] Rudro R Biswas and Pabitra N Sen. Taylor dispersion with absorbing boundaries: A stochastic approach. *Physical review letters*, 98(16):164501, 2007.

[69] Jonas Latt, Orestis Malaspinas, Dimitrios Kontaxakis, Andrea Parmigiani, Daniel Lagrava, Federico Brogi, Mohamed Ben Belgacem, Yann Thorimbert, Sébastien Leclaire, Sha Li, et al. Palabos: Parallel lattice boltzmann solver. *Computers & Mathematics with Applications*, 2020.

[70] Junjian Wang, Li Chen, Qinjun Kang, and Sheik S Rahman. The lattice boltzmann method for isothermal micro-gaseous flow and its application in shale gas flow: A review. *International Journal of Heat and Mass Transfer*, 95:94–108, 2016.

[71] Aydin Nabovati, Edward W Llewellin, and Antonio CM Sousa. A general model for the permeability of fibrous porous media based on fluid flow simulations using the lattice boltzmann method. *Composites Part A: Applied Science and Manufacturing*, 40(6-7):860–869, 2009.

[72] S Succi, E Foti, and F Higuera. Three-dimensional flows in complex geometries with the lattice boltzmann method. *EPL (Europhysics Letters)*, 10(5):433, 1989.

[73] Shiyi Chen, Karen Diemer, Gary D Doolen, Kenneth Eggert, Castor Fu, Semion Gutman, and Bryan J Travis. Lattice gas automata for flow through porous media. *Physica D: Nonlinear Phenomena*, 47(1-2):72–84, 1991.

[74] Qinjun Kang, Dongxiao Zhang, Shiyi Chen, and Xiaoyi He. Lattice boltzmann simulation of chemical dissolution in porous media. *Physical Review E*, 65(3):036318, 2002.

[75] Qinjun Kang, Peter C Lichtner, and Dongxiao Zhang. Lattice boltzmann pore-scale model for multicomponent reactive transport in porous media. *Journal of Geophysical Research: Solid Earth*, 111(B5), 2006.

[76] Guy R McNamara and Gianluigi Zanetti. Use of the boltzmann equation to simulate lattice-gas automata. *Physical review letters*, 61(20):2332, 1988.

[77] FJ Higuera, S Succi, and R Benzi. Lattice gas dynamics with enhanced collisions. *EPL (Europhysics Letters)*, 9(4):345, 1989.

[78] FJ Higuera and Javier Jimenez. Boltzmann approach to lattice gas simulations. *EPL (Europhysics Letters)*, 9(7):663, 1989.

[79] Gary D Doolen. *Lattice gas methods: theory, applications, and hardware*. MIT press, 1991.

[80] Hudong Chen, Shiyi Chen, and William H Matthaeus. Recovery of the navier-stokes equations using a lattice-gas boltzmann method. *Physical Review A*, 45(8):R5339, 1992.

[81] YH Qian. D. d'humi eres, and p. lallemand, lattice bgk models for navier-stokes equation. *Europhys. Lett*, 17(6):479–484, 1992.

[82] Zhaoli Guo, Baochang Shi, and Nengchao Wang. Lattice bgk model for incompressible navier–stokes equation. *Journal of Computational Physics*, 165(1):288–306, 2000.

[83] Romana Begum and M Abdul Basit. Lattice boltzmann method and its applications to fluid flow problems. *European Journal of Scientific Research*, 22(2):216–231, 2008.

[84] D Enskog. Théorie cinétique des opérations dans les n n n n a nsigdigen "u nten gaz: dis./d. *Enskog. Uppsala*, 1917.

[85] Sydney Chapman, Thomas George Cowling, and David Burnett. *The mathematical theory of non-uniform gases: an account of the kinetic theory of viscosity, thermal conduction and diffusion in gases*. Cambridge university press, 1990.

[86] Prabhu Lal Bhatnagar, Eugene P Gross, and Max Krook. A model for collision processes in gases. i. small amplitude processes in charged and neutral one-component systems. *Physical review*, 94(3):511, 1954.

[87] James E Broadwell. Study of rarefied shear flow by the discrete velocity method. *Journal of Fluid Mechanics*, 19(3):401–414, 1964.

[88] Takaji Inamuro and Bradford Sturtevant. Numerical study of discrete-velocity gases. *Physics of Fluids A: Fluid Dynamics*, 2(12):2196–2203, 1990.

[89] J Hardy, O De Pazzis, and Yves Pomeau. Molecular dynamics of a classical lattice gas: Transport properties and time correlation functions. *Physical review A*, 13(5):1949, 1976.

[90] Uriel Frisch, Brosl Hasslacher, and Yves Pomeau. Lattice-gas automata for the navier-stokes equation. *Physical review letters*, 56(14):1505, 1986.

[91] Shiyi Chen and Gary D Doolen. Lattice boltzmann method for fluid flows. *Annual review of fluid mechanics*, 30(1):329–364, 1998.

[92] Zhaoli Guo and Chang Shu. *Lattice Boltzmann method and its applications in engineering*, volume 3. World Scientific, 2013.

[93] Sauro Succi. Lattice boltzmann 2038. *EPL (Europhysics Letters)*, 109(5):50001, 2015.

[94] Yue-Hong Qian, Dominique d'Humières, and Pierre Lallemand. Lattice bgk models for navier-stokes equation. *EPL (Europhysics Letters)*, 17(6):479, 1992.

[95] Dominique d'Humieres. Multiple–relaxation–time lattice boltzmann models in three dimensions. *Philosophical Transactions of the Royal Society of London. Series A: Mathematical, Physical and Engineering Sciences*, 360(1792):437–451, 2002.

[96] Pierre Lallemand and Li-Shi Luo. Theory of the lattice boltzmann method: Dispersion, dissipation, isotropy, galilean invariance, and stability. *Physical Review E*, 61(6):6546, 2000.

[97] Irina Ginzburg. Equilibrium-type and link-type lattice boltzmann models for generic advection and anisotropic-dispersion equation. *Advances in water resources*, 28(11):1171–1195, 2005.

[98] Irina Ginzburg. Generic boundary conditions for lattice boltzmann models and their application to advection and anisotropic dispersion equations. *Advances in Water Resources*, 28(11):1196–1216, 2005.

[99] Irina Ginzburg, Dominique d'Humières, and Alexander Kuzmin. Optimal stability of advection-diffusion lattice boltzmann models with two relaxation times for positive/negative equilibrium. *Journal of Statistical Physics*, 139(6):1090–1143, 2010.

[100] Hiroaki Yoshida and Makoto Nagaoka. Multiple-relaxation-time lattice boltzmann model for the convection and anisotropic diffusion equation. *Journal of Computational Physics*, 229(20):7774–7795, 2010.

[101] Zhenhua Chai, Baochang Shi, and Zhaoli Guo. A multiple-relaxation-time lattice boltzmann model for general nonlinear anisotropic convection–diffusion equations. *Journal of Scientific Computing*, 69(1):355–390, 2016.

[102] Irina Ginzburg and Laetitia Roux. Truncation effect on taylor–aris dispersion in lattice boltzmann schemes: Accuracy towards stability. *Journal of Computational Physics*, 299:974–1003, 2015.

[103] Irina Ginzburg. Truncation errors, exact and heuristic stability analysis of two-relaxation-times lattice boltzmann schemes for anisotropic advection-diffusion equation. *Communications in Computational Physics*, 11(5):1439–1502, 2012.

[104] Irina Ginzburg. Prediction of the moments in advection-diffusion lattice boltzmann method. i. truncation dispersion, skewness, and kurtosis. *Physical Review E*, 95(1):013304, 2017.

[105] Weifeng Zhao, Liang Wang, and Wen-An Yong. On a two-relaxation-time d2q9 lattice boltzmann model for the navier–stokes equations. *Physica A: Statistical Mechanics and its Applications*, 492:1570–1580, 2018.

[106] Li-Shi Luo, Wei Liao, Xingwang Chen, Yan Peng, Wei Zhang, et al. Numerics of the lattice boltzmann method: Effects of collision models on the lattice boltzmann simulations. *Physical Review E*, 83(5):056710, 2011.

[107] Xiuya Guo, Baochang Shi, and Zhenhua Chai. General propagation lattice boltzmann model for nonlinear advection-diffusion equations. *Physical Review E*, 97(4):043310, 2018.

[108] Zhaoli Guo, Chuguang Zheng, and TS Zhao. A lattice bgk scheme with general propagation. *Journal of scientific computing*, 16(4):569–585, 2001.

[109] Xiuya Guo, Zhenhua Chai, Shengyong Pang, Yong Zhao, and Baochang Shi. Mixed bounce-back boundary scheme of the general propagation lattice boltzmann method for advection-diffusion equations. *Physical Review E*, 99(6):063316, 2019.

[110] Long Guo, Lizhi Xiao, Xiaowen Shan, and Xiaoling Zhang. Modeling adsorption with lattice boltzmann equation. *Scientific reports*, 6(1):1–9, 2016.

[111] Rui Xu, Maša Prodanović, and Christopher J Landry. Simulation of gas adsorption and capillary condensation in shale nanopores using lattice boltzmann modeling. Unconventional Resources Technology Conference (URTEC), 2018.

[112] Rui Xu, Maša Prodanović, and Christopher J Landry. Study of subcritical and supercritical gas adsorption behavior in different nanopore systems in shale using lattice boltzmann method. *International Journal of Coal Geology*, 212:103263, 2019.

[113] Yang Ning, Yang Jiang, Honglin Liu, and Guan Qin. Numerical modeling of slippage and adsorption effects on gas transport in shale formations using the lattice boltzmann method. *Journal of Natural Gas Science and Engineering*, 26:345–355, 2015.

[114] Michael C Sukop and Dani Or. Lattice boltzmann method for modeling liquid-vapor interface configurations in porous media. *Water Resources Research*, 40(1), 2004.

[115] Saurabh Agarwal, Nishith Verma, and Dieter Mewes. A lattice boltzmann model for adsorption breakthrough. *Heat and mass transfer*, 41(9):843–854, 2005.

[116] Nilesh Manjhi, Nishith Verma, Karijm Salem, and Dieter Mewes. Lattice boltzmann modelling of unsteady-state 2d concentration profiles in adsorption bed. *Chemical engineering science*, 61(8):2510–2521, 2006.

[117] Jean-Mathieu Vanson, François-Xavier Coudert, Benjamin Rotenberg, Maximilien Levesque, Caroline Tardivat, Michaela Klotz, and Anne Boutin. Unexpected coupling between flow and adsorption in porous media. *Soft Matter*, 11(30):6125–6133, 2015.

[118] AJC Ladd and R Verberg. Lattice-boltzmann simulations of particle-fluid suspensions. *Journal of statistical physics*, 104(5-6):1191–1251, 2001.

[119] RMH Merks, AG Hoekstra, and PMA Sloot. The moment propagation method for advection–diffusion in the lattice boltzmann method: validation and péclet number limits. *Journal of Computational Physics*, 183(2):563–576, 2002.

[120] Dominique d'Humières and Irina Ginzburg. Viscosity independent numerical errors for lattice boltzmann models: From recurrence equations to "magic" collision numbers. *Computers & Mathematics with Applications*, 58(5):823–840, 2009.

[121] Irina Ginzburg. Lattice boltzmann modeling with discontinuous collision components: Hydrodynamic and advection-diffusion equations. *Journal of Statistical Physics*, 126(1):157–206, 2007.

[122] Irina Ginzburg. Consistent lattice boltzmann schemes for the brinkman model of porous flow and infinite chapman-enskog expansion. *Physical Review E*, 77(6):066704, 2008.

[123] L Talon, D Bauer, N Gland, S Youssef, H Auradou, and I Ginzburg. Assessment of the two relaxation time lattice-boltzmann scheme to simulate stokes flow in porous media. *Water Resources Research*, 48(4), 2012.

[124] Irina Ginzburg, Frederik Verhaeghe, and Dominique d'Humieres. Study of simple hydrodynamic solutions with the two-relaxation-times lattice boltzmann scheme. *Communications in computational physics*, 3(3):519–581, 2008.

[125] Guillaume Batot, Laurent Talon, Yannick Peysson, Marc Fleury, and Daniela Bauer. Analytical and numerical investigation of the advective and dispersive transport in herschel–

bulkley fluids by means of a lattice–boltzmann two-relaxation-time scheme. *Chemical Engineering Science*, 141:271–281, 2016.

[126] Jacob N. Israelachvili. *Intermolecular and surface forces / Jacob N. Israelachvili*. Academic Press London ; San Diego, 2nd ed. edition, 1991.

[127] Saurabh S Soni, Nandhibatla V Sastry, Jayant V Joshi, Ekta Seth, and Prem S Goyal. Study on the effects of nonelectrolyte additives on the phase, thermodynamics, and structural changes in micelles of silicone surfactants in aqueous solutions from surface activity, small angle neutron scattering, and viscosity measurements. *Langmuir*, 19(17):6668–6677, 2003.

[128] R Strey. I. experimental facts: water-nonionic surfactant systems, and the effect of additives. *Berichte der Bunsengesellschaft für physikalische Chemie*, 100(3):182–189, 1996.

[129] Mario Corti, Vittorio Degiorgio, and Martin Zulauf. Nonuniversal critical behavior of micellar solutions. *Physical Review Letters*, 48(23):1617, 1982.

[130] Jess P Wilcoxon, James E Martin, and Judy Odinek. Anomalous phase separation kinetics observed in a micelle solution. *Physical review letters*, 75(8):1558, 1995.

[131] R. Atkin, V. S. J. Craig, and S Biggs. Adsorption kinetics and structural arrangements of cationic surfactants on silica surfaces. *Langmuir*, 16:9374–9380, 2000.

[132] Z Király and GH Findenegg. Calorimetric study of the adsorption of short-chain nonionic surfactants on silica glass and graphite: dimethyldecylamine oxide and octyl monoglucoside. *Langmuir*, 16(23):8842–8849, 2000.

[133] Dersy Lugo, Julian Oberdisse, Matthias Karg, Ralf Schweins, and Gerhard H Findenegg. Surface aggregate structure of nonionic surfactants on silica nanoparticles. *Soft Matter*, 5(15):2928–2936, 2009.

[134] R Denoyel, F Giordano, and J Rouquerol. Thermodynamic study of non-ionic—anionic surfactant mixtures: Micellization and adsorption on silica. *Colloids and Surfaces A: Physicochemical and Engineering Aspects*, 76:141–148, 1993.

[135] Rui Zhang and P. Somasundaran. Advances in adsorption of surfactants and their mixtures at solid/solution interfaces. *Advances in Colloid and Interface Science*, 123-126:213 – 229, 2006. Special Issue in Honor of Dr. K. L. Mittal.

[136] J Penfold and RK Thomas. Probing surfactant adsorption at the solid–solution interface by neutron reflectometry. *Interface Science and Technology*, 14:87–115, 2007.

[137] Pierre Levitz and Henri Van Damme. Fluorescence decay study of the adsorption of nonionic surfactants at the solid-liquid interface. 2. influence of polar chain length. *The Journal of Physical Chemistry*, 90(7):1302–1310, 1986.

[138] R Denoyel and J Rouquerol. Thermodynamic (including microcalorimetry) study of the adsorption of nonionic and anionic surfactants onto silica, kaolin, and alumina. *Journal of colloid and interface science*, 143(2):555–572, 1991.

[139] J Penfold, E Staples, I Tucker, and P Cummins. Adsorption of nonionic surfactants on silica sol particles: the effects of sol type and concentration, surfactant type, concentration, and temperature. *The Journal of Physical Chemistry*, 100(46):18133–18137, 1996.

[140] Ying Qiao, Monika Schönhoff, and Gerhard H Findenegg. 2h nmr investigation of the structure and dynamics of the nonionic surfactant c12e5 confined in controlled pore glass. *Langmuir*, 19(15):6160–6167, 2003.

[141] Tae Gyu Shin, Dirk Muter, Jens Meissner, Oskar Paris, and Gerhard H Findenegg. Structural characterization of surfactant aggregates adsorbed in cylindrical silica nanopores. *Langmuir*, 27(9):5252–5263, 2011.

[142] PE Levitz. Adsorption of non ionic surfactants at the solid/water interface. *Colloids and Surfaces A: Physicochemical and Engineering Aspects*, 205(1-2):31–38, 2002.

[143] GH Findenegg and AY Eltekov. Adsorption isotherms of nonionic surfactants in sba-15 measured by micro-column chromatography. *Journal of Chromatography A*, 1150(1-2):236–240, 2007.

[144] Julian Oberdisse. Small angle neutron scattering and model predictions for micelle-decorated colloidal silica beads. *Physical Chemistry Chemical Physics*, 6(7):1557–1561, 2004.

[145] Dersy M Lugo, Julian Oberdisse, Alain Lapp, and Gerhard H Findenegg. Effect of nanoparticle size on the morphology of adsorbed surfactant layers. *The Journal of Physical Chemistry B*, 114(12):4183–4191, 2010.

[146] Chester A Vause and James S Walker. Effects of orientational degrees of freedom in closed-loop solubility phase diagrams. *Physics Letters A*, 90(8):419–424, 1982.

[147] H Bock and KE Gubbins. Anomalous temperature dependence of surfactant self-assembly from aqueous solution. *Physical Review Letters*, 92(13):135701, 2004.

[148] Robert Sips. On the structure of a catalyst surface. ii. *The Journal of Chemical Physics*, 18(8):1024–1026, 1950.

[149] J Toth. State equation of the solid-gas interface layers. *Acta chim. hung.*, 69:311–328, 1971.

[150] M. I. Temkin. Adsorption equilibrium and kinetics of process on non-homogeneous surfaces and in the interaction between adsorbed molecules. *The Journal of Physical Chemistry*, 15:296–332, 1941.

[151] David A Reed and Gert Ehrlich. Surface diffusion, atomic jump rates and thermodynamics. *Surface Science*, 102(2-3):588–609, 1981.

[152] Terrell L.. Hill. *Statistical Mechanics: Principles and Selected Applications*. Dover Publications, 1987.

[153] G Ori, F Villemot, L Viau, A Vioux, and B Coasne. Ionic liquid confined in silica nanopores: molecular dynamics in the isobaric–isothermal ensemble. *Molecular Physics*, 112(9-10):1350–1361, 2014.

[154] KI Falk, RJMP Pellenq, FJ Ulm, and B Coasne. Effect of chain length and pore accessibility on alkane adsorption in kerogen. *Energy & Fuels*, 29(13):7889–7896, 2015.

[155] Maximilien Levesque, Magali Duvail, Ignacio Pagonabarraga, Daan Frenkel, and Benjamin Rotenberg. Accounting for adsorption and desorption in lattice boltzmann simulations. *Physical Review E*, 88(1):013308, 2013.

[156] M Th Van Genuchten, WJ Alves, et al. Analytical solutions of the one-dimensional convective-dispersive solute transport equation. Technical report, United States Department of Agriculture, Economic Research Service, 1982.

Thesis abstract

Surfactant adsorption is receiving increasing attention with numerous physical chemistry applications relevant to both science and engineering fields. This work is devoted to the complex interplay between surfactant adsorption and transport in porous materials. The strong lateral interactions and propensity to form self-assembled mesoscopic objects on adsorbing surfaces lead to a rich phase diagram with complex underlying mechanisms and kinetics. First, to address such difficult issues, a new adsorption formalism for surfactant adsorption is derived. This model is based on adsorption/desorption ratio that are surface concentration-dependent to account for hindered or facilitated adsorption. Additionally, it includes a packing parameter to characterize the aggregated objects so that any mesoscopic self-assemblies – ordered or disordered – can be taken into account in an effective fashion. Second, we investigate the strong impact of adsorption on the mobility of particles during transport processes using a robust numerical scheme: Lattice Boltzmann simulation within the two relaxation time framework. We perform such numerical simulations to elucidate the non-trivial coupling between surfactant adsorption and transport as a function of pore structure/geometry. By modeling the transport of both non-adsorbing and adsorbing surfactants in simple and complex pore structures, we highlight the particular effect of the adsorption/desorption ratio k as well as that of the initial concentration c_0 (for different adsorption models Henry, Langmuir, etc.). The results for the parallel plate geometry show that when small k and c_0 lead to small or negligible adsorption impact on transport. However, for larger values, adsorption significantly alters transport as it drastically increases the dispersion of the adsorbing particles within the confining geometry. The results for more complex/realistic porous geometries indicate that transport is significantly affected by the structure heterogeneity. Adsorption effects lead to a decrease in the displacement variance due to small pore size (i.e. smaller dispersion coefficient) which yields a lower displacement velocity.

Keywords: Surfactant and soft matter, Cooperative interactions, Transport, Adsorption,

Résumé de thèse

L'adsorption de tensioactifs fait l'objet d'une attention croissante avec de nombreuses applications physico-chimiques relevant à la fois des domaines de la science et de l'ingénierie. Ce travail est consacré à l'interaction complexe entre l'adsorption et le transport de molécules tensioactives dans des matériaux poreux. Les fortes interactions latérales et la propension à former des objets mésoscopiques auto-assemblés sur des surfaces adsorbantes conduisent à un riche diagramme de phase avec des mécanismes et une cinétique sous-jacents complexes. Pour répondre à ces questions difficiles, un nouveau modèle d'adsorption des agents de surface est proposé. Ce modèle repose sur des coefficients cinétiques d'adsorption/désorption qui dépendent de la concentration de surface pour tenir compte de l'adsorption entravée ou facilitée. De plus, ce modèle comprend un paramètre d'occupation de surface pour caractériser les objets agrégés de manière à ce que tout auto-assemblage mésoscopique – ordonné ou désordonné – puisse être pris en compte (au moins de manière effective). Dans un deuxième temps, nous étudions le fort impact de l'adsorption sur la mobilité des particules pendant les processus de transport en utilisant un schéma numérique robuste : les simulations de type Lattice Boltzmann combinée à une méthode dite 'deux temps de relaxation'. Nous réalisons ces simulations numériques pour étudier le couplage non trivial entre l'adsorption et le transport des tensioactifs en fonction de la structure/géométrie des pores. En modélisant le transport de tensioactifs adsorbants et non adsorbants dans des structures présentant des pores simples ou complexes, nous mettons en évidence l'effet particulier du rapport d'adsorption/désorption k ainsi que celui de la concentration initiale c_0 (pour différents modèles d'adsorption Henry, Langmuir, etc.). Les résultats pour la géométrie porale de type plans parallèles montrent que des petites valeurs de k et c_0 conduisent à un impact faible ou négligeable de l'adsorption sur le transport. Cependant, pour des valeurs plus élevées, l'adsorption modifie sensiblement le transport car elle augmente considérablement la dispersion des particules adsorbantes dans la géométrie de confinement. Les résultats pour des géométries poreuses plus complexes/réalistes indiquent que le transport est significativement affecté par l'hétérogénéité de la structure. De plus, les effets d'adsorption entraînent une diminution de la variance du déplacement en raison de la petite taille des pores (c'est-à-dire un coefficient de dispersion plus faible), ce qui conduit à un champ de vitesse de déplacement plus faible.

Mots clés: Surfactant et matière molle, Interaction Cooprative, Transport, Adsorption.